







EX LIBRIS  
UNIVERSITATIS  
ALBERTENSIS


---

The Bruce Peel  
Special Collections  
Library









Digitized by the Internet Archive  
in 2025 with funding from  
University of Alberta Library

<https://archive.org/details/0162014920506>





**UNIVERSITY OF ALBERTA**

**Library Release Form**

Name of Author: **Jane S. Eaket**

Title of Thesis: **Use of Stereoscopy for Dam Break Flow Measurement**

Degree: **Master of Science**

Year this Degree Granted: **2001**

Permission is hereby granted to the University of Alberta Library to reproduce single copies of this thesis and to lend or sell such copies for private, scholarly, or scientific research purposes only.

The author reserves all other publication and other rights in association with the copyright in the thesis, and except as hereinbefore provided, neither the thesis nor any substantial portion thereof may be printed or otherwise reproduced in any material form whatever without the author's prior written permission.





UNIVERSITY OF ALBERTA

**USE OF STEREOSCOPY FOR  
DAM BREAK FLOW MEASUREMENT**

by

JANE S. EAKET



A THESIS

SUBMITTED TO THE FACULTY OF GRADUATE STUDIES AND RESEARCH  
IN PARTIAL FULFILLMENT OF THE REQUIREMENTS FOR THE DEGREE OF  
MASTER OF SCIENCE

IN

WATER RESOURCES ENGINEERING

DEPARTMENT OF CIVIL & ENVIRONMENTAL ENGINEERING

EDMONTON, ALBERTA

FALL 2001





**UNIVERSITY OF ALBERTA**

**Faculty of Graduate Studies and Research**

The undersigned certify that they have read, and recommended to the Faculty of Graduate Studies and Research for acceptance, a thesis entitled **Use of Stereoscopy for Dam Break Flow Measurement** submitted by **Jane S. Eaket** in partial fulfillment of the requirements for the degree of **Master of Science in Water Resources Engineering**.





## ACKNOWLEDGEMENTS

The support and guidance provided by my supervisor, Dr. F. E. Hicks, is gratefully acknowledged, particularly during the writing phase of the study. She continually helped me to keep my focus on the “big picture”.

I would also like to sincerely thank Prof. A. E. Peterson for his invaluable assistance with the photogrammetric aspects of the study. His supplying of the photogrammetric equipment and software used in the study is greatly appreciated.

Mr. S. Lovell and Mr. P. Fedun were essential to the experimental phase of the study. Their generous and engaging demeanours made interacting with them a pleasure.

I greatly appreciate Dr. F. Zhou providing his LabView program, which was used to record the data from the wave probes.

My sincere gratitude goes to Dr. P. M. Steffler and Dr. O. Beattie for reviewing my thesis and sitting on my examining committee.

This thesis was financially supported by a Natural Sciences and Engineering Research Council (NSERC) scholarship and through equipment and research funding provided by NSERC. This support is gratefully acknowledged.

Special thanks goes to my parents, Mr. David Eaket and Ms. Dianne Stewart, for their continual support and encouragement throughout many years of academics.

Lastly, I wish to thank my life partner, Mr. Darren Shepherd. He has always been there to give me what I need, whether it is sound advice, loving support, or just a good laugh.



## TABLE OF CONTENTS

1.0	INTRODUCTION.....	1
2.0	LITERATURE REVIEW .....	4
2.1	Stereoscopy.....	4
2.1.1	<i>Theory of Stereoscopy.....</i>	4
2.1.2	<i>Previous Experimental Studies Utilizing Stereoscopy.....</i>	6
	<i>Ankamuthu, Balachandar, and Wood (1999) .....</i>	7
	<i>Obaidat, Al-Suleiman, and Abdul-Jabbar (1997).....</i>	8
2.2	Three-dimensional Dam Break Problem .....	10
2.2.1	<i>General .....</i>	10
2.2.2	<i>Two-Dimensional Numerical Models of the Dam Break Problem .....</i>	11
2.2.3	<i>Previous Experimental Studies .....</i>	15
	<i>Katopodes and Strelkoff (1978) .....</i>	16
	<i>Bellos, Soulis, and Sakkas (1992).....</i>	16
	<i>Bechteler, Kulisch, and Nujic (1992).....</i>	17
	<i>Fraccarollo and Toro (1995).....</i>	18
2.2.4	<i>Experimental Techniques.....</i>	19
	<i>Wave Probes .....</i>	20
	<i>Pressure Transducers .....</i>	21





<b>3.0</b>	<b>EXPERIMENTAL INVESTIGATIONS .....</b>	<b>30</b>
3.1	Experimental Apparatus .....	30
3.1.1	<i>General</i> .....	30
3.1.2	<i>Camera Arrangement</i> .....	33
3.1.3	<i>Camera Calibration</i> .....	34
3.1.4	<i>Wave Probes</i> .....	35
3.2	Experimental Procedure .....	38
3.3	Analysis .....	42
3.3.1	<i>Stereo Cameras</i> .....	42
3.3.2	<i>Wave Probes</i> .....	49
<b>4.0</b>	<b>EXPERIMENTAL RESULTS.....</b>	<b>62</b>
4.1	Stereoscopy.....	62
4.1.1	<i>Error Analysis</i> .....	63
4.1.2	<i>Water Surface Profiles</i> .....	67
4.1.3	<i>Surface Velocity Results</i> .....	70
	<i>Dry-Bed Case</i> .....	71
	<i>Wet-Bed Case</i> .....	73
	<i>Velocity Accuracy</i> .....	74
4.2	Wave Probes .....	77
4.3	Miscellaneous Results .....	80
4.3.1	<i>Three-dimensional Experiments with Tailwater</i> .....	80
4.3.2	<i>Two-dimensional Experiments with Tailwater</i> .....	82
4.3.3	<i>Wave Velocity</i> .....	85





5.0 CONCLUSIONS AND RECOMMENDATIONS..... 159

5.1 Summary and Conclusions ..... 159

5.1.1 Discussion of the Stereoscopy Results ..... 160

5.1.2 Discussion of the Wave Probes Results ..... 162

5.1.3 Discussion of the Results from the Experiments with Tailwater..... 162

5.2 Recommendations for Future Investigations..... 164

REFERENCES.....166

APPENDIX A.....170

APPENDIX B.....205



## LIST OF TABLES

Table	Description	Page
3.1	A summary of dam break experiments performed without tailwater.	50
3.2	A summary of dam break experiments performed with tailwater.	51
4.1	Experiments performed without tailwater for which stereoscopy was used.	88
4.2	Experiments performed with tailwater for which stereoscopy was used.	88





## LIST OF FIGURES

Figure	Description	Page
2.1	Stereoscopic depth perception as a function of parallax angle (Wolf & Dewitt, 2000).	24
2.2(a-b)	The relation between stereoscopic parallax and object elevation (Wolf, 1974).	25
2.3	Plan view of the dam break geometry used in the numerical model study by Katopodes & Strelkoff (1978).	26
2.4	Plan view of the dam break geometry used in the numerical model study by Fennema & Chaudhry (1990).	26
2.5	Experimental dam break geometry as used by Bechteler, Kulish & Nujic (1992).	27
2.6	Plan view of the dam break geometry used in the numerical simulations and experimental study by Fraccarollo & Toro (1995).	28
2.7	Plan view of the dam break geometry used in the numerical model study by Jha, Akiyama & Ura (2000).	28
2.8	Plan view of the experimental dam break geometry used by Bellos, Soulis & Sakkas (1992).	29
3.1	Elevation and plan views of the experimental tank.	52
3.2	Photograph of the VCRs and timer used in the experiments.	53
3.3	Photograph of the trial tracking particles.	53
3.4	Illustration of the field of view of each camera.	54
3.5	Oblique photograph of the calibration points.	55
3.6	Image of the calibration field from camera 2, superimposed with the three-dimensional coordinates (in mm) of the calibration points.	55
3.7	Illustration of the symmetrical probe arrangement (dimensions in m).	56



## LIST OF FIGURES (continued)

Figure	Description	Page
3.8	Illustration of the asymmetrical probe arrangement (dimensions in m).	57
3.9	Oblique photograph illustrating the water and the tracking particles flowing out of the reservoir.	58
3.10	A single video camera image used to illustrate the collinearity condition (Peterson & Durdle, 1991).	59
3.11	An image of <i>XYDIGIT</i> being used to manually determine the image coordinates of the calibration points.	60
3.12	Wave probe calibration for Run 30a.	61
4.1	Illustration of particle streaking for 0.10 m headwater event.	89
4.2	Illustration of particle streaking for 0.20 m headwater event.	89
4.3	Illustration of particle streaking for 0.30 m headwater event.	90
4.4	Illustration of particle tilting for 0.30 m headwater event.	90
4.5	Three-dimensional water surface profiles for Run 10a.	91
4.6	Three-dimensional water surface profiles for Run 10c.	96
4.7	Three-dimensional water surface profiles for Run 20c.	102
4.8	Three-dimensional water surface profiles for Run 30b.	106
4.9	Three-dimensional water surface profiles for Run 30d.	109
4.10	Velocity vectors for Run 10a.	112
4.11	Velocity vectors for Run 10c.	116
4.12	Velocity vectors for Run 20c.	120
4.13	Velocity vectors for Run 30b.	124





## LIST OF FIGURES (continued)

Figure	Description	Page
4.14	Velocity vectors for Run 30d.	126
4.15	Velocity vectors and corresponding images for Run 30-5d.	128
4.16	Velocity vectors and corresponding images for Run 30-10a.	133
4.17	Verification of experimental repeatability and symmetry for 0.10 m headwater.	140
4.18	Verification of experimental repeatability and symmetry for 0.20 m headwater.	141
4.19	Verification of experimental repeatability and symmetry for 0.30 m headwater.	142
4.20	Asymmetrical probe results for Run 10g.	143
4.21	Asymmetrical probe results for Run 20f.	144
4.22	Asymmetrical probe results for Run 30f.	145
4.23	Utilization of symmetry to duplicate the stereoscopy results for Run 30d (time = 0.867s).	146
4.24	Illustration of water flowing around wave probes for Run 30c (time = 0.5 s)	147
4.25	Elevation and plan views of separation zone downstream of a wave probe.	148
4.26	Progression of 6:1 flood wave for three-dimensional dam break (headwater = 0.30 m, tailwater = 0.05 m).	149
4.27	Progression of 3:1 flood wave for three-dimensional dam break (headwater = 0.30 m, tailwater = 0.10 m).	150
4.28	High-speed camera images illustrating the laminar wave followed by turbulent flow.	151



## LIST OF FIGURES (continued)

Figure	Description	Page
4.29	Elevation and plan views of flume used to conduct two-dimensional dam break experiments.	152
4.30	Progression of 6:1 flood wave for two-dimensional dam break (headwater = 0.24 m, tailwater = 0.04 m).	153
4.31	Progression of 3:1 flood wave for two-dimensional dam break (headwater = 0.24 m, tailwater = 0.08 m).	154
4.32	Illustration of roller locations.	155
4.33	Digitizing locations for the determination of wave velocity for the three-dimensional dam break experiments.	156
4.34	Determination of wave velocity for three-dimensional dam break experiments.	157
4.35	Determination of wave velocity for two-dimensional dam break experiments.	158





## LIST OF EQUATIONS

Equation	Description	Page
2-1	The relation between the parallax and height of an object.	5
3-1	The image point location (in camera space coordinates).	43
3-2	The camera location (in object space coordinates).	44
3-3	The object point location (in object space coordinates).	44
3-4	The relation between the image and object space coordinate systems.	44
3-5(a-c)	The components of the rotation matrix used to relate the image and object space coordinate systems.	44
3-6	The rotation matrix used to relate the image and object space coordinate systems.	45
3-7	The expanded relation between the image and object space coordinate systems.	45
3-8	The collinearity equations.	45
3-9	The calibration equations.	46
3-10(a-b)	The radial distortion equation.	46
4-1(a-c)	The interpolated $z$ value at a grid intersection, as used by SigmaPlot.	67-8
4-2	The equation used to determine the velocity error.	75
4-3	The distance travelled by a tracking particle from one frame to the next.	75
4-4(a-b)	The equations used to determine the error in the $x$ and $y$ distances travelled by a tracking particle.	75-6



## LIST OF SYMBOLS

$b$	distance between left and right eyes (eye base) or distance between two cameras
$c, c_x, c_y$	principal distances of the camera
$C_L$	left camera location
$C_R$	right camera location
$d$	distance a tracking particle travels from one frame to the next
$d_a$	distance from the eye to point A
$d_b$	distance from the eye to point B
$d_x$	distance a tracking particle travels in the $x$ direction
$d_y$	distance a tracking particle travels in the $y$ direction
$f$	camera focal length
$H$	height of the cameras above the datum
$H_1$	depth of headwater
$H_2$	depth of tailwater
$h_a$	elevation of point A above the datum
$i$	subscript used to indicate the $i$ th photograph
$j$	subscript used to indicate the $j$ th object point
$k$	scale factor
$K_1, K_2, \text{etc.}$	coefficients of radial distortion
$L$	vector representing the perspective centre of the camera
$L$	subscript used to indicate the perspective centre of the camera



## LIST OF SYMBOLS (continued)

$m$	subscript used to indicate a grid intersection
$\mathbf{M}$	$3 \times 3$ rotation matrix used to relate the object and image space systems
$m_{ab}$	elements of the matrix $\mathbf{M}$ , where a represents the row and b represents the column
$\mathbf{M}_\phi$	rotation matrix about the y-axis
$\mathbf{M}_\kappa$	rotation matrix about the z-axis
$\mathbf{M}_\omega$	rotation matrix about the x-axis
$n$	subscript used to indicate the total number of grid intersections
$o$	subscript used to indicate the principal point
$p$	weight value used to weight distant points in affecting the interpolation value
$\mathbf{p}$	vector representing the location of the image point, in the camera space coordinate system
$\mathbf{P}$	vector representing the location of the object point, in the object space coordinate system
$p_a$	parallax of point A
$r$	intermediate variable used to compute the radial distortion
$t$	time between frames
$v$	tracking particle velocity
$w$	intermediate variable used to compute the interpolated z values
$X, Y, Z$	coordinates defining the location of the object point, in the object space coordinate system
$x_a^l$	location of point A in the left image





## LIST OF SYMBOLS (continued)

$x_a^r$	location of point A in the right image
$x_c, y_c$	coordinates of the exact geometric centre of the image
$X_L, Y_L, Z_L$	coordinates defining the perspective centre of the camera
$x_o, y_o$	coordinates of the principal point
$\sigma_{d_x}$	error in the $x$ distance travelled by a tracking particle
$\sigma_{d_y}$	error in the $y$ distance travelled by a tracking particle
$\delta r$	radial distortion
$\partial v / \partial d$	partial derivative of the velocity equation with respect to distance
$\partial v / \partial t$	partial derivative of the velocity equation with respect to time
$\Delta x$	decentering distortion in the $x$ direction
$\Delta y$	decentering distortion in the $y$ direction
$\phi$	camera orientation angle about the $y$ -axis
$\phi_a$	parallactic angle associated with point A
$\phi_b$	parallactic angle associated with point B
$\kappa$	camera orientation angle about the $z$ -axis
$\sigma_d$	error in the distance travelled by a tracking particle
$\sigma_t$	error in the time between frames
$\sigma_v$	error in the tracking particle velocity
$\omega$	camera orientation angle about the $x$ -axis



## GLOSSARY

Perspective centre	The point in the lens where all the image rays converge.
Principal distance	The distance measured, along the optical axis, from the perspective centre of the lens to the image plane.
Principal point	The point where the optical axis of the camera intersects the image plane.
Fiducial centre	The exact geometric centre of the image.
Radial distortion	The displacement of an image point from its theoretically correct position.
Decentering distortion	Distortion resulting from errors in lens assembly, which affects the rotational symmetry of the lens.





## 1.0 INTRODUCTION

Highly unsteady open channel flow (*i.e.*, dynamic flow) is difficult to measure experimentally. By definition, the shape of the water surface changes rapidly with time, which results in the unsuitability of traditional flow depth measurement techniques used to measure steady flow in the laboratory. Pressure transducers are inapplicable due to the fact that the hydrostatic pressure distribution assumption is invalid because of strong vertical accelerations in the flow; wave probes are inaccurate because of interference with the flow; and point gauges are simply impossible to use due to the rapidly changing water surface. These measurement difficulties lead to the need for a technique to accurately measure dynamic flows.

The objective of this study was to investigate the potential for using video stereoscopy to measure dynamic open channel flows, specifically to measure the water surface profiles and flow velocities associated with scale model dam break events. Stereoscopy is a feasible measurement technique since it does not require the assumption of a hydrostatic pressure distribution, it is non-intrusive, and it is applicable to a rapidly changing water surface profile. The dam break problem was chosen as the focus of this experimental investigation in an attempt to improve the breadth of currently available three-dimensional dam break data, the lack of which can be directly attributed to the aforementioned measurement difficulties. It would be highly desirable to obtain meaningful experimental measurements (depths and velocities) for this and other dynamic open channel flow situations, particularly in terms of providing verification data



for computational models, which could then be used to explore a wider variety of practical flow scenarios.

The inspiration for this measurement approach came from the earlier work of Ankamuthu, Balachandar, and Wood (1999) who used stereoscopy to measure three-dimensional scour in channels. *Stereoscopic viewing* means to see objects in three dimensions. Humans with normal binocular (two-eyed) vision use this process to perceive depths or distances. This human phenomenon can be applied to two photographs of the same area taken from two slightly different perspectives (*i.e.*, stereo photographs). Due to the slightly different camera positions, an object will appear in different locations in each of the two photographs. This displacement between corresponding objects (*i.e.*, parallax) can be used to calculate the elevation of the object. In the past, stereoscopic viewing has most frequently been applied using air photos to obtain quantitative data on the shape of land features. This same process can be applied to close range stereo pairs of photographs in which corresponding points can be accurately located in each of the two images.

The focus of this work is concentrated on three-dimensional dam break flows (as opposed to two-dimensional), since the former is more representative of a prototype dam break. Three-dimensional dam break flows occur when the dam breach occupies only part of the channel width, so the flow spreads laterally as it is released from the dam. The resulting dynamic flow is strongly three-dimensional, in that the flow properties are changing rapidly in the longitudinal, transverse, and vertical directions. Conversely, two-dimensional dam breaks occur when the dam breach occupies the full width of the channel and the flow is restricted from propagating laterally; it simply propagates down



the length of the channel. Since the flow properties are only changing in the longitudinal and transverse directions, the flow is two-dimensional. This scenario rarely occurs in nature.

Since the experimental data for three-dimensional dam breaks is very limited, most numerical models which attempt to model this type of flow have not been experimentally verified. The models developed by the following researchers are examples of numerical models lacking experimental verification: Katopodes and Strelkoff (1978); Fennema and Chaudhry (1990); Alcrudo and Garcia-Navarro (1993); Ghanem, Steffler, Hicks, and Katopodis (1995); and Wang, Ni, and Hi (2000).

The purpose of this thesis is twofold: primarily, to explore a possible measurement technique for dynamic waves propagating in open channels and, secondarily, while completing the first objective, perhaps obtain data describing the three-dimensional dam break problem which may be useful for experimentally validating unsteady flow models. Chapter 2 is used to familiarize the reader with stereoscopy and the three-dimensional dam break problem. The first section is a brief discussion of the theory of stereoscopy, followed by a literature review of stereo imaging techniques. The second section is a literature review of numerical models applied to the dam break problem and previous experimental dam break studies. In Chapter 3 the experimental investigations are explained. This includes a discussion of the experimental apparatus, the calibration method, the experimental procedure, and the analysis technique. Chapter 4 is used to summarize the results obtained from the dam break experiments and to discuss the estimated error. Chapter 5 gives recommendations to be considered in future studies as well as providing a conclusion to the thesis.





## 2.0 LITERATURE REVIEW

The following literature review is intended to familiarize the reader with both stereoscopy and the dam break problem. The first section focuses on stereoscopy, which encompasses the theory of stereoscopy as well as a brief history of previous experimental studies utilizing stereoscopy. The second section gives a detailed explanation of the three-dimensional dam break problem. Within this section is a description of two-dimensional numerical models which have been applied to the dam break problem and previous experimental studies which have attempted to obtain data to verify these numerical models.

### 2.1 Stereoscopy

#### 2.1.1 Theory of Stereoscopy

Humans achieve depth perception through the use of stereoscopy. Figure 2.1 shows left and right eyes separated by a distance  $b$ , termed the eye base. When the eyes focus on an object, the optical axis of the eyes converge to form an angle called the *parallactic angle* (Wolf and Dewitt, 2000). The parallactic angle associated with point  $A$  is  $\phi_a$  and the angle associated with point  $B$  is  $\phi_b$ . As can be seen in the figure, the further away the object is from the eyes, the smaller the angle and vice versa. The brain unconsciously associates the angle  $\phi_a$  with distance  $d_a$  and angle  $\phi_b$  with distance  $d_b$ . The difference between the distances of the two objects,  $d_b - d_a$ , is discerned through the comparison of the two parallactic angles.



Three-dimensional information can be obtained by applying this concept to two photos of the same scene taken from two slightly different perspectives. Although humans use stereoscopy to perceive approximate relative distances, it can be applied to stereo images to calculate more precise distances between objects or to calculate the distance of objects from the camera (Russ, 1995). In practice, this is done at scales ranging from aerial photography to electron microscopy (Russ, 1995).

Object distances can be calculated through the use of *parallax*. Parallax is the lateral displacement of objects, with respect to a reference point, in images taken from two different viewpoints (Russ, 1995). The lateral position of the objects in the images (parallax) is directly related to the distance between the camera and the object (*i.e.*, the elevation of the object). The closer the objects are to the camera, the larger the parallax and vice versa. This principle is illustrated in Figures 2.2a and 2.2b. Figure 2.2a shows images taken from two different cameras locations,  $C_L$  and  $C_R$ . Point  $o$  is the reference point and point  $a$  indicates the position of object  $A$  in the photographs. In Figure 2.2b, the two photographs are shown in superposition. The parallax of point  $A$ ,  $p_a$ , is the difference between the displacement of point  $A$  in the two images (*i.e.*,  $p_a = x_a^l - x_a^r$ ). Based on similar triangles and the knowledge of: the height of the cameras; the distance between the cameras; and the focal length of the cameras, the parallax of the object can be related to the height of the object. The object height equation is:

$$h_a = H - \frac{bf}{p_a} \dots\dots\dots [2-1]$$

where  $h_a$  is the elevation of point  $A$  above the datum,  $H$  is the height of the cameras above the datum,  $b$  is the distance between the cameras,  $f$  is the focal length of the cameras, and  $p_a$  is the parallax of point  $A$ .



To determine the parallax, corresponding points in the stereo images need to be identified. There are two matching approaches: manual and automatic. Manual matching is a simple approach, however it can be quite laborious if a large number of points are to be matched. Conversely, automatic matching is complex to implement, but the points are matched relatively quickly. The algorithms that have been developed for automatic matching can be divided into two groups: area-based matching and feature based matching.... Area-based matching works well if the images are textured and properly lit; however, if the number of identifiable features is limited or if the view angle is wide, the method fails.... Feature based matching is widely used, since it is faster than area-based matching; however, it also fails if the identifiable features in the stereo images are not reliable (Ankamuthu *et al.*, 1999).

### ***2.1.2 Previous Experimental Studies Utilizing Stereoscopy***

Stereoscopy has been used in the past to obtain three-dimensional coordinates from stereo photographs. An extensive literature search revealed that its application to river engineering is limited to one study: Ankamuthu *et al.* (1999) applied stereoscopy to obtain three-dimensional scour depth measurements. The details of this study are discussed below. Two examples of stereoscopy used for other applications are: in 1997, Obaidat, Al-Suleiman, and Abdul-Jabbar used stereovision to quantify pavement rut depth; and in 1998, Obaidat and Al-Masaeid used the same technology, with minor enhancements, to map a historical statue. The former study is discussed in detail, however the latter study is not discussed due to similarities with the 1997 research.



*Ankamuthu, Balachandar, and Wood (1999)*

The goal of this study was to develop a video image analysis system to measure the three-dimensional coordinates of an eroded sand bed. To do this, two video cameras, with similar specifications, were mounted over the sand bed model and images were simultaneously captured. The stand the cameras were mounted on could be adjusted so that the elevation of the cameras over the bed and the view angle of the cameras could be varied. The cameras were calibrated by placing eleven objects of known position on the sand bed. Their heights ranged from 9.5 to 38.5 cm. To establish a frame of reference between the two stereo images of the eroded sand bed, stones were placed on the bed prior to the images being taken.

Although details of the experimental procedure were not provided, the methodology outlined below is consistent with virtually all stereoscopic experiments. Stereo images would have been taken of the calibration objects on the sand bed. This could have been done either before or after the sand bed was eroded. Using the images of the calibration objects and their known heights, the cameras would have been calibrated. As a point of reference, stones were placed on the eroded sand bed and then stereo images were captured. The corresponding stones in the sand bed stereo images were automatically matched using a feature-based matching technique. More information about this procedure can be found in the original reference. The three-dimensional coordinates of these stones were determined using the camera calibration and the parallax between the matched points.

The scour depths resulting from the stereoscopy were not compared to the actual scour depths, so an error estimation is not available. The manual matching of the image





points was compared with the automatic matching. Since the number of false matches was few, it was concluded that the automatic matching technique worked well. However, when fewer stones were placed on the sand surface, the automatic matching worked poorly. This was due to the lack of distinguishable features in the images.

***Obaidat, Al-Suleiman, and Abdul-Jabbar (1997)***

In this study, stereovision was used to quantify pavement rut depth. The experimental setup consisted of two camcorders, with identical specifications, mounted such that the distance between the cameras was fixed at 0.80 m. The cameras were then mounted on a 1.3 m high stand. Images from the two cameras were simultaneously captured. A planar wall containing approximately 50 image calibration points was used as the calibration facility. The camera stand was set up in front of the calibration wall to obtain the calibration stereo images. To capture stereo images of the rutted pavement areas, this stand was placed on the trunk of a stationary vehicle or on the surface of the pavement. To establish a frame of reference between the two stereo images, white dots, sized three to four pixels (*i.e.*, 4.5 to 6.0 cm), were sprayed onto the surface of the pavement.

To obtain the three-dimensional coordinates for the pavement ruts, the researchers used the following methodology: (1) stereo images of the calibration wall were captured; (2) stereo images of the pavement rut area were captured; (3) as a precaution, stereo images of the calibration facility were recaptured; (4) the images were digitized; (5) the image coordinates for the calibration stereo images were manually determined; (6) the camera calibration parameters were calculated using the calibration wall image



coordinates and their corresponding three-dimensional coordinates; (7) image coordinates of the white dots in the pavement rut stereo images were manually determined; and (8) the camera calibration parameters and the parallax of the white dot image coordinates were used to calculate the three-dimensional coordinates of the white dots.

The three-dimensional stereoscopy coordinates of the white dots were compared to the measured coordinates. It was determined that the stereovision method had an error of approximately one pixel (*i.e.*, 1.5 cm). This error is substantial as typical rut depths were in the order of 1 cm. The researchers attributed some of this error to the large dot size, however the dots had to be made large enough to enable manual matching. It was found that the human matching error of the dots varied between 1 and 2 pixels (*i.e.*, 1.5 to 3.0 cm). Other sources of error were due to lack of repeatability in the camera set up, low image resolution (752 by 480 pixels), and manual matching of the image points. The researchers concluded that the scale, resolution, camera configuration, and camera stability should be further investigated. They also emphasized the importance of automating the matching of the points in the stereo images.



## **2.2 Three-dimensional Dam Break Problem**

The intention of this section is to give the reader an overview of the previous computational and experimental research completed on the three-dimensional dam break problem. The first sub-section is a general explanation of the dam break problem. This is followed by a literature review focusing on two-dimensional numerical models which have been applied to the lateral spreading of flow released from a dam breach. The final sub-section summarizes the experimental dam break studies that have been completed to date.

### **2.2.1 General**

When a dam fails, the breached portion usually does not encompass the full width of the channel, so the flow spreads laterally as it releases. In some cases the dammed river possesses a floodplain and the flow will overtop the river banks and spread out into the floodplain. The resulting dynamic flow is strongly three-dimensional, in that the flow properties are changing rapidly in the longitudinal, transverse, and vertical directions. Even in the simplest cases, where the dam break flood is contained in the channel (*e.g.*, entrenched rivers) there will still be a region near the dam itself where the flow will be highly three-dimensional. This is because the breached section of the failed dam rarely encompasses the full width of the structure.

When these types of flood waves are modelled numerically, the flow properties are generally assumed to be uniform in the vertical direction. This simplification greatly reduces the data and computer requirements, since two-dimensional flows can be approximated with one-dimensional computational models and three-dimensional flows





can be approximated with two-dimensional models. Generally one-dimensional models are used to analyze long river reaches where variations of flow properties across the channel and throughout the depth are not important. However, they provide crude results in the immediate vicinity of the dam for cases where a partial breach occurs.

Consequently, a number of researchers have been investigating the development of two-dimensional numerical models to model the spreading flow in the vicinity of the breach. Unfortunately, there is still very little data available with which to verify these models.

### ***2.2.2 Two-Dimensional Numerical Models of the Dam Break Problem***

A number of researchers have formulated two-dimensional models and numerical schemes, which attempt to compute the flood waves in the zone close to the dam. The researchers recognize that the flow in this area, where the water is spreading laterally, is highly three-dimensional. This zone has often been modelled with one-dimensional models; however it is acknowledged by both Katopodes and Strelkoff (1978) and Fennema and Chaudhry (1990) that, at the very minimum, a two-dimensional model should be used.

Many different numerical schemes have been used by researchers; however, when the models are applied certain commonalities are apparent. When testing the models, all of the researchers used a partial dam breach in a simple rectangular channel (*i.e.*, the breach was narrower than the receiving channel). All the researchers admitted that experimental data is required to verify their model results; however few were able to do so, because of a paucity of such data.



In 1978, Katopodes and Strelkoff constructed a two-dimensional dam break model based on the method of characteristics. The model was tested by performing a number of computational runs consisting of a 1.0 ft (0.305 m) high dam failing over 33 % of its width in a 4.0 ft (1.21 m) wide rectangular channel with a dry downstream bed (see Figure 2.3). The bed slope in the direction of flow was 0.5 % and 0.009 was used as the Manning's roughness. Their approximations were qualitatively compared to the results of a simple laboratory experiment that they conducted as part of their study. Katopodes and Strelkoff emphasized the need for quantitative experimental data for verification of two-dimensional dam break models.

In 1990, Fennema and Chaudhry used both the MacCormack and Gabutti two-dimensional, explicit finite-difference schemes to approximate flows resulting from a dam break. They tested the schemes by modelling a partial, nonsymmetrical dam breach in a 200 m long by 200 m wide channel. The breach was 75 m wide and the dam was 10 m long (in the direction of flow). The channel, as shown in Figure 2.4, was assumed to be frictionless and horizontal with 10 m of water upstream of the dam and 5 m of water downstream of the dam. Fennema and Chaudhry (1990) compared their results from the MacCormack and Gabutti schemes to each other and to the results of the Beam and Warming scheme (Fennema, 1985). Unfortunately, these comparisons were not entirely meaningful since, without experimental data, it was unknown which, if any, of the models produced accurate results.

Bechteler, Kulisch, and Nujic (1992) discussed, in a conference paper, their use of the two-dimensional MacCormack finite difference and Runge Kutta finite volume schemes to simulate the flood waves resulting from a dam breach. The problems tested



computationally were based on experiments they conducted themselves (and reported in this same conference paper). It involved a computational domain consisting of a 5 m wide by 10 m long plate with an adjustable slope. As illustrated in Figure 2.5, a channel (2 m wide by 30 m long) ran alongside the plate in the direction of the 10 m length. There was a breach in the side of the channel that allowed the water to spill out onto the plate. Open boundaries existed on three sides of the plate, thus the water could fall off the plate into a basin. Two of the experiments involving different plate slopes were presented; the first with a horizontal plate and the second with an inclined slope of 3 %. For both cases, the initial depth in the channel was 0.2 m. The results of the numerical tests were compared to those obtained from the physical model, with very good agreement.

In 1993, Alcrudo and Garcia-Navarro modelled the dam break problem by using a two-dimensional, finite volume technique based on a high-order Godunov type scheme. They used the same testing configuration that was presented by Fennema and Chaudhry (1990) (see Figure 2.4); computational predictions were not compared to other computational or experimental data.

Fraccarollo and Toro (1995) also used a two-dimensional Godunov type scheme to model the dam break problem. The problems tested computationally were based on their own experiments (described in the same paper), which, as illustrated in Figure 2.6, consisted of a channel 3.0 m long by 2.0 m wide with a symmetrical partial dam breach dividing the 1.0 m long upstream section from the 2.0 m long downstream section. Two series of simulations were performed. A horizontal channel and an upstream depth of 0.6 m was used for the first test and a channel slope of 7 % and an upstream depth of 0.64 m,



measured at the dam site, was used for the second test. Both tests were conducted for the case of a dry bed downstream. Stage hydrographs were used at different points in the computational domain to compare the numerical results to their experimental results with fair agreement.

In 1995, Ghanem, Steffler, Hicks, and Katopodis presented the two-dimensional version of the Characteristic-Dissipative-Galerkin (CDG) finite element model. To evaluate the performance of the model, Ghanem *et al.* (1995) numerically simulated a partial dam breach using the same dam configuration introduced by Fennema and Chaudhry in 1990 (see Figure 2.4). The results of the CDG scheme were compared to the results of the MacCormack and Gabutti schemes (Fennema and Chaudhry, 1990) and the results of the Beam and Warming scheme (Fennema, 1985), however they were not compared to any experimental data. Ghanem *et al.* (1995) stated that due to a lack of experimental data, the accuracy of the CDG scheme could not be verified.

Jha *et al.* (2000) presented two two-dimensional numerical models for computing dam break flood flows. One of the models was based on Roe's numerical flux and the other model was based on the Lax-Wendroff numerical flux. As shown in Figure 2.7, they tested their model using the same dam configuration as Fraccarollo and Toro (1995), except the length of the area downstream of the dam was extended by one metre. Like Fraccarollo and Toro (1995), they tested two cases of bed slope: horizontal and 7 %. The upstream water depths tested were 0.60 m and 0.64 m in the cases of the horizontal and sloping bed, respectively. For both scenarios, the area downstream of the dam was modelled as dry. The models were verified by comparing the numerical data to the





experimental dam break data collected by Fraccarollo and Toro (1995) and the agreement was fair.

In 2000, a hybrid type of total variation diminishing (TVD) finite difference scheme was presented by Wang, Ni, and Hi. The model was tested using Fennema and Chaudhry's (1990) partial, nonsymmetrical dam breach configuration, which is shown in Figure 2.4. They performed wet bed tests with 10 m of water upstream and 5 m of water downstream, and dry bed tests using the same upstream water level. The computational results were not experimentally validated.

It is apparent that there has been extensive research done into developing two-dimensional numerical models to predict the flow characteristics in the zone immediately downstream of a partial dam breach. However, to date, very few of these models have actually been verified, and this can be primarily attributed to a serious lack of experimental data. Furthermore, as we will see in the next section, the experimental data that is available is quite limited and, in some cases, is of questionable accuracy.

### ***2.2.3 Previous Experimental Studies***

Only four experimental studies of the two-dimensional dam break problem are reported in the literature; of these four studies, three deal with unconfined lateral spreading of flow in the area immediately downstream of the dam and of these three, only one has been published as a conference paper. Although these researchers generally refer to their experiments as two-dimensional, they are actually three-dimensional.



Experiments were performed by Katopodes and Strelkoff in 1978; by Bellos, Soulis, and Sakkas in 1992; by Bechteler, Kulisch, and Nujic in 1992; and by Fraccarollo and Toro in 1995. These experiments will be discussed below. One set of experiments that were found in the literature but will not be discussed were performed by Bell, Elliot, and Chaudhry (1992). The title of their journal article, “Experimental results of two-dimensional dam break flows”, leads one to believe that the research would be relevant to this thesis. However, their experiments were performed in a 180-degree curved channel and therefore are not relevant. The sub-section will conclude with a summary of the experimental techniques used by the researchers in their experiments.

#### ***Katopodes and Strelkoff (1978)***

One of the earliest experimental studies reported in the literature was a qualitative study performed by Katopodes and Strelkoff (1978). A simple experiment was set up in which there was a narrow breach in a barrier that divided the upstream part of the flume from the downstream part of the flume (see Figure 2.3). Water flowed through this breach like a jet and caused standing waves to form on the sidewalls of the flume. Photos were taken of this experiment and then qualitatively compared to numerical modelling efforts.

#### ***Bellos, Soulis, and Sakkas (1992)***

The first major quantitative experiments on two-dimensional dam breaks were performed in 1992 by Bellos *et al.*. These experiments were conducted in a converging-diverging flume, which is pictured in Figure 2.8. The flume was 21.2 m long, 1.40 m



wide, and 0.60 m deep. The ‘dam’ was located at the narrowest point of the variable width section of the flume. A movable plexi-glass gate was manually raised to simulate an instantaneous dam break. The water depth variation with time was measured at eight locations along the centreline of the flume. Since the flow was not allowed to spread laterally once released from the gate, but instead was confined by the flume sidewalls, their experiments are not relevant to this work. However, the experimental techniques used are common to all dam break experiments to date, thus, they are discussed in section 2.2.4, entitled, Experimental Techniques.

***Bechteler, Kulisch, and Nujic (1992)***

In a 1992 conference paper, Bechteler *et al.* summarized their three-dimensional dam break experiments. Although they commented that they did not have space in the conference paper to present a lot of details, they unfortunately do not seem to have published subsequently in a journal. As illustrated in Figure 2.5, the experimental apparatus consisted of a channel (2 m wide by 30 m long) with a 5 m wide by 10 m long plate running alongside the channel. The plate had an adjustable slope and open boundaries on all three sides, so that the released flow could freely spread laterally with the water falling off the plate at the edges. There was a breach in the side of the channel (see Figure 2.5 for breach geometry), which was initially closed by a flap. When the flap was opened, a dam break was simulated and the water was allowed to spill out onto the plate. Due to the open boundaries on the receiving plate, the experiments were limited to the case of an initially dry plate.





Two experiments with different plate slopes were presented in the conference paper. The first experiment involved a horizontal slope and the second an inclined slope of 3 %. For both experiments, the initial depth in the channel was 0.2 m. The variation of water depth with respect to time was measured at thirty locations spaced out on one half of the plate. Also, the leading edge propagation was recorded by a video camera installed above the plate. Using the measured water depths, the leading edge propagation, and the assumption that the shape of the flood wave was symmetrical, the whole shape of the free surface was reconstructed. For the case of the horizontal plate, the results were displayed as stage hydrographs for four locations along the edge of the plate. The maximum difference between the measured and calculated stage hydrographs was approximately 1.0 cm. A three-dimensional view of the flood wave (at a time of 2.1 seconds after release) was also used to illustrate these results. The free surface of the flood wave appeared smooth. For the case of 3 % slope, the results were presented as stage hydrographs at three locations along the edge of the plate. The inclination of the plate resulted in the formation of a hydraulic jump that developed in the outer region of the plate and quickly moved toward the breach. Again, the maximum difference between the measured and calculated stage hydrographs was approximately 1.0 cm.

### ***Fraccarollo and Toro (1995)***

Figure 2.6 illustrates the test apparatus used in these experiments, consisting of a tank 3.0 m in length and 2.0 m in width. The dam rupture was simulated by the sudden removal of a gate activated by a pneumatic cylinder. This automatic opening ensured that the gate was lifted in less than 0.1 s. Upstream of the gate there was a 1 m long by 2



m wide storage tank. The storage tank could be filled with water to a maximum height of 0.80 m. The area downstream of the gate was 2 m in length by 2 m in width and had open boundaries on all three sides. Due to the open boundaries, the experiments were limited to the dry-bed condition. The gate was centered within the channel and had a width of 0.40 m. The bottom slope of the tank was varied from 0 % to 10 %.

The researchers performed experiments with bottom slopes of 0 % and 7 % and initial upstream water depths, measured at the gate, of 0.60 m and 0.64 m, respectively. Using different initial depths resulted in storage of the same approximate water volume in the tank prior to the experiment. The water depth and the  $x$  and  $z$  velocity components were measured with respect to time at fourteen locations distributed over the upstream and downstream sides of the gate. The measured depths were presented as stage hydrographs and the measured velocity components were presented as velocity versus time graphs. The velocity measurements started at a height 0.05 m from the bottom and increased in increments of 0.05 m to a height of 0.40 m from the bottom. Fraccarollo and Toro (1995) then took an average of the measurements over the depth for comparisons with two-dimensional models. Upstream of the gate this depth averaged velocity showed an oscillating pattern that was gradually decreasing. At the gate the velocity also showed a decreasing trend, however there were no oscillations.

#### **2.2.4 Experimental Techniques**

In the various studies, two different techniques were used to measure the flow depths with time. Bellos *et al.* (1992) used wave probes and pressure transducers to measure the water depths. Four wave probes were used upstream of the gate location and



four pressure transducers were used downstream of the gate. Bechteler *et al.* (1992) used only pressure transducers. Fraccarollo and Toro (1995) measured the water depths with both wave probes and pressure transducers. With a few exceptions, wave probes were used upstream of the gate and pressure transducers were used downstream of the gate. In addition, Fraccarollo and Toro (1995) measured velocity components by use of an electromagnetic velocity meter.

### ***Wave Probes***

Both Bellos *et al.* (1992) and Fraccarollo and Toro (1995) used wave probes to measure the water depth with respect to time. Each wave probe used by Bellos *et al.* (1992) was made up of a pair of 500 mm long stainless steel rods, 3 mm in diameter, spaced 8 mm apart, with a frequency response of up to 1000 Hz. The principle of their operation was based on the electrical conductivity of the water depth between the two rods. The output was in the form of a voltage, which was then converted to a depth. Bellos *et al.* (1992) stated that the use of wave probes was limited to areas of subcritical and critical flow (upstream of and at the gate). They were not used in supercritical flow (downstream of the gate) because of the strong wakes resulting from the probe-flow interaction.

Fraccarollo and Toro (1995) used wave probes composed of a pair of stretched 0.3 mm wires spaced about 10 mm apart, with a fixed sampling rate of 100 Hz. The wires were made of nickel and chrome. Like the wave probes used by Bellos *et al.* (1992), the output voltage was obtained by measuring the electrical conductivity of the water depth between the wires. Since the diameter of the wires used by Fraccarollo and



Toro (1995) was one-tenth the diameter of the rods used by Bellos *et al.* (1992), Fraccarollo and Toro (1995) were able to use their wave metres in supercritical flow regimes (downstream of the gate). They found that the small diameter wires did not significantly impact the flow. Fraccarollo and Toro (1995) discovered that the response of the wave probe was strongly influenced by temperature and salt concentration in the water, thus, the wave probes had to be calibrated frequently in still water.

### ***Pressure Transducers***

Pressure transducers were used by Bellos *et al.* (1992), Bechteler *et al.* (1992), and Fraccarollo and Toro (1995) to measure the pressure at the base of the tank or channel. This pressure was then converted to depth by assuming the water above had a hydrostatic pressure distribution (which provides a linear relationship between pressure and depth).

Bellos *et al.* (1992) measured the static pressure with absolute piezoresistive transducers. The transducers were placed in 4 mm diameter pressure tappings on the bottom of the channel. They were of type 4043A made by Kistler Instrument AG, Swiss. The hydrostatic pressure distribution assumption was believed to be valid everywhere except for near the leading edge of the wave. Bellos *et al.* (1992) believed that the error introduced by this assumption was not significant and would be eliminated soon after an adequate flow depth was established.

Bechteler *et al.* (1992) also used pressure transducers to measure the static pressure as a function of time. By assuming a hydrostatic pressure distribution, the





depth, as a function of time, was calculated. This conference paper did not give any additional details about the pressure transducers.

Pressure transducers were also used by Fraccarollo and Toro (1995) to measure the static pressure values, as a function of time, at the bottom of the water column. Pressure tapings were drilled in the bottom of the experimental apparatus in which the BHL 4310 low range pressure transducer, produced by IMO Transinstruments, was placed. By assuming a hydrostatic pressure distribution, the pressure gauges gave an indirect measurement of depth, with respect to time.

Although not investigated by the researchers, it is necessary to assess the hydrostatic pressure assumption. Thinking intuitively, it would likely be concluded that the hydrostatic pressure assumption was not valid at the gate or in the immediate vicinity of the gate because of the large vertical accelerations that would be present as the water released. This conclusion was confirmed by Fraccarollo and Toro's (1995) experiments. There were two locations at the gate where the depth was measured with both a wave probe and a pressure transducer. The initial depths predicted by the pressure transducer and the wave metre were 0.2 m and 0.35 m, respectively. With time, the difference between the two measurements became smaller. There was one location upstream and downstream of the gate where Fraccarollo and Toro (1995) took measurements with a pressure transducer and a wave probe. Both upstream and downstream of the gate, the two measured depths were in close agreement with each other. This lead to the conclusion that the hydrostatic assumption was valid everywhere, except in the immediate vicinity of the gate.



Only two researchers have obtained experimental data for three-dimensional dam breaks. Bechteler et al. (1992) did acquire measurements, however their data has not been used by other researchers to validate numerical models. This may be due to the lack of stage hydrographs published, and the fact that their breach geometry is complex and may be difficult to model numerically. It also may be because they used only pressure transducers to measure the water depths and it is believed that the pressure distribution in the area of the gate is not hydrostatic, therefore their experimental results may be inaccurate.

Fraccarollo and Toro (1995) also obtained three-dimensional dam break data and their experiments are the most valuable experiments of this kind to date. They presented numerous stage hydrographs and their experimental setup is very simple. They used both wave metres and pressure transducers to measure the depths. Their data has been used by Jha et al. (2000) to validate a computational model.

There is obviously an acute lack of research in this area. More studies would be beneficial, so the results of different studies can be compared to each other. Improvements are also needed in terms of the measurement techniques, given that, at the gate and in the immediate vicinity of the gate, the hydrostatic assumption is not valid. Wave probes have been used to obtain accurate depth measurements, however, due to the large velocities, thick probes cannot be used effectively in the areas of supercritical flow and thin probes are sensitive to water chemistry. A non-intrusive measuring technique, which does not assume a hydrostatic pressure distribution, would be valuable.



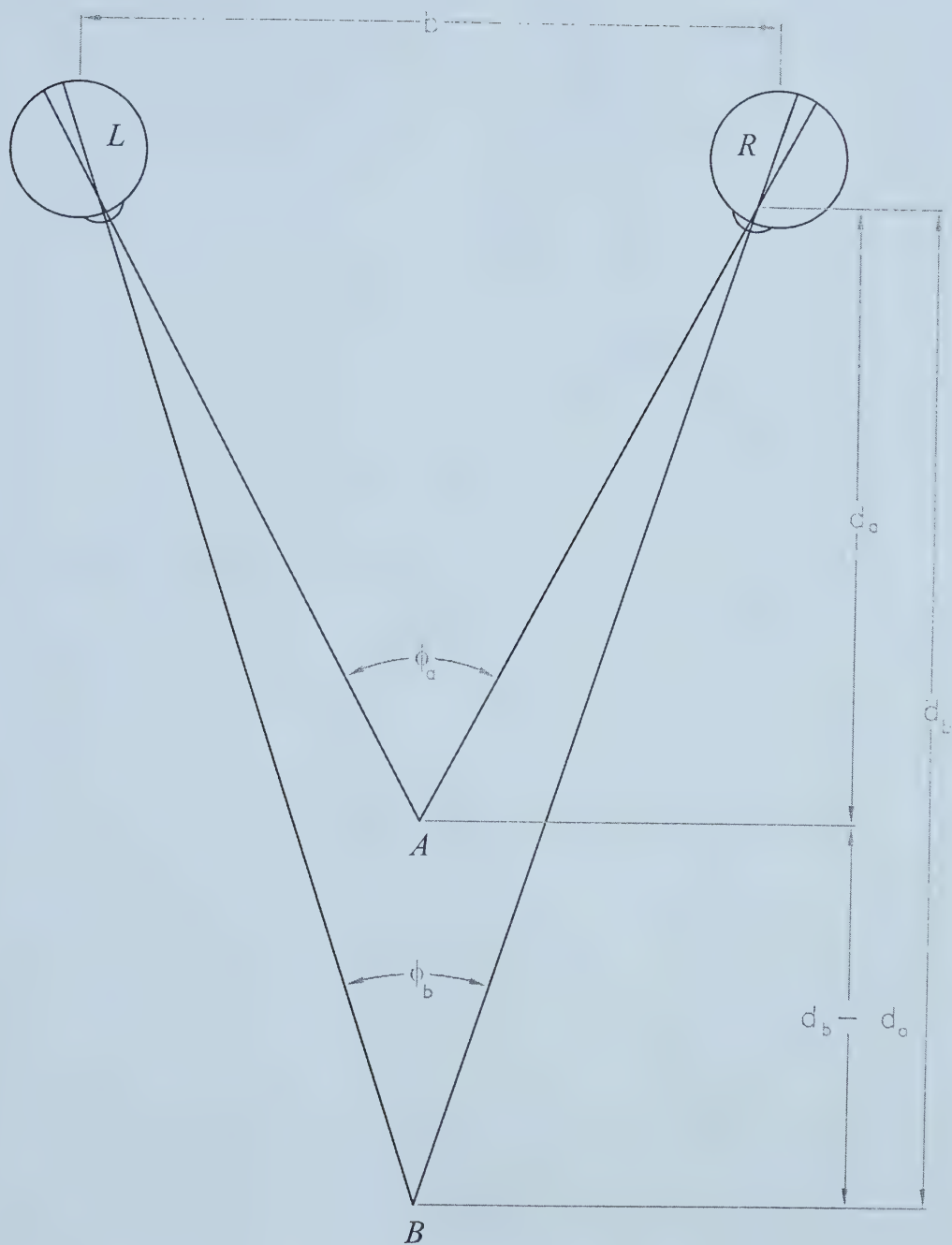
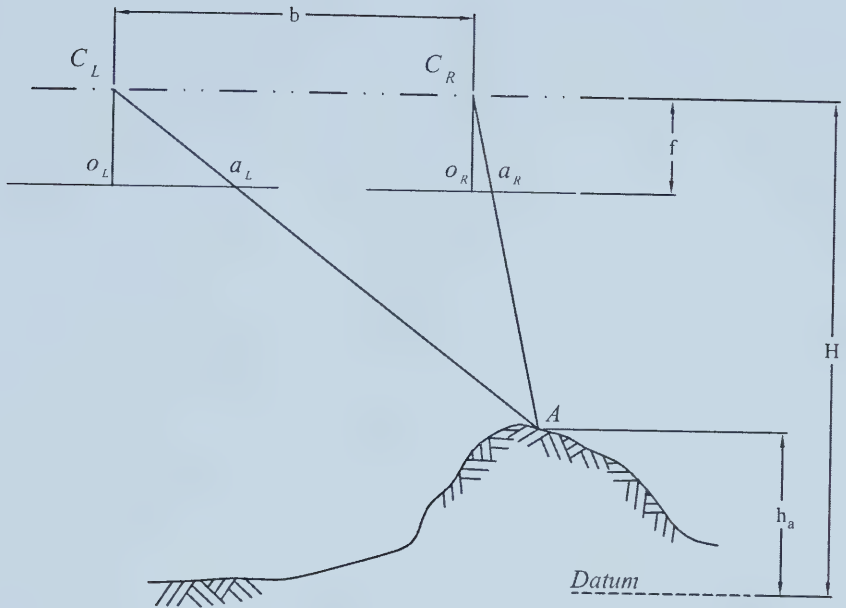


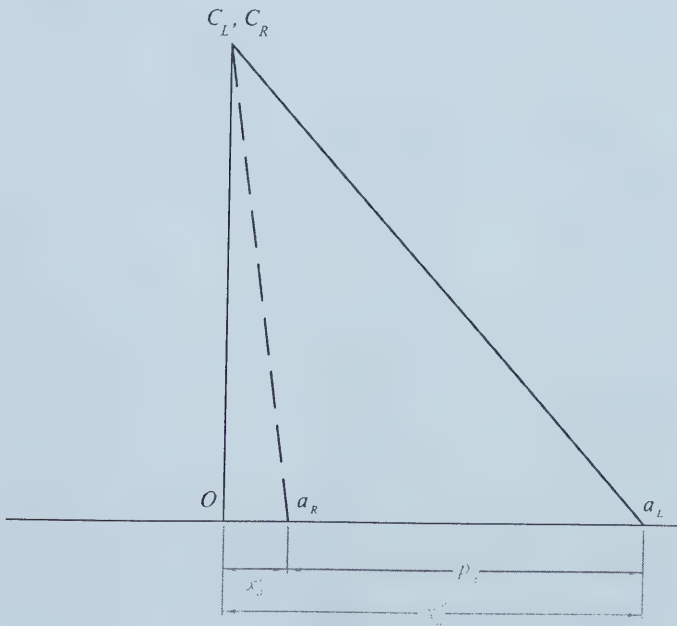
Figure 2.1: Stereoscopic depth perception as a function of parallax angle (Wolf & Dewitt, 2000).







a) Left and right images taken of point 'A'.



b) The left and right images shown in superposition.

Figure 2.2: The relation between stereoscopic parallax and object elevation (Wolf, 1974).



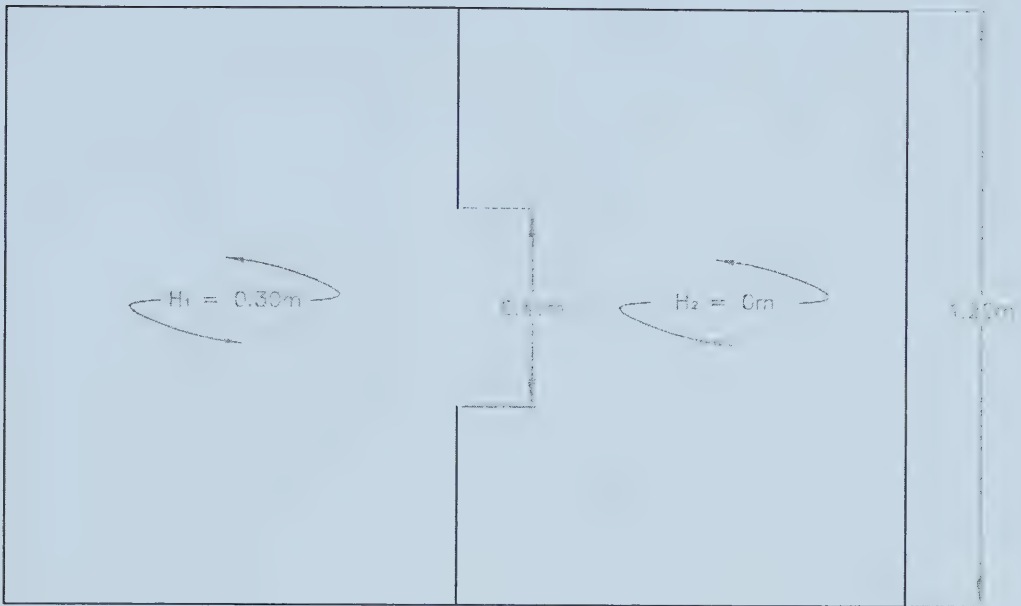


Figure 2.3: Plan view of the dam break geometry used in the numerical model study by Katopodes & Strelkoff (1978).

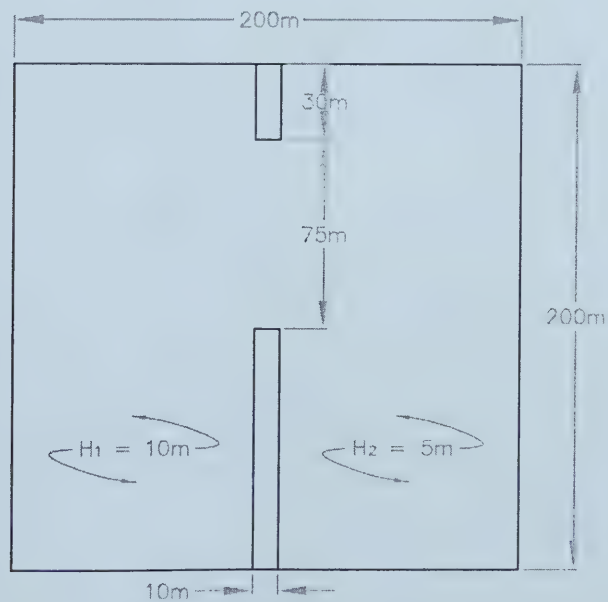


Figure 2.4: Plan view of the dam break geometry used in the numerical model study by Fennema & Chaudhry (1990).



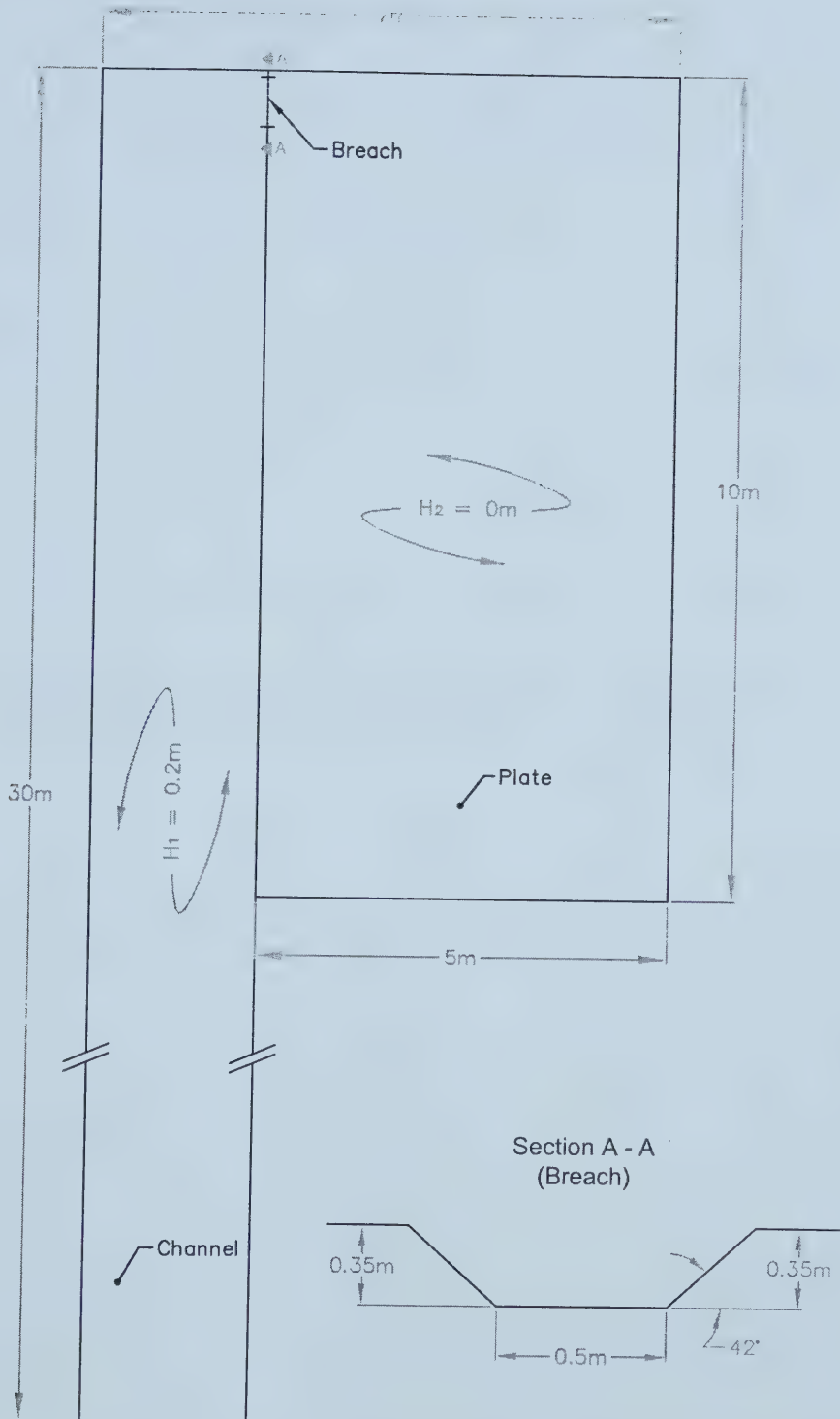


Figure 2.5: Experimental dam break geometry as used by Bechteler, Kulish & Nujic (1992).



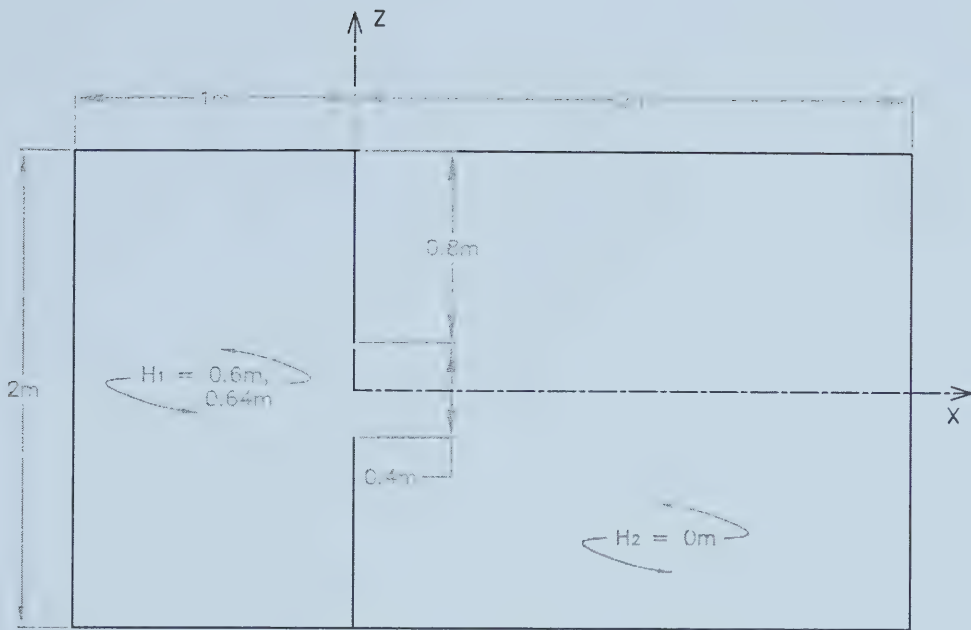


Figure 2.6: Plan view of the dam break geometry used in the numerical simulations and experimental study by Fraccarollo & Toro (1995).

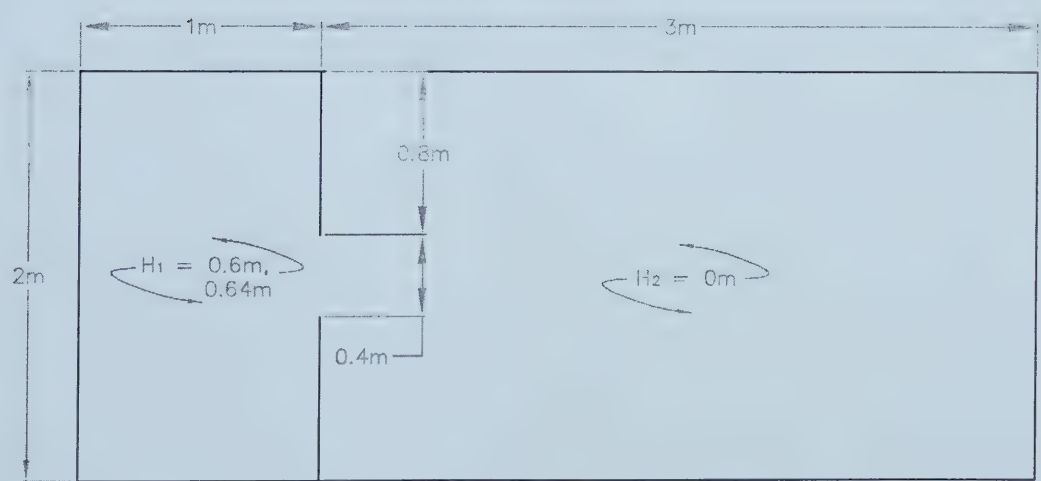


Figure 2.7: Plan view of the dam break geometry used in the numerical model study by Jha, Akiyama & Ura (2000).





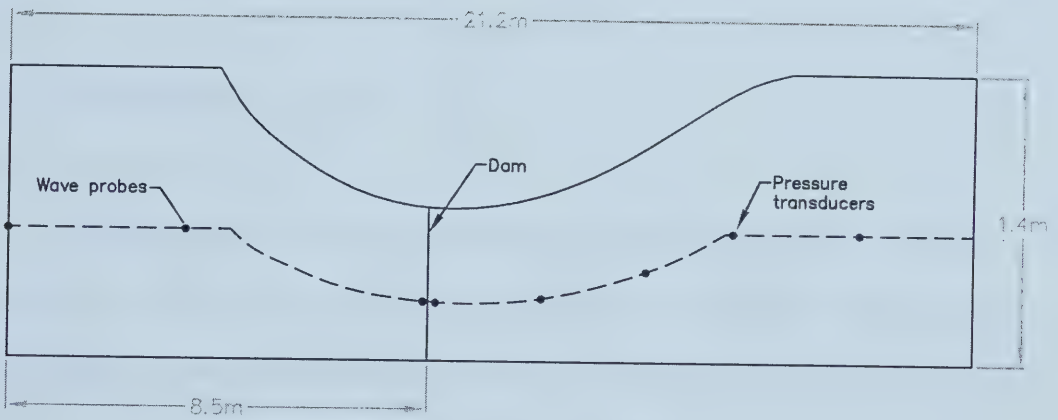


Figure 2.8: Plan view of the experimental dam break geometry used by Bellos, Soulis and Sakkas (1992).



### 3.0 EXPERIMENTAL INVESTIGATIONS

The objective of this chapter is to familiarize the reader with specific aspects of the experimental investigation. The first section deals with the apparatus used to perform the experiments. Within this section is an explanation as to what was done prior to performing the experiments. This is followed by the experimental procedure, which provides a summary of steps taken during the experiments. The chapter concludes with a section discussing the analysis performed.

#### 3.1 Experimental Apparatus

##### 3.1.1 *General*

The experiments were conducted at the University of Alberta in the T. Blench Hydraulics Laboratory. They were performed in the 2.31 m wide by 4.75 m long by 1.23 m deep tank, depicted in Figure 3.1. The tank has Plexiglas walls and a sheet metal floor. The length of the tank was divided in half by a wooden dam that was 0.36 m high. Centered across the dam was a movable sheet metal gate, which could be manually raised to simulate a dam break event. Downstream of the gate, a black grid, spaced 0.20 m square, was superimposed over a white floor. A brace that was adjustable in height was installed above the tank. Three video cameras (used for stereoscopy) were attached to this brace and positioned over the downstream half of the tank, as shown by Figure 3.1.

The cameras were JVC colour video camera heads (model number TK-12800) with Cosmimar/ Pentax lenses (6 mm, F/1.2). The adjustable shutter speed was set at 1/60 second. Three JVC Super-VHS video cassette recorders (VCRs) were used to record the



dam break event onto Super-VHS video tapes. A timer connected to the VCRs displayed the time of the experiment in terms of hour, minute, second, and frame number. This time was stamped onto the video images from each camera and was used to synchronize the images obtained from the three cameras. The VCRs recorded in the standard format of 30 frames per second. This setup can be seen in Figure 3.2.

In addition to using video cameras to record the dam break events, a high-speed digital camera was also used. It was a Motion Scope camera made by Redlake Imaging Corporation (USA), model PCI 1000 s (No. 1108-0008). Unlike the video cameras, which were used for stereoscopy, the high-speed camera was used to gain qualitative information about the dam break event and to quantify the gate opening time. The recording speed of the camera could be set to record from 60 to 1000 frames per second. As the recording speed increased, the requirement for light increased, and the image resolution decreased. When the images were being used primarily to gain an understanding of the wave behaviour, the recording speed was set to 60 frames per second. For the experiments which quantified the gate opening time, extra light was provided and the recording speed was set to 125 frames per second. To obtain a satisfactory view of the gate, the camera was mounted such that its focus was zoomed in on the downstream side of the gate. By viewing these images, the lifting of the gate could be seen and the time could be estimated. The gate lifting time was assessed for all the headwater and tailwater scenarios.

The start and finish times of the experiments were estimated. The dam break event started when the lifting of the gate was initiated. To simplify the determination of this point in time, a light bulb fixed to the top of the dam came on when the gate was





closed and turned off when the gate lifting started. Thus, by viewing the images of the dam break event, and noting the time at which the light turned off, the initiation of the event (and the exact frame) was determined. Estimating the finish time of the experiments involved keen observation of each dam break event. It was determined that when the water was released from the reservoir, the wave reached the sides of the tank before it reached the end of the tank. When the wave hit the sidewalls it was reflected back towards the centre of the tank. The water was no longer free flowing once it came into contact with the walls of the tank; it was influenced by the tank walls. Therefore, the experiment was considered to be complete at this point.

To perform the stereoscopy there was a requirement for recognizable features on the water surface that would be apparent in each camera image. By determining the three-dimensional coordinates of these features, the water surface profile could be resolved. For the sake of accuracy, it was desirable to make these features (*i.e.*, tracking particles) as small as possible; however, it was also necessary for the tracking particles to be large enough to be visible in the camera images. To find the optimal size, a number of different particles were tested (see Figure 3.3). The particles were placed on the water surface and, as the water was released through the gate opening, they were carried along with the flow. All of the trial particles were black in colour, since black is the most contrasting to the white background of the tank floor. Plastic was chosen as the particle material so that the tracking particles would float on the water surface during the dam break event. The 23 mm square particle was chosen to be the optimal size, since it was the smallest particle that could be distinguished in the stereo images during a dam break event.



### 3.1.2 Camera Arrangement

The cameras were arranged such that, for the duration of the experiment, the propagating wave was captured by at least two of the three cameras. At the completion of the experiment the wave had reached the sidewalls of the tank but had not yet reached the back wall of the tank. Therefore, it was important that the field of view of the cameras cover the entire width of the tank and the length of the tank to the point that the wave had reached by the time the experiment was complete. To cover the entire width of the tank, the three video cameras were placed 2.07 m above the downstream section of the tank. They were centred across the width of the tank and were spaced along the length of the tank as shown in Figure 3.1. This camera arrangement resulted in certain areas of the tank being covered by more than one camera. Figure 3.4 shows images from each of the three cameras with labels illustrating the field of view for each camera. It can be seen that the first 0.6 m measured downstream from the gate was captured by cameras one and two; the next 0.6 m was captured by cameras one, two, and three; and the next 0.6 m was covered by cameras two and three. There was approximately 0.5 m at the end of the tank, which was only covered by camera three.

It is noteworthy that stereo imaging requires at least two images of the same scene be taken from different viewpoints (*i.e.*, stereo images). Therefore, only those areas of the tank that were viewed by at least two cameras were usable for stereoscopy. Stereoscopy was utilized for the entire width of the tank and the length of the tank up to approximately 0.5 m from the end of the tank. This was acceptable in all cases since the experiments were complete before the wave reached the last 0.5 m of the tank.



### 3.1.3 Camera Calibration

One of the primary objectives in this study was to determine the three-dimensional coordinates of the tracking particles. The first step in this process was to determine the location of each camera and to correct for camera distortion, termed *camera calibration*. The calibration field, as shown in Figure 3.5, consisted of forty-two calibration points spread out to cover the entire area of the tank that would be used for stereoscopy. Twenty-one of the calibration points were grid line intersections on the base of the tank and the other twenty-one were the top of wooden blocks placed on grid line intersections. To accurately locate the centre of the blocks, a black and white bullseye was glued to the top of each block. Of the twenty-one blocks that were used, there were an equal number of each height: 0.10 m, 0.20 m, and 0.30 m. These heights were chosen since they covered the full range of water depths that were expected in the dam break experiments. Blocks of equal height were dispersed to prevent them from being clustered in one area of the tank.

High-precision leveling equipment was used to measure the elevation of all the grid line intersections on the tank floor. This was done for two reasons: to obtain an accurate elevation of the intersection points and to map the levelness of the tank floor. The level was a Wild NA2 made by Wild Heerbrugg and the rod (No. 328113) was made by Kern Aaru (Switzerland). Using this equipment, the elevation of the grid line intersections could be measured with a precision of one hundredth of a millimetre. The level survey was performed twice to verify the precision of the survey results, which were duplicated within 0.25 mm. Although this is not within the measuring precision, it is considered to be reasonable for this application. The elevations from the two surveys



were averaged, and these values were taken to be the true elevations of the grid line intersections. There was minimal vertical variance over the length of the tank and the variation over the width of the tank resembled a smooth wave, with a minimum elevation of 0.0 mm and a maximum elevation of 3.5 mm.

The three-dimensional coordinates of the calibration points were determined by assigning two-dimensional ( $x, y$ ) coordinates to all of the grid line intersections (see Figure 3.1 for coordinate system) and using the surveyed elevation as the  $z$ -coordinate. For calibration points on top of the blocks, the elevation was determined by adding the height of the block to the surveyed elevation of its corresponding grid line intersection. The calibration field, as viewed from camera 2, is shown in Figure 3.6. Superimposed on this image are the three-dimensional coordinates of the calibration points.

The  $x, y, z$  coordinates of the calibration points on the base of the tank and the  $z$  coordinate of the calibration points on top of the blocks were deemed accurate within 1 mm. The accuracy of the  $x, y$  coordinates of the block calibration points were considerably less accurate since some of the blocks were slightly tilted. To compensate for this, only the  $z$  coordinates of the blocks were used in the calibration procedure. Thus, the entire calibration field was accurate within 1 mm.

### **3.1.4 Wave Probes**

In addition to determining the flow depth through stereoscopy, an attempt was made to determine the depth using wave probes made by HR Wallingford (UK). Each of the five wave probes consisted of a pair of 0.6 m long, 6 mm diameter stainless steel rods that were placed in one of two arrangements. It was understood that thinner wave probes,





which would reduce the flow disturbance, would give better results, however the researchers did not have access to such equipment. Figures 3.7 and 3.8 illustrate the symmetrical and asymmetrical probe arrangements, respectively. Since only five wave probes were available, the water level could only be determined at five locations in the tank. These five water levels were not sufficient to reconstruct a water surface profile, however the results were used to investigate the symmetry and repeatability of the experiments.

The wave probes operate on the principle that the current flowing between the two rods is proportional to the depth of immersion. This current is converted to an output voltage proportional to the instantaneous depth of immersion. The output voltage (range equal to  $\pm 10$  Volts) can be calibrated with respect to the water level by varying the depth of immersion in still water by a known amount and noting the change in output voltage.

Prior to using the wave probes, the datum was adjusted and compensation for the resistance of the connecting cable was completed. The former is an adjustment which enables the output voltage to be set to zero for any given depth of probe immersion. To utilize the full range of the output voltage, the datum was adjusted such that the voltage was at the minimum ( $-10$  V) when the water depth was at a minimum and the voltage was at the maximum ( $10$  V) when the water depth was at a maximum. The latter was performed to greatly reduce or eliminate linearity errors in the output voltage due to cable resistance. Since these adjustments did not change for the duration of the testing, they were performed only once at the beginning of all the experiments.

The data from the wave probes was recorded using an in-house program developed by Dr. Fayi Zhou, a former graduate student at The University of Alberta. The user-



friendly program was written using the software package LabVIEW. The required input was: the name of the file to record the data to; which probes to record data for; the total number of samples to record; the number of samples per second to record; and the voltage range to record. This automated recording method allowed a large number of samples to be recorded in real time.



### 3.2 Experimental Procedure

Experiments were performed with both dry bed and wet bed initial conditions downstream of the dam. For the dry bed case, the upstream half of the tank was filled with water to a depth of 0.10, 0.20, or 0.30 m. For the wet bed case, the upstream water depth was 0.30 m and the downstream tailwater was set to either 0.05 or 0.10 m. The experiments were named such that the initial headwater and tailwater conditions were apparent. For example, Run 20a was the first run performed with 0.20 m headwater and no tailwater, and Run 30-10a was the first run performed with a headwater of 0.30 m and a tailwater of 0.10 m.

Table 3.1 details the dam break events performed without tailwater. The experiments are subdivided into two groups: tests in which wave probes were not used (Table 3.1a) and tests in which wave probes were used (Table 3.1b). The two groups of experiments were completed since stereoscopy could not be performed when the wave probes were used due to the large area they obstructed. From Table 3.1a, it can be seen that two experiments were performed for the initial conditions: headwater equal to 0.10 m and headwater equal to 0.30 m, and one experiment was performed for the initial condition: headwater equal to 0.20 m. Table 3.1b illustrates that five experiments were performed for a headwater of 0.10 m and four experiments were performed for headwaters of both 0.20 m and 0.30 m. Within Tables 3.1a and b is a column for the high-speed camera. This column states if the high-speed camera was used, and if it was used, its field of view is specified. There is also a column in Table 3.1b stating whether the probe arrangement was symmetrical or asymmetrical. For all of the experiments



summarized in Tables 3.1 a and b, tracking particles were placed on the water surface, upstream of the dam site, prior to the gate being lifted.

The dam break experiments performed with tailwater are summarized in Table 3.2. It can be seen that nine experiments were performed with the tailwater equal to 0.05 m, and four experiments were performed with the tailwater equal to 0.10 m. For both tailwater depths the headwater was equal to 0.30 m. In Table 3.2 there is a column titled high-speed camera, which states the field of view of the high-speed camera, if it was used. There is also a column for the wave probe arrangement. Wave probes were not used for the majority of the tailwater experiments, however for the events that did use probes, their arrangement is specified. For visualization purposes, red dye was used in the upstream water of some of the tailwater tests. There is a column in Table 3.2 stating for which tests dye was used. Since the nature of the use of tracking particles varied for the tailwater experiments, there is also a column for tracking particles. Some events used tracking particles upstream of the gate, some used tracking particles upstream and downstream of the gate, and some did not use any tracking particles.

A standard procedure was followed for each experiment. Prior to filling the tank with water, the twenty-one calibration blocks were placed on the grid line intersections. The blocks were numbered so that the same block was placed on the same intersection for each experiment. To ensure the bulls eye target on the block was directly over the grid point, care was taken to line each block corner up with each grid line. Once the blocks were set up, the three video cameras were used to record a video segment of the calibration field. The calibration blocks were then removed, and, if probes were being used, they were placed in the desired position. For the experiments with no tailwater, the





gate was closed and the reservoir was filled with water to the desired depth. For the experiments with tailwater, the gate was left open and the entire tank was filled with water until the water in the downstream half of the tank reached the desired level. The gate was then closed and the filling of the reservoir continued until the desired depth was obtained. Once the water surface stilled, the tracking particles were scattered on the water surface. Then the recording was manually started for the LabView program and the three time-synchronized VCRs. The high-speed camera had the capability of being linked to the light on the gate such that when the lifting of the gate was initiated, the light turned off and the high-speed camera started recording. The gate was opened as swiftly as possible, which, as indicated by the high-speed camera, resulted in a maximum opening time of 0.25 s. Once the gate was lifted, the water, along with the tracking particles, was released through the gate opening (see Figure 3.9). At the completion of the dam break event the recording devices were stopped.

Once each experiment using wave probes was complete, the output voltage of the wave probes was calibrated with respect to the depth of immersion. It was crucial for the calibration water to be the same temperature as the experimental water, since the electrical conductivity of the water increases by approximately 2 % for an increase in water temperature of 1°C and this change in conductivity directly affects the calibration. Since the calibration must be completed in still water, the water was allowed to calm before conducting the wave probe calibration. The water depth was then measured with a point gauge and the output voltage from each wave probe was noted. The water depth in the tank was lowered by a small amount (between 15 and 35 mm). Once the water was still, the water depth was measured and the voltage was noted. This process was repeated



until four depth and voltage measurements were obtained. Due to the linearity of the wave probe calibration, four data points were sufficient.



### 3.3 Analysis

This section covers the steps that were taken to analyze the stereo images and the output from the wave probes. The stereo images for the duration of the dam break event were analyzed to obtain the three-dimensional coordinates of the tracking particles. This data was used to approximate a water surface profile of the dam-break event and to calculate the velocity of the tracking particles, which is equivalent to the surface velocity of the dam-break wave. The wave probe calibration data was employed to convert the output voltage readings to water depths.

#### 3.3.1 *Stereo Cameras*

For each experiment there existed two sets of stereo images: images of the calibration field and images of the dam break event. The two sets of analog images were taken from the video tapes and converted to digital images using a personal computer equipped with a frame grabber (Meteor II, Matrox Electronic Systems, Ltd.). This process split the video segment into individual '*jpeg*' image files which could be viewed with any program capable of displaying '*jpeg*' files. The digital image resolution was 640 x 480 pixels.

The primary difficulty in utilizing stereoscopy to determine the three-dimensional coordinates of the tracking particles was in the number of unknowns: the stereo camera locations and attitude, the camera calibration variables, and the tracking particle locations. In order to reduce the number of unknowns, the camera locations, attitude, and calibration variables were pre-determined by a calibration process. The process involved taking images of a calibration field of targets whose three-dimensional coordinates were



known. The unknown camera parameters were then solved for by fixing the target coordinates. For subsequent images, the camera parameters were held fixed to allow solution for the three-dimensional coordinates of the tracking particles. This calibration technique used known information about targets contained in the images to solve for the camera parameters. The primary requirement for this type of calibration is that the camera remain undisturbed during the image sequence (*i.e.*, the camera position and focus must remain fixed) (Sturm, 1998). The utmost care was taken to ensure that the cameras were not disturbed during the period between the time when the images were taken of the calibration field and the images were taken of the experiment.

The *collinearity equations* are considered to be the fundamental photogrammetric relationship (Milhail, Bethel, and McGlone, 2001). Figure 3.10, showing a single video camera image for simplicity, illustrates the collinearity condition, which states that the perspective centre of the camera, the image point, and the corresponding object point all lie on a line in space (Peterson and Durdle, 1991). Following the derivation of Mikhail *et al.* (2001) and Peterson and Durdle (1991), the image space coordinates can be related to the object space coordinates. The vector from the perspective centre of the camera to the image point, in the camera space coordinate system, is equal to

$$\mathbf{p} = \begin{Bmatrix} x - x_o \\ y - y_o \\ -c \end{Bmatrix} \dots\dots\dots [3-1]$$

where  $x$  and  $y$  are the image point coordinates,  $x_o$  and  $y_o$  are the coordinates of the principal point, which cause a slight shift in the image point coordinates, and  $c$  is the principal distance of the camera. The origin of  $\mathbf{p}$  is the perspective centre of the camera, which, in the object space coordinate system, is located at





$$\mathbf{L} = \begin{Bmatrix} X_L \\ Y_L \\ Z_L \end{Bmatrix} \dots\dots\dots [3-2]$$

In the object space coordinate system the corresponding object point is located at

$$\mathbf{P} = \begin{Bmatrix} X \\ Y \\ Z \end{Bmatrix} \dots\dots\dots [3-3]$$

The relationship between the image and object space coordinate systems is defined by the following equation, which relates the three vectors,  $\mathbf{p}$ ,  $\mathbf{P}$ , and  $\mathbf{L}$ :

$$\mathbf{p} = k\mathbf{M}\{\mathbf{P}-\mathbf{L}\} \dots\dots\dots [3-4]$$

in which  $k$  is a scale factor and  $\mathbf{M}$  is a  $3 \times 3$  rotation matrix. The rotation matrix is used to relate the object space and image space systems and is typically constructed by using the three orientation angles for the camera axis:  $\omega$  about the  $x$ -axis,  $\phi$  about the  $y$ -axis, and  $\kappa$  about the  $z$ -axis.

$$\mathbf{M}_\omega = \begin{bmatrix} 1 & 0 & 0 \\ 0 & \cos \omega & \sin \omega \\ 0 & -\sin \omega & \cos \omega \end{bmatrix} \dots\dots\dots [3-5a]$$

$$\mathbf{M}_\phi = \begin{bmatrix} \cos \phi & 0 & -\sin \phi \\ 0 & 1 & 0 \\ \sin \phi & 0 & \cos \phi \end{bmatrix} \dots\dots\dots [3-5b]$$

$$\mathbf{M}_\kappa = \begin{bmatrix} \cos \kappa & \sin \kappa & 0 \\ -\sin \kappa & \cos \kappa & 0 \\ 0 & 0 & 1 \end{bmatrix} \dots\dots\dots [3-5c]$$

The rotation matrix is then,



$$\mathbf{M} = \mathbf{M}_\kappa \mathbf{M}_\phi \mathbf{M}_\omega$$

$$\mathbf{M} = \begin{bmatrix} \cos \phi \cos \kappa & \cos \omega \sin \kappa + \sin \omega \sin \phi \cos \kappa & \sin \omega \sin \kappa - \cos \omega \sin \phi \cos \kappa \\ -\cos \phi \sin \kappa & \cos \omega \cos \kappa - \sin \omega \sin \phi \sin \kappa & \sin \omega \cos \kappa + \cos \omega \sin \phi \sin \kappa \\ \sin \phi & -\sin \omega \cos \phi & \cos \omega \cos \phi \end{bmatrix} \dots [3-6]$$

To obtain the collinearity equations, Equation 3-4 can be expanded such that  $\mathbf{M}$  is expressed in terms of its elements:

$$\begin{Bmatrix} x - x_o \\ y - y_o \\ -c \end{Bmatrix} = k \begin{bmatrix} m_{11} & m_{12} & m_{13} \\ m_{21} & m_{22} & m_{23} \\ m_{31} & m_{32} & m_{33} \end{bmatrix} \begin{Bmatrix} X - X_L \\ Y - Y_L \\ Z - Z_L \end{Bmatrix} \dots [3-7]$$

By multiplying the matrix and the vector on the right-hand side of the equation, three scalar equations are obtained. By dividing the first two equations by the third equation, the scale factor,  $k$  is eliminated and the resulting collinearity equations are in the most commonly used form, expressed in terms of the image coordinates:

$$\begin{aligned} x - x_o &= -c \frac{[m_{11}(X - X_L) + m_{12}(Y - Y_L) + m_{13}(Z - Z_L)]}{[m_{31}(X - X_L) + m_{32}(Y - Y_L) + m_{33}(Z - Z_L)]} \\ y - y_o &= -c \frac{[m_{21}(X - X_L) + m_{22}(Y - Y_L) + m_{23}(Z - Z_L)]}{[m_{31}(X - X_L) + m_{32}(Y - Y_L) + m_{33}(Z - Z_L)]} \dots [3-8] \end{aligned}$$

The collinearity equations are non-linear and, for ease of implementation, can be linearized using a Taylor Series expansion, as shown in Mikhail *et al.* (2001).

The mathematical formulation of the equations required for calibration involves a modification of the collinearity equations by the addition of the radial and decentering lens distortion equations (Karara, 1989). Following Karara's (1989) modification of the collinearity equations, the equations used for calibration can be expressed as:



$$\begin{aligned}
 x_{ij} - x_o + \frac{(x_{ij} - x_o)}{r} \delta r + \Delta x &= c_x \frac{m_{11}(X_j - X_{il}) + m_{12}(Y_j - Y_{il}) + m_{13}(Z_j - Z_{il})}{m_{31}(X_j - X_{il}) + m_{32}(Y_j - Y_{il}) + m_{33}(Z_j - Z_{il})} \\
 y_{ij} - y_o + \frac{(y_{ij} - y_o)}{r} \delta r + \Delta y &= c_y \frac{m_{21}(X_j - X_{il}) + m_{22}(Y_j - Y_{il}) + m_{23}(Z_j - Z_{il})}{m_{31}(X_j - X_{il}) + m_{32}(Y_j - Y_{il}) + m_{33}(Z_j - Z_{il})} \dots\dots\dots [3-9]
 \end{aligned}$$

where  $x$  and  $y$  are the image point coordinates and  $X$  and  $Y$  are the object point coordinates. The subscripts indicate:  $i$  is the  $i$ th photograph;  $j$  is the  $j$ th object point;  $o$  is the principal point; and  $L$  is the perspective centre. The terms  $\Delta x$  and  $\Delta y$  represent the decentering distortion and  $\delta r$  is the radial distortion, which is expressed in terms of a polynomial series of odd powered terms,

$$\delta r = K_1 r^3 + K_2 r^5 + K_3 r^7 + \dots \dots\dots [3-10a]$$

where  $K_1$ ,  $K_2$ ,  $K_3$ , etc. are the coefficients of radial distortion and

$$r^2 = (x_c - x_o)^2 + (y_c - y_o)^2 \dots\dots\dots [3-10b]$$

where  $x_c$  and  $y_c$  are the coordinates of the exact geometric center of the image.

The modified and the classical collinearity equations were used in a series of in-house, DOS-based programs (A. E. Peterson, University of Alberta) which were capable of solving for the camera parameters and calculating the three-dimensional coordinates of the tracking particles. The procedure is outlined below.

- 1) A control point file was developed, which contained the known coordinates of the forty-two calibration points.
- 2) The two-dimensional image coordinates of the calibration points were manually determined using the program *XYDIGIT*, which allowed the images of the calibration field to be viewed on the computer screen (see Figure 3.11). To obtain the image



coordinates, each calibration point was zoomed in on, and its  $x, y$  coordinate digitized. This resulted in a file of the two-dimensional image coordinates of the calibration points.

- 3) To obtain a first estimation of the camera location parameters, the program *NDLT*, based on the *Direct Linear Transformation* (Karara, 1989) was used. The required input was the control point file, which contained the three-dimensional coordinates (in mm) of the control points, and the image data file, which contained the two-dimensional image coordinates (in pixels) of the calibration points seen by the corresponding camera. The two-dimensional image coordinates of the calibration points were compared to the analogous three-dimensional object coordinates of the calibration points to iteratively solve for the following parameters: the three-dimensional spatial coordinates of the camera ( $X_L, Y_L, Z_L$ ); the camera rotation angles ( $\omega, \phi$ , and  $\kappa$ ); the principal point coordinates ( $x_o, y_o$ ); the principal distances ( $c_x$  and  $c_y$ ); the mean radial distortion coefficient; and the decentering coefficients. This data constituted the first estimation of the camera location and was used to obtain the final camera location parameters. This process was completed for each of the three cameras.
- 4) The photogrammetric program *TRIPLET*, based on the collinearity condition equation, was run to refine the first estimation of the camera location parameters. The input to the program consisted of the first estimation of the camera location parameters, the image data file, the control point file, and an estimation of the three





dimensional coordinates of each camera. The output was the final camera location parameters. The difference between *TRIPLET* and *NDLT* is that the former uses the data from all three cameras to simultaneously solve for the three camera location files, and the latter uses the data from each individual camera to solve for the corresponding camera location file.

- 5) The program *XYDIGIT* was again used to manually determine the two-dimensional coordinates of the tracking particles for each time frame of the experiment. A two-dimensional image coordinate file for each time frame of the experiment resulted.
- 6) Now that the camera location parameters and the two-dimensional tracking particle image coordinates were known, they could be used in a program called *SPACO*, also based on the collinearity condition, to determine the corresponding three-dimensional coordinates.
- 7) To reduce the error in the measurements, steps 5 and 6 were repeated to obtain a second set of three-dimensional coordinates to be averaged with the first set. The average coordinates were used as the actual three-dimensional coordinates.



### 3.3.2 *Wave Probes*

The output from LabVIEW was a file containing voltage measurements taken every 0.05 seconds. The voltage was converted to a water depth by employing the wave probe calibration data, which consisted of measured depths of immersion and the corresponding output voltage. The “goodness of fit” coefficient (square of the correlation coefficient) was determined by fitting the data points to a linear trendline. For the majority of the tests, the “goodness of fit” coefficient was at least 0.999. The equation of this linear trendline was calculated, and was used to convert the output voltage to the depth of immersion. Figure 3.12 illustrates a sample wave probe calibration for an experiment with headwater equal to 0.30 m and tailwater equal to 0.0 m.



Table 3.1: A summary of dam break experiments performed without tailwater.

## a) no wave probes

test	headwater (m)	tailwater (m)	high-speed camera <sup>1</sup>
Run 10a	0.10	0	yes
Run 10c	0.10	0	yes
Run 20c	0.20	0	yes
Run 30b	0.30	0	yes
Run 30d	0.30	0	yes

<sup>1</sup> The high-speed camera was obliquely focused on the gate for all tests.

## b) probes

test	headwater (m)	tailwater (m)	high-speed camera	probe arrangement
Run 10b	0.10	0	yes - oblique	symmetrical
Run 10d	0.10	0	yes - oblique	symmetrical
Run 10e	0.10	0	no	symmetrical
Run 10f	0.10	0	yes - perpendicular	symmetrical
Run 10g	0.10	0	yes - oblique	asymmetrical
Run 20a	0.20	0	yes - oblique	symmetrical
Run 20b	0.20	0	yes - oblique	symmetrical
Run 20d	0.20	0	yes - perpendicular	symmetrical
Run 20e	0.20	0	yes - oblique	asymmetrical
Run 30a	0.30	0	no	symmetrical
Run 30c	0.30	0	yes - oblique	symmetrical
Run 30e	0.30	0	yes - perpendicular	symmetrical
Run 30f	0.30	0	yes - oblique	asymmetrical



Table 3.2: A summary of dam break experiments performed with tailwater.

test	headwater (m)	tailwater (m)	high-speed camera	probe arrangement	dye	tracking particles
Run 30-5a	0.30	0.05	yes <sup>1</sup>	symmetrical	no	u/s
Run 30-5b	0.30	0.05	yes <sup>1</sup>	symmetrical	no	u/s
Run 30-5c	0.30	0.05	yes <sup>1</sup>		no	u/s
Run 30-5d	0.30	0.05	no	no	no	u/s & d/s
Run 30-5e	0.30	0.05	yes <sup>1</sup>	no	no	u/s & d/s
Run 30-5f	0.30	0.05	yes <sup>1</sup>	no	u/s	no
Run 30-5g	0.30	0.05	yes <sup>1</sup>	no	u/s	no
Run 30-5h	0.30	0.05	yes <sup>3</sup>	no	u/s	no
Run 30-5i	0.30	0.05	yes <sup>3</sup>	no	u/s	no
Run 30-10a	0.30	0.10	yes <sup>2</sup>	no	no	u/s & d/s
Run 30-10b	0.30	0.10	yes <sup>1</sup>	no	u/s	no
Run 30-10c	0.30	0.10	yes <sup>3</sup>	no	u/s	no
Run 30-10d	0.30	0.10	yes <sup>4</sup>	no	u/s	no

<sup>1</sup> The high-speed camera was obliquely focused on the gate

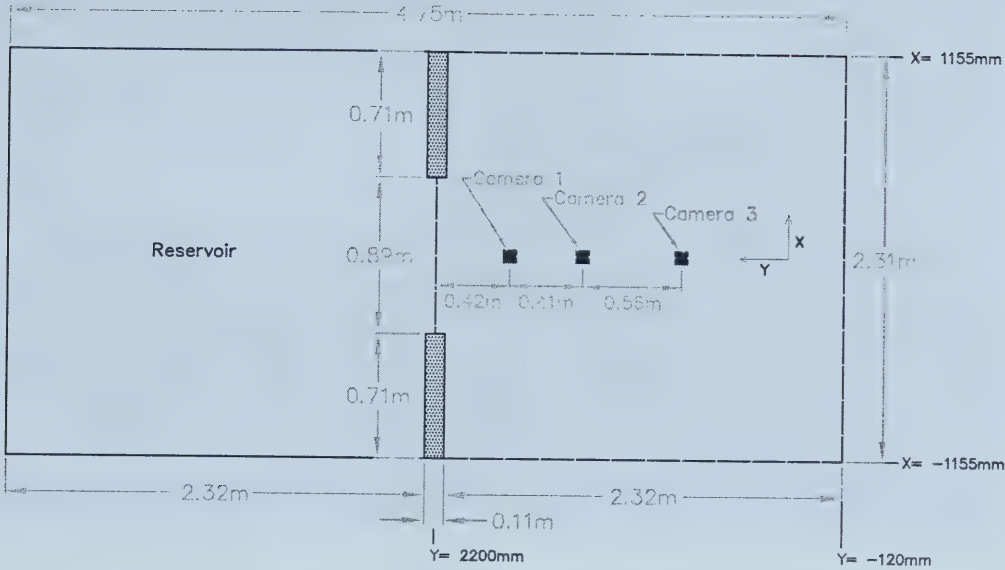
<sup>2</sup> The high-speed camera was perpendicularly focused on the back wall

<sup>3</sup> The high-speed camera was perpendicularly focused on the back wall d/s of the <sup>2</sup> case

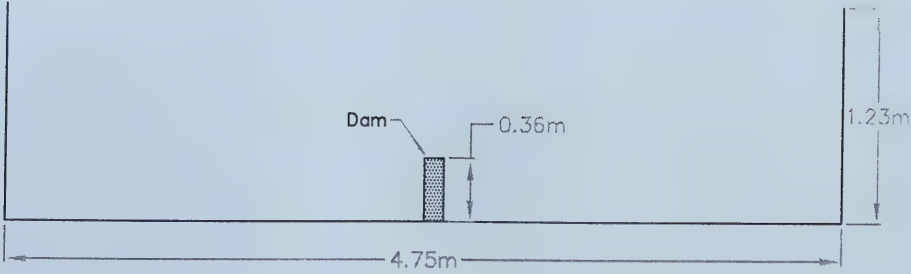
<sup>4</sup> The high-speed camera was obliquely focused on the back wall







PLAN VIEW



ELEVATION VIEW

Figure 3.1: Elevation and plan views of the experimental tank.





Figure 3.2: Photograph of the VCRs and timer used in the experiments.



Figure 3.3: Photograph of the trial tracking particles.



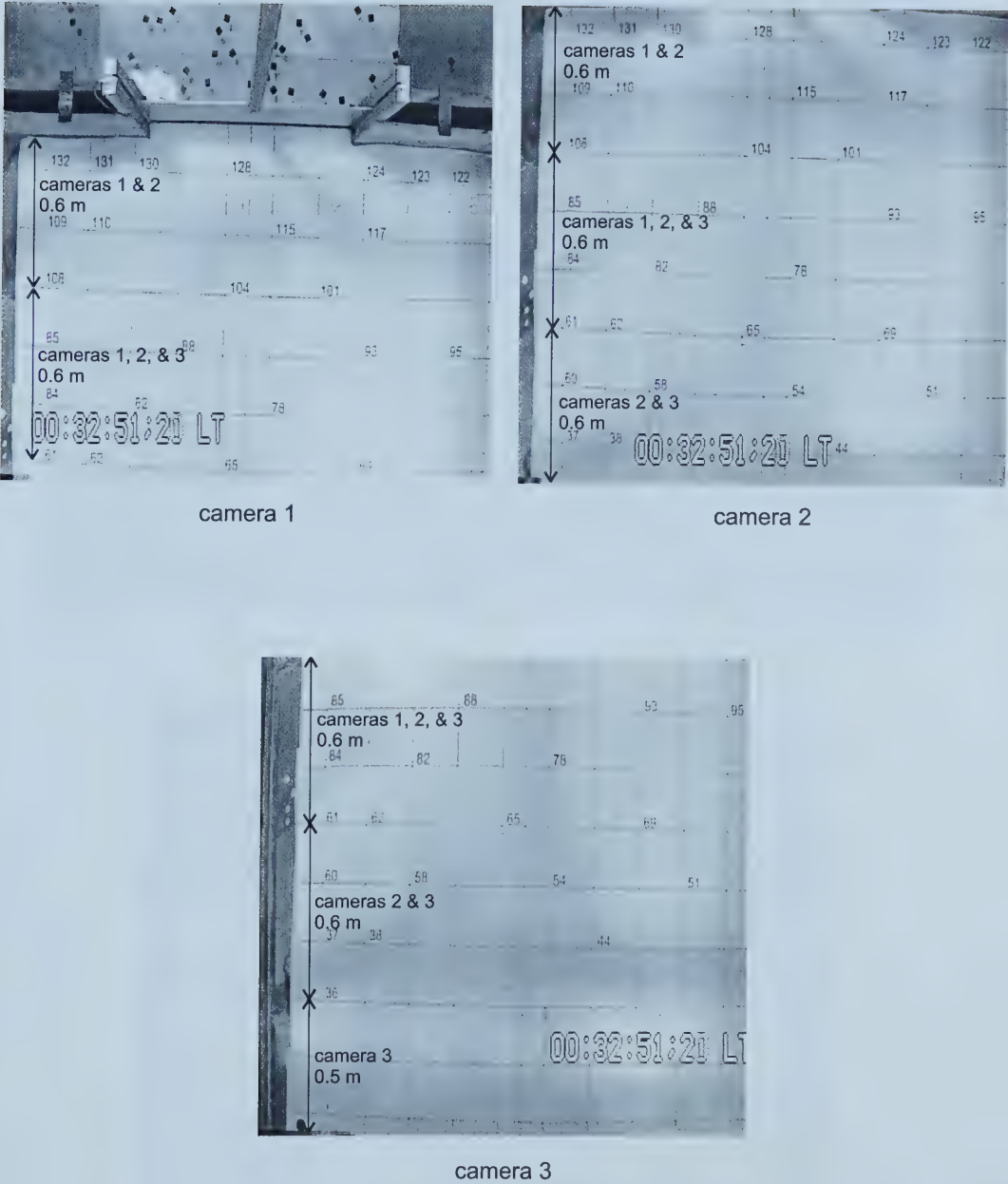


Figure 3.4: Illustration of the field of view of each camera.



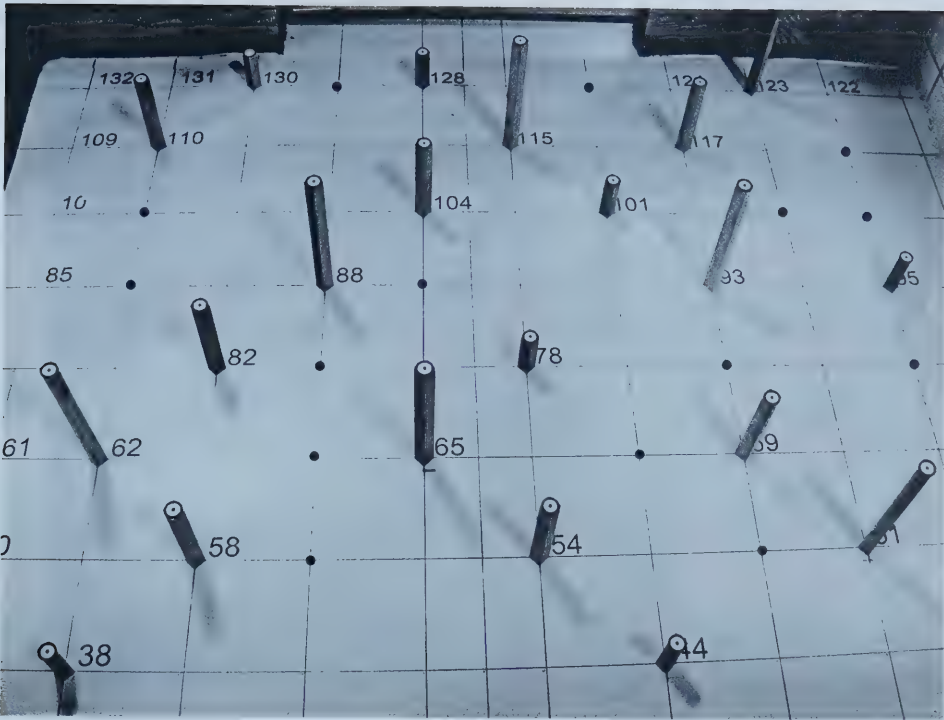


Figure 3.5: Oblique photograph of the calibration points.

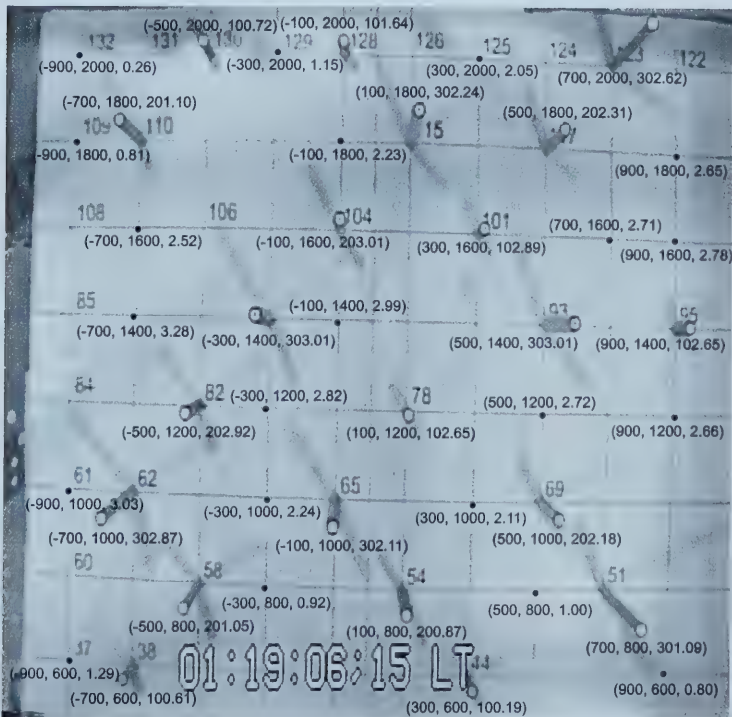


Figure 3.6: Image of the calibration field from camera 2, superimposed with the three-dimensional coordinates (in mm) of the calibration points.





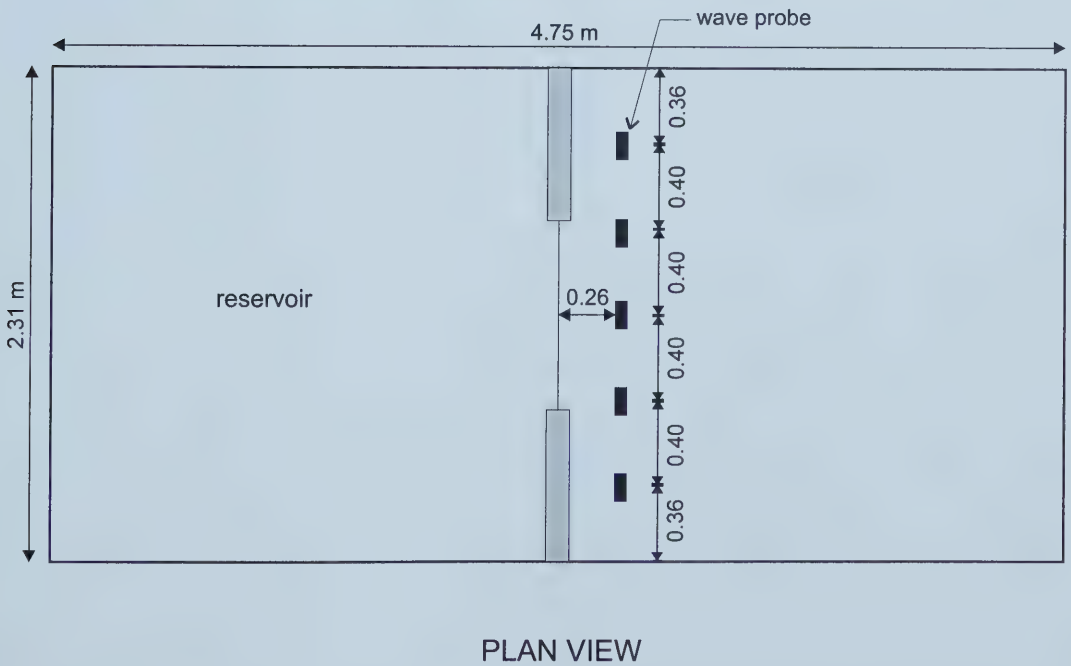
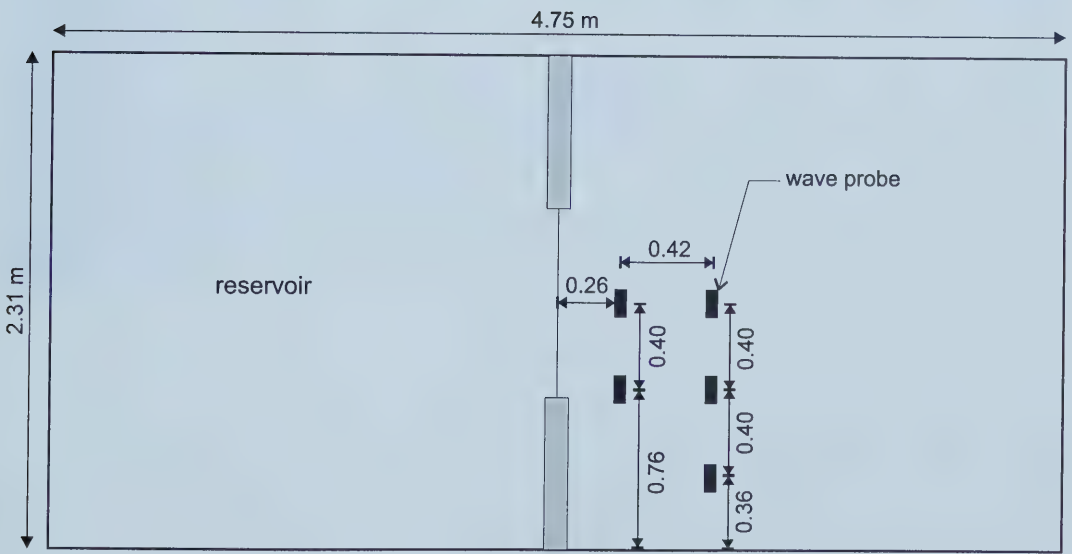


Figure 3.7: Illustration of the symmetrical probe arrangement (dimensions in m).





PLAN VIEW

Figure 3.8: Illustration of the asymmetrical probe arrangement (dimensions in m).



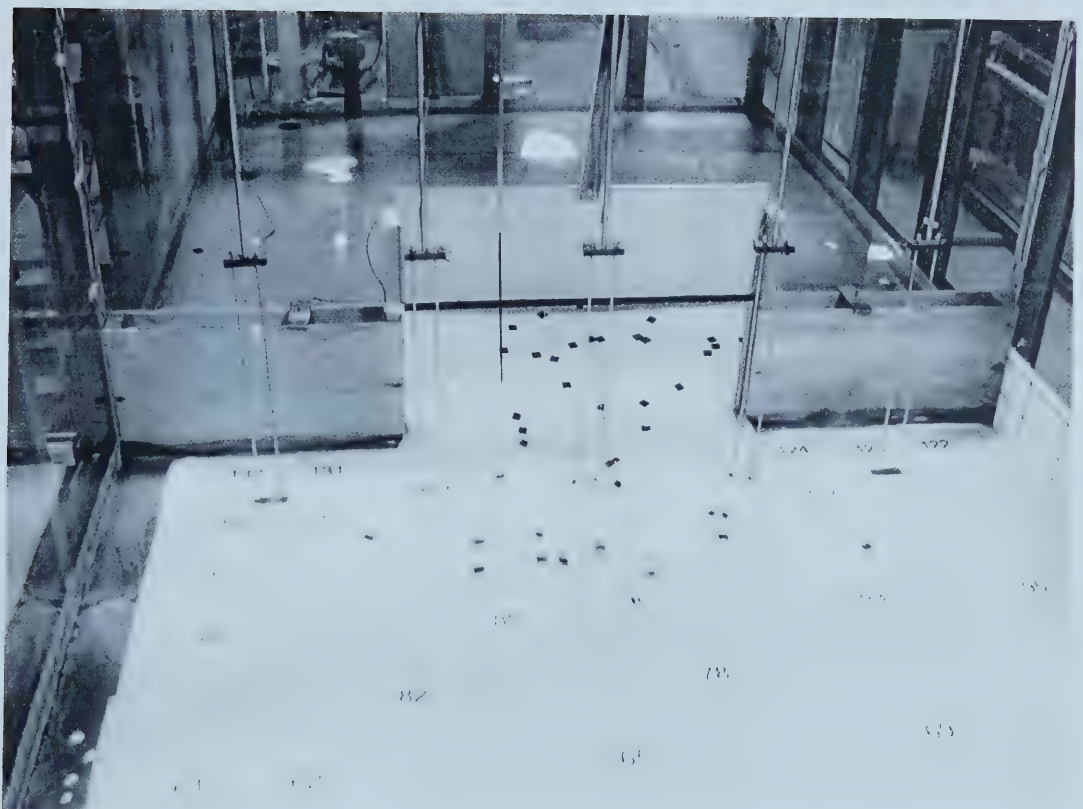


Figure 3.9: Oblique photograph illustrating the water and the tracking particles flowing out of the reservoir.



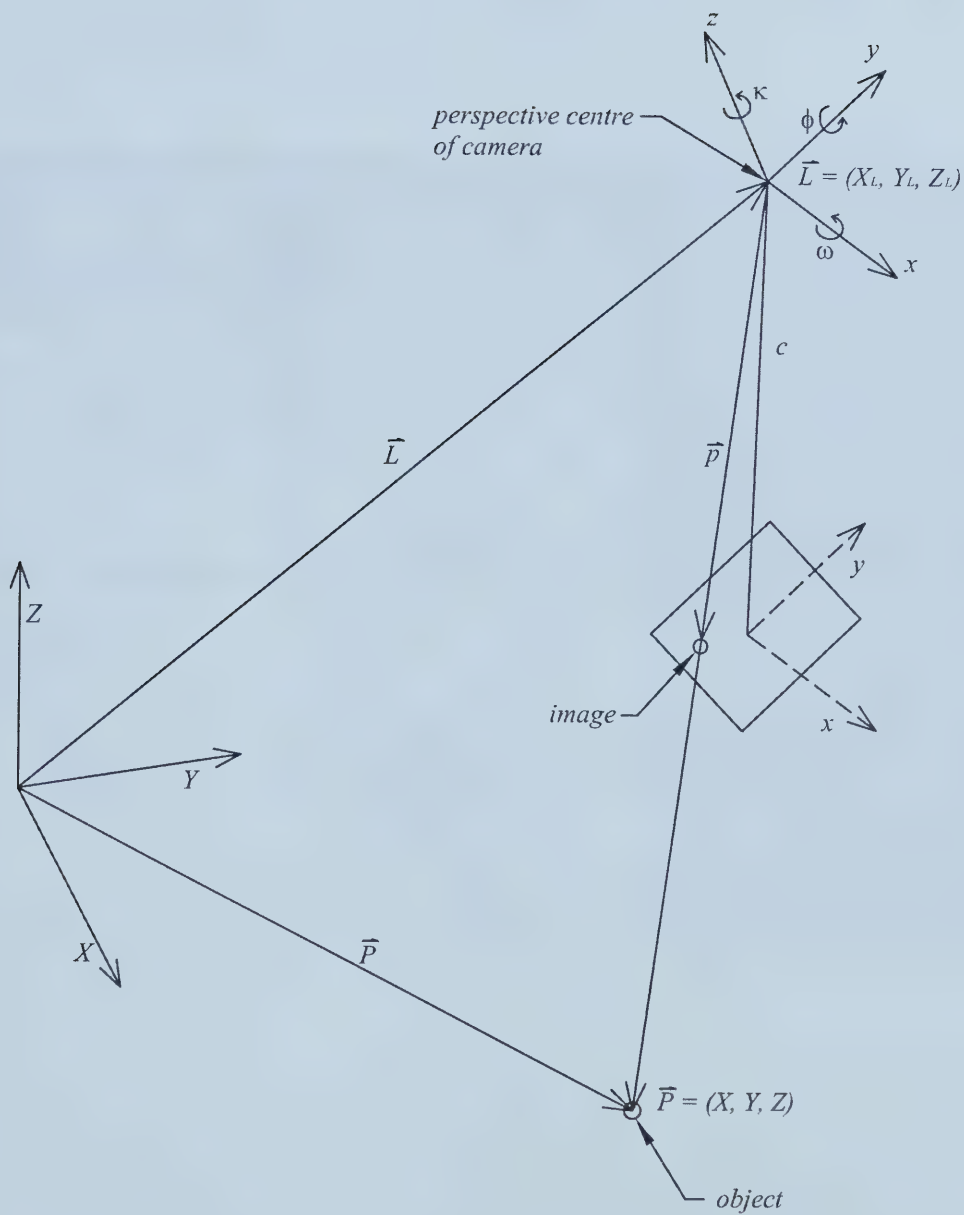


Figure 3.10: A single video camera image used to illustrate the collinearity condition (Peterson & Durdle, 1991).





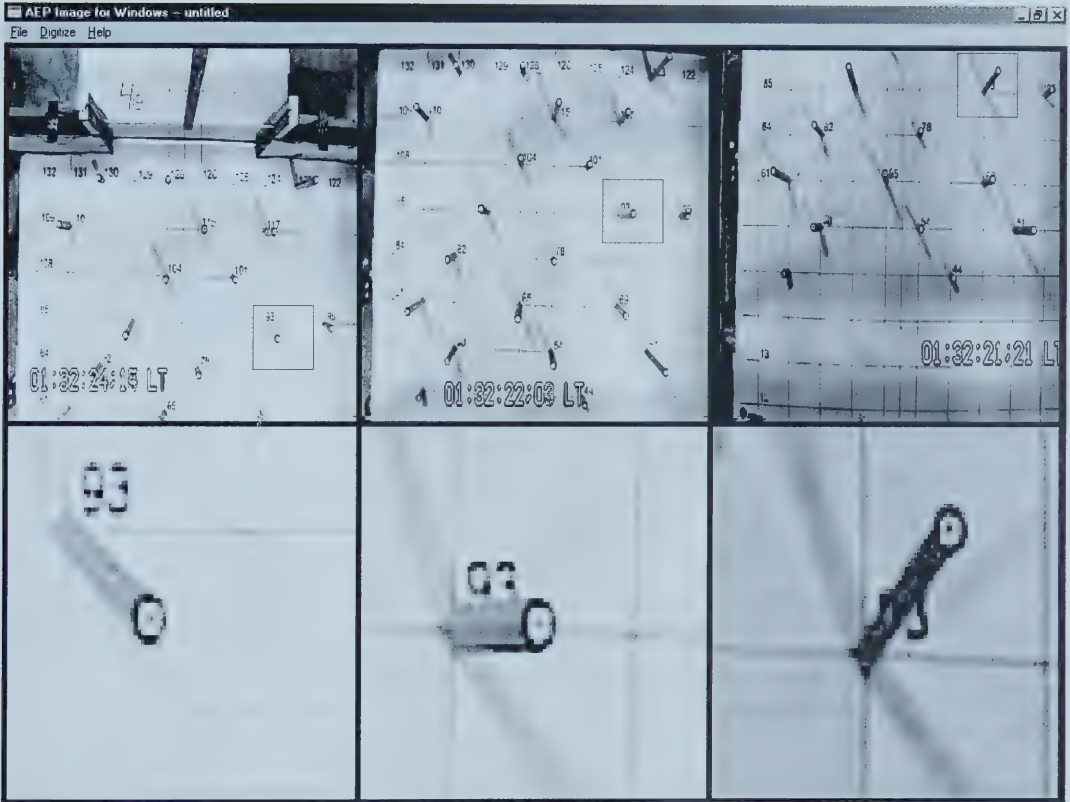


Figure 3.11: An image of *XYDIGIT* being used to manually determine the image coordinates of the calibration points.



point gauge measurements (ft)			Voltage (V)					
water level	ground level	water depth (ft)	probe 0	probe 1	probe 2	probe 3	probe 4	water depth (mm)
0.576	0.092	0.484	5.08	5.56	5.59	3.39	5.79	148
0.448	0.092	0.356	0.92	1.36	1.3	-0.37	1.47	109
0.326	0.092	0.234	-3.17	-2.75	-2.91	-4.06	-2.78	71
0.196	0.092	0.104	-7.42	-7.04	-7.29	-7.88	-7.2	32

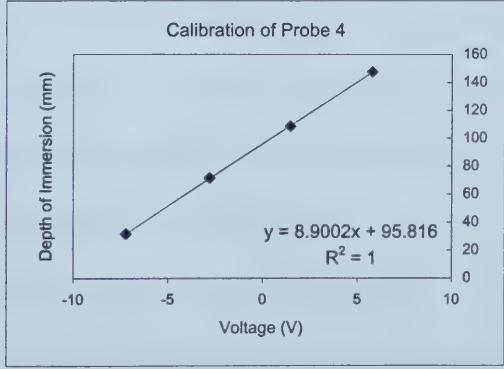
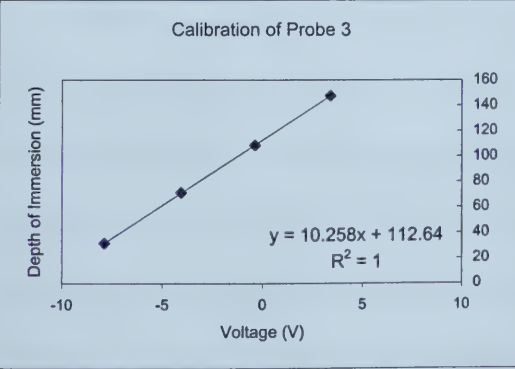
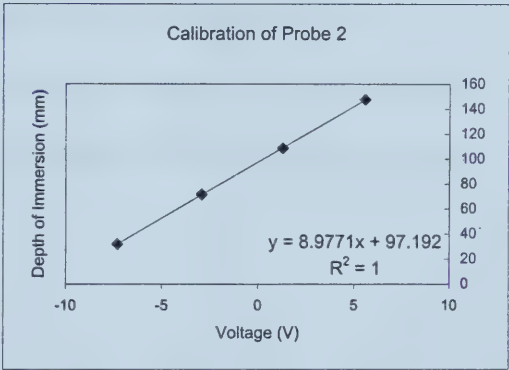
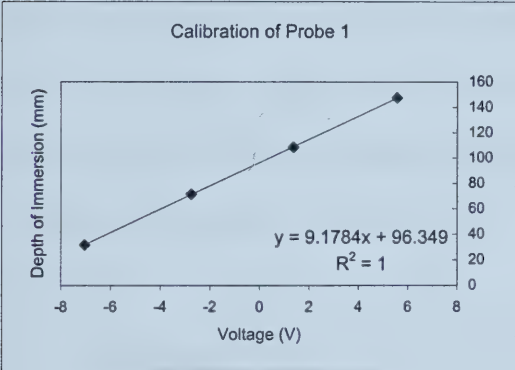
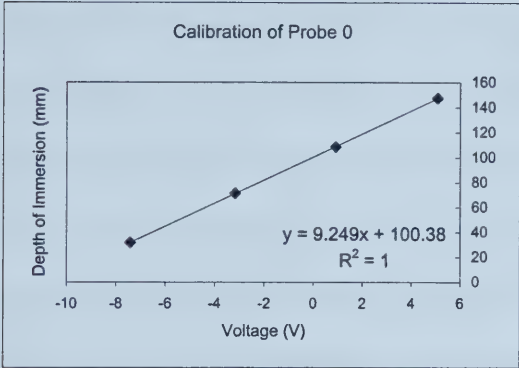


Figure 3.12: Wave-probe calibration for Run 30a.



## 4.0 EXPERIMENTAL RESULTS

This chapter is divided into the following sections: stereoscopy results for experiments both with and without tailwater, wave probes results for dry-bed experiments, and miscellaneous results for the experiments with tailwater. The stereoscopy results were used to obtain three-dimensional water surface profiles and surface velocity vector plots; however, prior to summarizing these results, the error in the stereoscopy method is discussed. Within the wave probe results section is a discussion of the error in the measurements, the depth hydrographs obtained, and the use of these hydrographs to assess the symmetry and repeatability of the experiments. The miscellaneous results section details the noteworthy quantitative and qualitative results obtained from the experiments conducted with tailwater, including supplementary two-dimensional dam break experiments.

### 4.1 Stereoscopy

Stereoscopy was used to obtain the three-dimensional coordinates of the tracking particles for the experiments listed in Tables 4.1 and 4.2. The stereoscopy results for the aforementioned experiments can be seen in Appendices A and B. Since stereoscopy requires at least two images, data acquisition commenced when the tracking particles could be seen by at least two cameras. For the experiments with no tailwater, the tracking particles were all initially located upstream of the gate, therefore data acquisition could only commence once the first particle was seen by both cameras 1 and 2. Since the leading edge of the flood wave escaped from the reservoir without tracking particles on



its surface, stereoscopy could not be used to obtain data for the leading edge. For future studies, it may be advantageous to place tracking particles on the dry bed downstream of the gate in an attempt to obtain data in this area. For the experiments conducted with tailwater, the tracking particles were initially located both upstream and downstream of the gate, therefore data acquisition could start as soon as the gate was fully lifted.

#### 4.1.1 Error Analysis

Prior to discussing the results, it is necessary to examine the error and the sources of error in the stereoscopy method. As stated by Wolf and Dewitt (2000), the error can be divided into *systematic* and *random errors*. Systematic errors are nonrandom deviations which follow a mathematical or physical law (*e.g.*, lens distortion and the displacement of the principal point from the exact geometric centre of the image) (Wolf and Dewitt, 2000). Through the self-calibration process, the conditions causing systematic error can be measured, and a correction can be calculated. Therefore the systematic error can be eliminated, such that only random errors remain. Random errors cannot be predicted, so they can only be estimated, not eliminated (Wolf and Dewitt, 2000).

In this investigation, the primary random error occurred when attempting to accurately locate the tracking particles in the stereo images. Due to the high velocity of the flood wave and the small scale of the image (height of the cameras), the particles appeared as blurred streaks in the stereo images. This streak represented the distance that the particle traveled during the time period that the camera shutter was open (*i.e.*, 1/60 second). It was noticed that the particle velocity, and thus the streaking, was a minimum





when the headwater was at a minimum (*i.e.*, 0.10 m) and was maximum when the headwater was at a maximum (*i.e.*, 0.30 m). Figures 4.1, 4.2, and 4.3 illustrate the streaking of the particles for headwaters of 0.10 m, 0.20 m, and 0.30 m, respectively. This particle streaking made it very difficult to accurately locate the centre of the particle. For future studies, if the streaking was reduced and the particle edges were better defined, a corner of the particle could be digitized instead of the center, which would likely be easier to accurately locate from frame to frame.

To attempt to reduce the error, the process of locating the image coordinates of the tracking particles was conducted twice and the resulting three-dimensional coordinates from these two separate efforts were then averaged. The repeatability between the two data sets was quite good for the  $x$  and  $y$  coordinates, with differences typically less than 5 mm, however the repeatability of the depth measurement was relatively poor, with differences up to 20 mm. The poor repeatability of the depth measurement was more pronounced when the particles were first released from the gate, since the initial water surface gradient was large and the particles (being located on the water surface) were quite tilted. When the headwater depth was maximum, the water surface was steepest and thus this particle tilt was greater for these experiments. Figure 4.4 is an image taken from the high-speed camera, which illustrates tilted particles during an experiment with 0.30 m headwater. It can be seen that the particles at the edge of the flood wave are close to vertical, while the particles towards the middle of the wave are tilted by a maximum angle of approximately 30 degrees.

In addition to computing the three-dimensional coordinates of the tracking particles, the program *SPACO* also computed the standard deviation of the  $x$ ,  $y$ , and  $z$



coordinates. This standard deviation is an additional method of estimating the error in the results. Similar to the repeatability, the standard deviation for the  $x$  and  $y$  coordinates was less than 5 mm in most instances and the standard deviation for the  $z$  coordinates was in the order of 20 mm. The computed standard deviation is based on the target digitizing accuracy of one pixel, which was input to the program *SPACO*. If a fraction of one pixel was input, the standard deviation values would be smaller and if a value greater than one pixel was used, the standard deviations would be larger. One pixel was chosen as the digitizing accuracy, since for most particles, the difference in image coordinates between successive digitizing efforts on the same image was usually one pixel or less.

The depth error appeared to be minimized when the particles were viewed by all three cameras. This is partially due to coordinate averaging, which took place with the addition of the third camera. However, the error reduction can be primarily attributed to the fact that the error in the  $z$  coordinate decreased substantially as the distance between the cameras increased, and since the distance between cameras 1 and 3 was larger than the distance between cameras 1 and 2, the depth error was greatly reduced when the particles were viewed by all three cameras. The  $z$  coordinate error was most obvious for the experiments with 0.10 m headwater. If the particles were only seen by cameras 1 and 2, the computed depths were greater than 0.10 m, which is physically impossible. When those same particles moved into the field of view of camera 3, such that they were seen by all three cameras, the depth immediately decreased to less than 0.10 m. This anomaly, which did not occur when the headwater was greater than 0.10 m, is likely attributable to the small initial depth and the fact that the errors were absolute rather than a function of the initial depth.



By assessing the repeatability of results and the standard deviations computed by *SPACO*, it was estimated that the spatial accuracy was quite good, with the maximum error in the  $x, y$  coordinates being in the order of 5 mm. The depth accuracy was relatively poor, with the maximum error estimated to be in the order of 20 mm (which is large considering that typical depths were in the order of 100 mm). The best results for depth accuracy were obtained when the particles appeared in all three images. Cases where the particles were tilted more than 45 degrees (*i.e.*, on the face of steep waves) resulted in the highest error. Still, in the best cases it is estimated that the depth accuracy was never better than 10 mm. The primary source of error was poor target definition (*i.e.*, blurred tracking particles), which could be attributed to both the scale of the image and the speed of propagation of the particles.

The previously discussed error analysis pertains to the dry-bed experiments. The stereoscopic imaging approach was considerably less successful for the wet-bed case than for the dry-bed case, since numerous tracking particles were entrained in the flow due to the considerable interaction between the headwater and tailwater. By assessing the repeatability and the standard deviation of the particle coordinates, it was concluded that the particle entrainment primarily affected the elevation of the particles and not their planar coordinates.

To determine the potential accuracy of the stereoscopy method, the known three-dimensional coordinates of the calibration blocks were compared to the coordinates computed by *SPACO*. In general, the computed  $x, y$  coordinates were within 1 mm of the actual coordinates and the computed  $z$  coordinates were within 5 mm of the actual



coordinates. Therefore, the potential accuracy of the stereoscopy method is 1 mm in the  $x$  and  $y$  directions and 5 mm in the  $z$  direction.

#### 4.1.2 Water Surface Profiles

The three-dimensional coordinates of the tracking particles defined the shape of the flood wave as it was released from the dam. For visualization purposes, water surface profiles, for the duration of the experiments, were constructed for the experiments with no tailwater. Water surface profiles were not constructed for the experiments with tailwater, since they were found to be unrepresentative of the actual water surface profile, due to inaccuracies in the computed elevations resulting from entrainment.

Due to the limited number of data points (*i.e.*, tracking particles) on the water surface, a water surface profile could not be constructed with this data alone, so the program SigmaPlot was used to convert the scattered data into a mesh plot. The Inverse Distance Method (Jandel Corporation, 1994) was used to generate  $z$  values for an evenly spaced  $x, y$  grid. The grid extremities were taken to be the maximum and minimum  $x$  and  $y$  values from the inputted tracking particle coordinates and the mesh intervals were spaced evenly between the grid borders. The program used the following formula to calculate the interpolated  $z$  values corresponding to the  $x$  and  $y$  values at grid intersections:

$$z = \frac{\sum_{m=1}^n w_m z_m}{\sum_{m=1}^n w_m} \quad \text{if } x_m \neq x, y_m \neq y \dots \dots \dots [4-1a]$$

or,





$z = z_m$  if  $x_m = x, y_m = y$ ..... [4-1b]

where

$w_m = \left[ (x_m - x)^2 + (y_m - y)^2 \right]^{-\frac{p}{2}}$  ..... [4-1c]

In the preceding equations, the subscript *m* indicates a grid intersection and the subscript *n* represents the total number of grid intersections. The variable *p* (*p*=1 to 10) is a weight value, which is used to specify the weight of distant points in affecting the interpolation values. By using a larger weight, a smoother curve results by placing less emphasis on the distant points. For this study, the recommended *p* value of 3 (Jandel Corporation, 1994) was used such that substantial weight was placed on distant points and the resulting curve was not deceptively smooth.

The interpolated water surface profiles are displayed as follows: for a headwater of 0.10 m, see Figures 4.5 and 4.6; for a headwater of 0.20 m, see Figure 4.7; and for a headwater of 0.30 m, see Figures 4.8 and 4.9. In the figures, the black squares superimposed on the mesh represent the locations of the tracking particles as determined from the stereoscopic analysis. Included on each page of the water surface profile figures is an image from the high-speed camera taken at the average time of the figures on the corresponding page.

The water surface profiles are not very meaningful at the start of each dam break event, since not enough particles are available to interpolate a representative water surface profile. However, as the wave spreads out and more particles are in view, the interpolated water surface appears to better represent the actual water surface. By comparing the interpolated plots with the high-speed camera images, a qualitative accuracy estimation can be made.



The worst case was seen in the 0.10 m headwater experiments, where low depths and high depth error result in a very poor match between the observed flood wave shape and the interpolated water surface profiles. As stated in subsection 4.1.1, when the particles can only be seen by cameras 1 and 2, the error in the computed tracking particle depths was significant. This is known since the computed tracking particle depths are larger than the initial headwater, which is physically impossible. When the particles move into the field of view of the third camera, their depths immediately reduce to values less than the initial headwater, which appear to be physically reasonable. As can be seen in Figures 4.5 and 4.6, all the tracking particle depths are above the 0.10 m mark up until times of 0.800 s and 0.833 s, respectively. After this time it is obvious that the downstream particles start to be seen by camera 3, since there is a sharp drop in the water surface profile. Towards the end of the experiments, a considerable number of particles are seen by camera 3 and the interpolated water surface profile is relatively smooth and flat. This portion of the interpolated water surface profile is a better estimate of the actual water surface profile.

For the experiment conducted with 0.20 m headwater, the interpolated water surface profiles and the water surface observed from the high-speed camera images compare fairly for the beginning and middle of the event and poorly towards the end of the event. This is mainly due to the uneven nature of the interpolated water surface profiles, which is likely a result of the error in the tracking particle depths (approximately 10 to 20 mm). As with the water surface profiles for the 0.10 m headwater events, the small initial depth causes the errors to appear quite pronounced.



For both experiments conducted with 0.30 m headwater (Figures 4.8 and 4.9), the actual wave shape is well represented by the interpolated water surface profiles, after a time of approximately 0.633 s. However, from the high-speed camera images, it is apparent that the actual water surface is fairly smooth, and the interpolated water surface profiles are quite bumpy. Due to the larger initial headwater, the unevenness is less apparent than for the 0.20 m headwater event.

#### **4.1.3 *Surface Velocity Results***

Given the good accuracy obtained with the  $x, y$  coordinates (5 mm), surface velocities were estimated for experiments conducted both with and without tailwater. The  $x$  and  $y$  velocity coordinates of the tracking particles were computed by dividing the difference between the  $x$  and  $y$  coordinates from one frame to the next by the time period between frames of 1/30 second. The results were displayed as velocity vector plots in which the  $x, y$  velocity coordinates were used to compute the magnitude and orientation of the velocity vectors.

In addition to determining the average velocity between frames, it was also attempted to determine the instantaneous velocity within a frame. The four corners of the tracking particles were digitized and the shape of the streaked tracking particles were compared to the actual tracking particle shape to determine the distance traveled. This distance was divided by the shutter speed of 1/60 second to obtain an estimate of the instantaneous velocity. This procedure was independently repeated for the same particles and the results were not consistent; this is due to unclear particle edges which made it



difficult to distinguish the four corners. In future, if the particle edges were less blurred, this instantaneous velocity approach would likely prove successful.

It is noteworthy to mention that there is an advantage to using stereoscopy for the computation of the surface velocity as opposed to simply determining the tracking particle  $x, y$  coordinates from a single image. This is especially true if the water surface is steep, as illustrated in Figure 4.4. On a steep wave such as this, a tracking particle moves approximately 25 mm in elevation from one frame to the next. Therefore if stereoscopy was not used, the elevation traveled by the particle would not be taken into account and the distance traveled, and thus the velocity, would be underestimated.

### ***Dry-Bed Case***

The velocity vector plots for the two experiments conducted with 0.10 m headwater can be seen in Figures 4.10 and 4.11, where the two black lines at the left-hand-side of each plot represent the edges of the gate opening. The length and orientation of each vector represents the magnitude and direction of the tracking particle's surface velocity. By visually comparing the velocity vectors to the legend vector, it can be seen that the surface velocity was approximately 1.0 m/s for the entire duration of both experiments. The minimum velocities for Runs 10a and 10c were 0.29 and 0.41 m/s; the maximum velocities were 1.29 and 1.35 m/s; and the average velocities were 0.95 and 1.01 m/s. As can be seen in Figure 4.11 (Run 10c), for approximately the first second of the experiment, the transverse velocity was negligible. After the first second, the transverse component became slightly more prominent and the surface velocity shifted slightly toward the sidewalls of the tank. For Run 10a (Figure 4.10), the





surface velocity at the edges of the gate opening had a substantial transverse component from the outset. This continued for the duration of the experiment. There was virtually no difference between the velocity magnitudes for the two experiments and the slight difference in the vector orientation is likely attributable to the initial tracking particle spacing rather than a difference in wave propagation between the two experiments, illustrating the value of having as many tracking particles as possible.

Figure 4.12 illustrates the velocity vector plots for the experiment conducted with a headwater of 0.20 m (Run 20c). It can be seen that the tracking particle velocity was approximately 1.5 m/s for the duration of the experiment. The minimum, maximum, and average velocities were 0.97 m/s, 1.79 m/s, and 1.49 m/s, respectively. This average velocity is approximately 50 percent greater than the average velocity for the 0.10 m headwater experiments. As with Run 10c, the transverse component of the surface velocity was negligible until approximately 0.9 seconds into the experiment. For the last part of the experiment, the velocity vectors were orientated slightly towards the tank sidewalls.

The velocity vectors for the two experiments conducted with 0.30 m of headwater can be seen in Figures 4.13 (Run 30b) and 4.14 (Run 30d). Through comparison with the legend, it can be seen that the surface velocity was approximately 2.0 m/s. The minimum velocities for Runs 30b and 30d were 1.25 and 1.30 m/s, respectively; the maximum velocities were 2.19 and 2.16 m/s; and the average velocity for both experiments was 1.78 m/s. When this average velocity was compared to the average velocities resulting from the two other headwaters, it was found to be 80 percent larger than the average velocity for the 0.10 m headwater experiments and 20 percent larger than the average



velocity for the 0.20 m headwater experiment. For Run 30b, the transverse components of surface velocity were almost negligible for virtually the entire experiment. For Run 30d, the velocity vectors for particles near the edges of the gate opening displayed noticeable transverse components. As with the 0.10 m headwater experiments, this discrepancy between the orientation of the vectors is likely due to a different initial placement of the tracking particles as opposed to a variation in the movement of the flood wave.

### ***Wet-Bed Case***

The velocity vector plots for the experiments conducted with 0.30 m of headwater and 0.05 m and 0.10 m tailwater can be seen in Figures 4.15 and 4.16, respectively. These figures are of a slightly different format, in that the image from camera 1, corresponding to the time of the velocity vector plot, is also displayed. This was done to enable the reader to appreciate the location of the particles in relation to the flood wave. As with the velocity vector plots for the dry-bed case, the length and orientation of the vectors represents the magnitude and direction of the surface velocity. Towards the beginning of both experiments, the tracking particles downstream of the flood wave are resting on relatively still water, and therefore are barely moving. Thus, the location of these particles is represented by an arrowhead pointing in a direction which is dictated by slightly different  $x, y$  particle coordinates from frame to frame. The coordinate variation is due to a small amount of particle movement and to a different pixel chosen as the centre of the particle.



By looking at both Figures 4.15 and 4.16, it can be seen that the surface velocity was quite small at the start of the experiments. However, once the flood wave began to propagate outwards, the tracking particle velocity increased substantially. For the 0.05 m tailwater test, the maximum surface velocity was 0.5 m/s at 0.200 seconds; 1.0 m/s at 0.333 seconds; and by the end of the experiment (0.600 seconds), the surface velocity had reached 2.3 m/s. This same scenario (although delayed) was seen to occur for the experiment with the larger tailwater depth. The maximum surface velocity did not reach 0.5 m/s until 0.367 seconds; it reached 1.0 m/s at 0.500 seconds; it reached 1.5 m/s at 0.733 seconds; and by the end of the experiment (0.900 seconds) it had reached 2.0 m/s.

It is apparent from the plots in Figures 4.15 and 4.16 that the surface velocity is maximum close to the centreline of the tank and is considerably reduced towards the edges of the tank. Those particles closer to the sidewalls of the tank also took a lot longer to begin moving when compared with the particles towards the centre of the tank. These observations led to the conclusion that the wave propagation in the longitudinal direction is significantly faster than the wave propagation in the transverse direction. The scarcity of velocity vectors at the end of the experiments was due to particle entrainment as the flood wave propagated.

### ***Velocity Accuracy***

To compute the error in the velocity, the known error quantities for the  $x$  and  $y$  coordinates and the time were used. This technique is termed error propagation and is discussed in Davis, Foote, Anderson, and Mikhail (1981). The following equation has been adapted from Davis *et al.* (1981) and is used to obtain the error of a quantity



(velocity) computed from measurements (distance and time) used in a known mathematical relationship (velocity equals distance divided by time):

$$\sigma_v^2 = \left(\frac{\partial v}{\partial d}\right)^2 \sigma_d^2 + \left(\frac{\partial v}{\partial t}\right)^2 \sigma_t^2 \dots\dots\dots [4-2]$$

In the above equation,  $v$  is the tracking particle velocity,  $d$  is the distance the particle traveled from one frame to the next,  $t$  is the time the particle took to travel the aforementioned distance (time between frames),  $\sigma$  represents the error in the corresponding quantities,  $\partial v/\partial d$  is the partial derivative of the velocity equation with respect to distance, and  $\partial v/\partial t$  is the partial derivative of the velocity equation with respect to time.

To compute the velocity error, the error in the distance and the time are required. The error in the time ( $\sigma_t$ ) was estimated to be half of the smallest time count, which is 1/30 second, so  $\sigma_t$  is equal to 1/60 second. The distance the tracking particle traveled was computed using the following equation:

$$d = \sqrt{d_x^2 + d_y^2} \dots\dots\dots [4-3]$$

where  $d_x$  represents the distance the particle traveled in the  $x$  direction and  $d_y$  represents the distance the particle traveled in the  $y$  direction;  $d_x$  and  $d_y$  were determined by computing the difference between the  $x$  coordinates ( $d_x = x_2 - x_1$ ) and  $y$  coordinates ( $d_y = y_2 - y_1$ ) from one frame to the next, respectively. The errors associated with  $d_x$  and  $d_y$  were computed using error propagation and the known error in the  $x$  and  $y$  coordinates. The following equations were adapted from Davis *et al.* (1981),

$$\sigma_{d_x}^2 = \sigma_{x_2}^2 + \sigma_{x_1}^2 \dots\dots\dots [4-4a]$$





$\sigma_{d_y}^2 = \sigma_{y_2}^2 + \sigma_{y_1}^2$  .....[4-4b]

Thus, with  $\sigma_{x_2}$  and  $\sigma_{x_1}$  equal to 5 mm,  $\sigma_{d_x}$  was found to be equal to 7 mm. Similarly,  $\sigma_{d_y}$  was also equal to 7 mm. Through computations, it was confirmed that the error in the distance ( $\sigma_d$ ) is equivalent to the error in the distance traveled in one direction ( $\sigma_{d_x}$  or  $\sigma_{d_y}$ ). By using the estimated time error, the computed distance error, and  $x, y$  coordinates for a specific tracking particle together with equation 4.2, the velocity error for both the dry-bed and wet-bed experiments was found to be 13 percent.



## 4.2 Wave Probes

The wave probes were used, in two different arrangements (*i.e.*, symmetrical and asymmetrical), to measure the water depth variation with time for the dry-bed experiments. Their use was attempted for the tailwater experiments; however, due to significant probe-flow interaction, it was impossible to obtain meaningful results. As discussed in Chapter 3, water depths were measured for the following experiments using the symmetrical probe arrangement (shown in Figure 3.7): four runs with 0.10 m headwater; three runs with 0.20 m headwater; and three runs with 0.30 m headwater. The water depths were also measured using the asymmetrical probe arrangement (shown in Figure 3.8) for one run with each of the three headwater depths.

The symmetrical probe arrangement results can be seen in Figures 4.17, 4.18, and 4.19, for the 0.10 m, 0.20 m, and 0.30 m headwaters, respectively. Each figure contains the following two graphs in which results of all applicable runs are combined: (a) the water depth variation with time measured by the centreline probe; and (b) the water depth variation with time measured by the probes left and right of centre. The results were not displayed for the probes on the extreme left and right sides, since the water depths they measured were minimal. For visualization purposes, there is also a high-speed camera image (c) of the probes taken at a time of 1.0 second. The wave probe results do not start at time equal to zero, instead they start at the time when the water comes in contact with the first wave probe and it registers a voltage reading.

By looking at the wave probe results for the centreline probe and the probes left and right of centre, both the repeatability and symmetry of the experiments can be assessed. The repeatability was estimated by comparing the results from the same probe



for different experiments and the symmetry was assessed by comparing the results of the wave probes left and right of centre for the same experiment. The maximum differences observed were as follows: 5 mm for the 0.10 m headwater event, 16 mm for the 0.20 m headwater event, and 9 mm for the 0.30 m headwater event. The symmetry of measured depths around the centreline was within 3 mm for the 0.10 m event, 7 mm for the 0.20 m event, and 6 mm for the 0.30 m event. These results lead to the conclusion that the experiments were both repeatable and symmetrical.

Once the symmetrical nature of the experiments was assured, the probes were arranged on one side of the tank in an asymmetrical fashion and experiments were performed with headwater depths of 0.10 m, 0.20 m, and 0.30 m. These results are displayed in Figures 4.20, 4.21, and 4.22. The figures include (a) a graph displaying the water depths with time for all five wave probes and (b) an image of the experiment taken from the high-speed camera at a time of 1.0 second.

Confirmation of the symmetry of the experiments meant that the available stereoscopy data was essentially doubled. As shown in Figure 4.23 (a), the duplicated data was used to reconstruct the water surface profile and velocity vector plot for Run 30d at a time of 0.867 seconds. Also included in the figure is (b) an image of the event captured with the high-speed camera at the same time. This experiment was chosen because the majority of the tracking particles migrated to the right side of the tank and thus, by duplicating the data, considerable improvement was observed. By viewing the figure, it can be seen that the additional data on the left side of the tank resulted in a more defined water surface profile, which compares more favorably to the image from the high-speed camera. The improvement in velocity data also is apparent in Figure 4.23 (c);



instead of being clustered one side of the tank, the velocity vectors cover the entire width of the tank.

Although the probe results are useful for assessing the repeatability and symmetry of the experiments, the measured depths are not equal to the actual water depths. This is because when the water comes in contact with the probe, it is forced to flow around the probe and then join up again a distance downstream of the probe (see high-speed camera image in Figure 4.24). As shown in Figure 4.25, this causes a dry area to form downstream of the probe, which is termed the *zone of separation*. This zone does not extend to cover the full height of the probe; due to circulation downstream of the probe, the probe is immersed from its base up to the depth where the zone of separation begins. Since the probes measure the lowest point of immersion, which would be the depth on the downstream side of the probe, the measured water depth is substantially less than the actual water depth at the corresponding location if the probe was not present. If the probe was absent, it is expected that the actual water surface would be somewhere between the high depth on the upstream side of the probe and the low depth on the downstream side of the probe. The height of the separation zone (*i.e.*, the difference between the depth on the upstream side of the probe and the depth on the downstream side of the probe) was estimated by viewing the high-speed camera images. The maximum separation zone heights were approximately 50 mm, 40 mm, and 20 mm for headwater depths of 0.30 m, 0.20 m, and 0.10 m, respectively. These heights are equal to the maximum error in the wave probe depths.





### 4.3 Miscellaneous Results

This section is used to discuss the notable quantitative and qualitative results from the experiments with tailwater. Since the majority of the tracking particles became entrained for the experiments conducted with tailwater, the stereoscopy was not very effective. However, by viewing the images from these experiments, the nature of the flow was found to be quite interesting; the reservoir water became extremely turbulent and the tailwater moved forward as a laminar wave. To further examine the flow characteristics, additional tailwater experiments were performed without tracking particles, in which dye was placed in the reservoir water to enable differentiation between the headwater and the tailwater. In addition to these experiments, it was decided to also conduct two-dimensional dam break experiments in a long, rectangular flume to determine if the flow characteristics exhibited in the three-dimensional experiments were also apparent in the two-dimensional experiments. First in this section is a qualitative description of the three-dimensional dam break behaviour, next is a qualitative description of the two-dimensional dam break behaviour, and finally is a discussion of the propagating wave velocity for both two- and three-dimensional dam break experiments.

#### 4.3.1 *Three-dimensional Experiments with Tailwater*

The three-dimensional dam break experiments were conducted in the tank pictured in Figure 3.1 and recorded with the three video cameras described in section 3.1.1. In addition to capturing the top view of the dam break with the video cameras, the high-speed camera was placed on the side of the tank to capture the side view of the



event. The top view of the progression in time of the three-dimensional flood waves with initial depth ratios of 6:1 and 3:1 can be seen in Figures 4.26 and 4.27, respectively. To differentiate the headwater from the tailwater, red dye was used in the upstream section of the flume and the tailwater was left clear.

Qualitative observations, which were very similar for both depth ratios, were made by viewing Figures 4.26 and 4.27 and by examining the corresponding video images. It can be seen that for both depth ratios, there was minimal mixing between the headwater and tailwater, which resulted in a distinct separation between the clear tailwater and the coloured headwater. As can be seen in the top view images (Figures 4.26 and 4.27) and the side view images from the high-speed camera (Figure 4.28), the initial release of the headwater forced the tailwater to shape into a smooth, laminar wave and, in contrast, the water leaving the reservoir (identified with dye) quickly became quite turbulent and turbulence continued to be generated as the water flowed out of the reservoir. As the water propagated downstream, the laminar wave appeared to pull away from the coloured headwater and its width (in the direction of flow) increased substantially with time. Concurrently, the front face of the laminar wave became steeper and steeper, until the wave crest developed a tongue that curled forward (see Figure 4.28(a)) and plunged into the downstream tailwater. It was observed that the propagating wave bulge remained relatively turbulence free until the point where the wave broke, which, as seen in the figures, occurred much sooner for the case of lower tailwater.

These qualitative results were interesting to the researchers due to the fascinating nature of the images and the fact that similar observations had not been reported previously by other researchers. It was desirable to understand the internal dynamics of



the flow and the cause for the smooth tailwater bulge and the turbulent headwater. To explore this flow further and to determine if the same characteristics were exhibited in two dimensions, two-dimensional dam break experiments were performed which essentially represented a cross-section along the centreline of the three-dimensional dam break wave.

#### ***4.3.2 Two-dimensional Experiments with Tailwater***

The two-dimensional dam break experiments were conducted in the 9.8 m long by 0.4 m wide by 0.3 m deep flume pictured in Figure 4.29. Like the tank used for the three-dimensional experiments, the flume had Plexiglas walls and a sheet metal floor. For comparison purposes, the experiments were conducted with the same headwater to tailwater ratios as for the three-dimensional experiments: 6:1 (0.24 m headwater and 0.04 m tailwater) and 3:1 (0.24 m headwater and 0.08 m tailwater). To divide the upstream and downstream sections of the flume, a Plexiglas gate was installed, which was manually raised to release the headwater into the downstream portion of the flume. By viewing the video images of the experiments, the gate opening time was estimated to be 0.25 seconds, which is the same as for the three-dimensional dam break experiments. Two colour video camera heads (model number TK-12800) with Cosmicar/ Pentax lenses (6 mm, F/1.2) were connected to two JVC Super-VHS VCRs. As shown in Figure 4.29, the cameras were placed on the side of the flume and staggered along its length to capture the entire dam break event. The experiments were also viewed from the side by a Motion Scope high-speed camera made by Redlake Imaging Corporation (USA), model PCI 1000 s (No. 1108-0008), which was placed on a moving trolley. The camera was



manually advanced along the length of the flume in an attempt to capture the leading edge of the wave. The depth variation across the width of the flume was observed to be negligible; therefore, the shape of the flood wave from the side of the flume was representative of the shape across the width of the flume.

Figures 4.30 and 4.31 show a side-view of the progression of the two-dimensional flood-wave for the initial depth ratios of 6:1 and 3:1, respectively. In the figures, the wave propagation is from right to left; the scale on the bottom of the images is in centimetres and the zero point on the scale is at the gate. All the images in Figure 4.30 are from the upstream camera, and in Figure 4.31, the first three images are from the upstream camera and the last three images are from the downstream camera. Again, for visualization purposes, red dye was used to colour the headwater and the tailwater was left clear. Since the leading edge of the propagating wave was difficult to see in the printed images, it was delineated based on viewing the actual video images. For future studies, using a slight amount of dye in the tailwater may make the propagating wave easier to distinguish.

By viewing the still and video images of the two-dimensional dam break experiments, it was found that the flow characteristics seen for the two-dimensional experiments closely duplicated the characteristics previously observed for the three-dimensional experiments. The water from the reservoir remained separate from the tailwater, which was pushed forward as a smooth bulge in the flow while what was once the headwater, became extremely turbulent flow following behind the smooth wave. As was observed for the three-dimensional dam break, the propagating wave was seen to break much sooner for the case of lower tailwater.







By viewing the video images of the two-dimensional dam break event from the side, the internal flow dynamics could be deduced. Figure 4.32 is an illustration of the estimated flow behaviour (a) as the gate was being lifted, (b) once the gate was fully removed, and (c) a short period after the gate was fully removed. As the gate left the flume floor, to adjust the upstream and downstream pressure differences, the headwater began to flow underneath the gate and it pushed the tailwater up, which resulted in the initiation of roller (1) as illustrated in Figure 4.32 (a). Once the tailwater was forced up and forward by the headwater, a forward moving roller in the tailwater (2) resulted (see Figure 4.32 (b)). With time, these small rollers developed into larger rollers with an approximate size equal in magnitude to the depth of flow (see Figure 4.32 (c)). It is also believed that a secondary, smaller roller developed on the water surface (3) which was a result of the headwater moving forward and down. The approximate location of these rollers are drawn on Figures 4.30 and 4.31.

Since the characteristics of the two-dimensional flows were observed to behave very similar to those of the three-dimensional dam break flows, it is assumed that the internal flow dynamics of the two-dimensional dam break are representative of those for the three-dimensional dam break. Through this assumption, Figure 4.32 can be used to understand that the initial release of the headwater into the tailwater caused an upward moving roller (1) to develop which pushed the tailwater up and the smooth bulge resulted. Then, the resultant, forward moving roller in the tailwater bulge (2) caused this bulge to propagate forward until it eventually broke. By the development of roller (1) and the formation of roller (3), turbulence resulted in the tailwater due to the opposing nature of the rollers.



### 4.3.3 Wave Velocity

The leading edge velocity for both the two- and three-dimensional experiments was computed by digitizing the location of the leading edge in the experimental images. For the three-dimensional experiments, two locations on the centreline of the flood wave were digitized: the front of the wave and the back of the wave (see Figure 4.33). The wave peak was not digitized, since it was difficult to locate in the images, as is apparent in Figure 4.33. The front and back of the wave was digitized for the duration of the experiments and their locations were plotted against time for both depth ratios, as shown in Figure 4.34. To determine the velocity of the leading edge, linear trendlines were fit to both the front of the wave and the back of the wave data points; the slope of the trendline is the wave velocity. Also included on the graphs are lines which represent the progression of the two-dimensional theoretical flood wave for the given initial conditions. The properties of the theoretical flood wave were computed by the *Method of Characteristics* outlined in Henderson (1966) and Chow (1959).

It is apparent by looking at the graphs and by the ‘coefficient of determination’ ( $R^2$ ) that the data points obtained for the front of the wave follow the linear trendline better than the data points obtained for the back of the wave. This is likely due in part to the difficulties encountered in accurately defining the back of the wave. The front of the wave was very smooth and it was relatively easy to identify the leading edge; however, the back of the wave was very turbulent and thus it was quite difficult to accurately locate the back of the wave. For this reason, the velocity resulting from the front of the wave data points was taken to be the wave propagation velocity.



For the 6:1 depth ratio, the leading edge velocity was found to be 1.98 m/s and for the 3:1 depth ratio, the velocity was found to be 1.64 m/s. The two-dimensional theoretical velocities for the 6:1 and 3:1 depth ratios are 1.64 m/s and 1.61 m/s, respectively. Although the experimental and theoretical velocities for the 6:1 depth ratio are considerably different (1.98 m/s versus 1.64 m/s), the agreement is not actually that bad for the initial period of wave propagation when one graphically compares the slope. For the 3:1 depth ratio, the experimental and theoretical velocities are very close (1.64 m/s versus 1.61 m/s), and the graphical comparison between the slope of the line representing the theoretical velocity and the line representing the experimental velocity is also very good.

For the two-dimensional experiments, the point where the tailwater depth deviated from the initial depth was taken as the leading edge. As for the three-dimensional experiments, this location was digitized for the entire duration of the experiments and was then plotted versus the time (see Figure 4.35). A trendline was fit to the data points and the slope of the trendline was taken to be the wave velocity. The wave velocity was 0.92 m/s for the 6:1 depth ratio and 1.24 m/s for the 3:1 depth ratio. The theoretical wave velocities are 1.47 m/s and 1.44 m/s for the 6:1 and 3:1 depth ratios, respectively. By viewing the graph and by comparing the numerical values, the velocity for the 3:1 depth ratio more closely matches the theoretical velocity than for the 6:1 depth ratio. This may be due to friction, which is not included in the computation of the theoretical wave velocity, and is more prominent for the 6:1 depth ratio, due to the smaller tailwater depth.



The preceding experiments were conducted to investigate the application of stereoscopy to the measurement of three-dimensional dam breaks. This measuring technique was explored since it is non-intrusive and it does not assume a hydrostatic pressure distribution; characteristics which make its use very attractive for the measurement of unsteady flow. Although inaccuracies were incurred in obtaining the coordinates of the water surface, these preliminary experiments illustrate the promising nature of the stereoscopic measurement techniques for dynamic open channel flow problems.





Table 4.1: Experiments performed without tailwater for which stereoscopy was used.

test	headwater (m)	tailwater (m)
Run 10a	0.10	0
Run 10c	0.10	0
Run 20c	0.20	0
Run 30b	0.30	0
Run 30d	0.30	0

Table 4.2: Experiments performed with tailwater for which stereoscopy was used.

test	headwater (m)	tailwater (m)
Run 30-5d	0.30	0.05
Run 30-10a	0.30	0.10





Figure 4.1: Illustration of particle streaking for 0.10 m headwater event.



Figure 4.2: Illustration of particle streaking for 0.20 m headwater event.



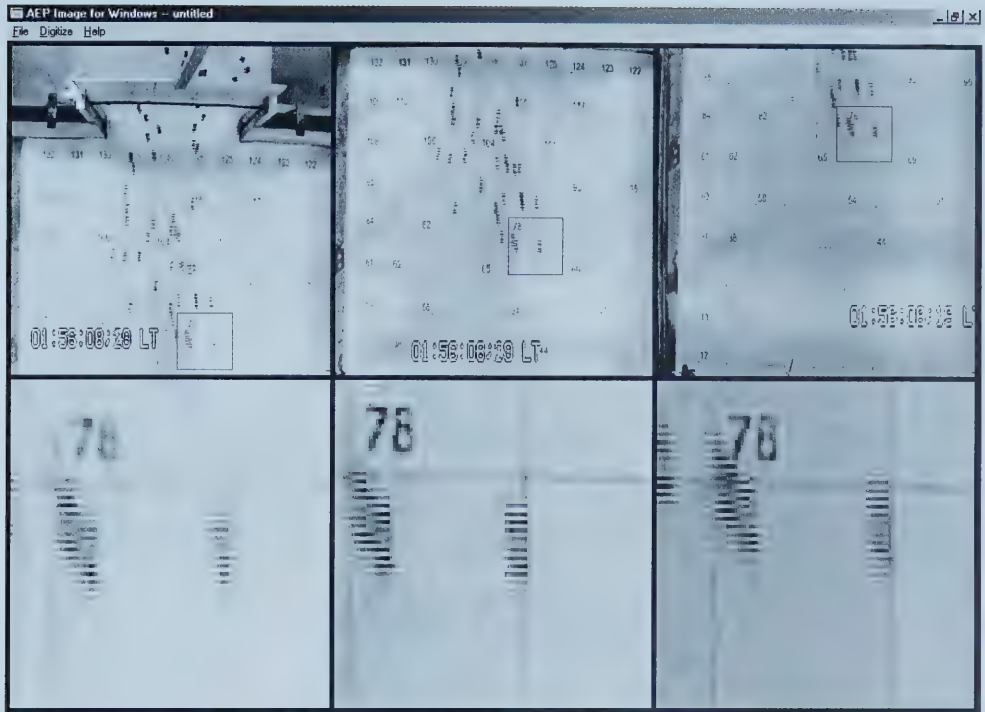


Figure 4.3: Illustration of particle streaking for 0.30 m headwater event.



Figure 4.4: Illustration of particle tilting for 0.30 m headwater event.



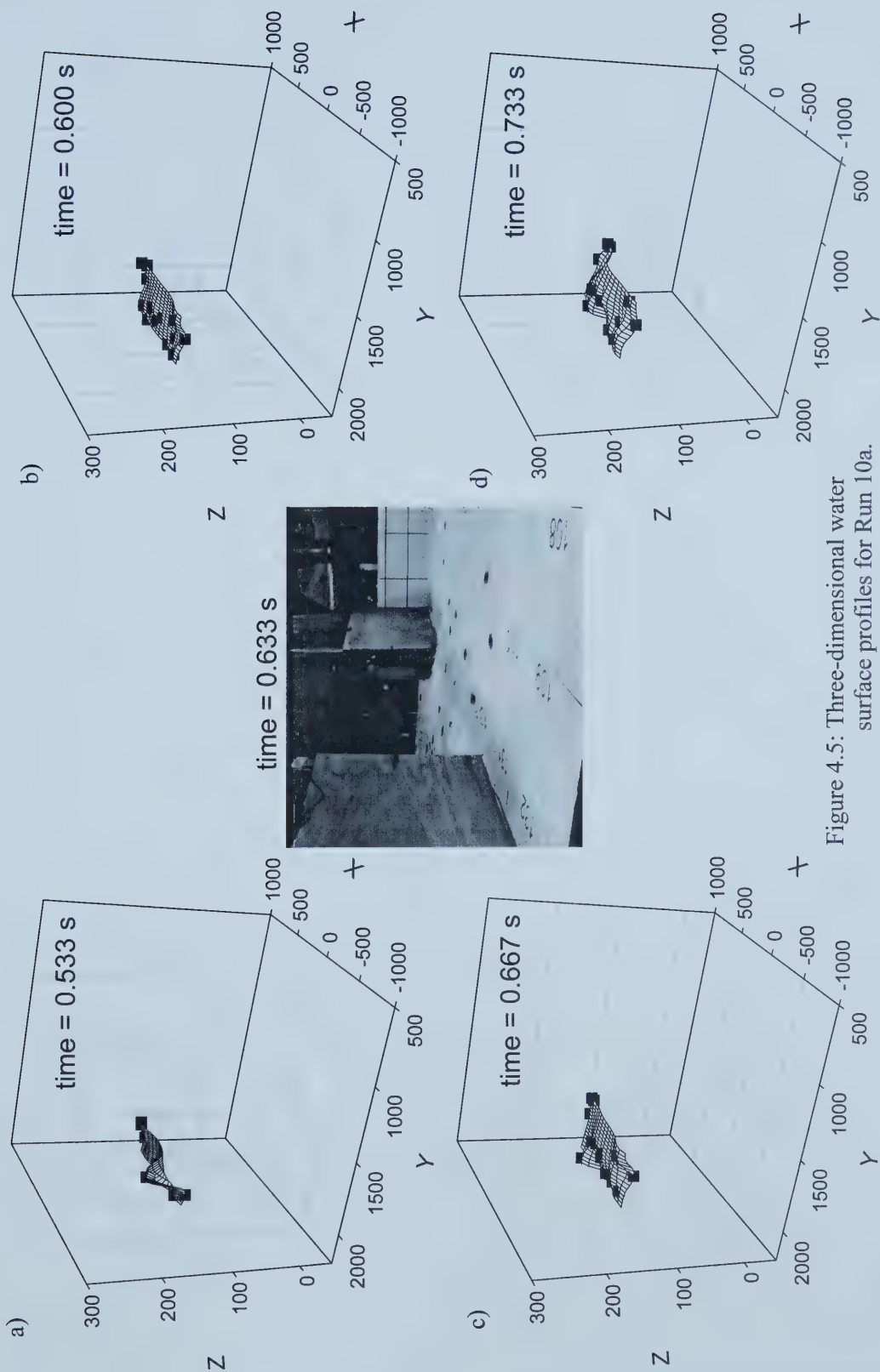


Figure 4.5: Three-dimensional water surface profiles for Run 10a.





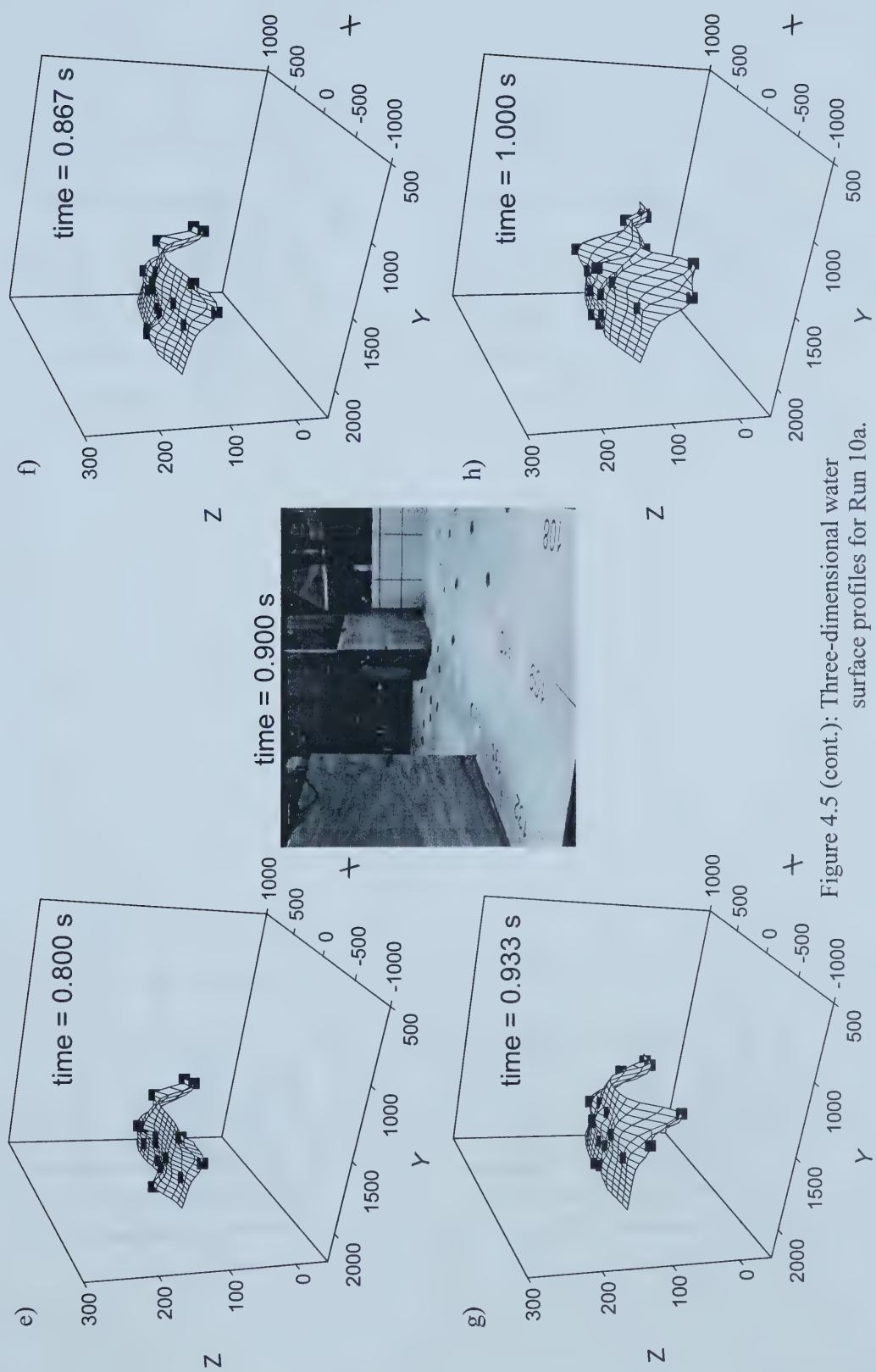


Figure 4.5 (cont.): Three-dimensional water surface profiles for Run 10a.



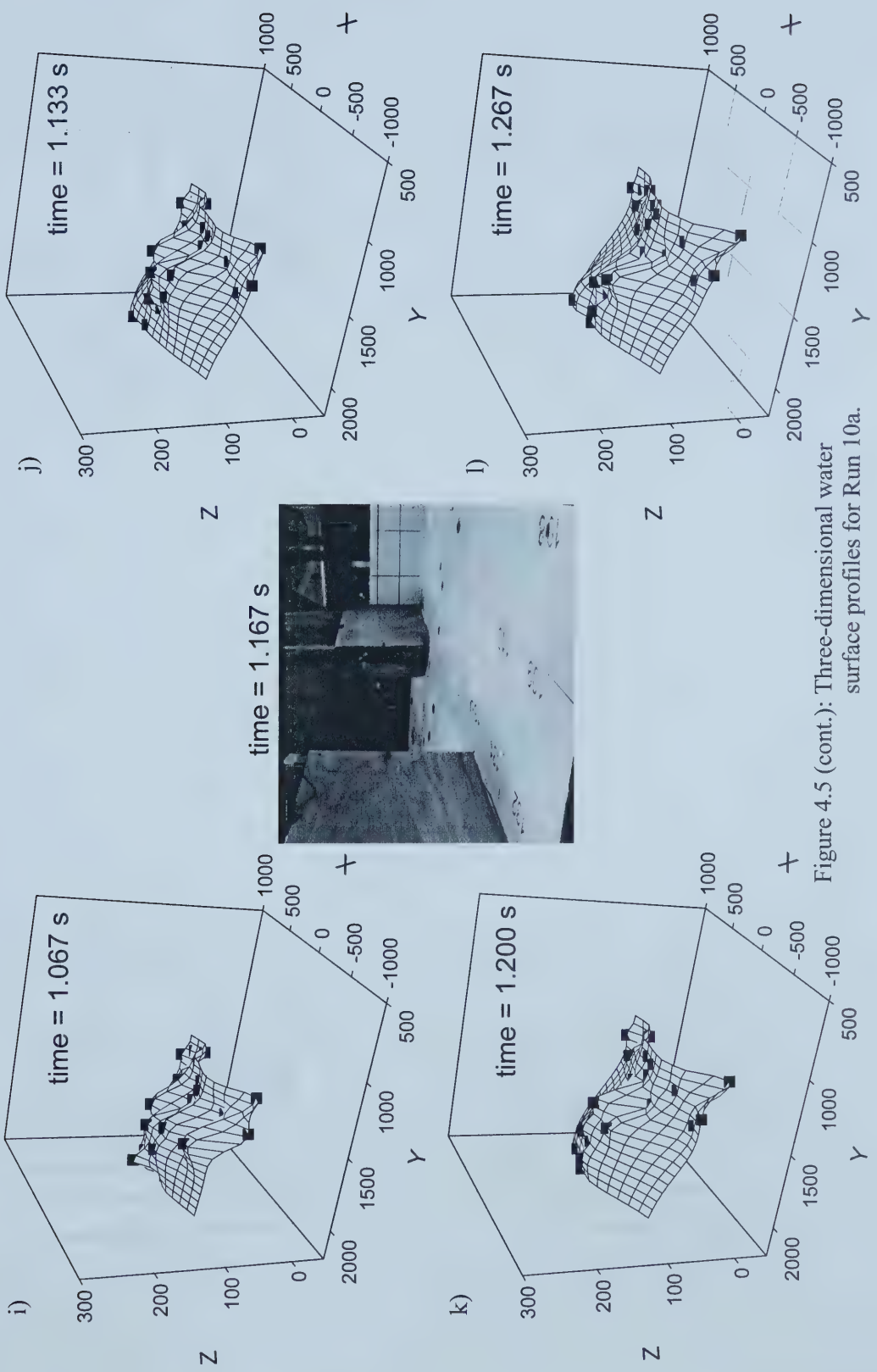
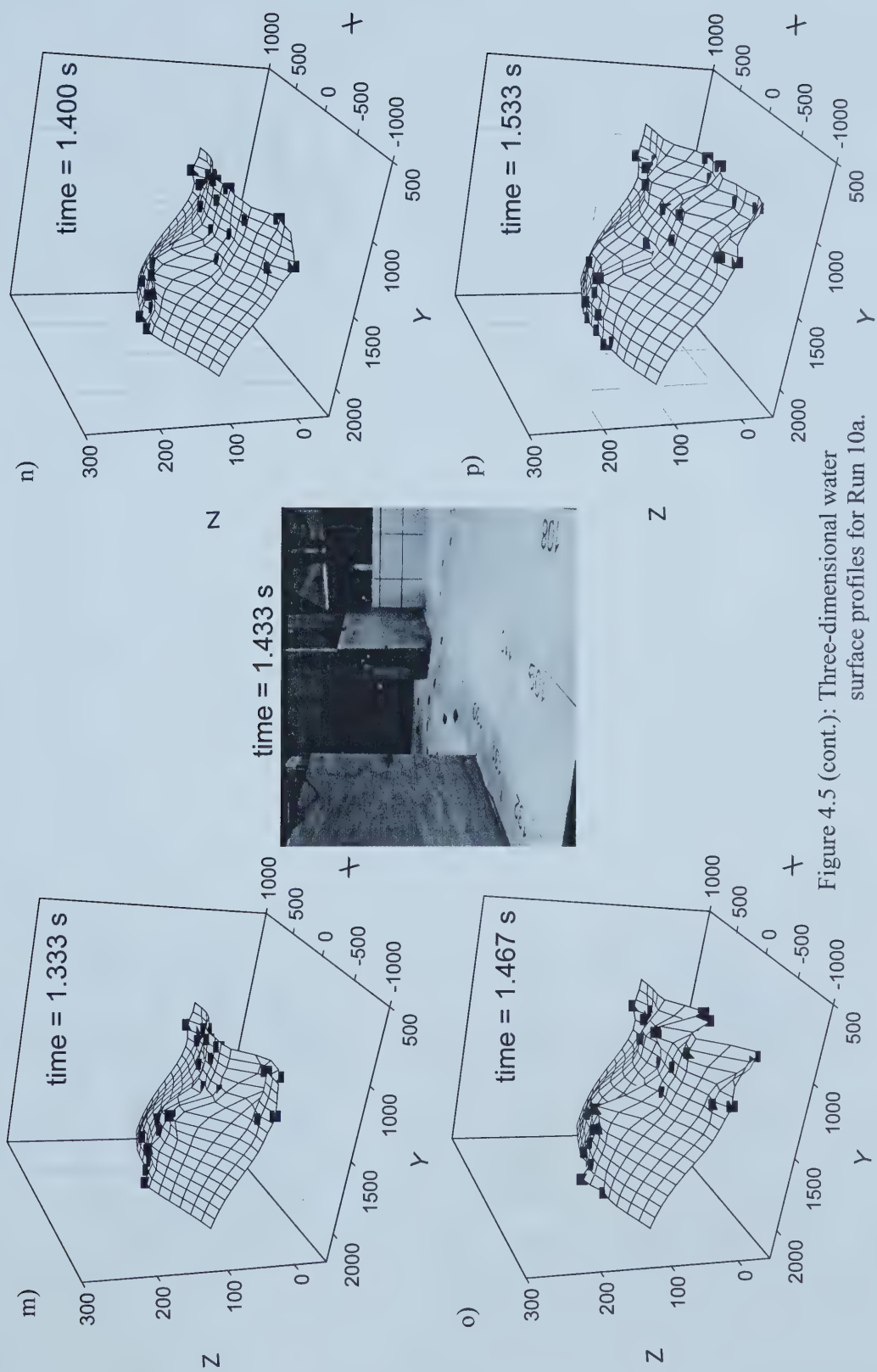


Figure 4.5 (cont.): Three-dimensional water surface profiles for Run 10a.







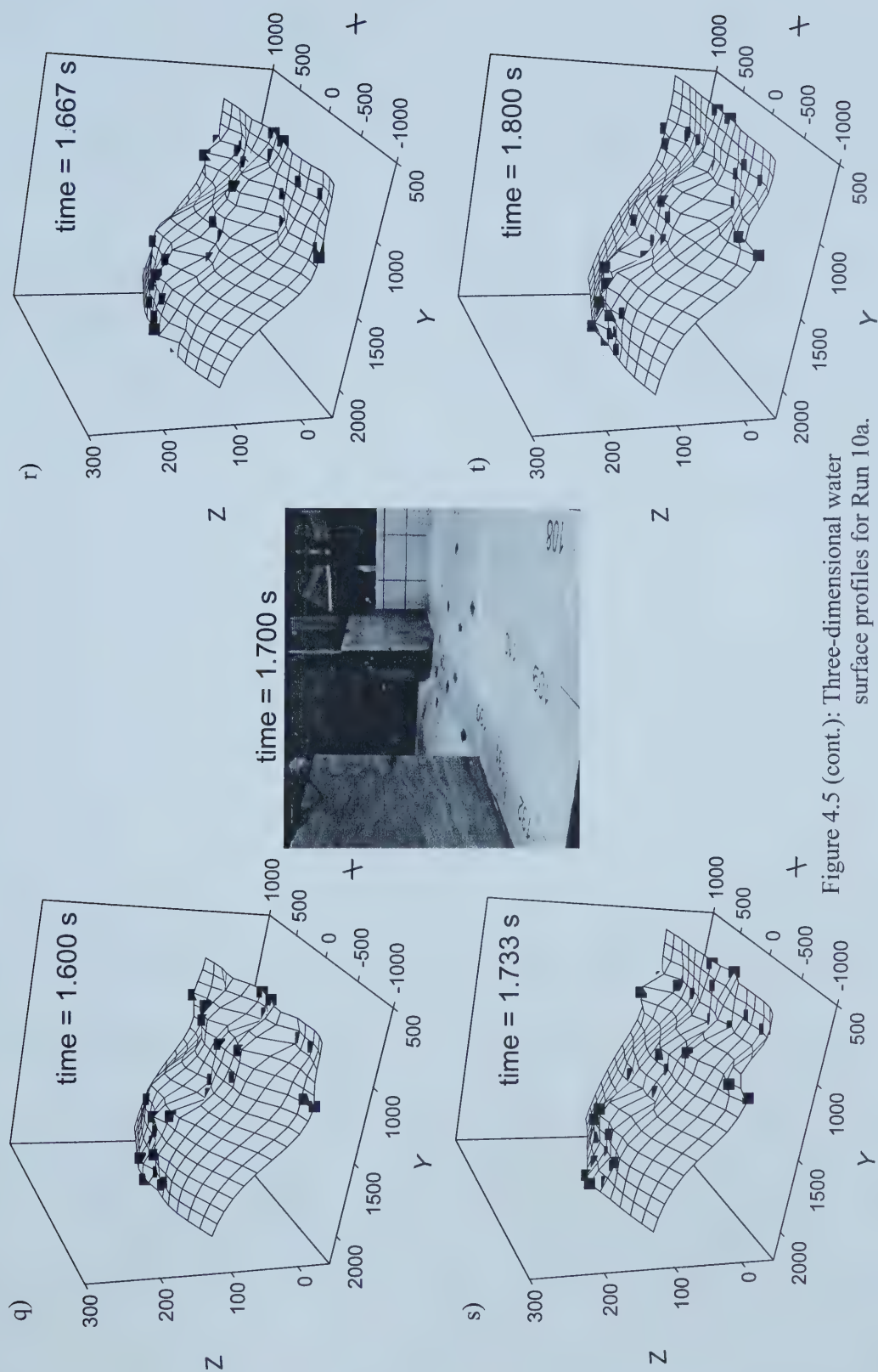


Figure 4.5 (cont.): Three-dimensional water surface profiles for Run 10a.





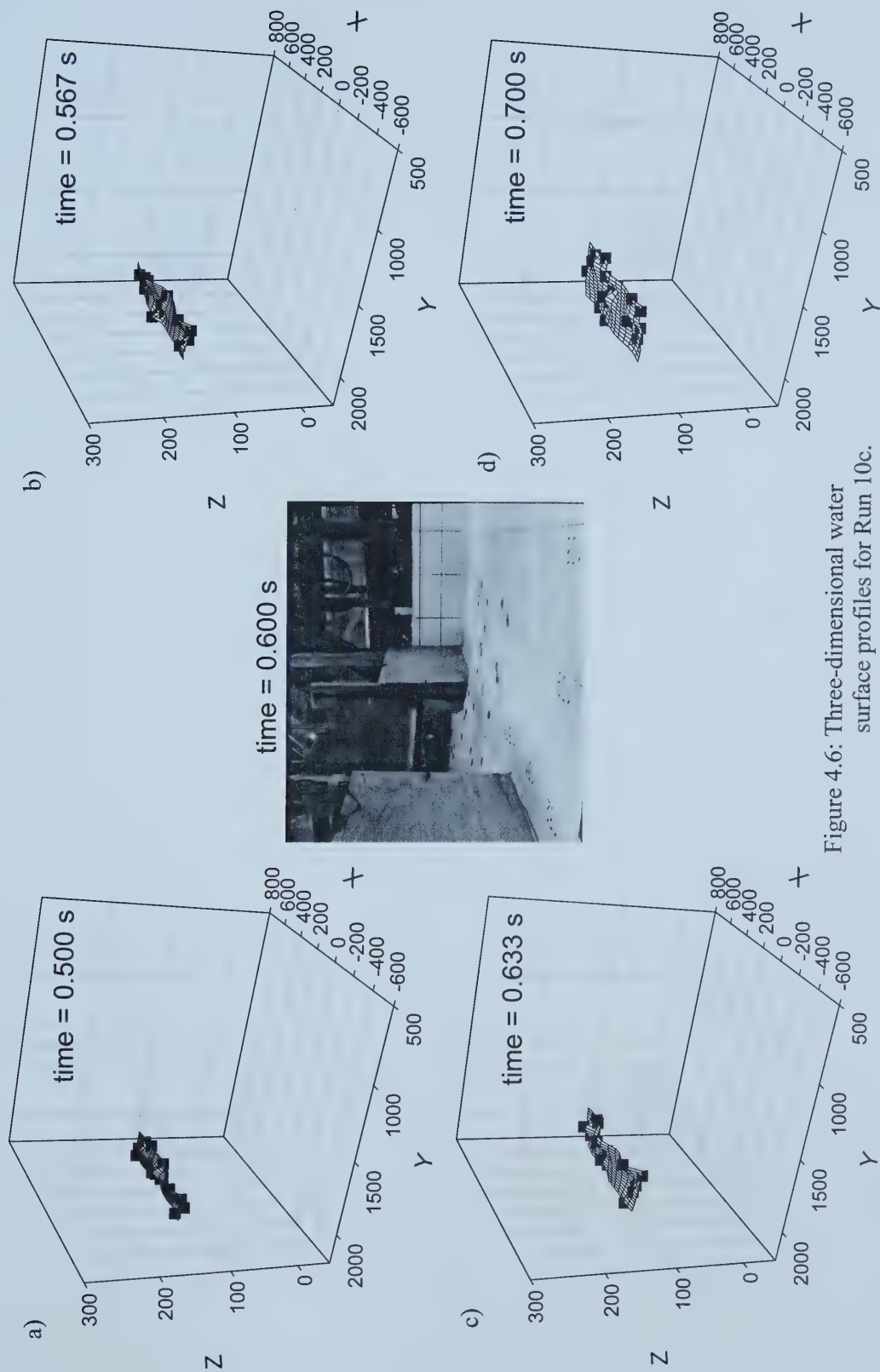


Figure 4.6: Three-dimensional water surface profiles for Run 10c.



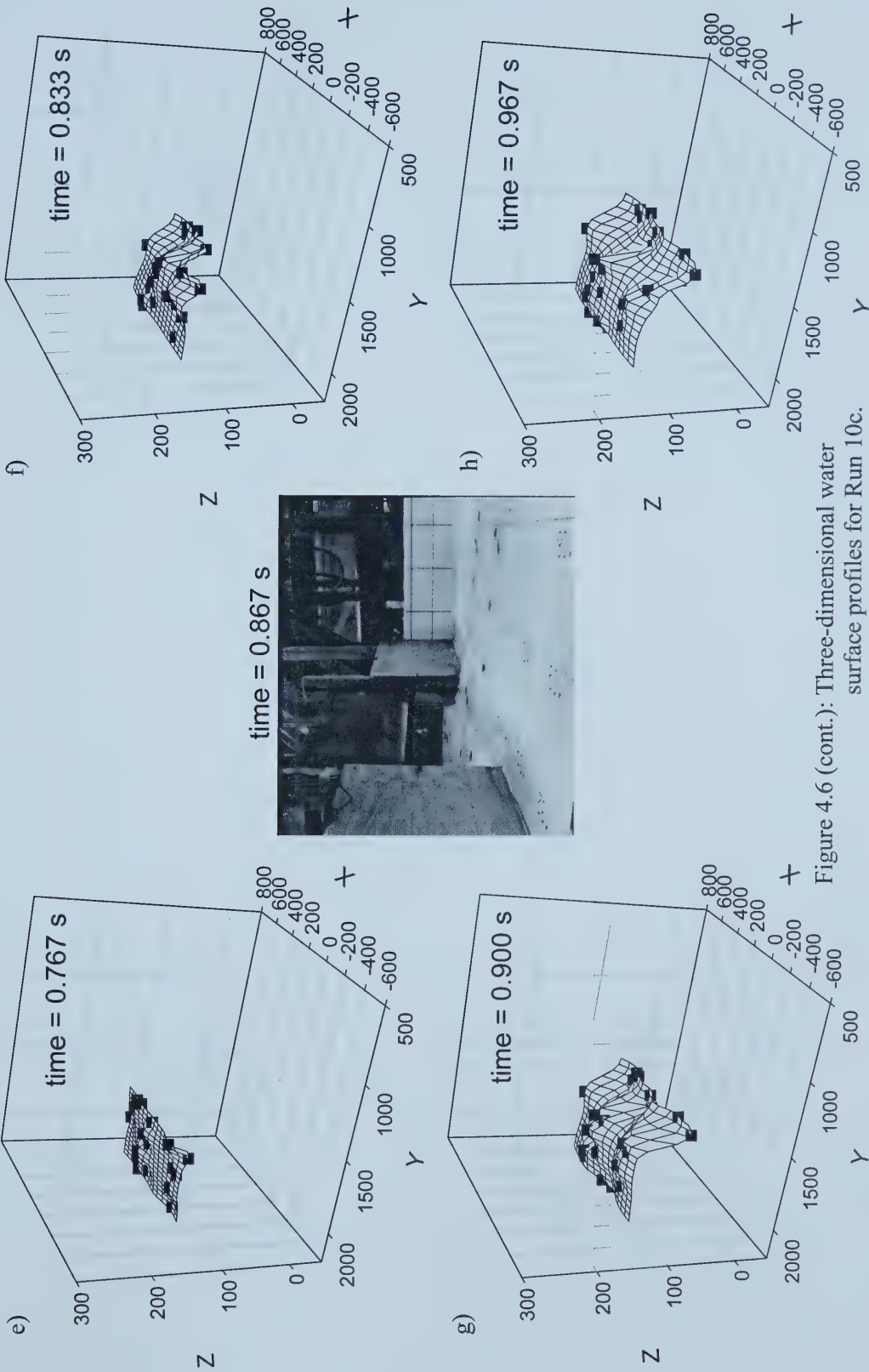


Figure 4.6 (cont.): Three-dimensional water surface profiles for Run 10c.



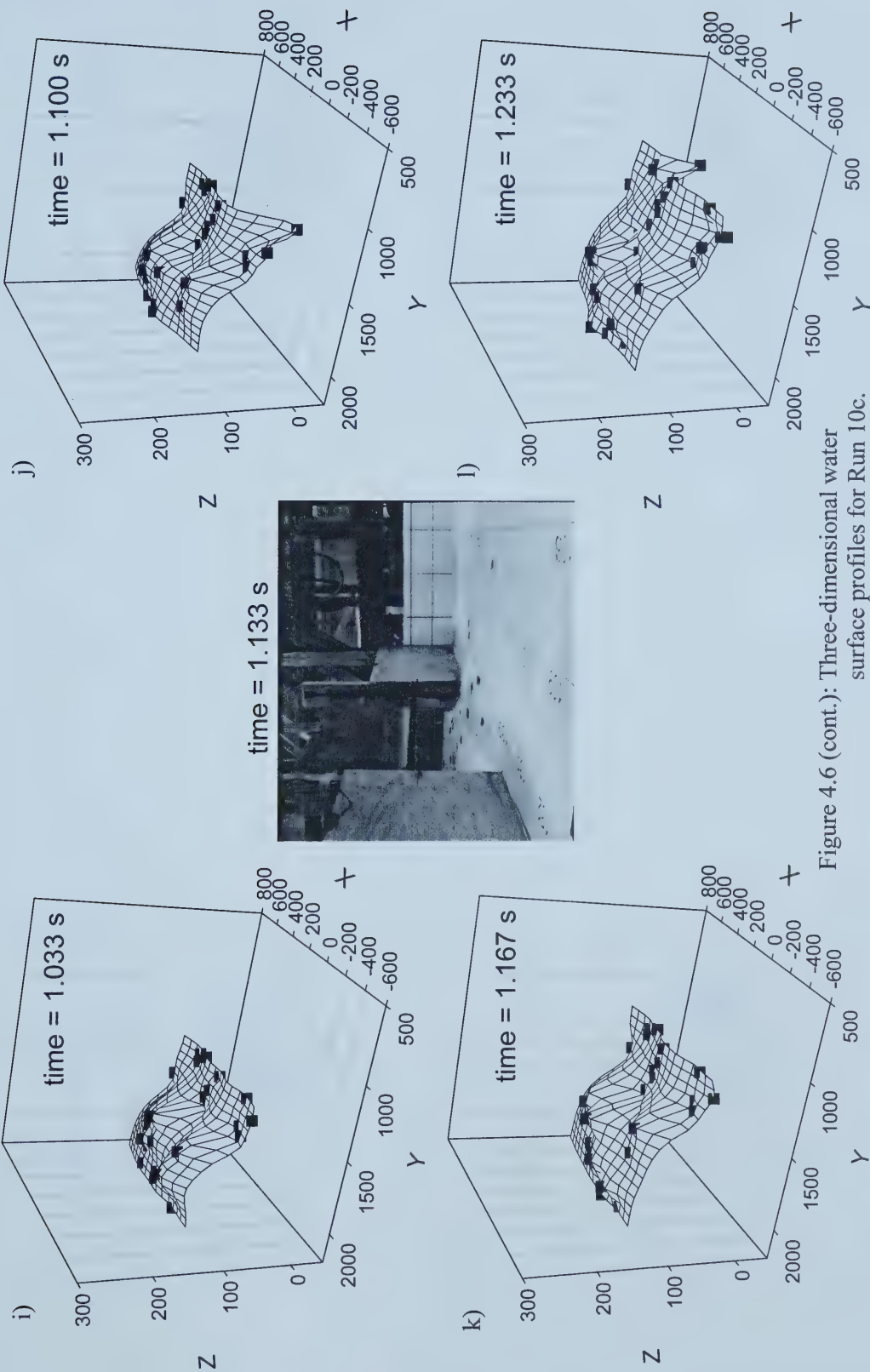


Figure 4.6 (cont.): Three-dimensional water surface profiles for Run 10c.



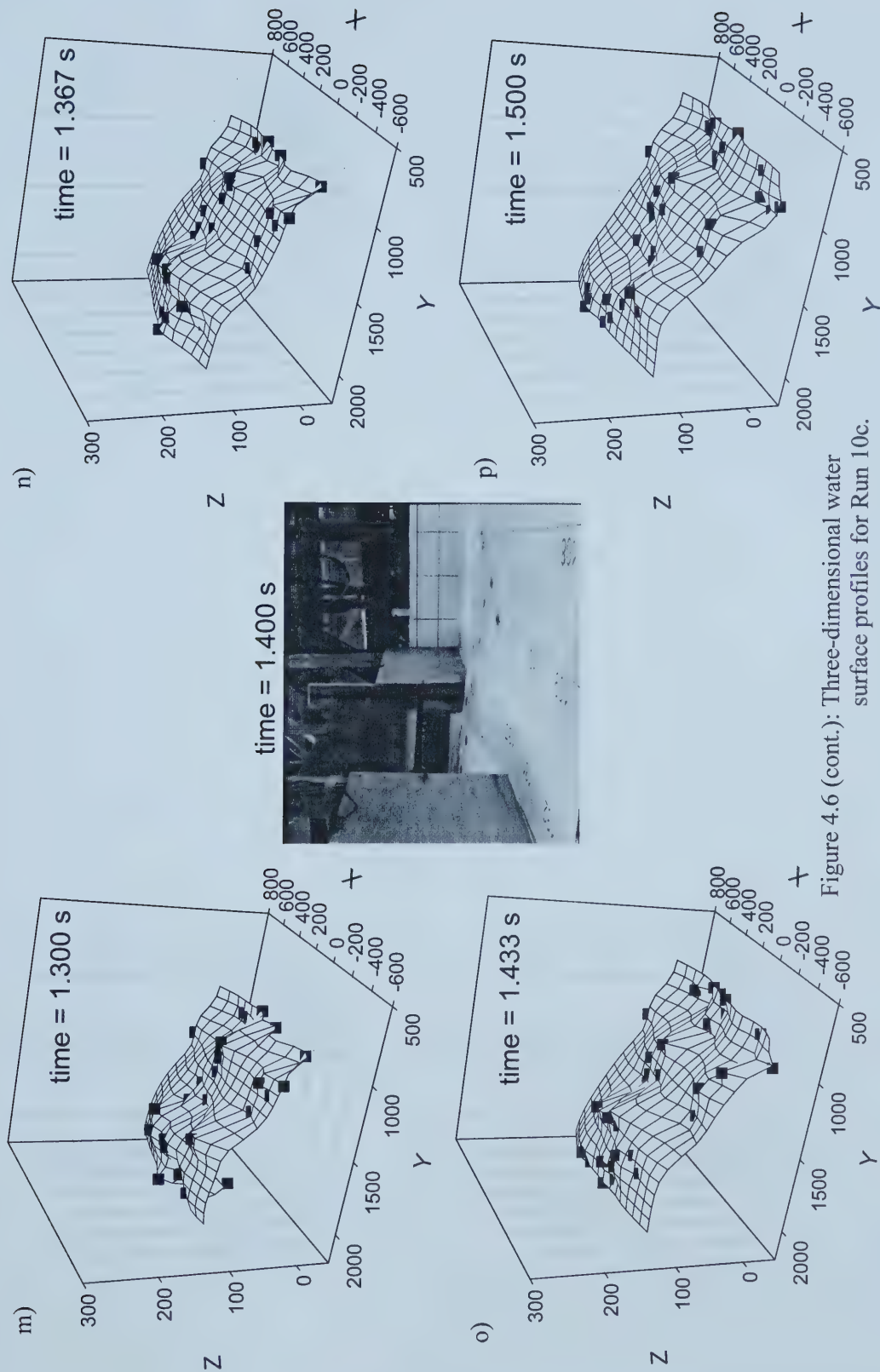
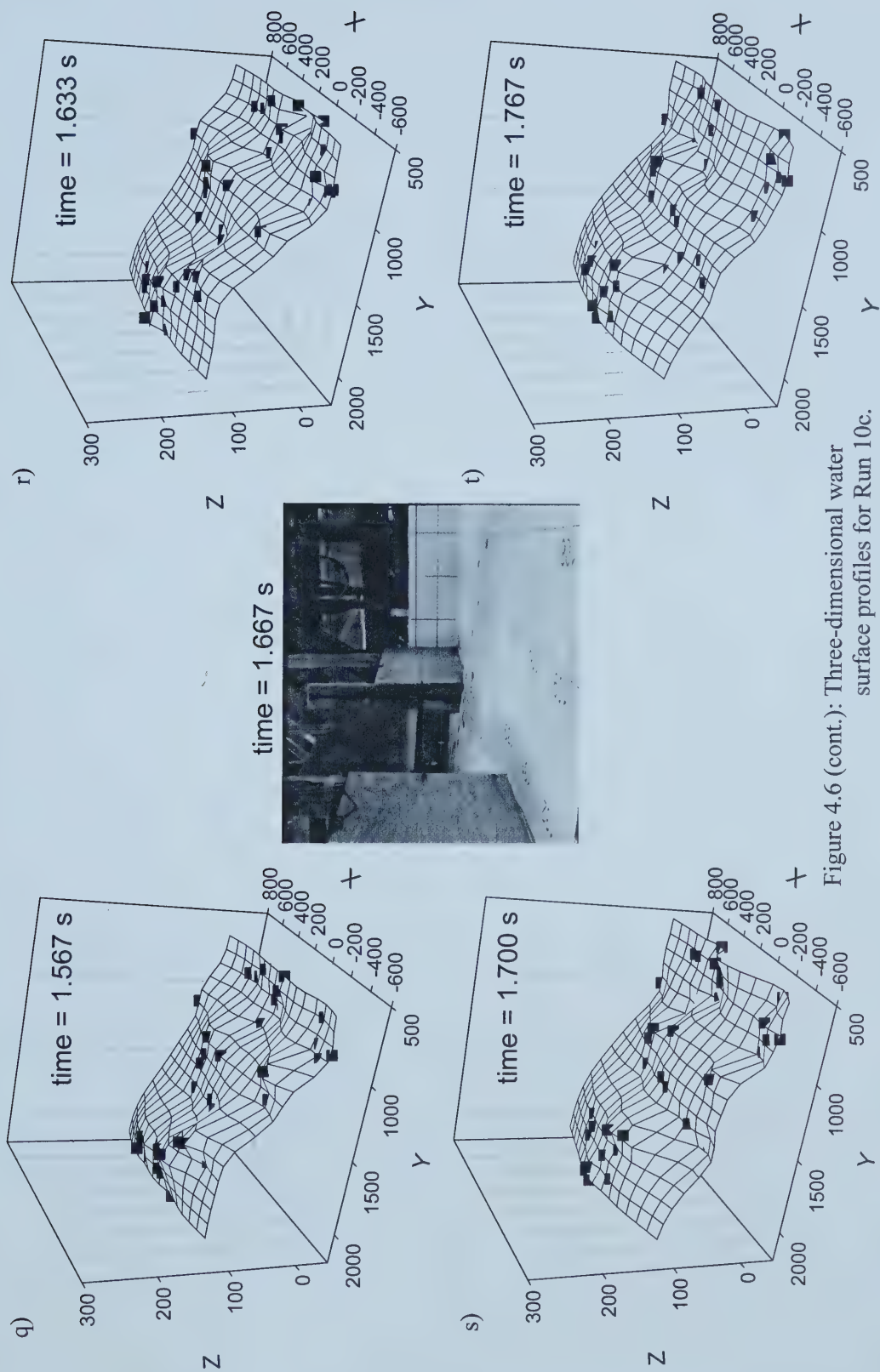


Figure 4.6 (cont.): Three-dimensional water surface profiles for Run 10c.









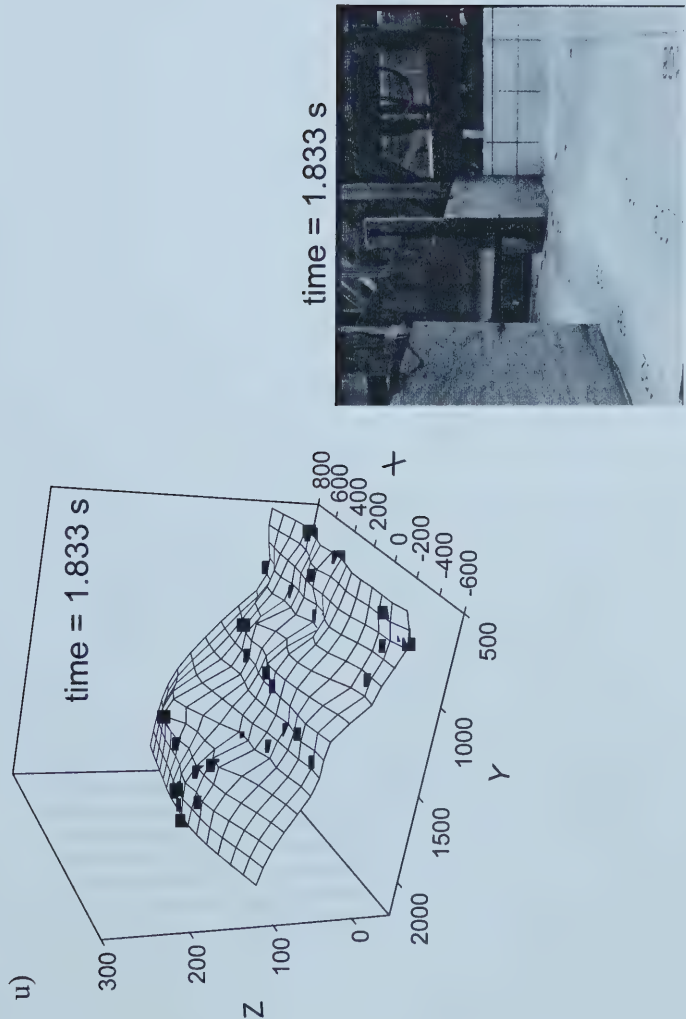


Figure 4.6 (cont.): Three-dimensional water surface profiles for Run10c.



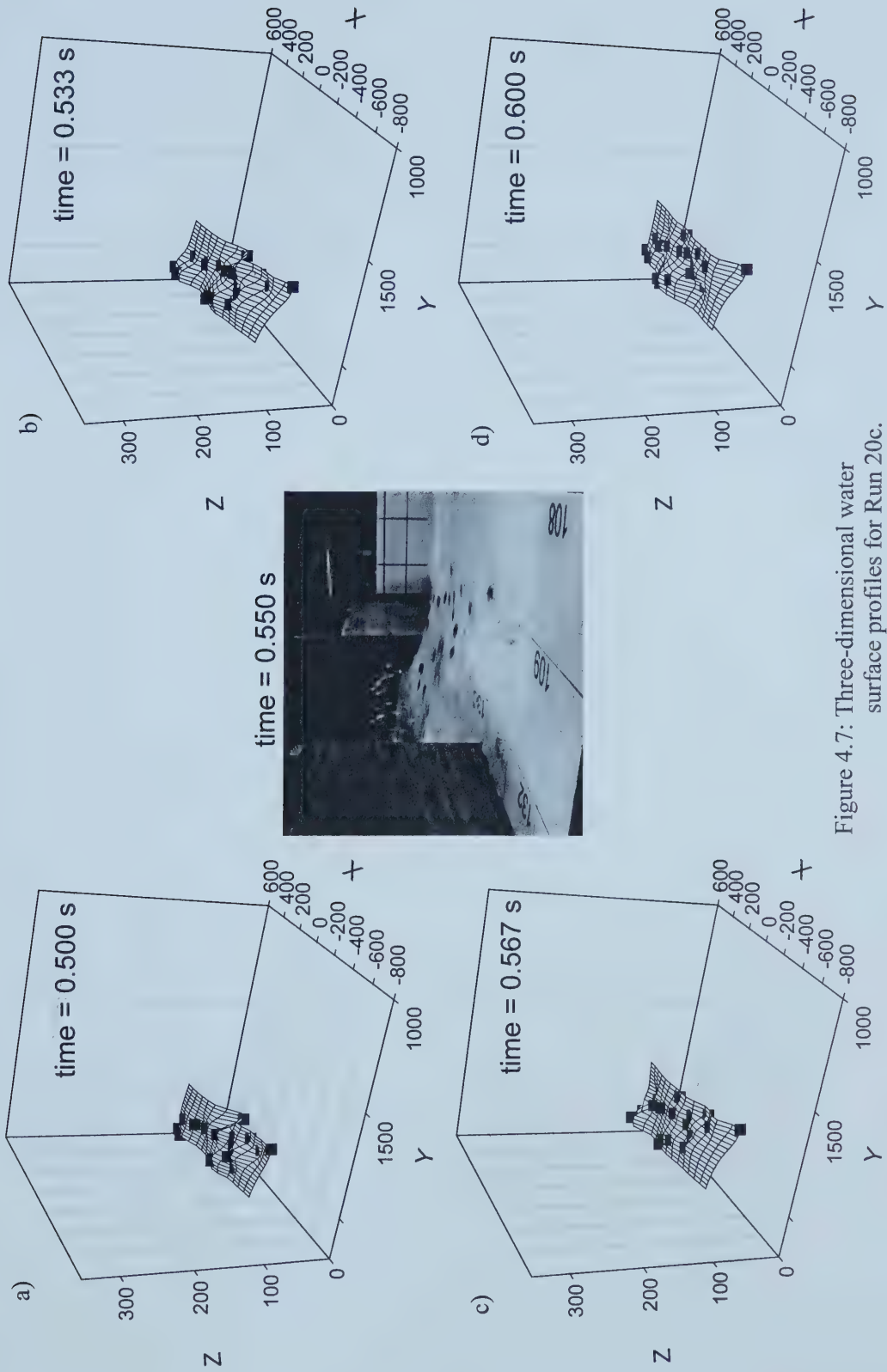


Figure 4.7: Three-dimensional water surface profiles for Run 20c.



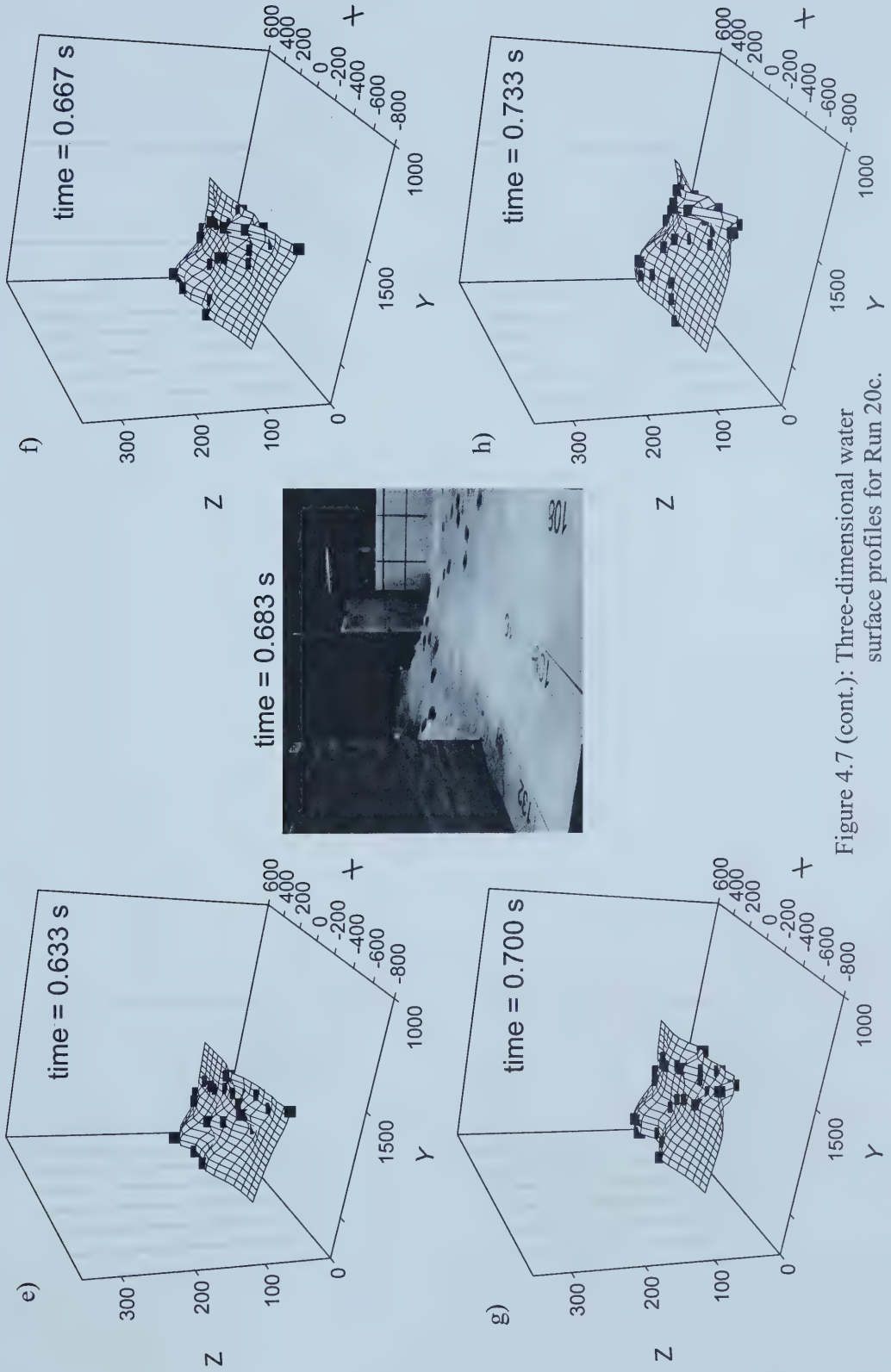


Figure 4.7 (cont.): Three-dimensional water surface profiles for Run 20c.





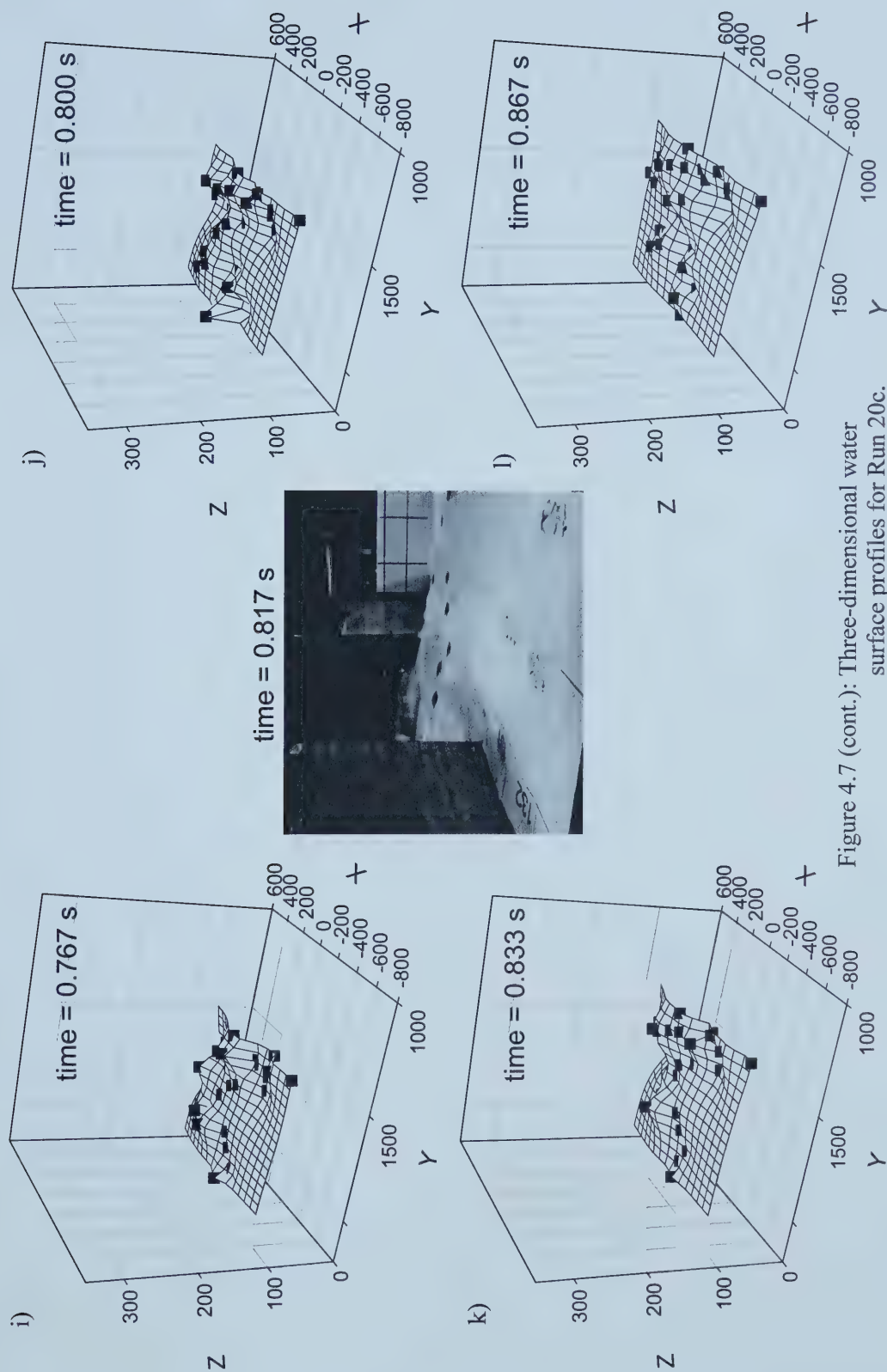
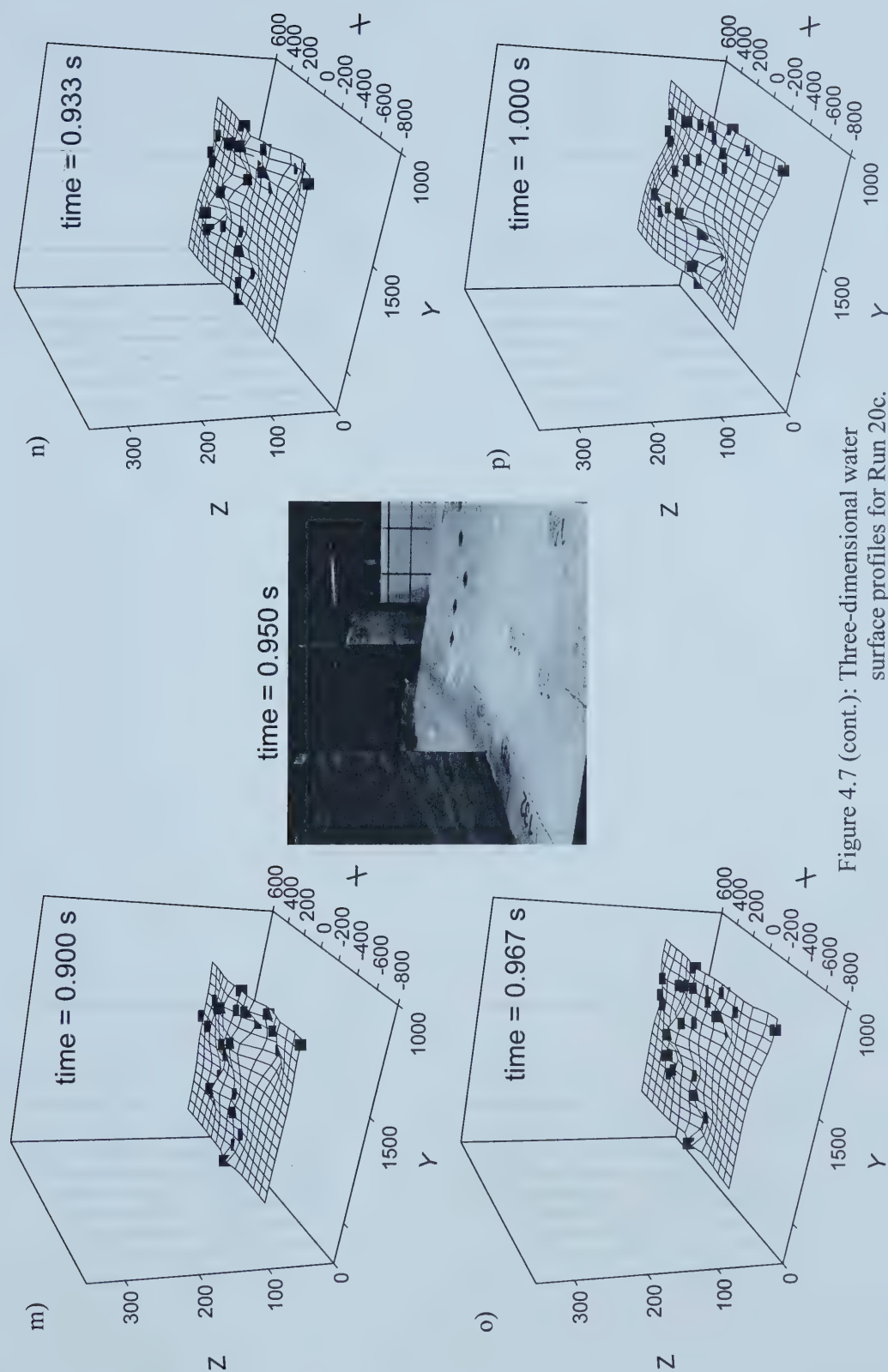


Figure 4.7 (cont.): Three-dimensional water surface profiles for Run 20c.







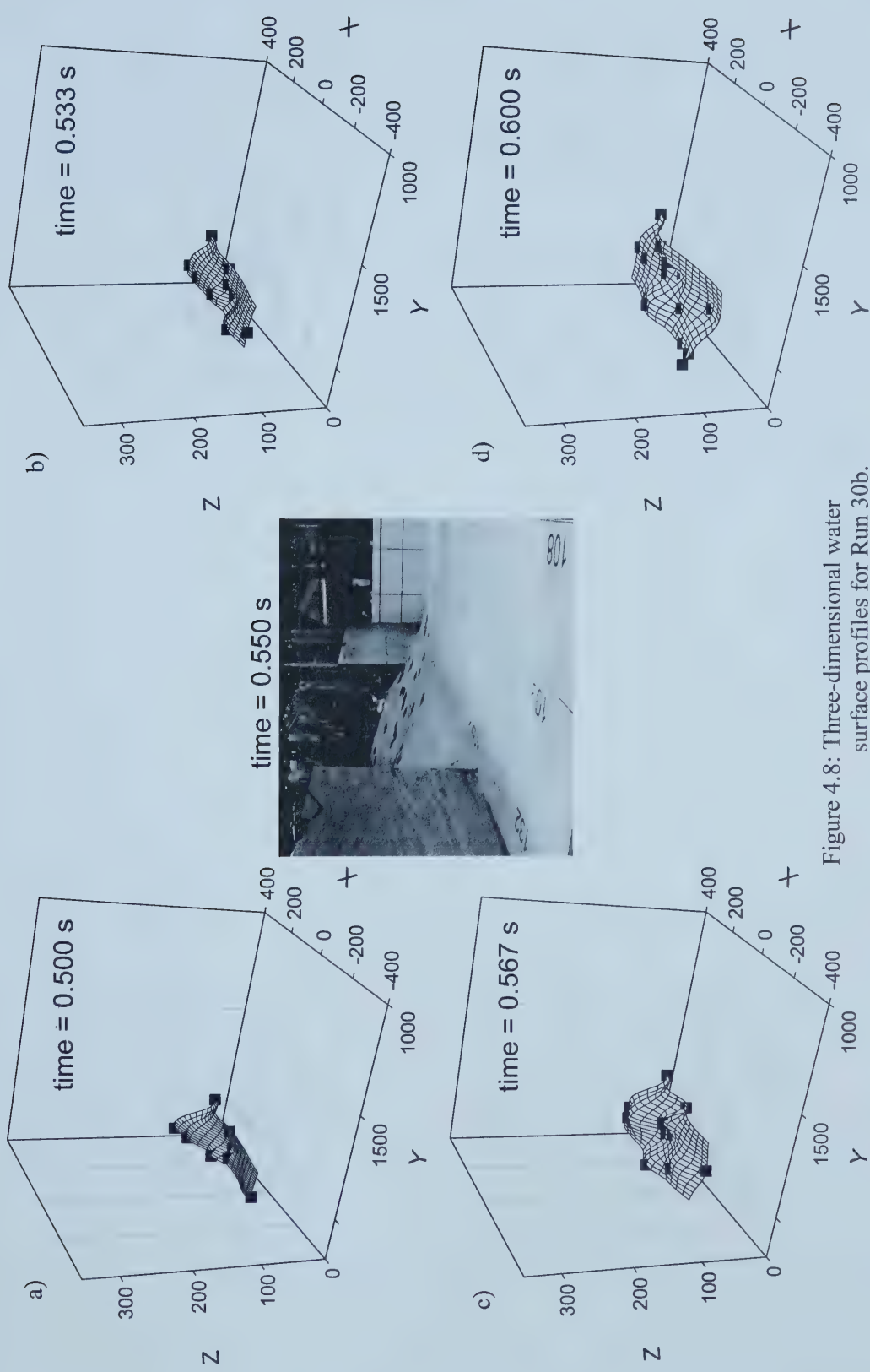


Figure 4.8: Three-dimensional water surface profiles for Run 30b.



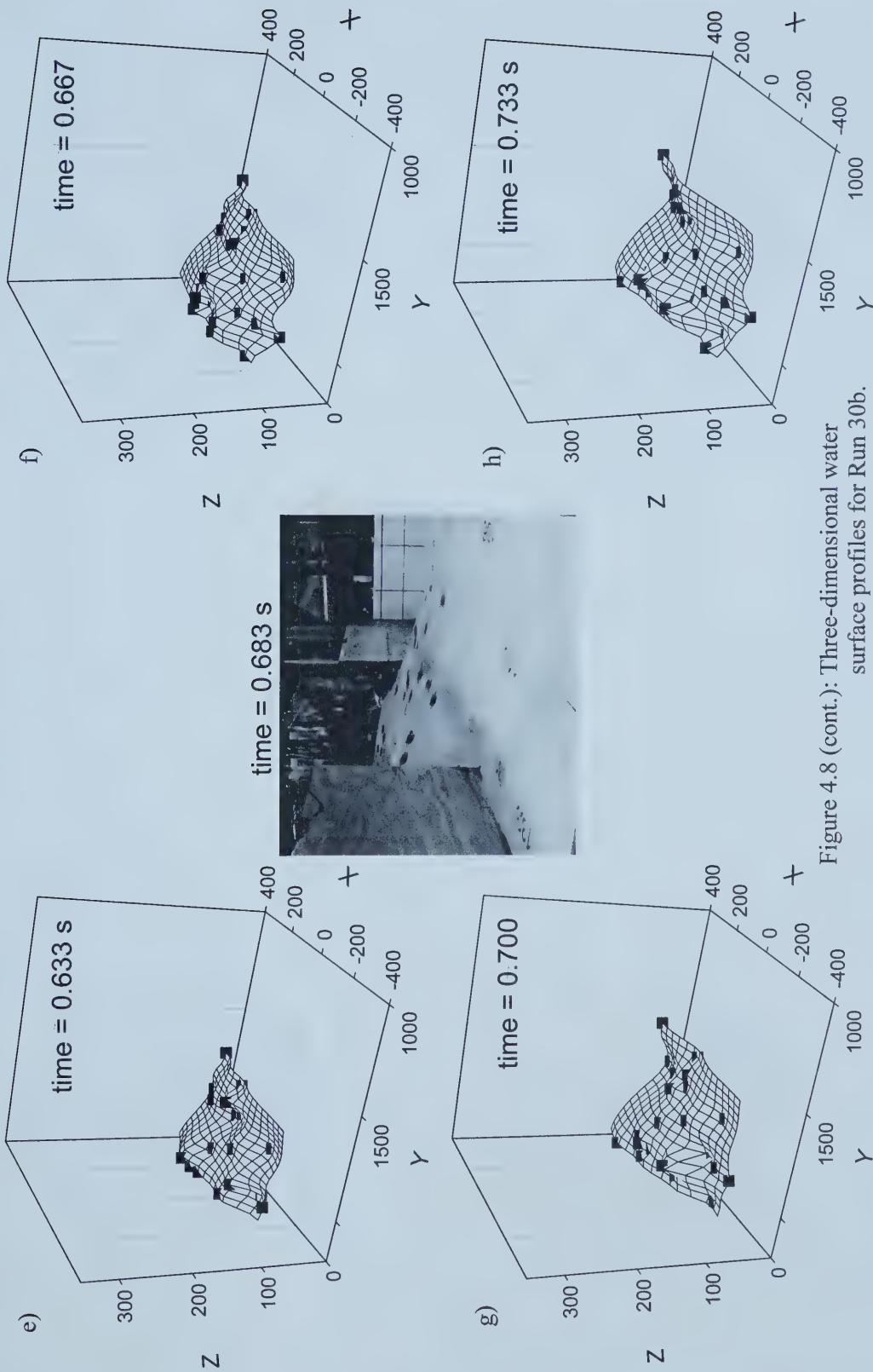


Figure 4.8 (cont.): Three-dimensional water surface profiles for Run 30b.





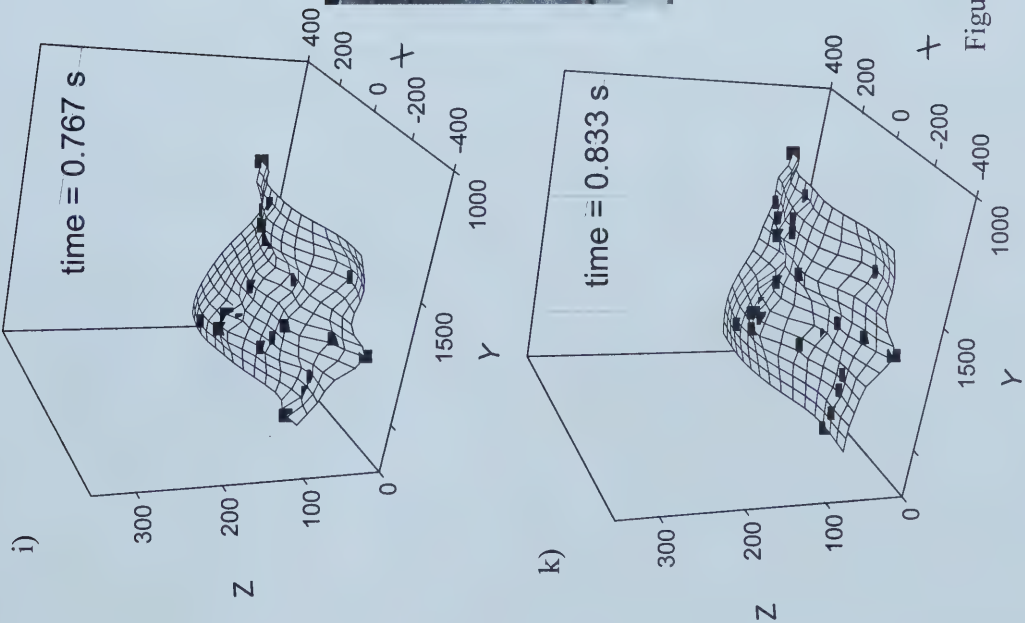
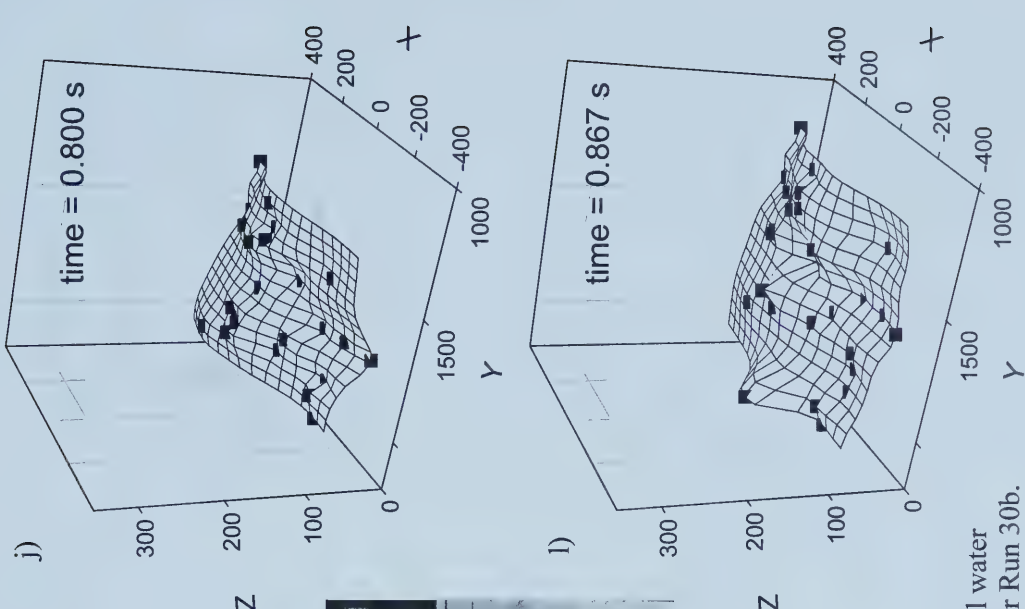


Figure 4.8 (cont.): Three-dimensional water surface profiles for Run 30b.





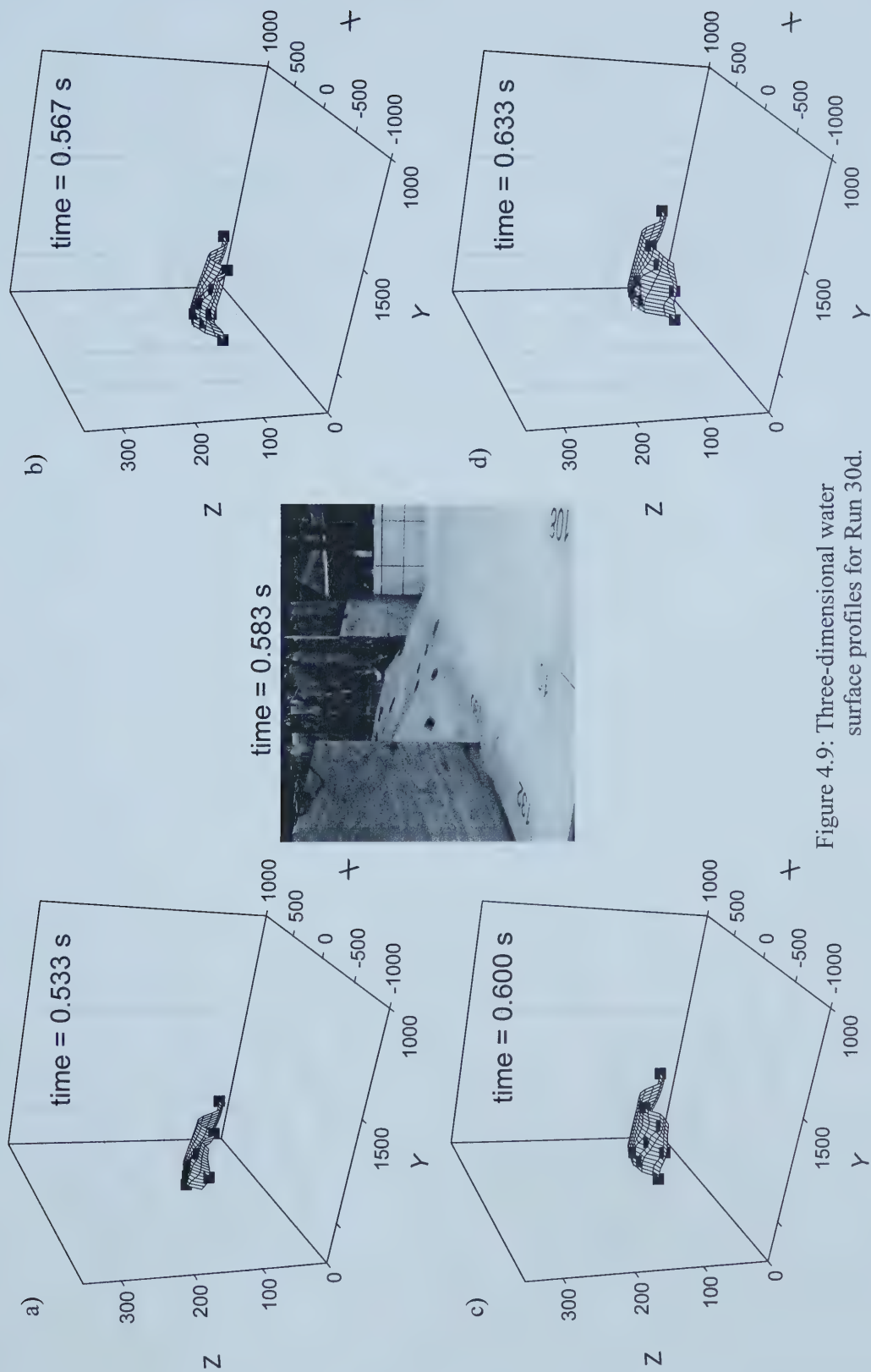


Figure 4.9: Three-dimensional water surface profiles for Run 30d.



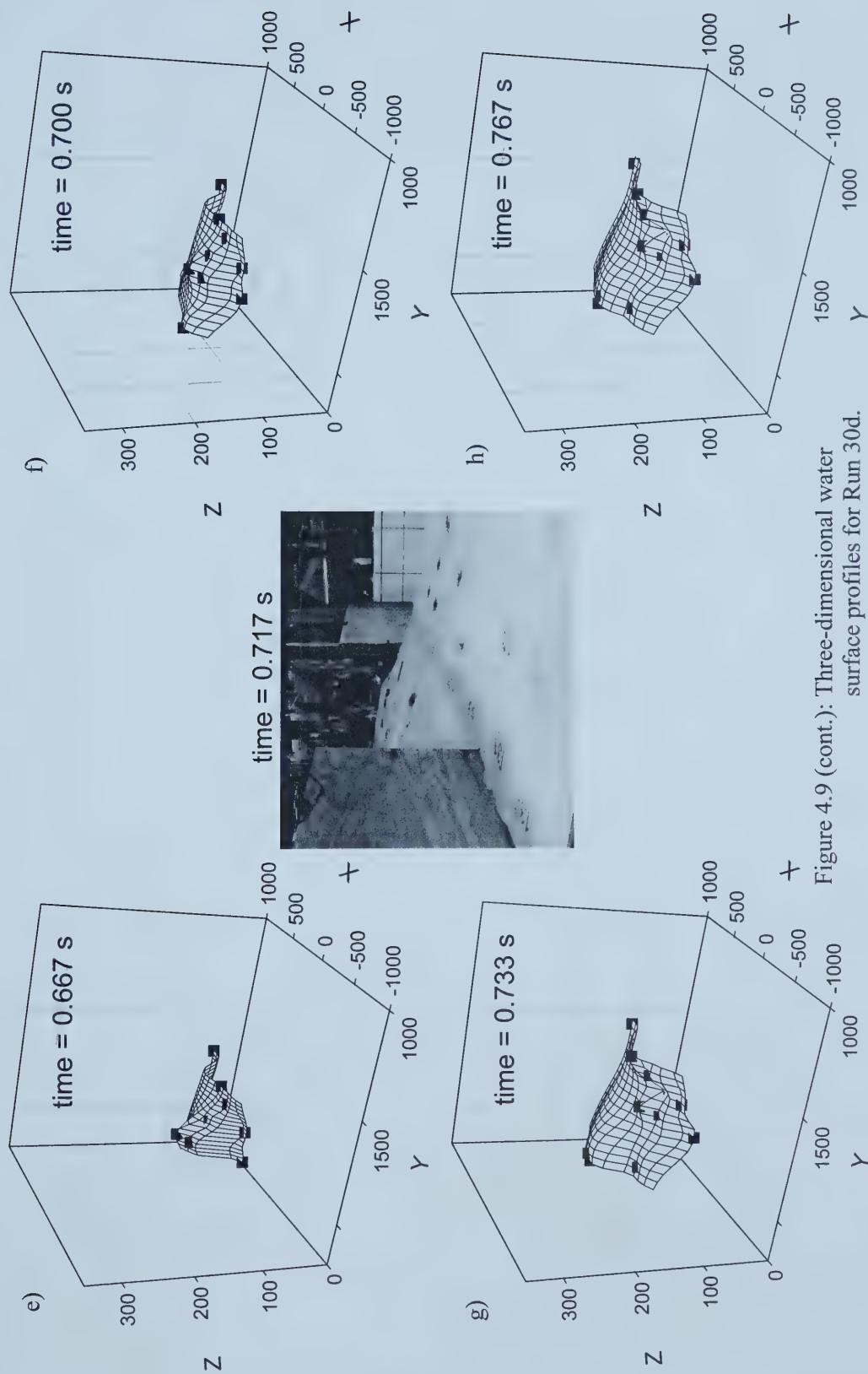


Figure 4.9 (cont.): Three-dimensional water surface profiles for Run 30d.



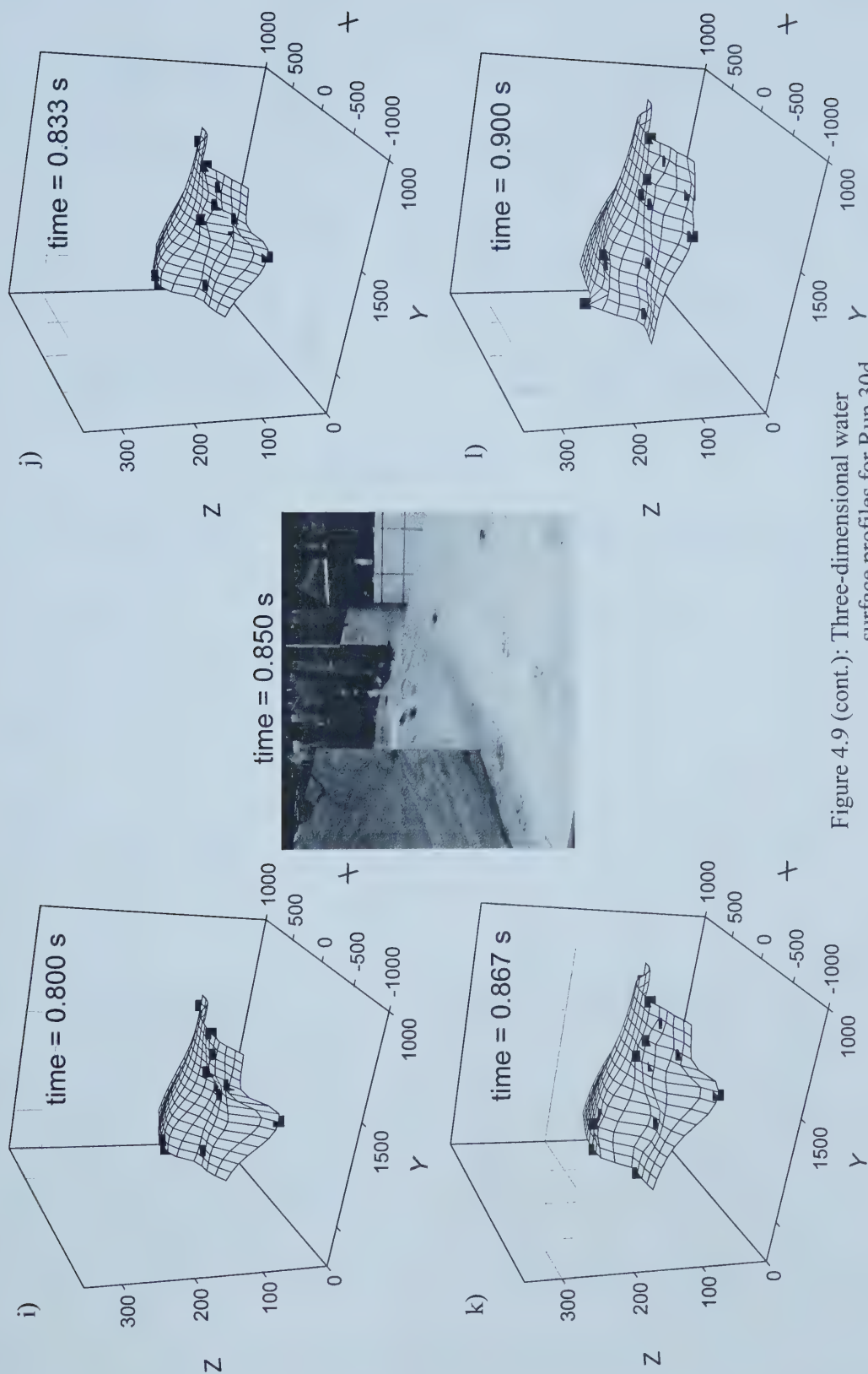


Figure 4.9 (cont.): Three-dimensional water surface profiles for Run 30d.





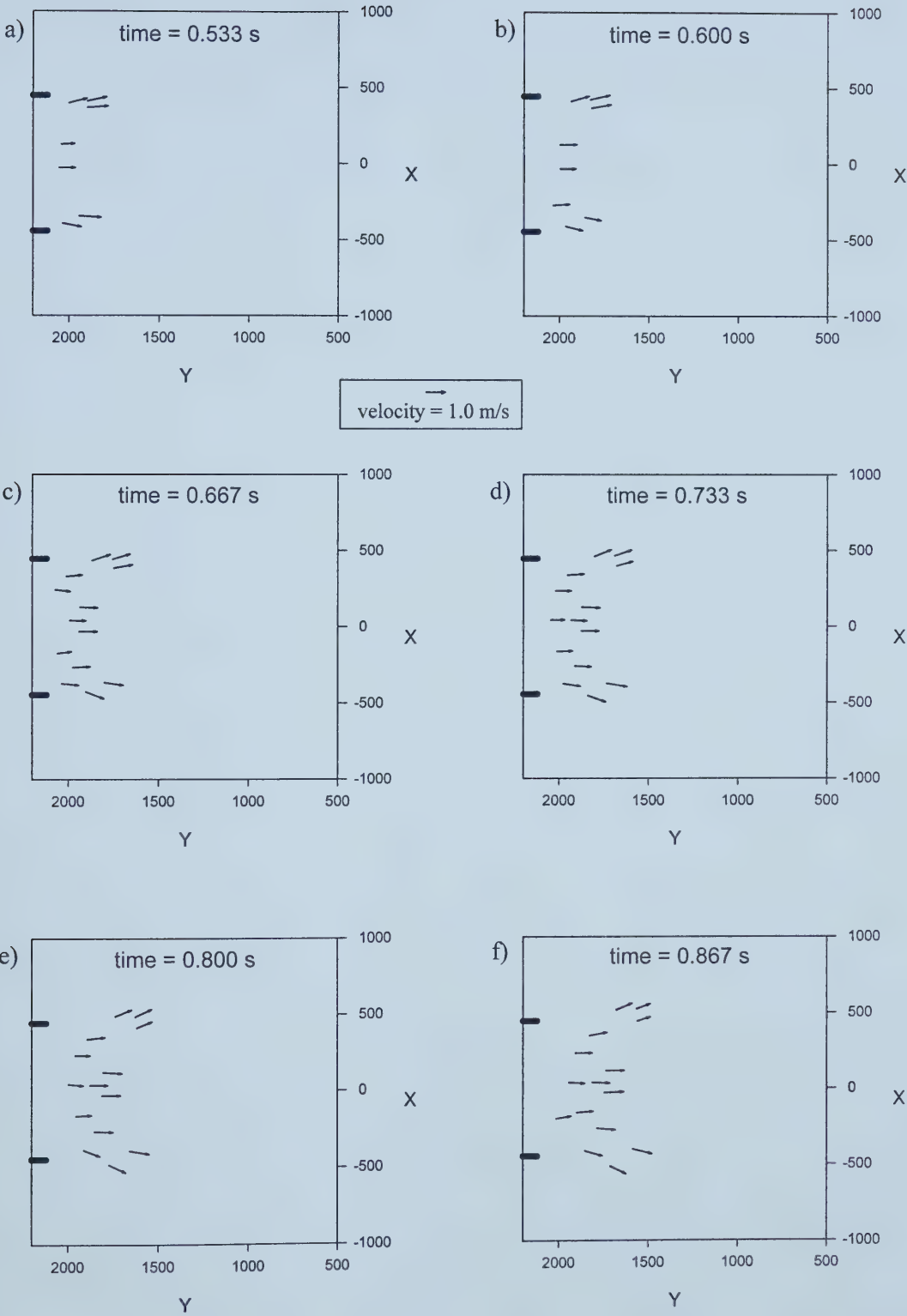


Figure 4.10: Velocity vectors for Run 10a.



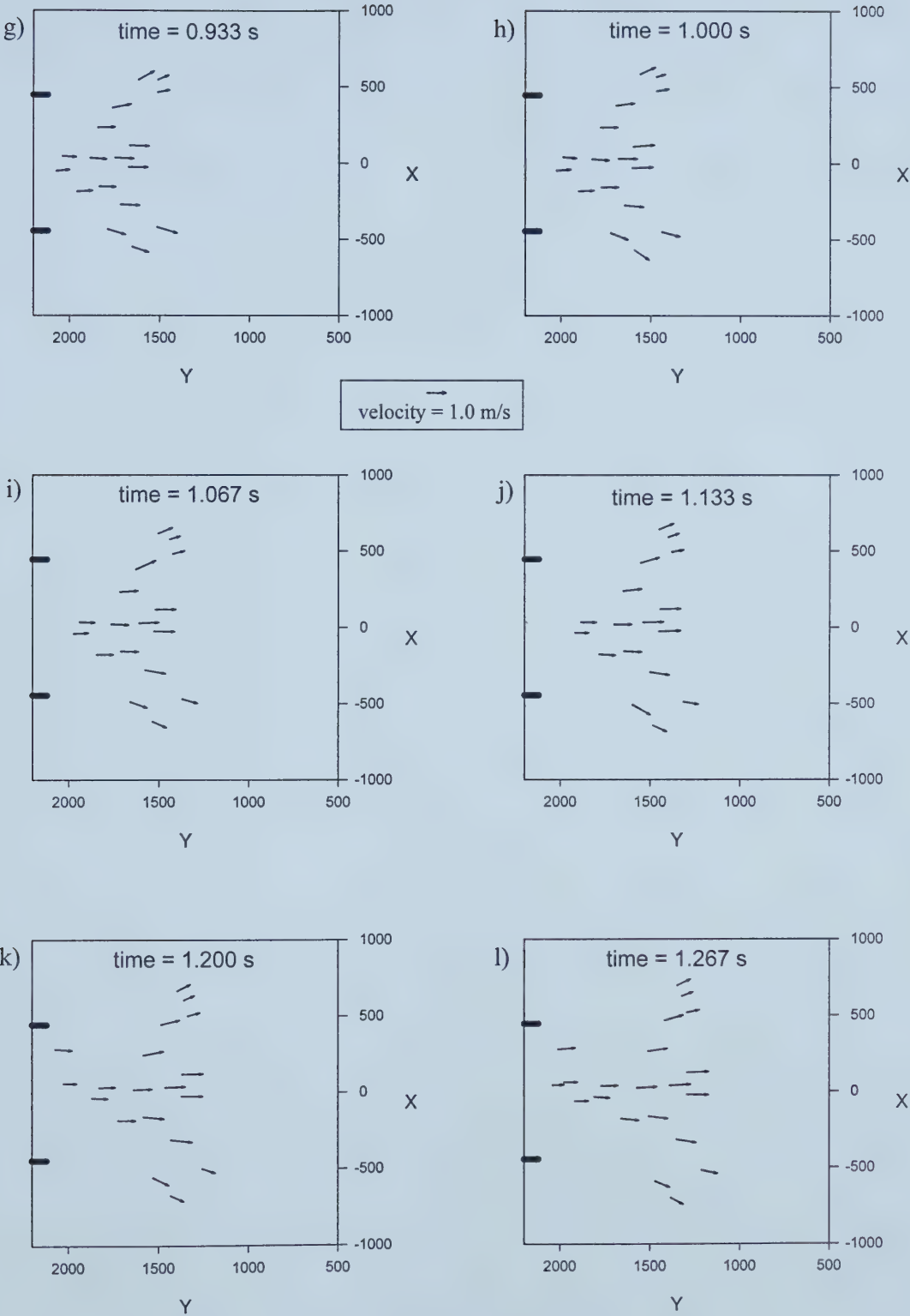


Figure 4.10 (cont.): Velocity vectors for Run 10a.



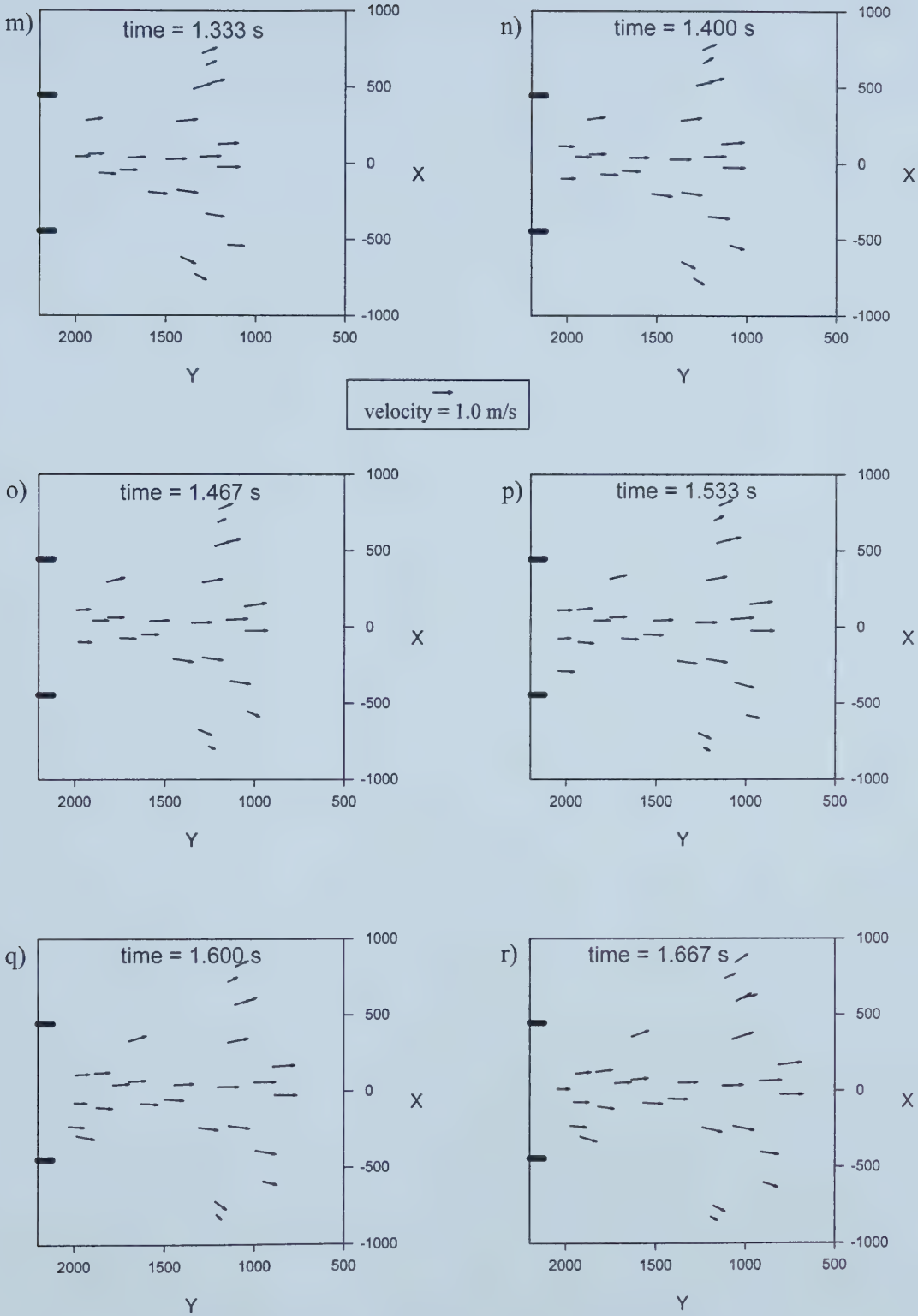


Figure 4.10 (cont.): Velocity vectors for Run 10a.



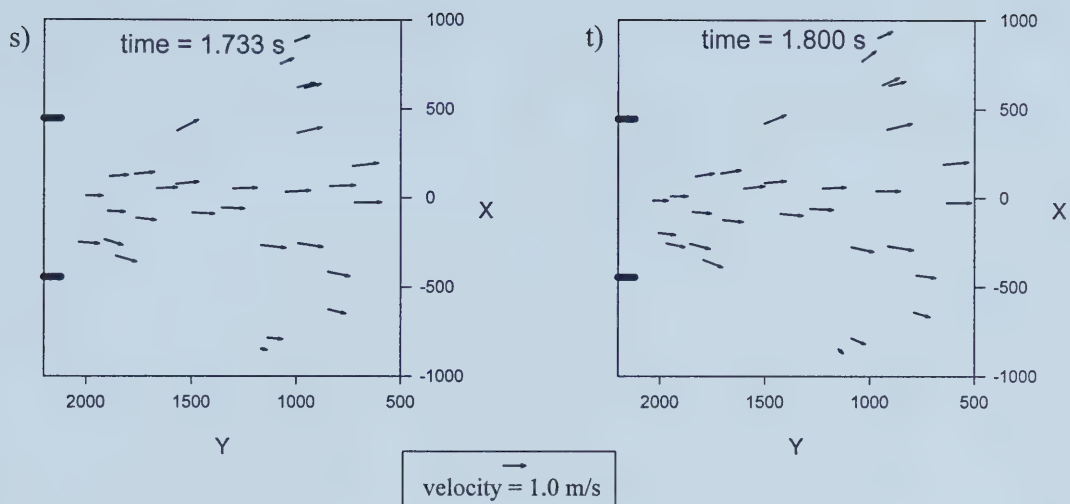


Figure 4.10 (cont.): Velocity vectors for Run 10a.





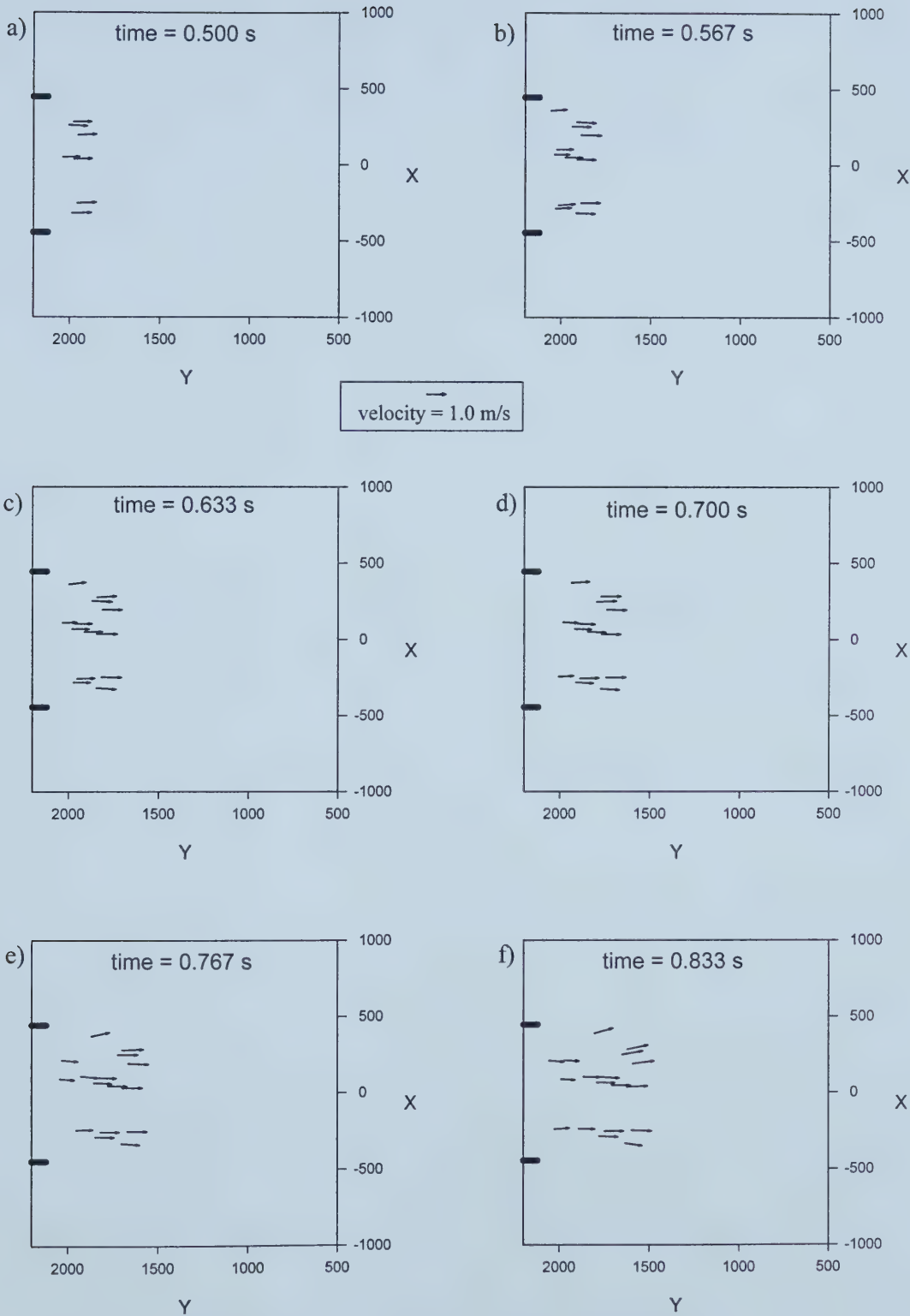


Figure 4.11: Velocity vectors for Run 10c.



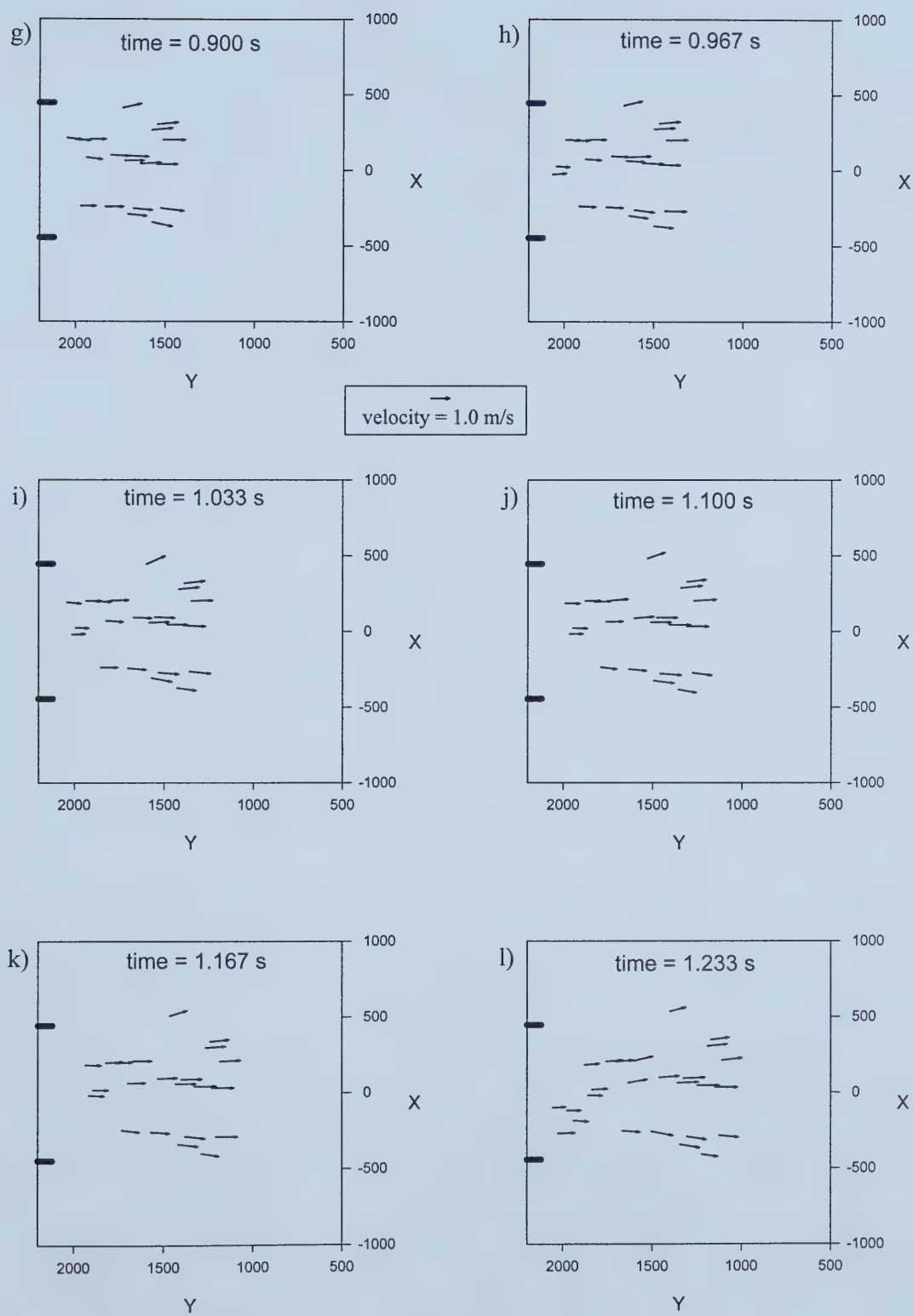


Figure 4.11 (cont.): Velocity vectors for Run 10c.



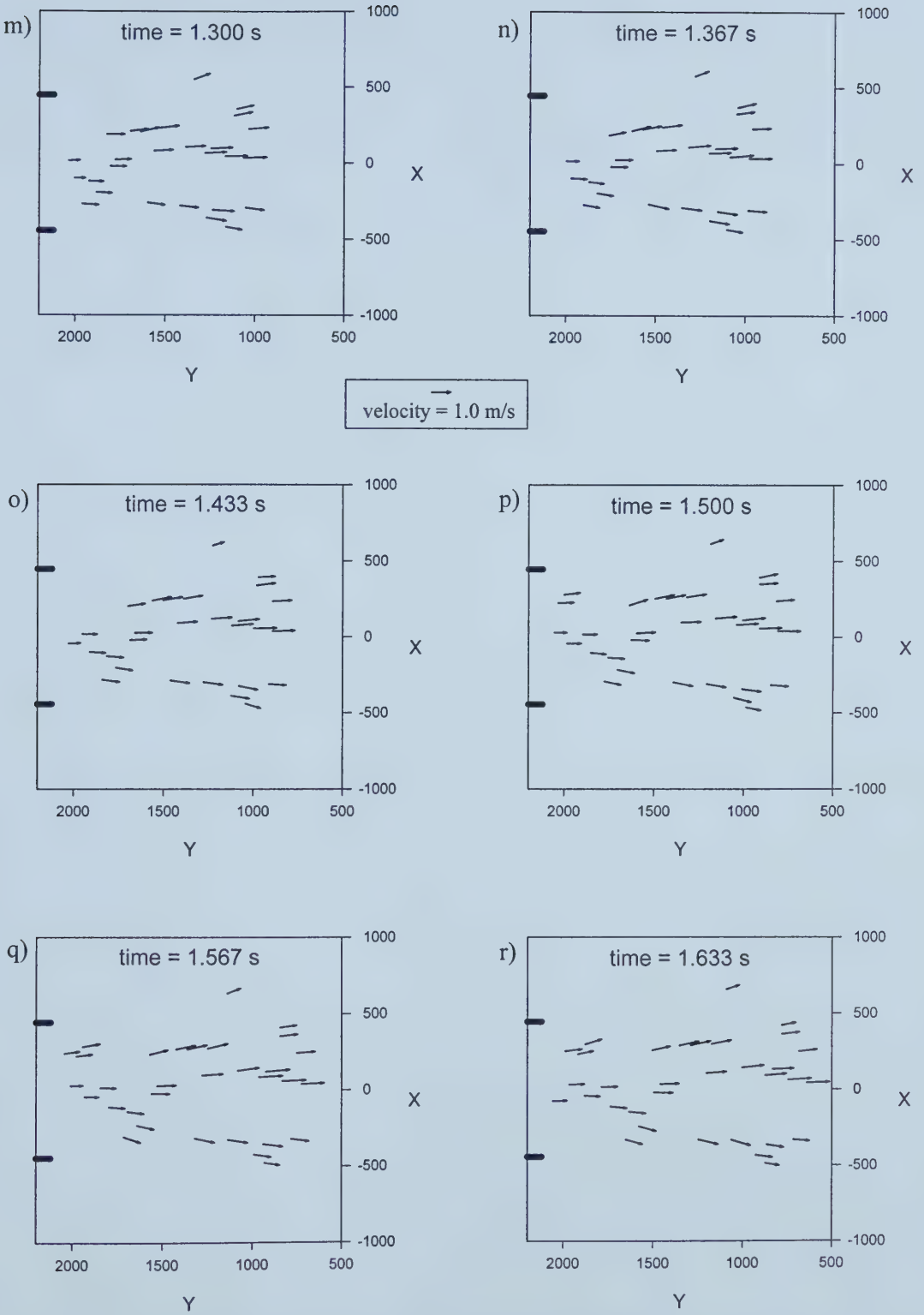


Figure 4.11 (cont.): Velocity vectors for Run 10c.



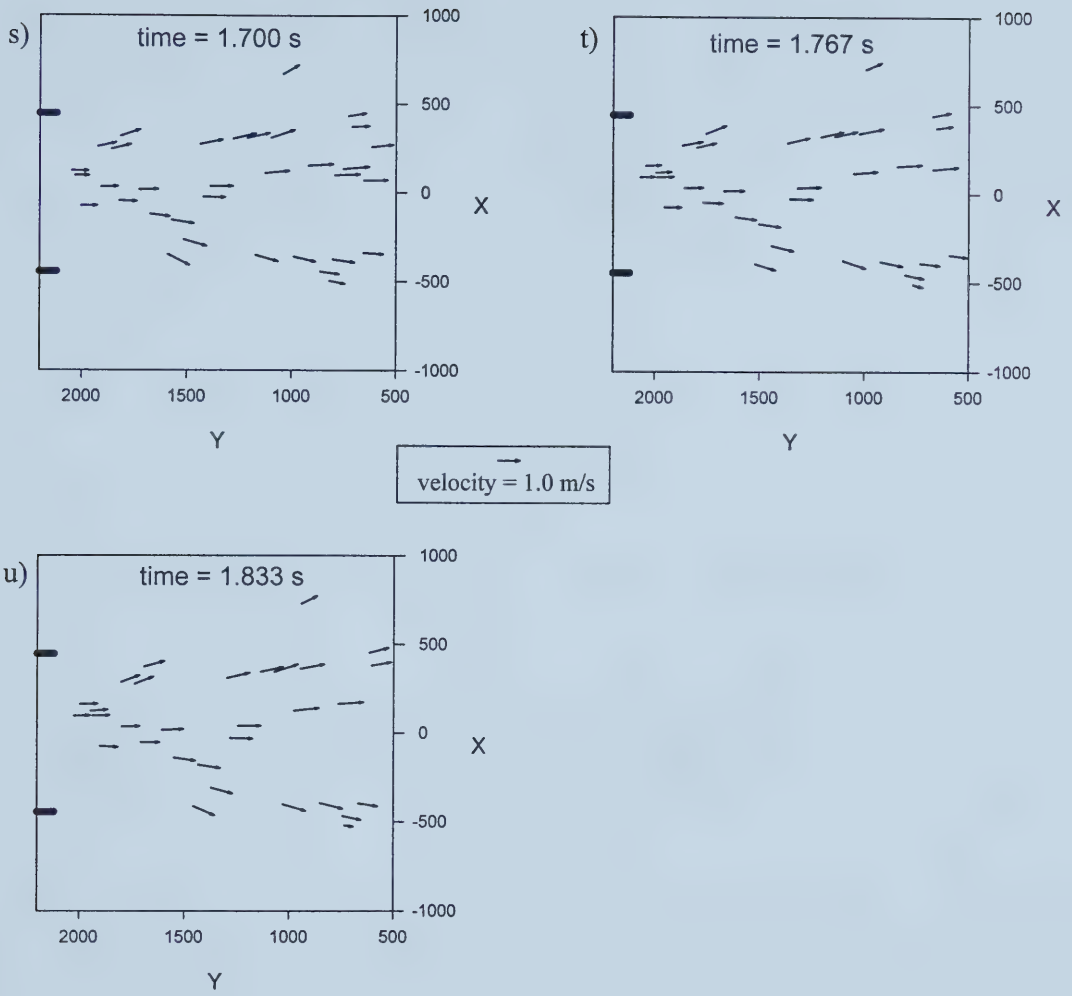


Figure 4.11 (cont.): Velocity vectors for Run 10c.





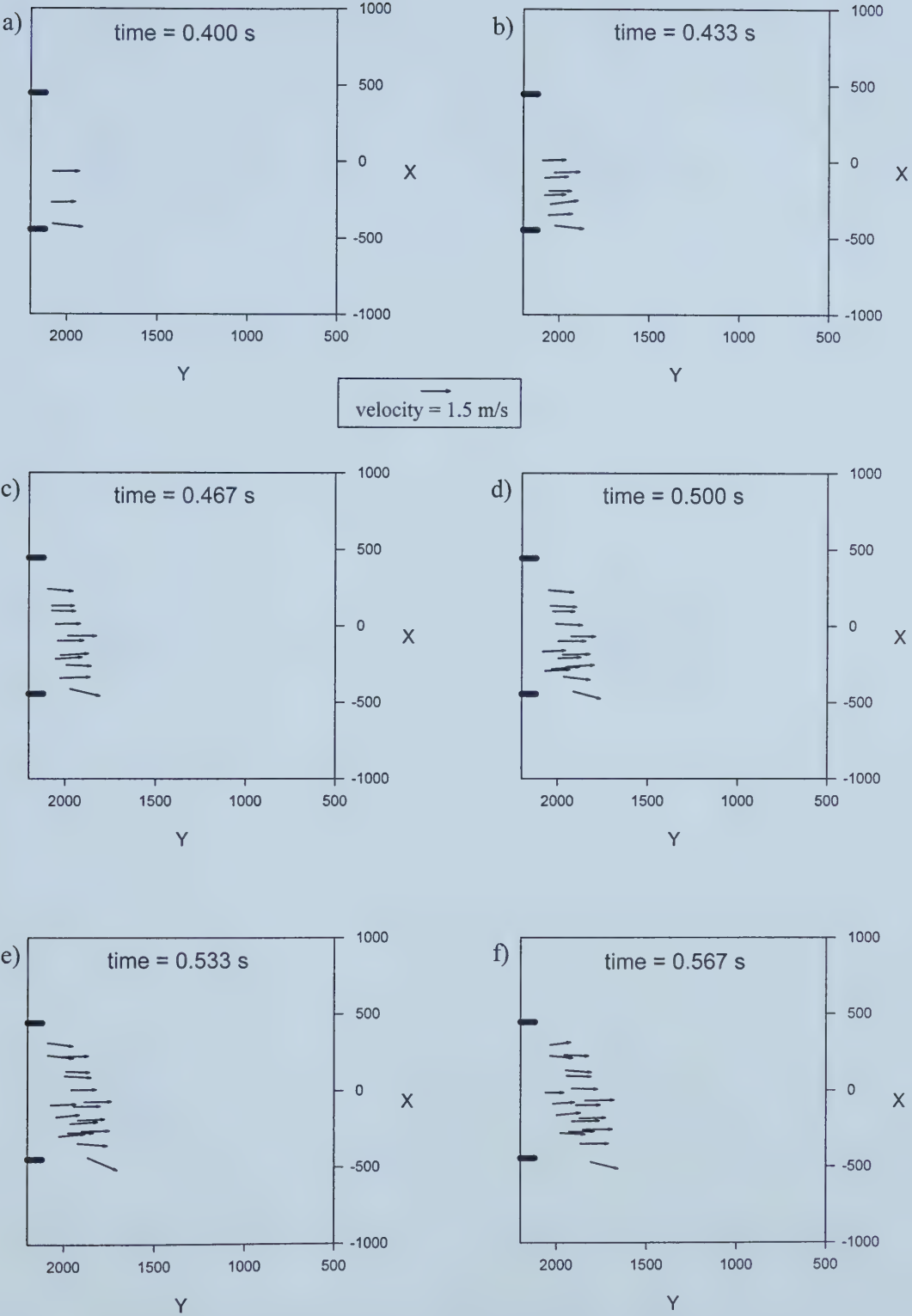


Figure 4.12: Velocity vectors for Run 20c.



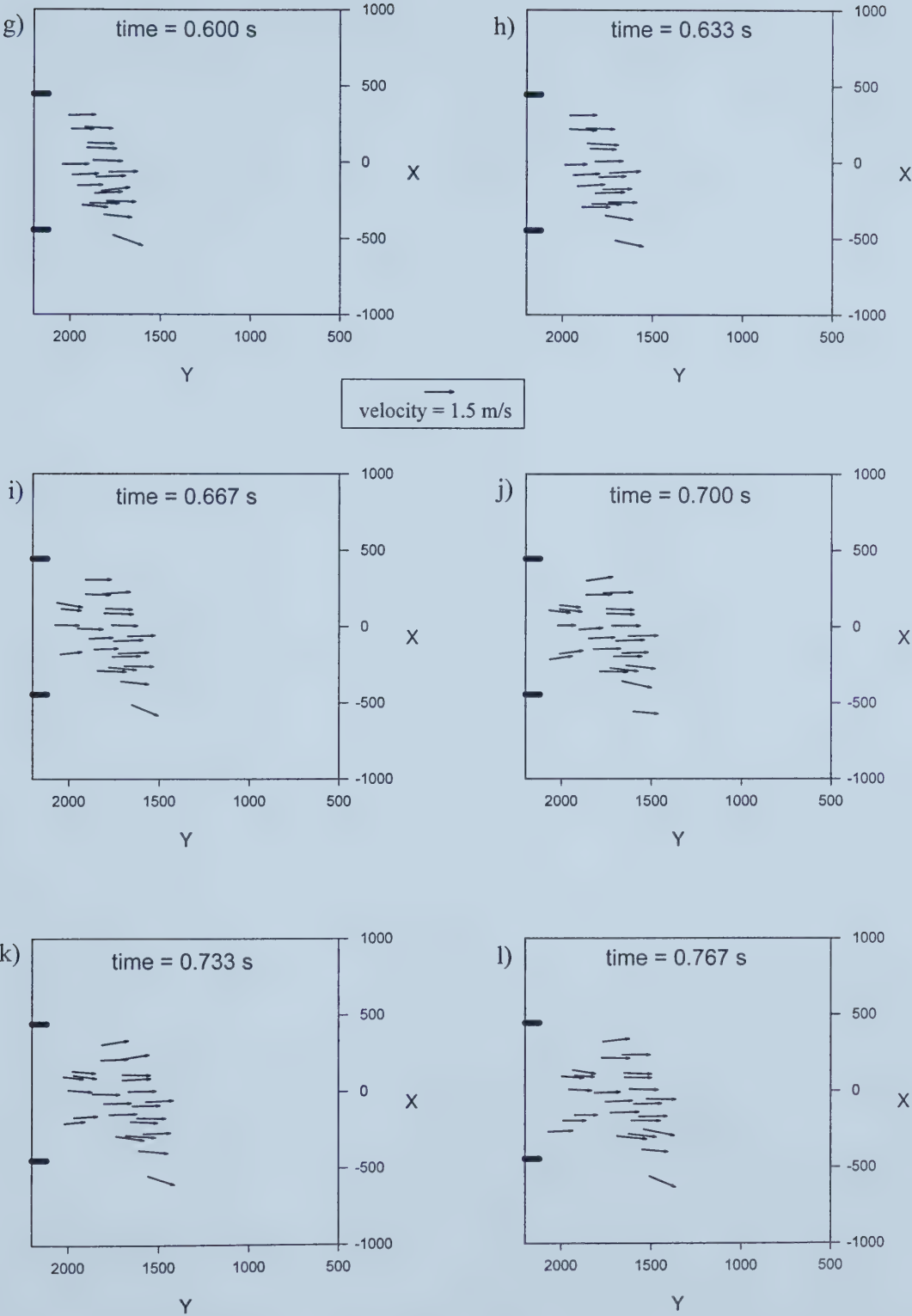


Figure 4.12 (cont.): Velocity vectors for Run 20c.



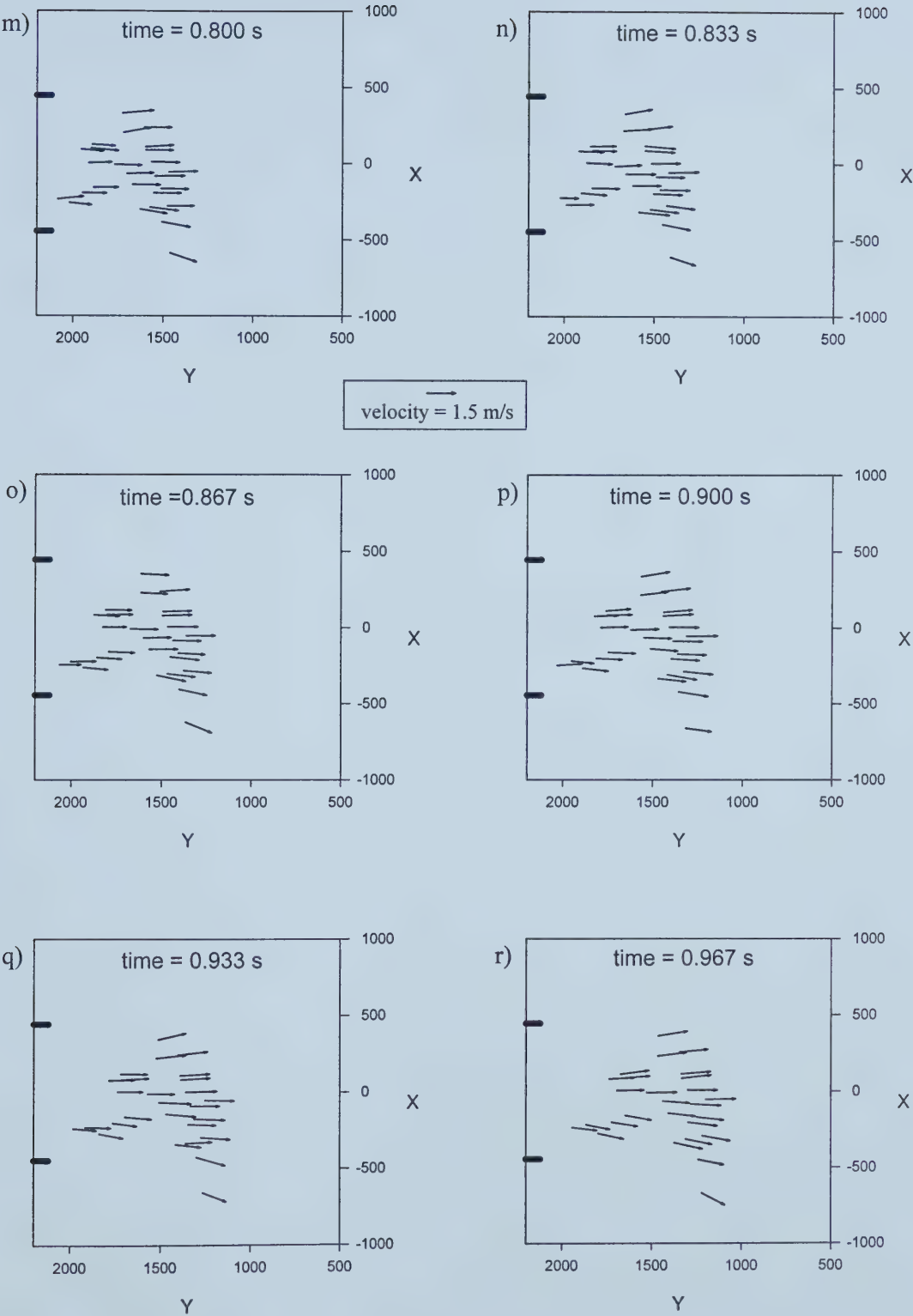


Figure 4.12 (cont.): Velocity vectors for Run 20c.



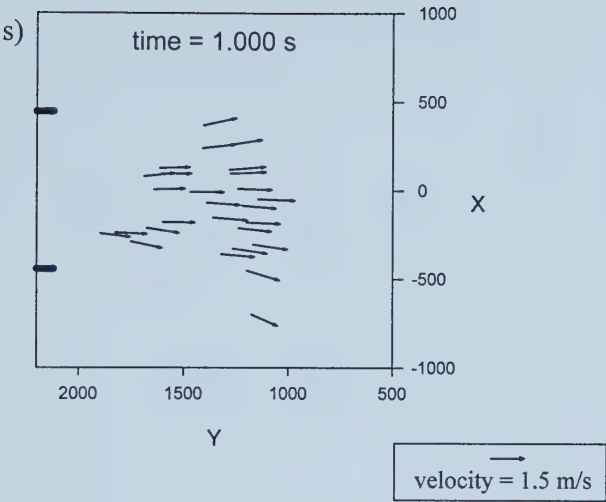


Figure 4.12 (cont.): Velocity vectors for Run 20c.





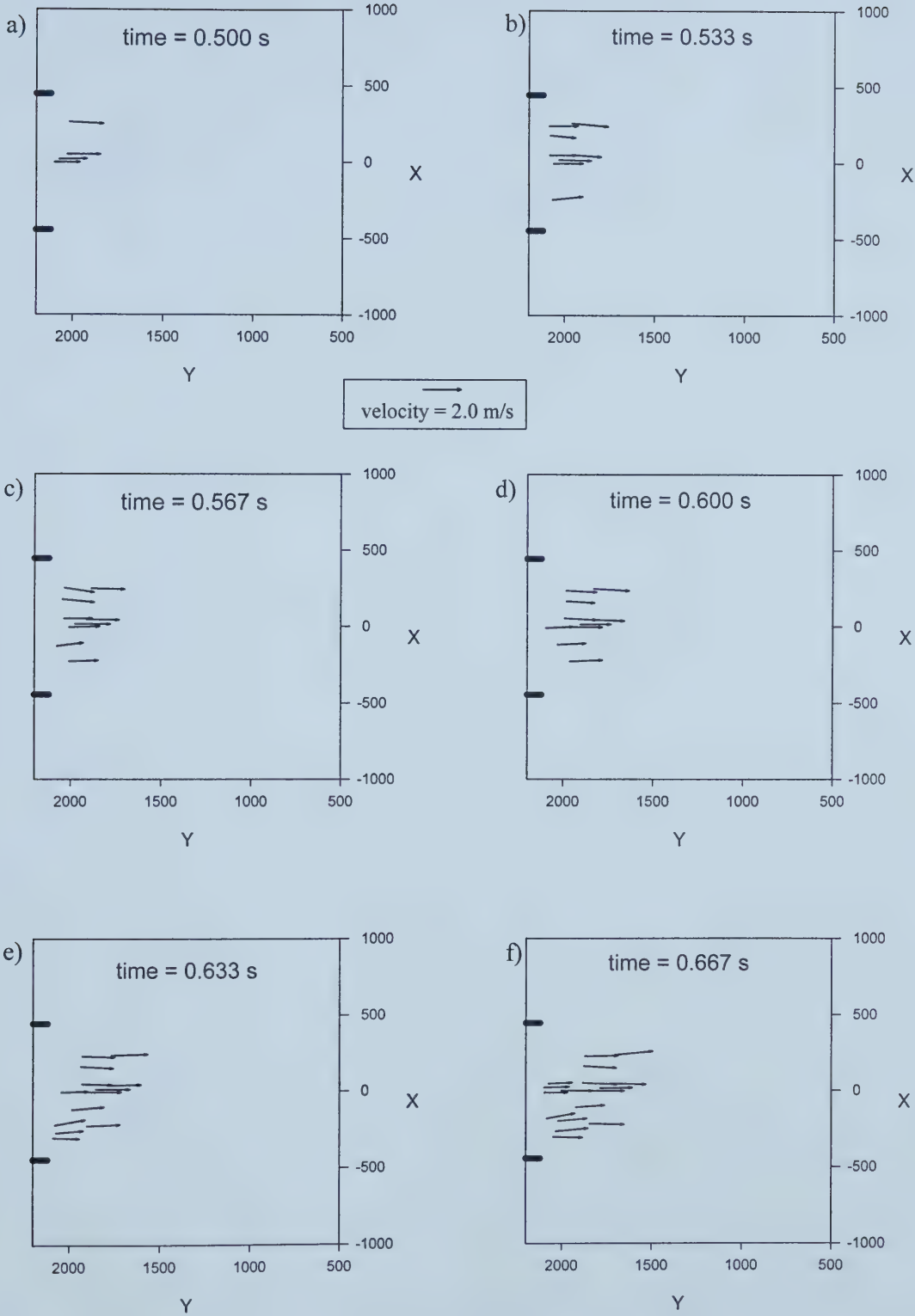


Figure 4.13: Velocity vectors for Run 30b.



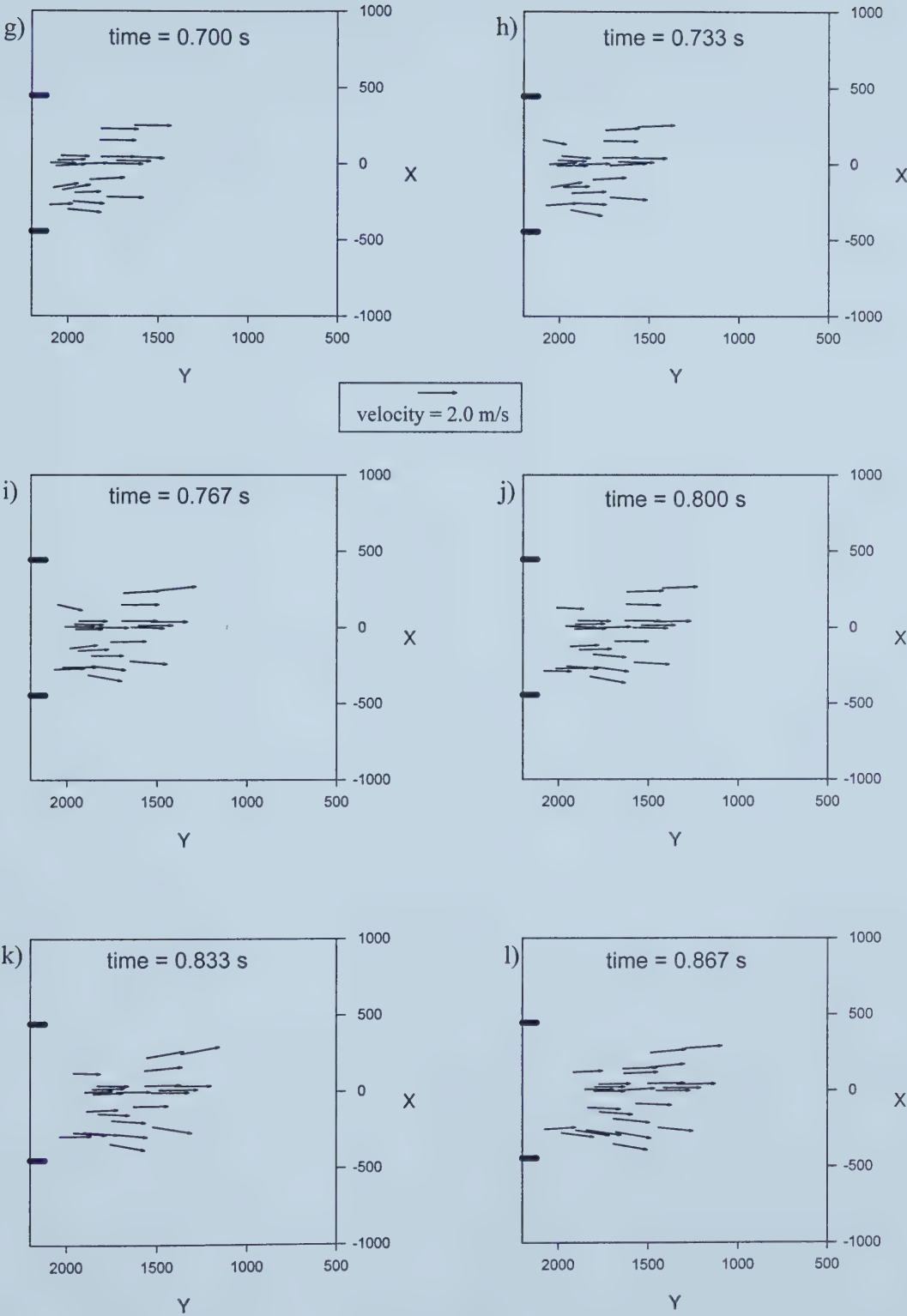


Figure 4.13 (cont.): Velocity vectors for Run 30b.



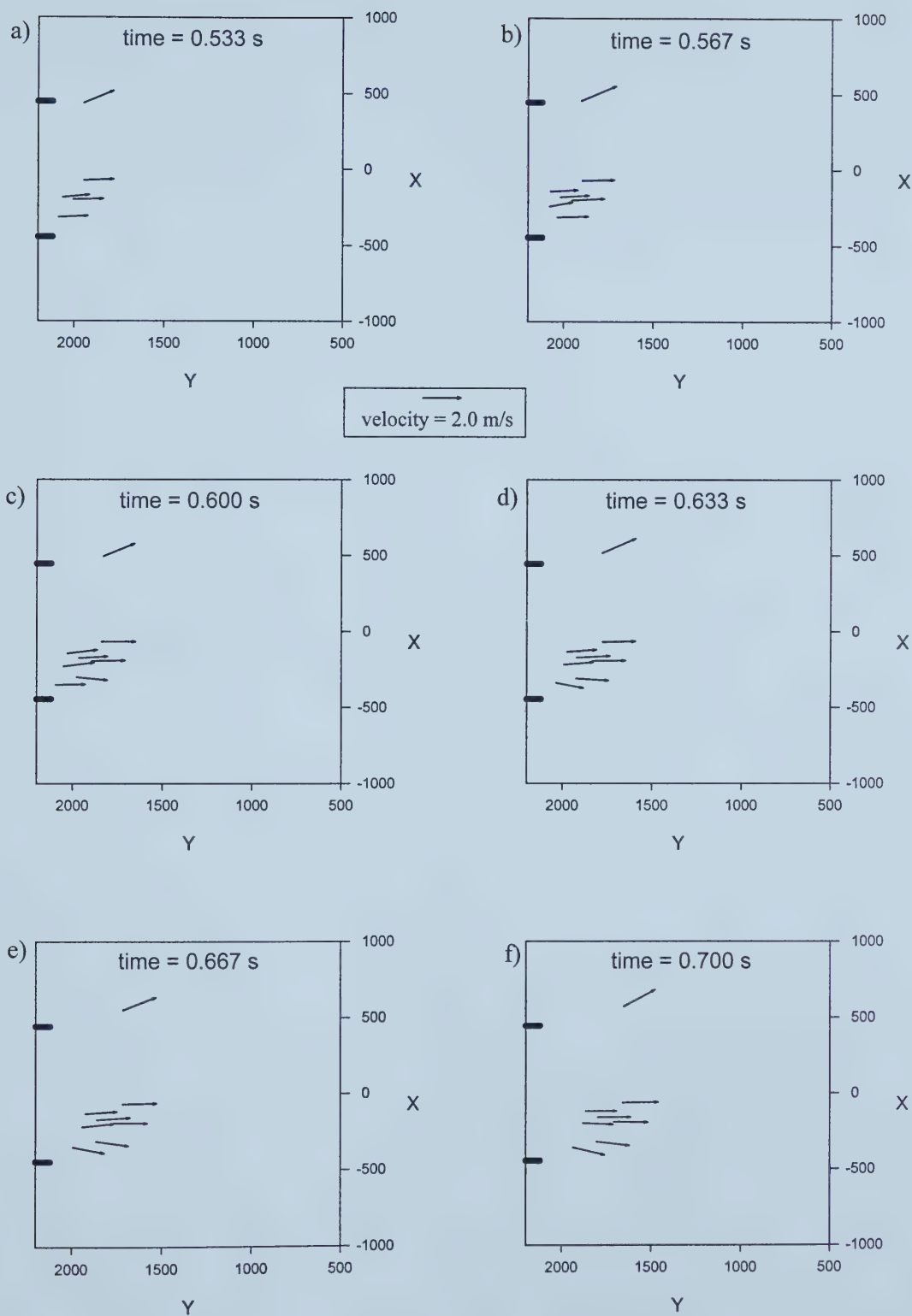


Figure 4.14: Velocity vectors for Run 30d.



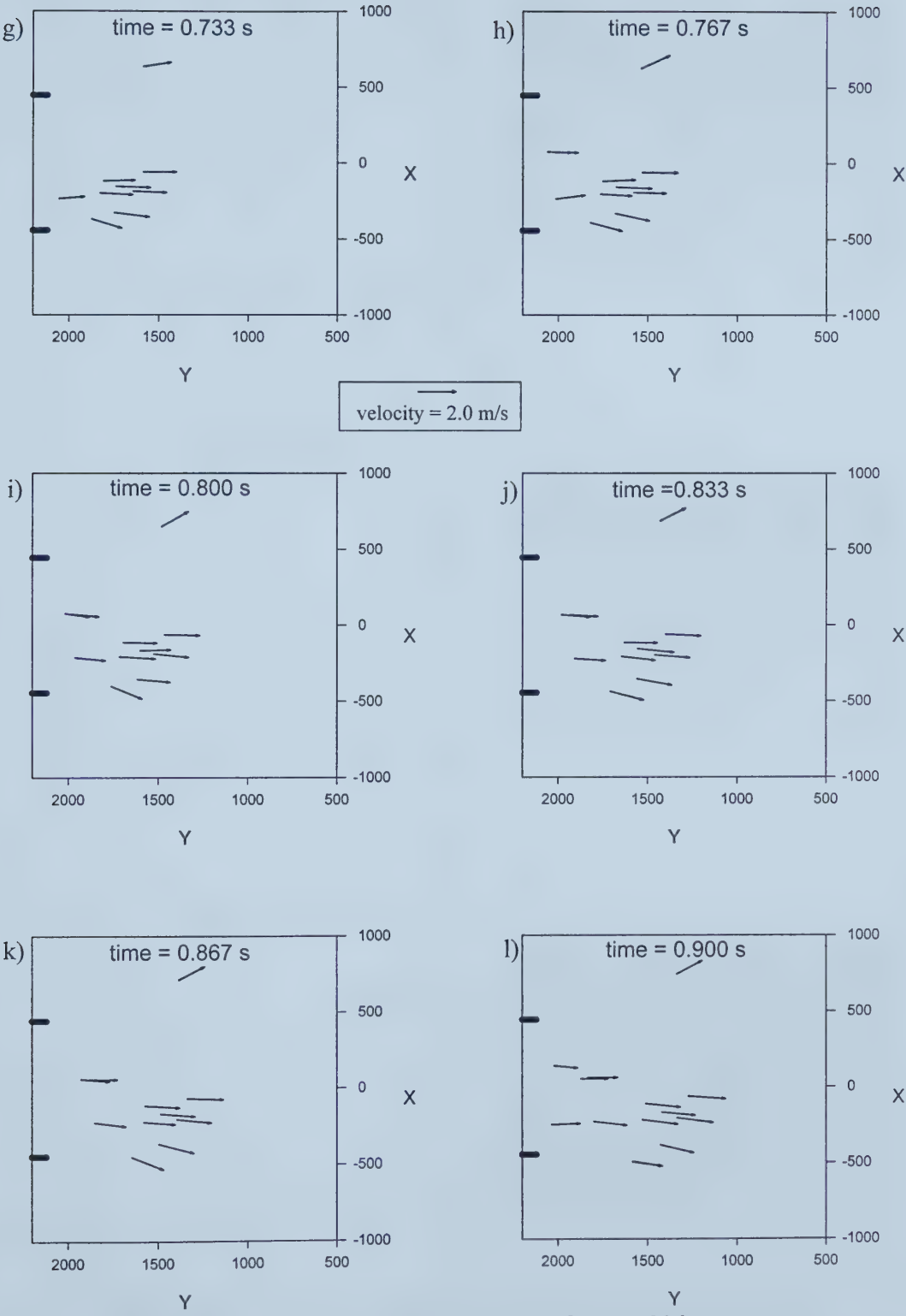


Figure 4.14 (cont.): Velocity vectors for Run 30d.





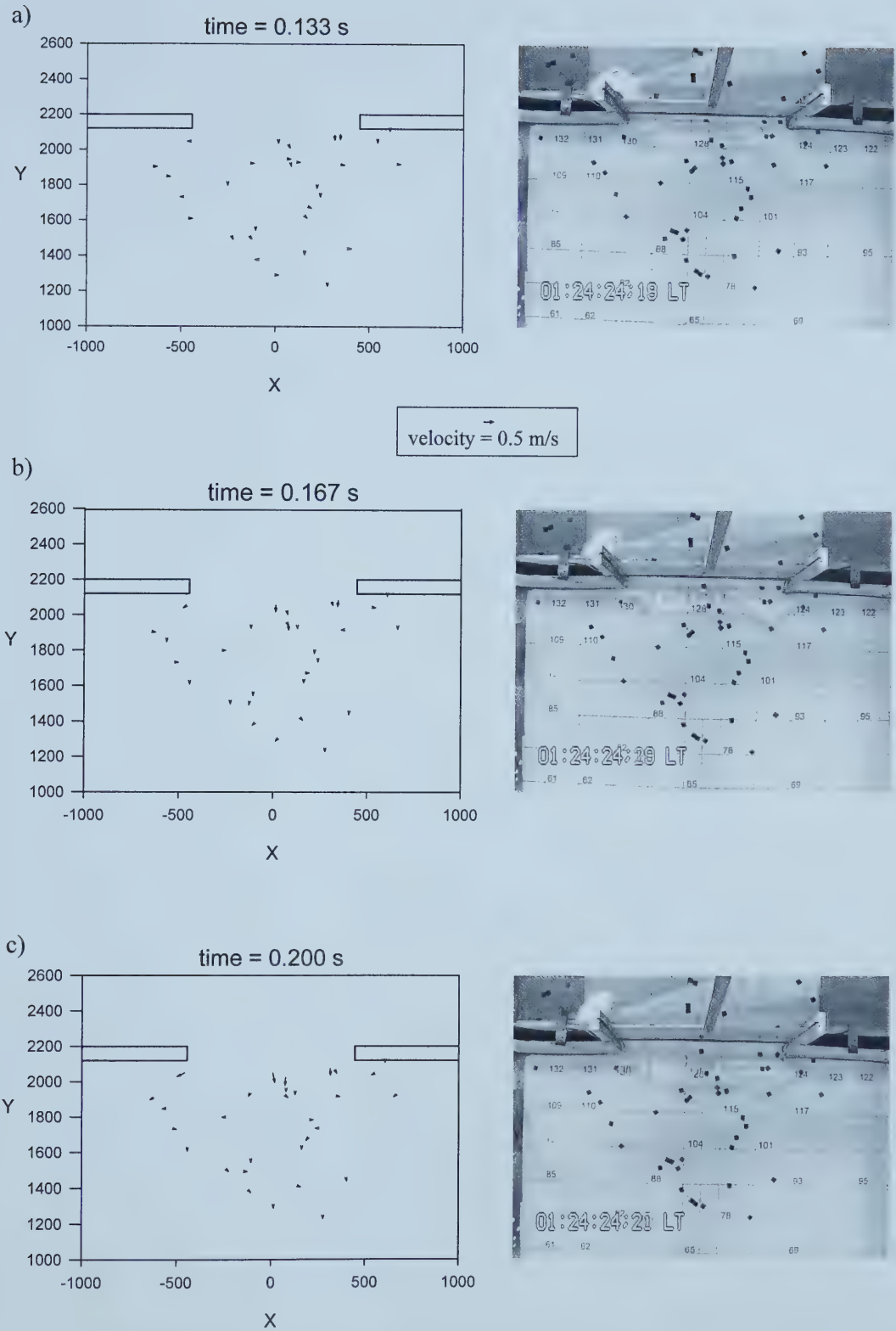


Figure 4.15: Velocity vectors and corresponding images for Run 30-5d.



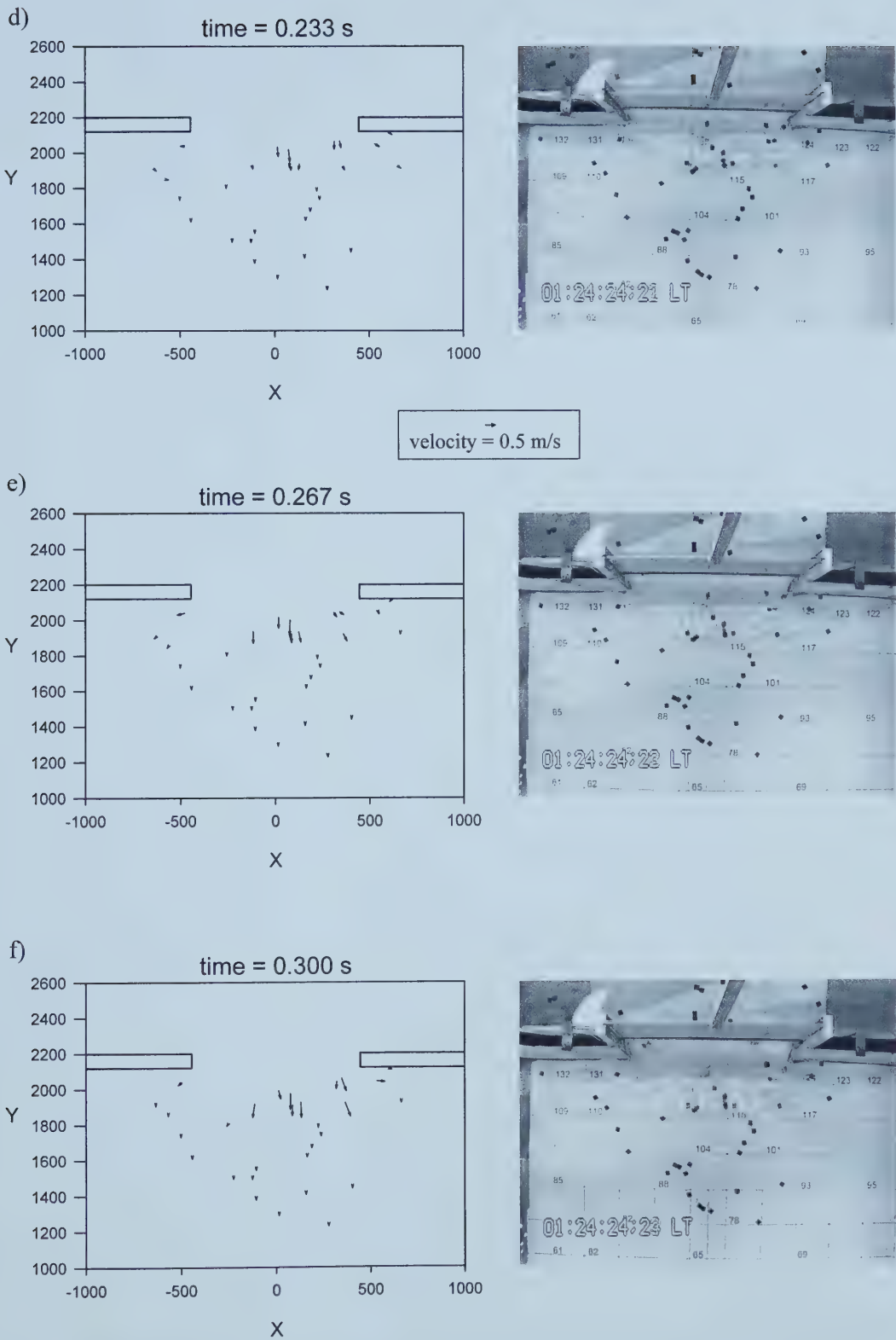


Figure 4.15 (cont): Velocity vectors and corresponding images for Run 30-5d.



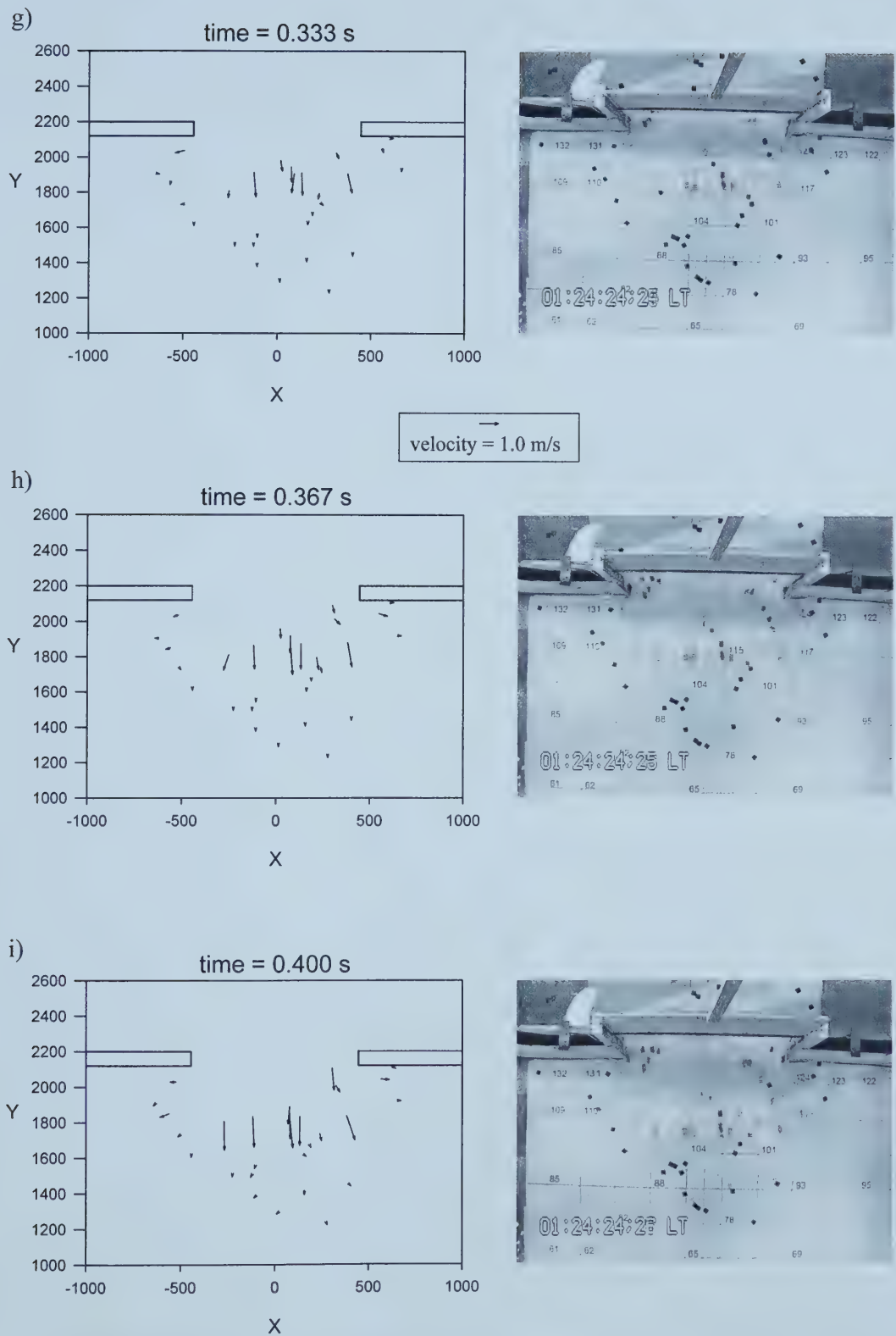
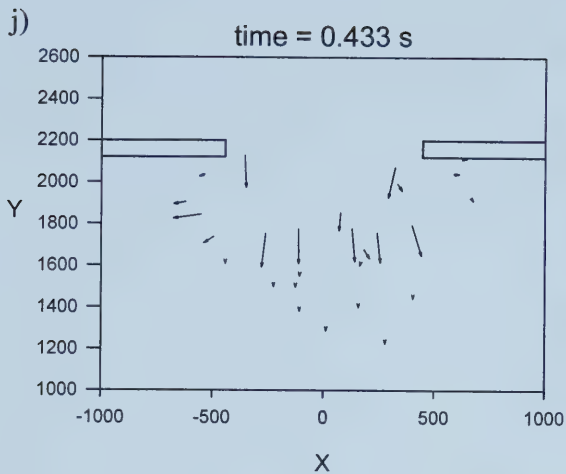


Figure 4.15 (cont.): Velocity vectors and corresponding images for Run 30-5d.





velocity = 1.5 m/s

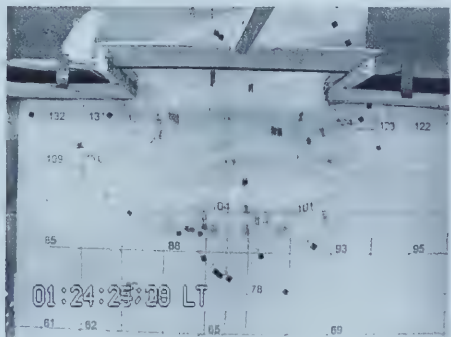
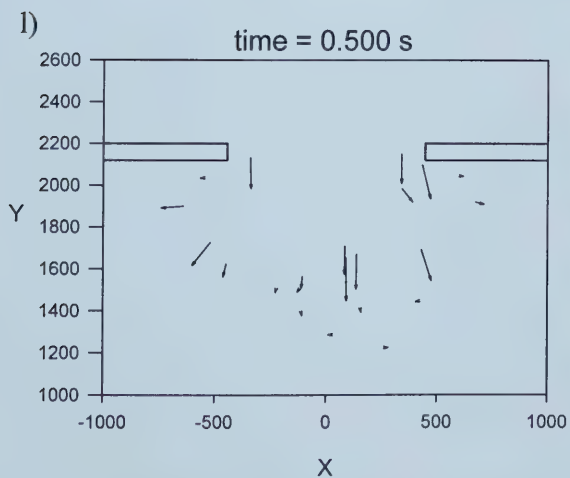
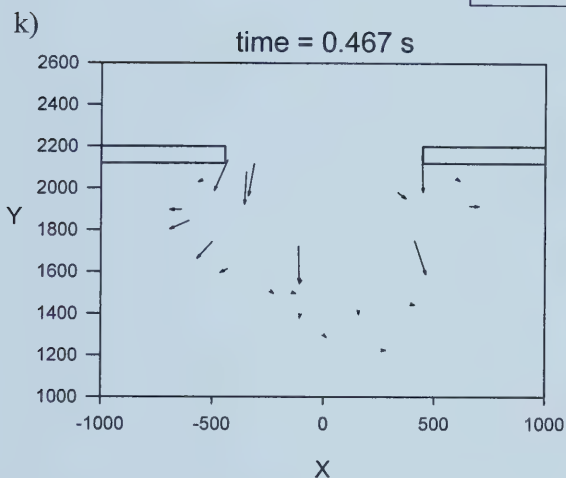


Figure 4.15 (cont.): Velocity vectors and corresponding images for Run 30-5d.





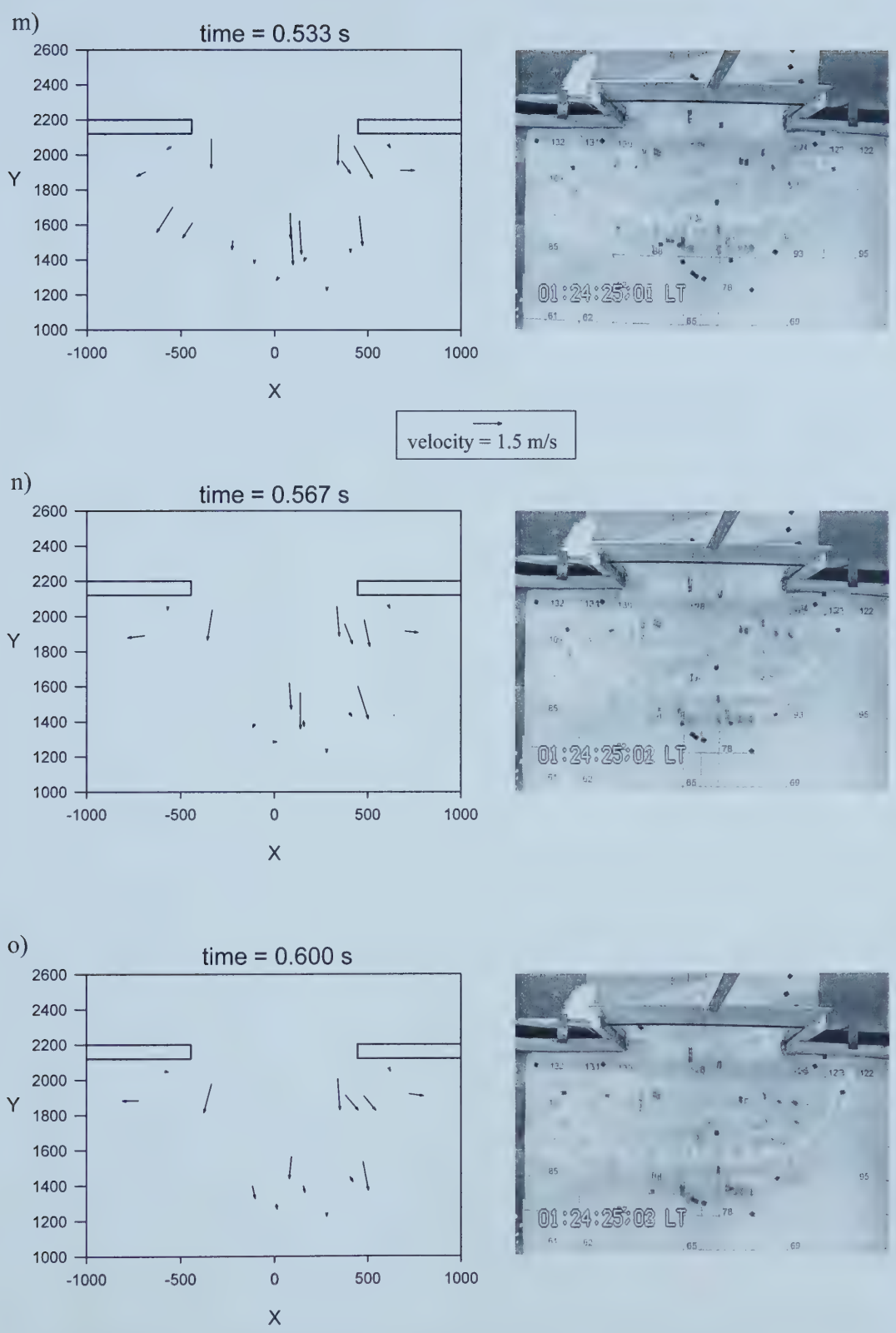


Figure 4.15 (cont.): Velocity vectors and corresponding images for Run 30-5d.



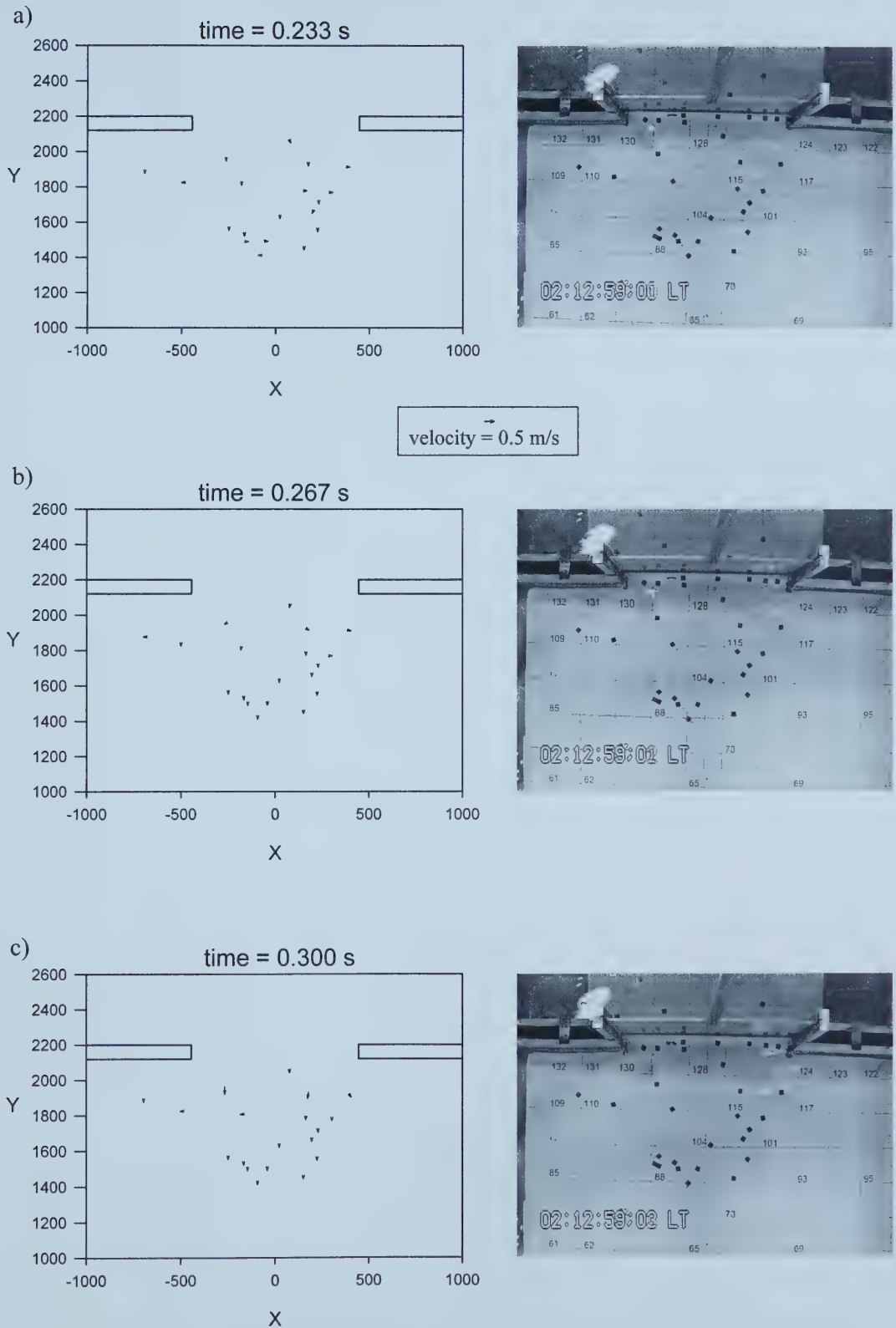


Figure 4.16: Velocity vectors and corresponding images for Run 30-10a.



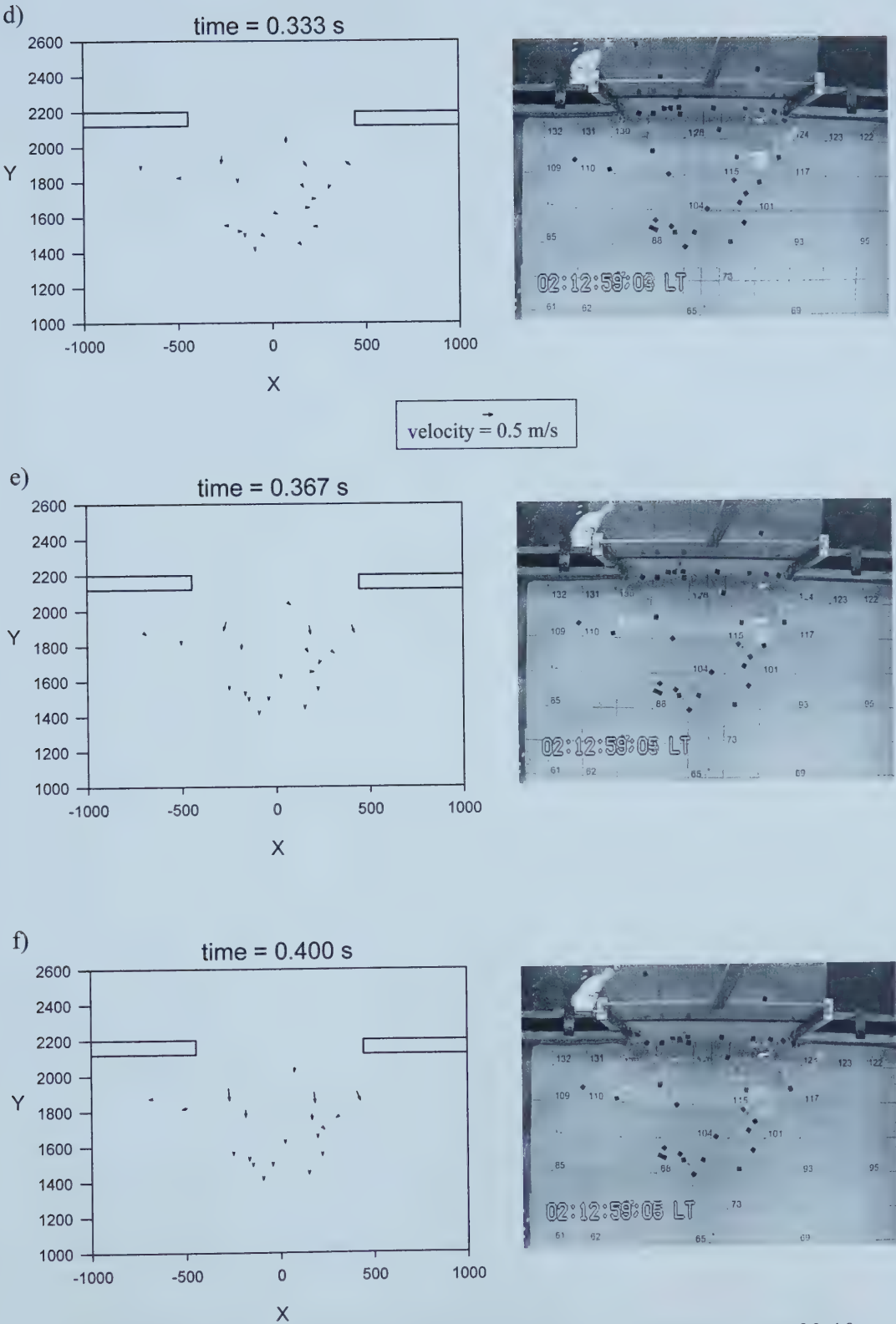


Figure 4.16 (cont.): Velocity vectors and corresponding images for Run 30-10a.



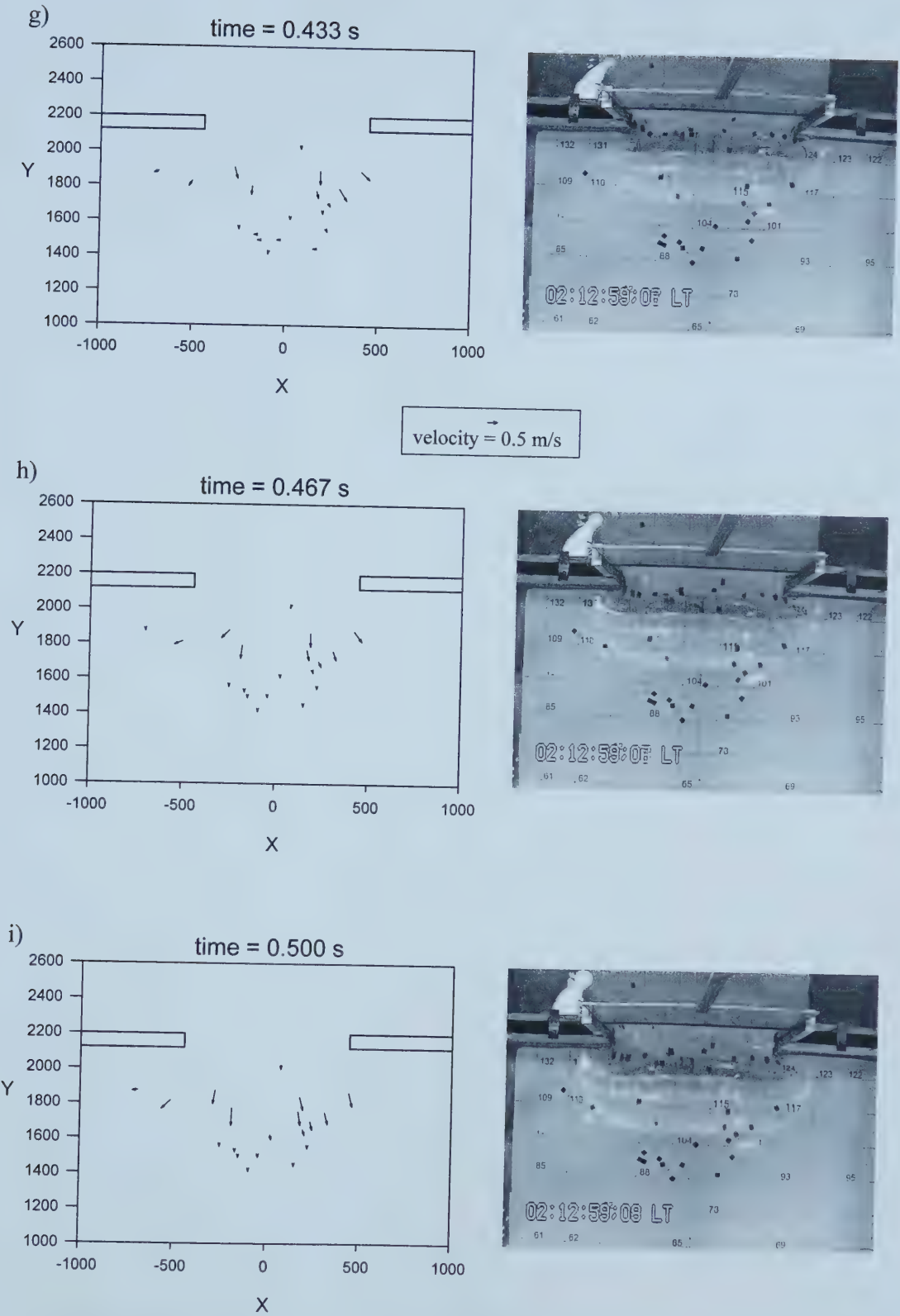


Figure 4.16 (cont.): Velocity vectors and corresponding images for Run 30-10a.





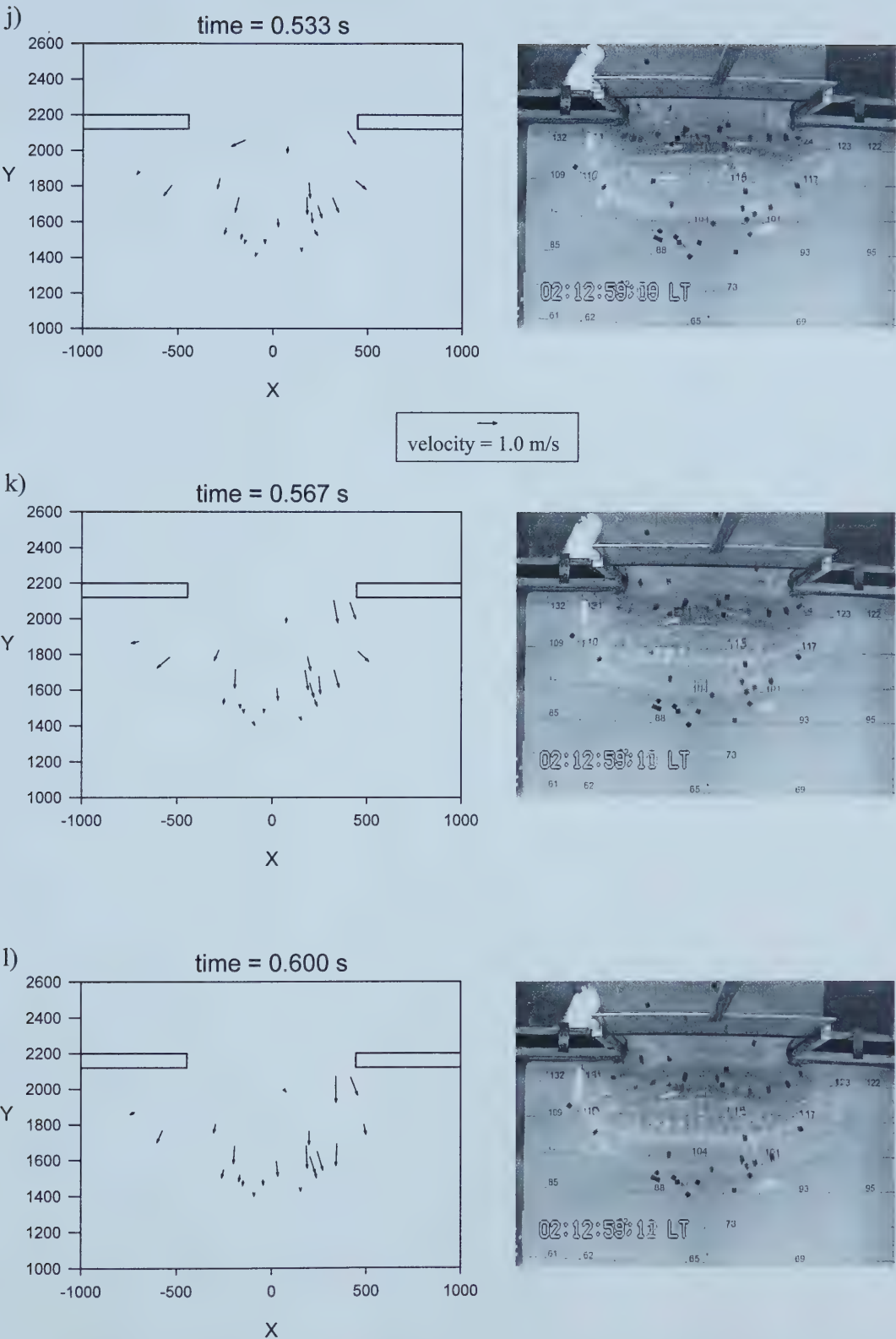


Figure 4.16 (cont.): Velocity vectors and corresponding images for Run 30-10a.



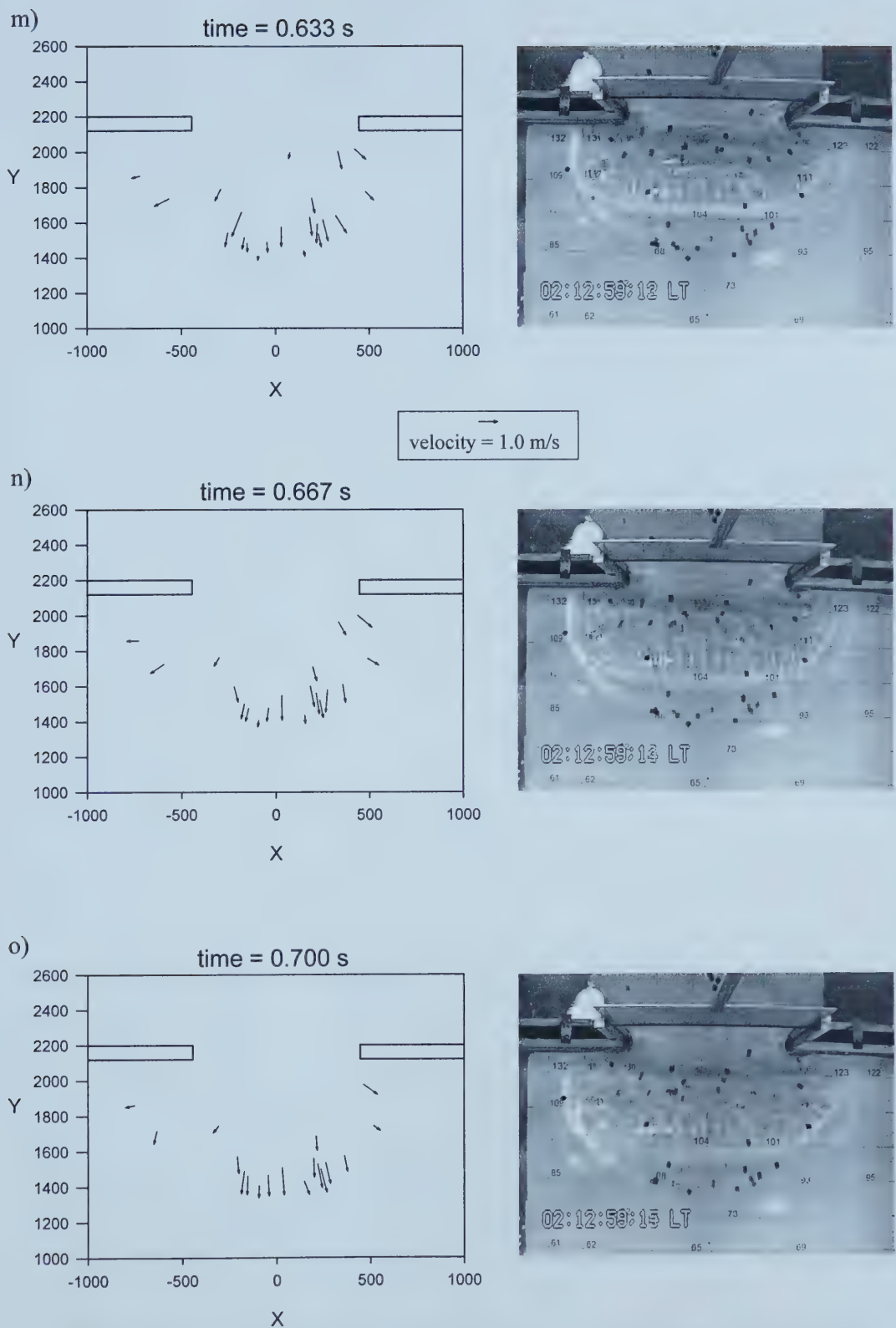


Figure 4.16 (cont.): Velocity vectors and corresponding images for Run 30-10a.



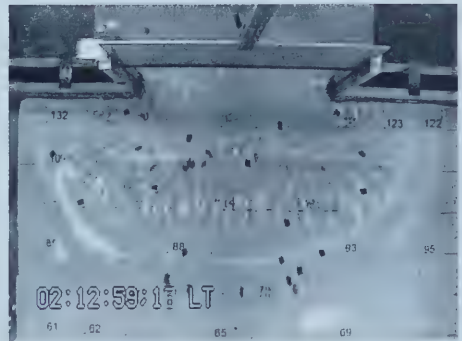
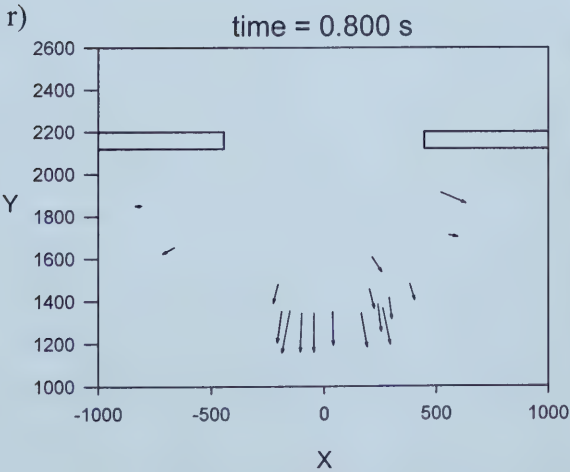
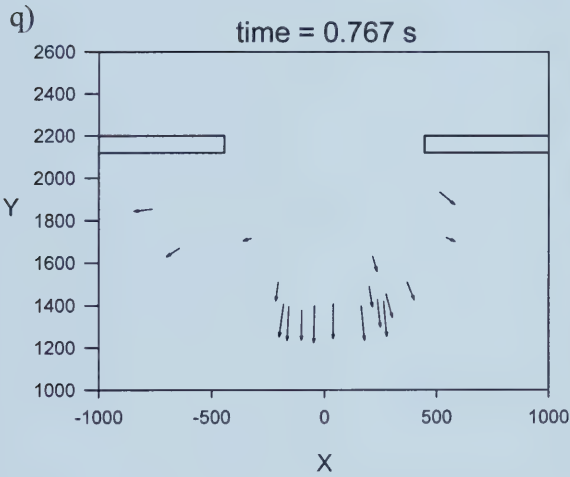
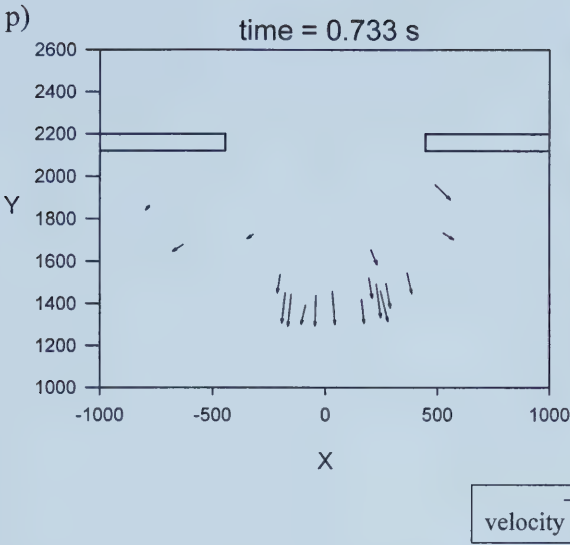
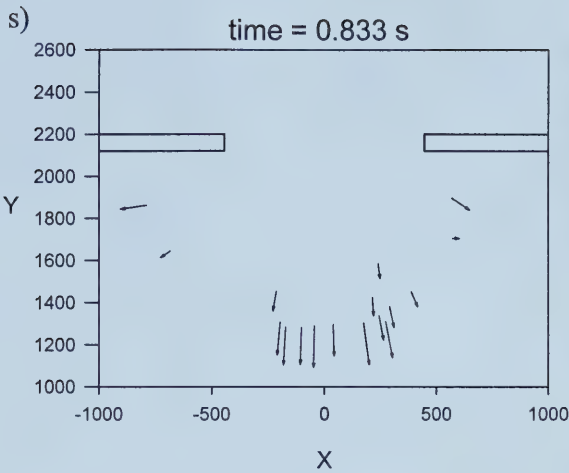


Figure 4.16 (cont.): Velocity vectors and corresponding images for Run 30-10a.





velocity = 1.5 m/s

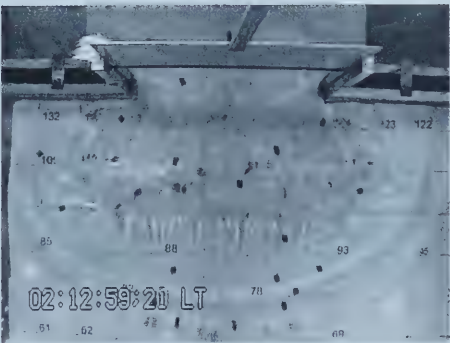
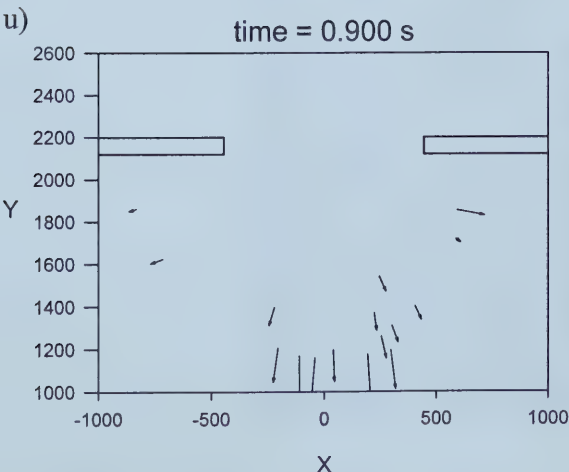
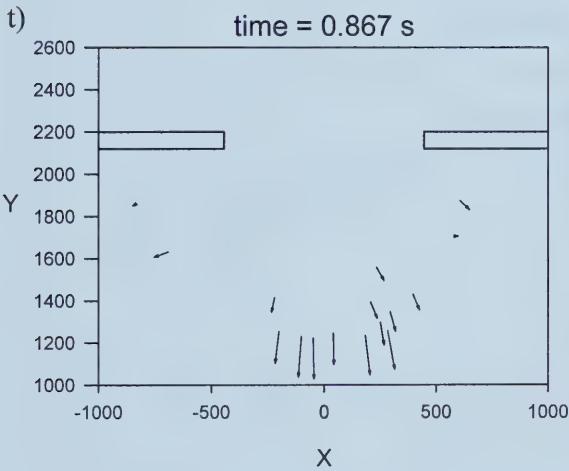
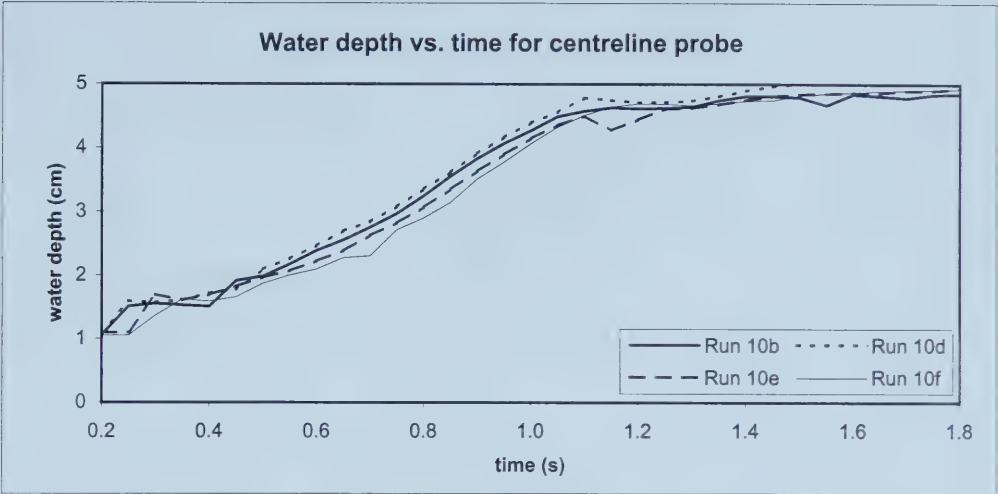


Figure 4.16 (cont.): Velocity vectors and corresponding images for Run 30-10a.

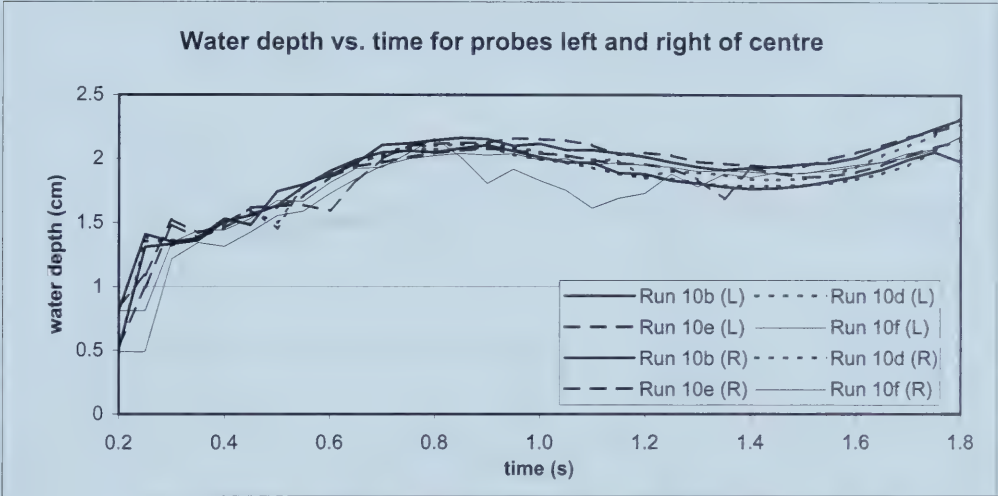




a)



b)

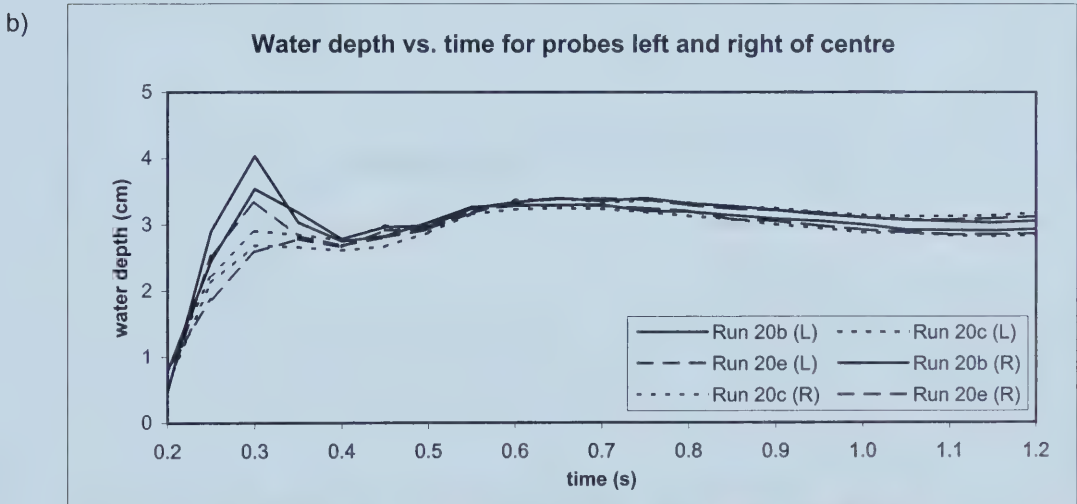
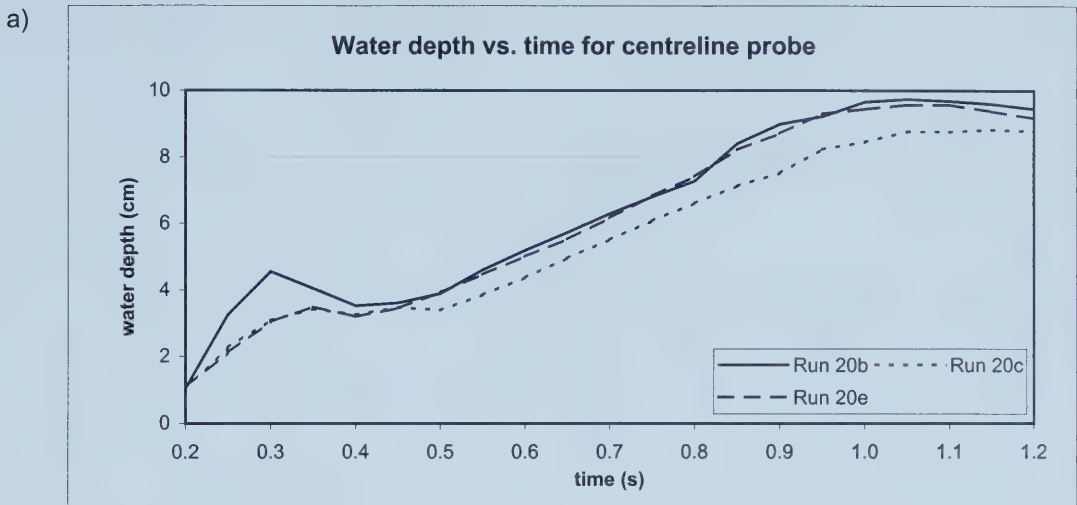


c) time = 1.00 s



Figure 4.17: Verification of experimental repeatability and symmetry for 0.10 m headwater.





c) time = 1.00 s



Figure 4.18: Verification of experimental repeatability and symmetry for 0.20 m headwater.



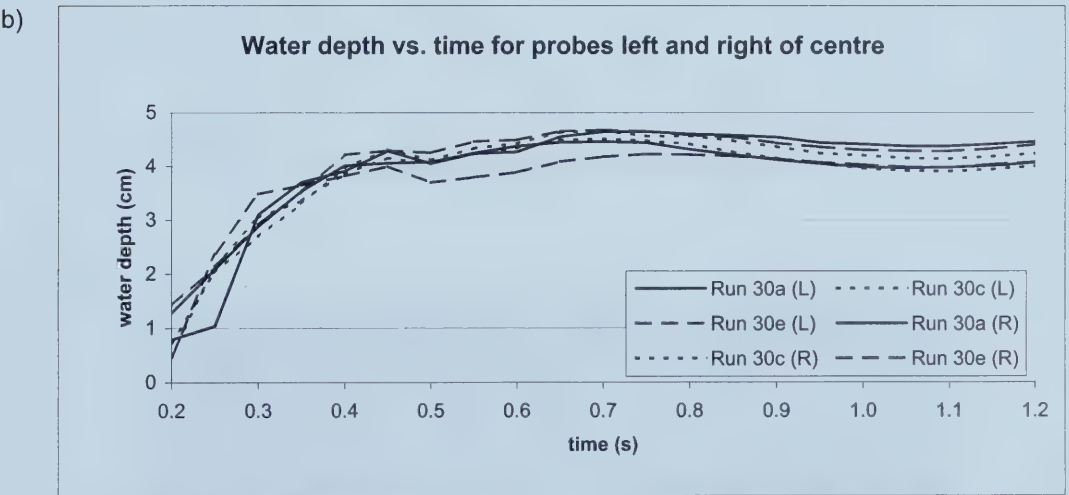
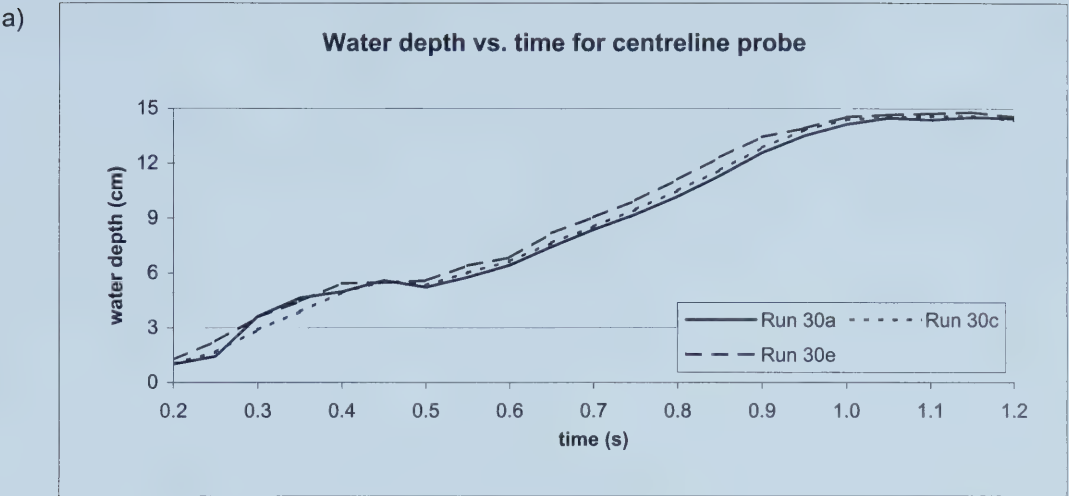
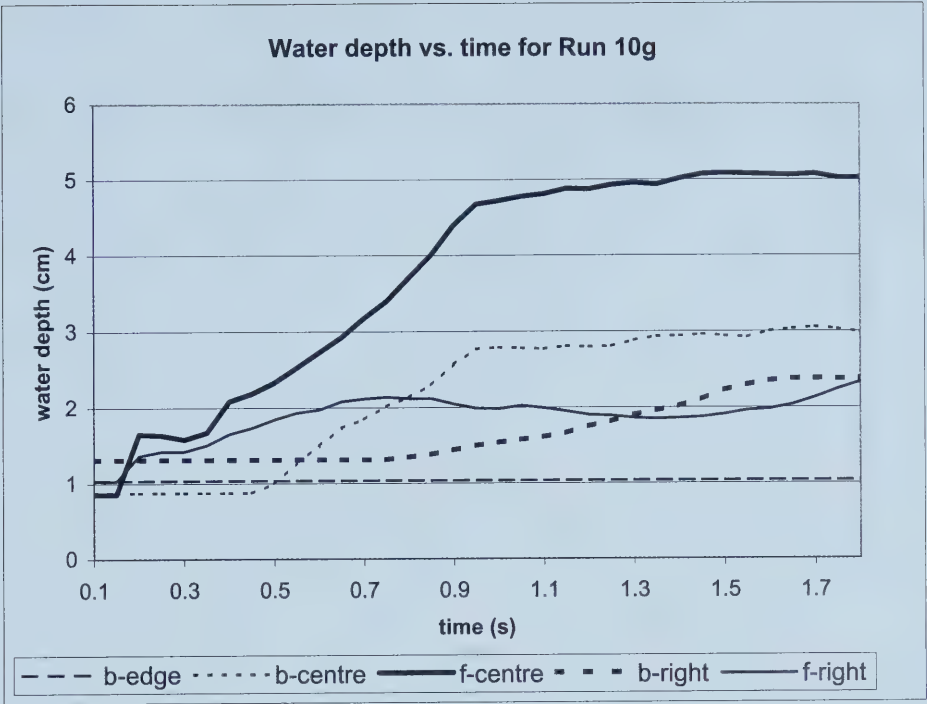


Figure 4.19: Verification of experimental repeatability and symmetry for 0.30 m headwater.



a)



b)     time = 1.0 s

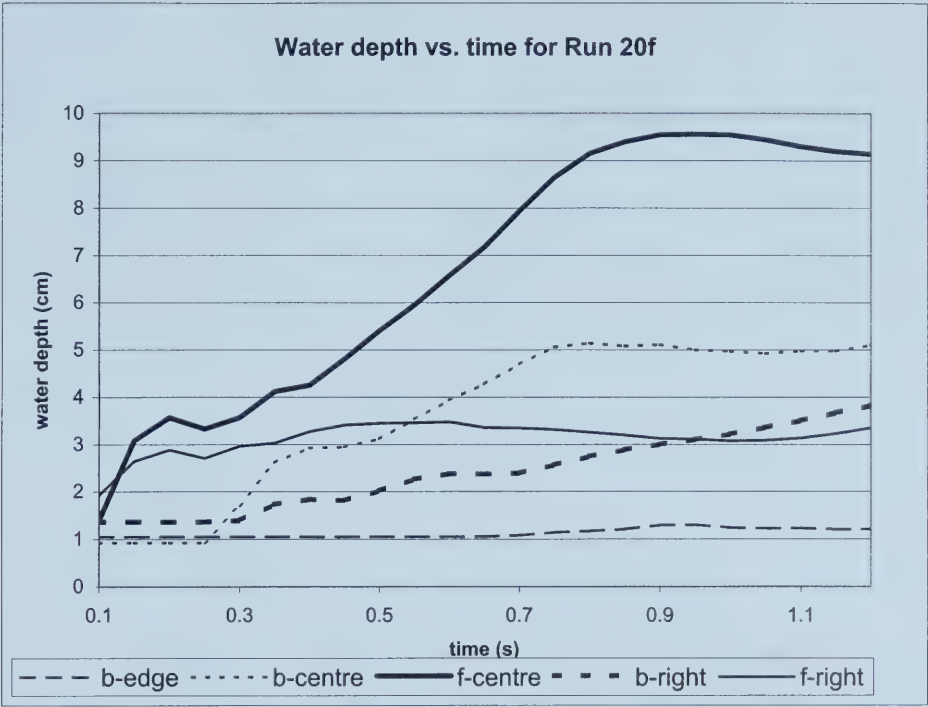


Figure 4.20: Asymmetrical probe results for Run 10g.





a)



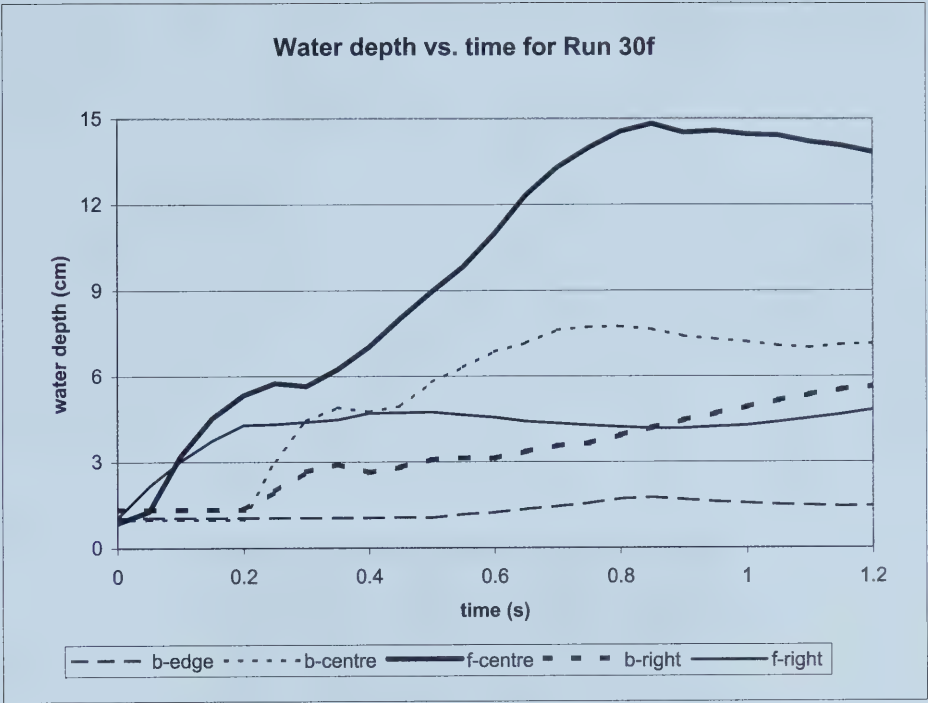
b) time = 1.0 s



Figure 4.21: Asymmetrical probe results for Run 20f.



a)



b) time = 1.0 s



Figure 4.22: Asymmetrical probe results for Run 30f.



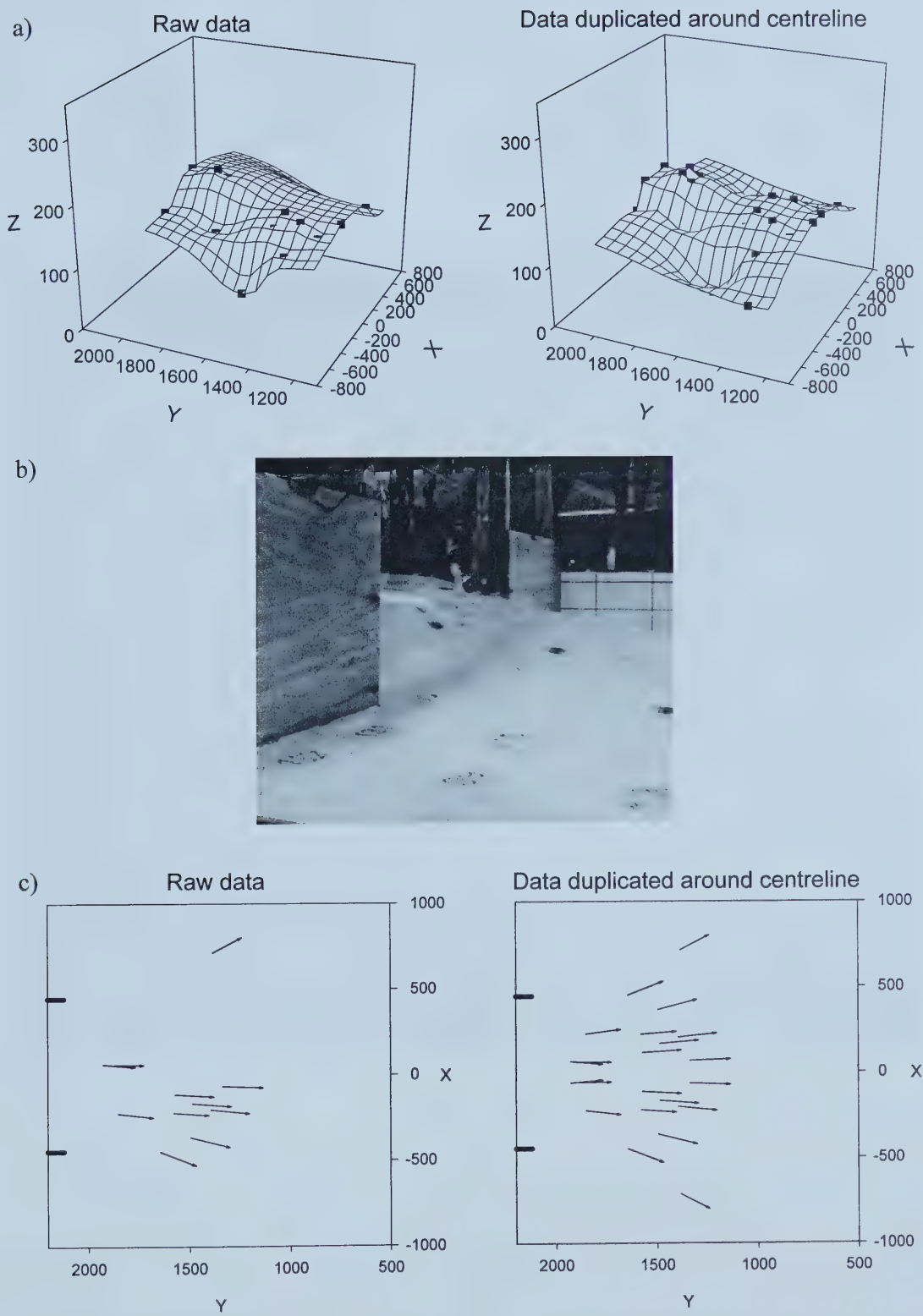


Figure 4.23: Utilization of symmetry to duplicate the stereoscopy results for Run 30d (time = 0.867 s).





Figure 4.24: Illustration of water flowing around wave probes for Run 30c (time = 0.5 s).





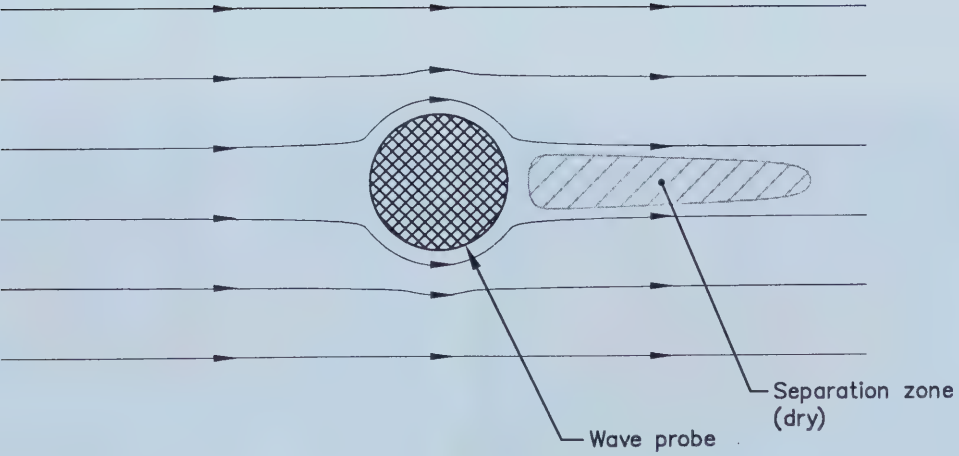
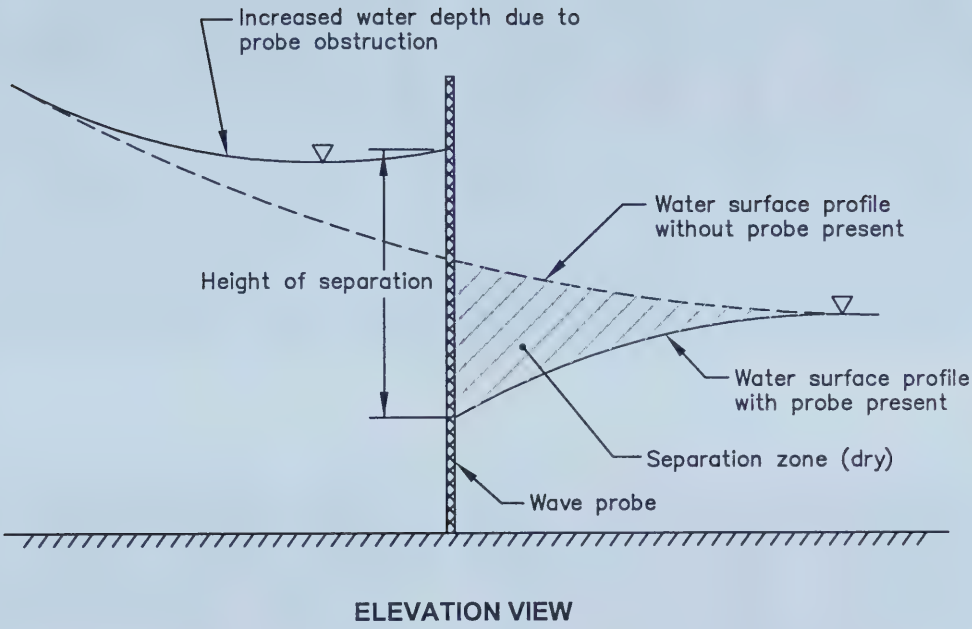


Figure 4.25: Elevation and plan views of separation zone downstream of a wave probe.



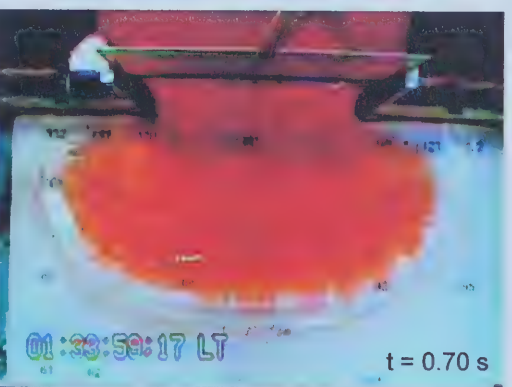
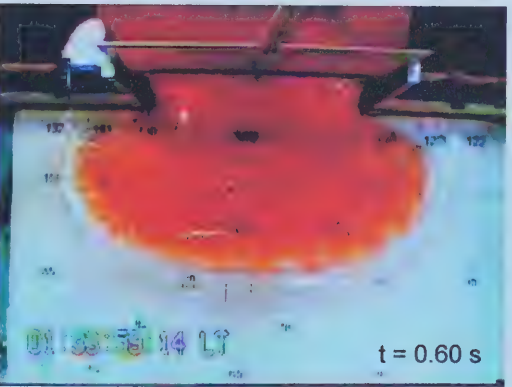
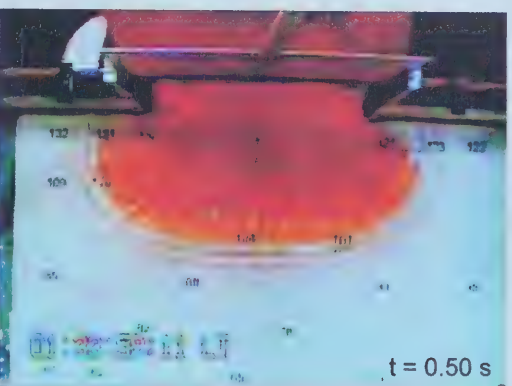
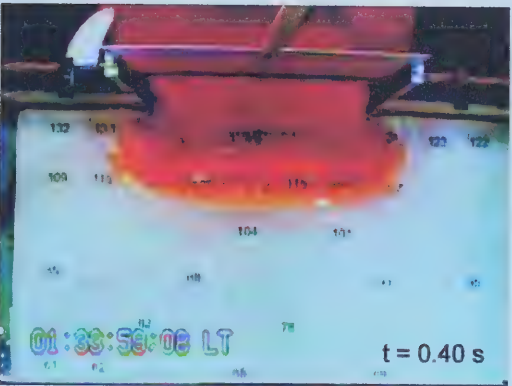
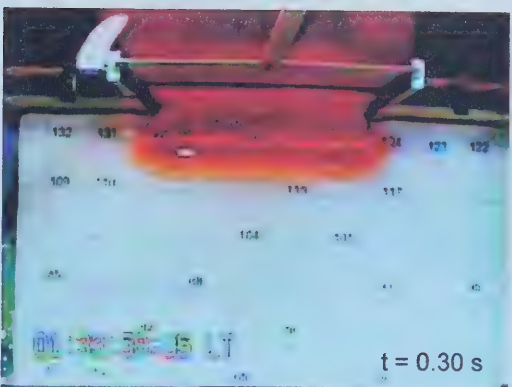
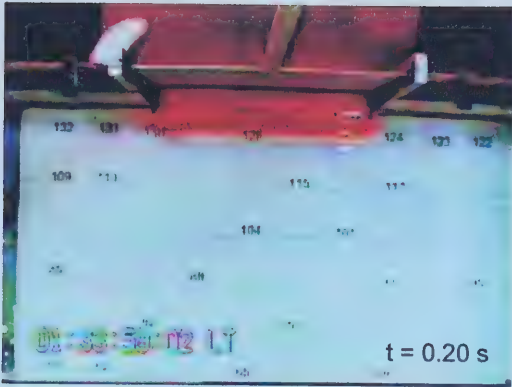


Figure 4.26: Progression of 6:1 flood wave for three-dimensional dam break (headwater = 0.30 m, tailwater = 0.05 m).



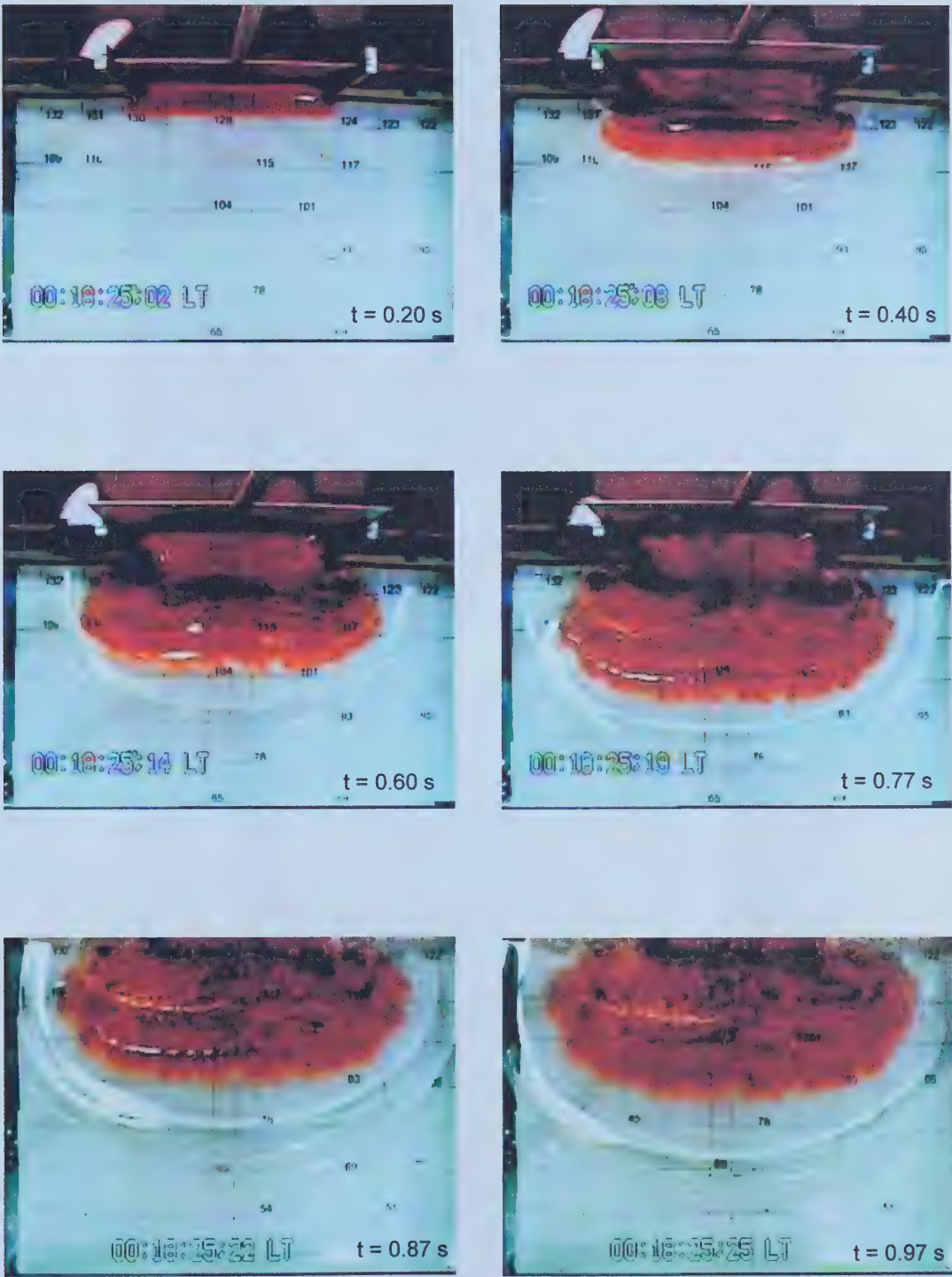
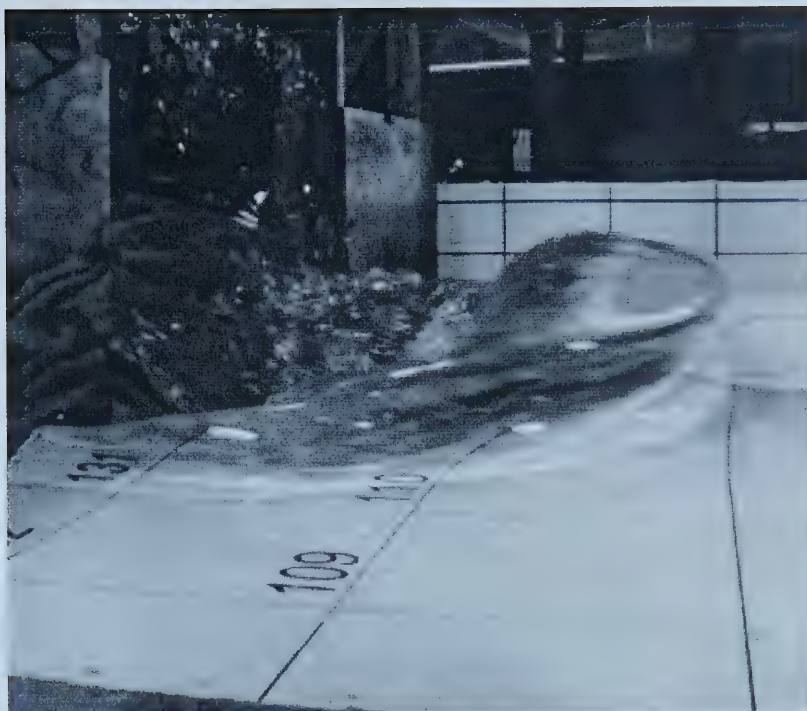


Figure 4.27: Progression of 3:1 flood wave for three-dimensional dam break (headwater = 0.30 m, tailwater = 0.10 m).







a) 6:1 depth ratio; time = 0.45 s

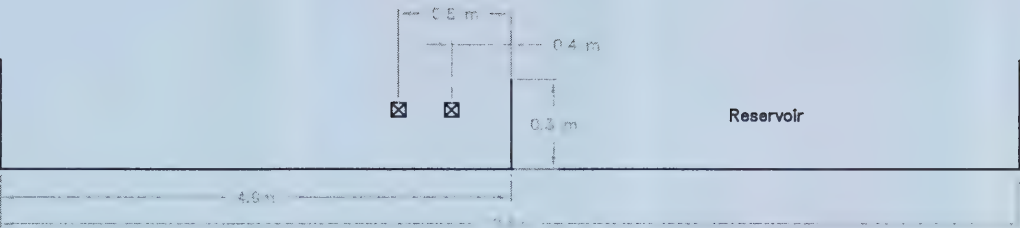


b) 3:1 depth ratio; time = 0.55 s

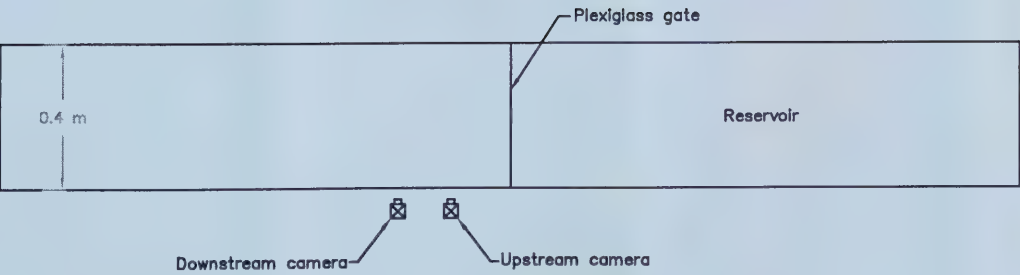
Figure 4.28: High-speed camera images illustrating the laminar wave followed by turbulent flow.







ELEVATION VIEW



PLAN VIEW

Figure 4.29: Elevation and plan views of flume used to conduct two-dimensional dam break experiments.



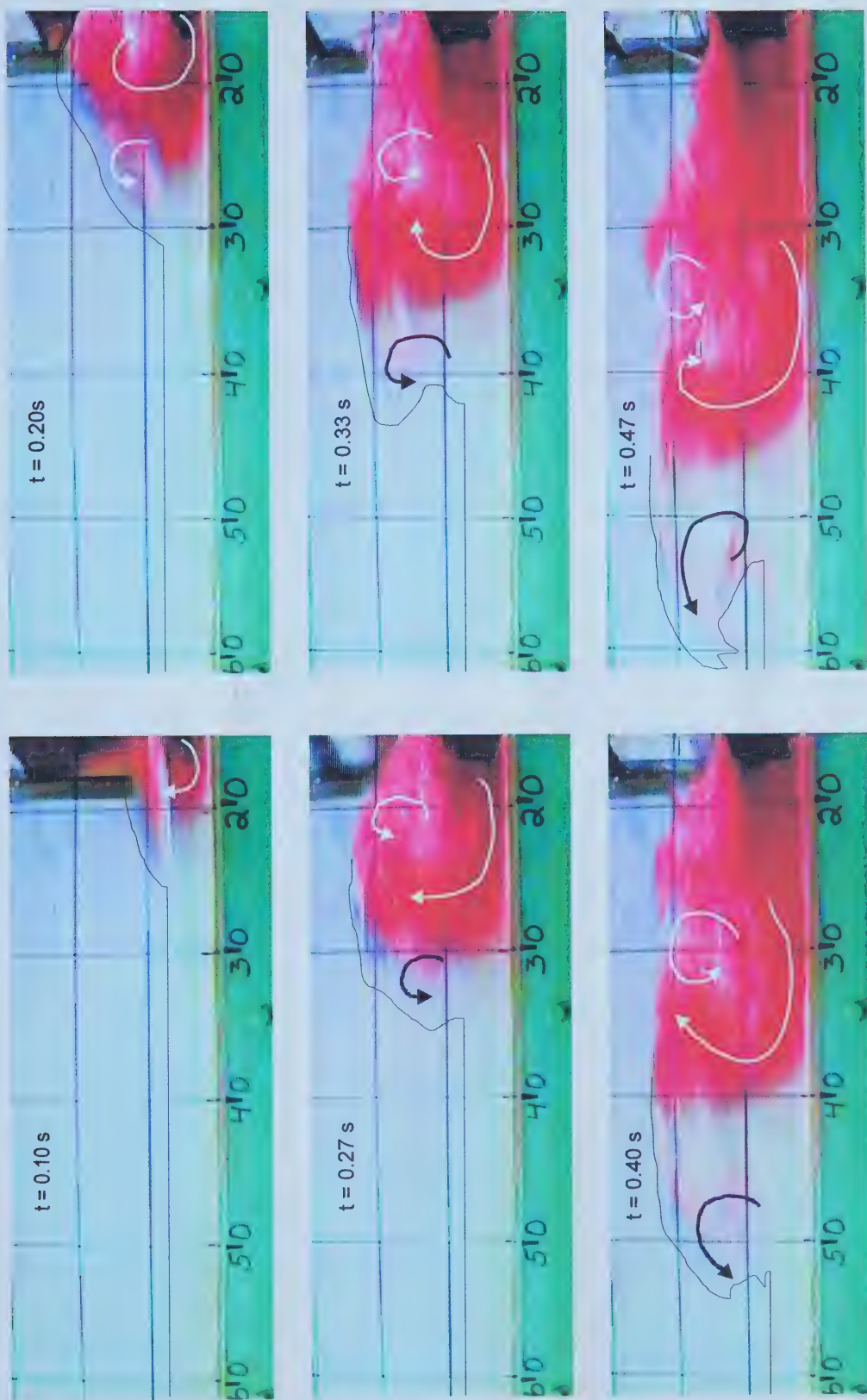


Figure 4.30: Progression of 6:1 flood wave for two-dimensional dam break (headwater = 0.24 m, tailwater = 0.04 m).



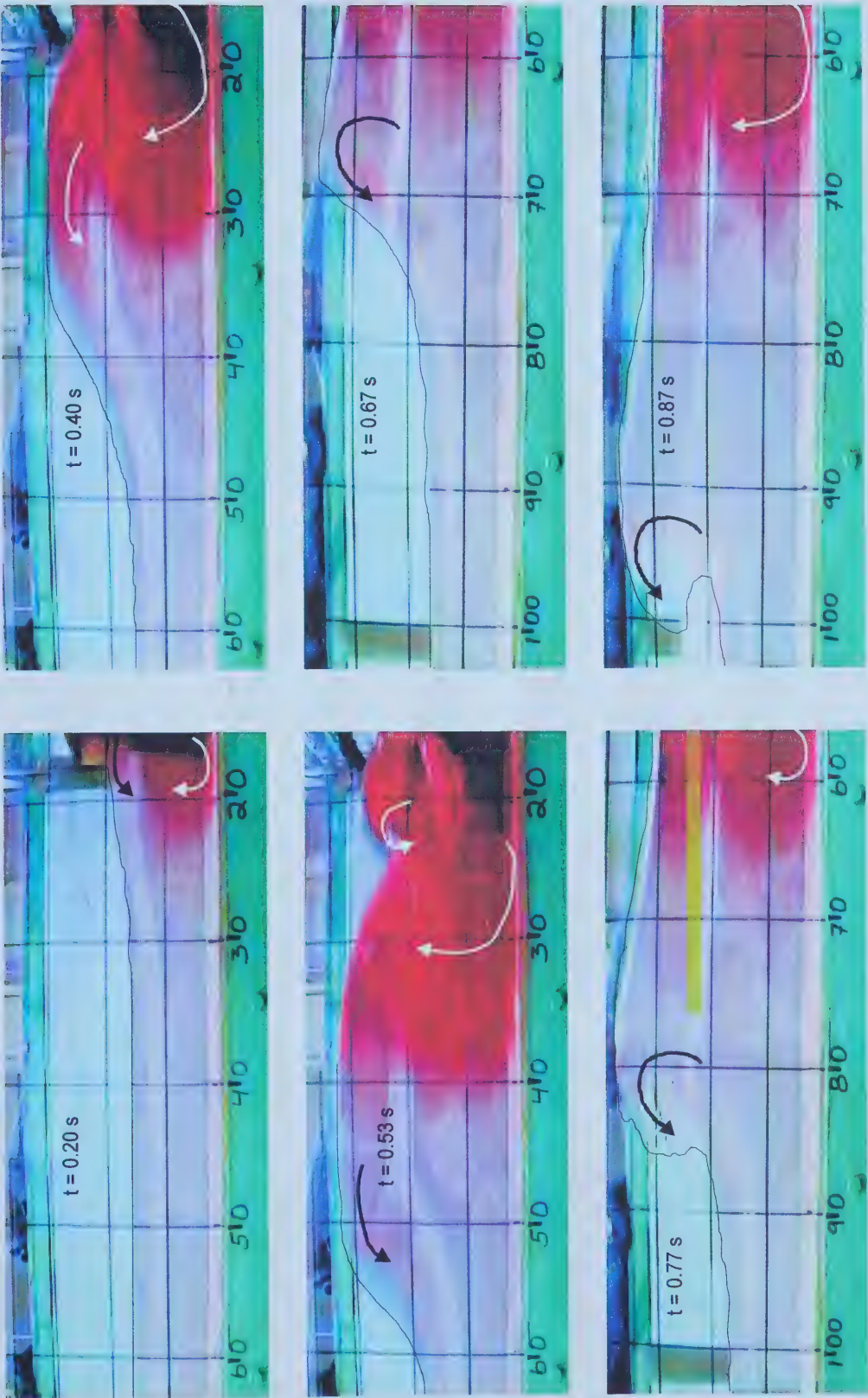
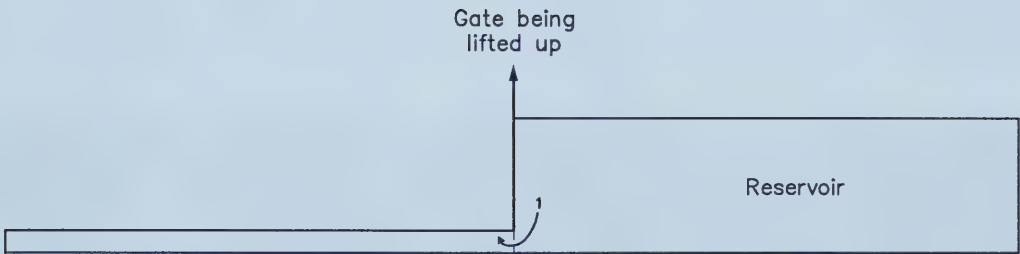


Figure 4.31: Progression of 3:1 flood wave for two-dimensional dam break (headwater = 0.24 m, tailwater = 0.08 m).

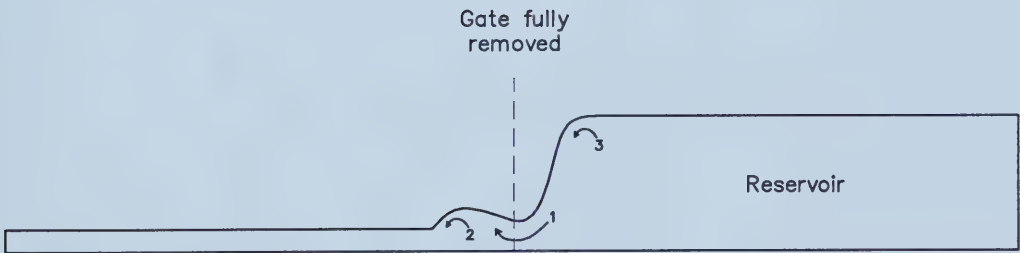




a)



b)



c)

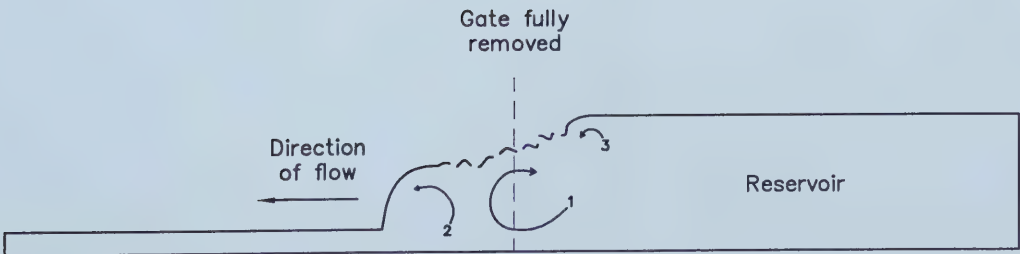


Figure 4.32: Illustration of roller locations.







Figure 4.33: Digitizing locations for the determination of wave velocity for the three-dimensional dam break experiments.



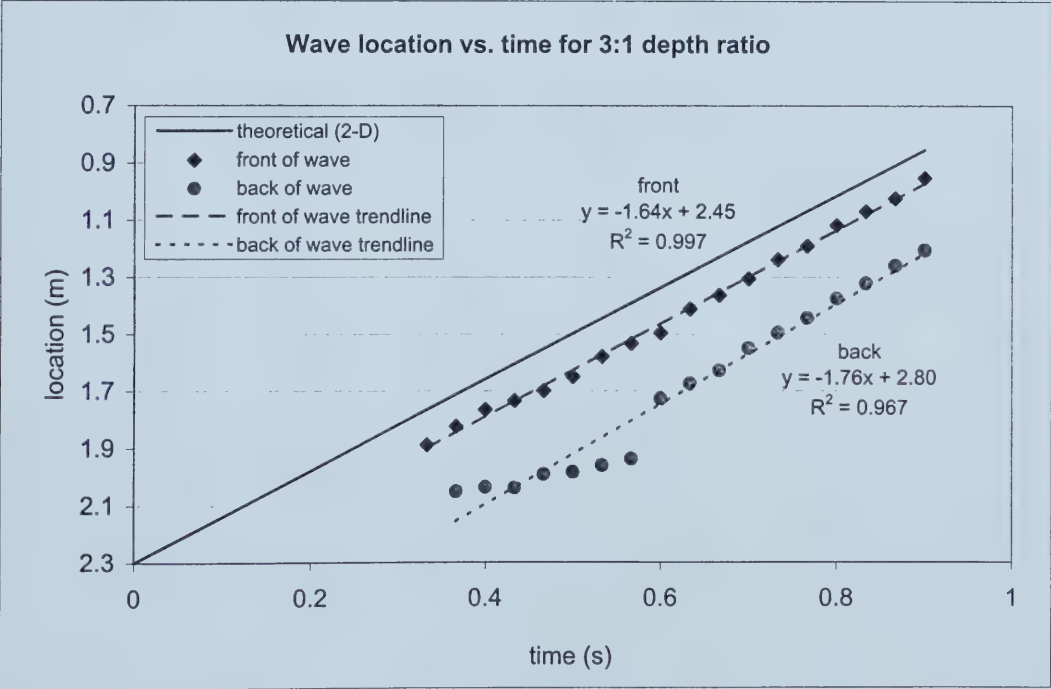
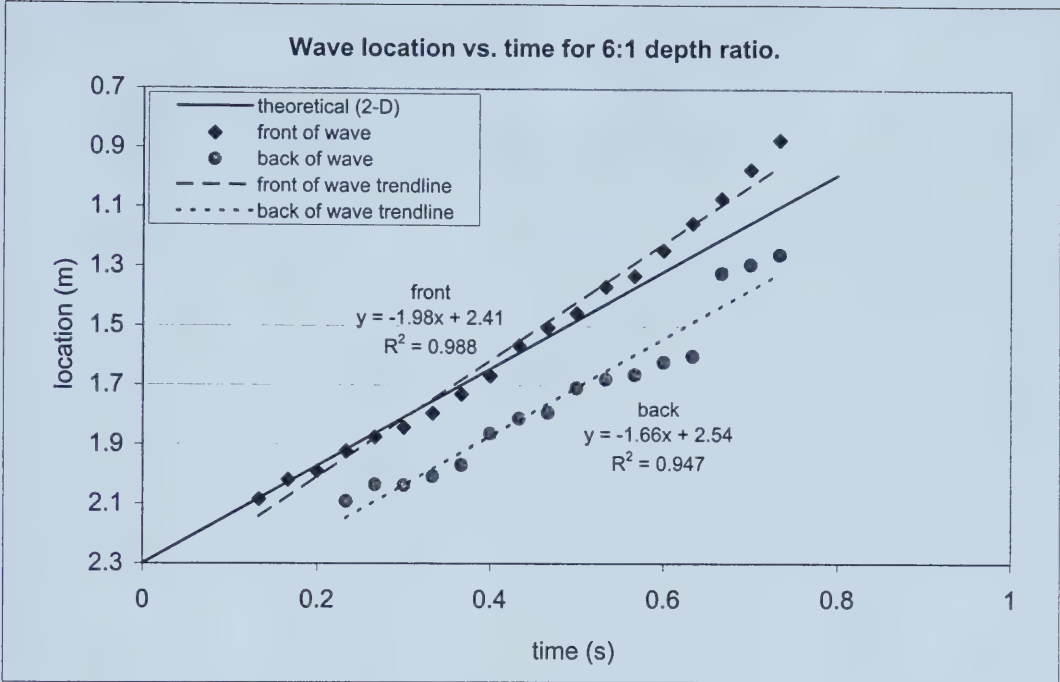


Figure 4.34: Determination of wave velocity for three-dimensional dam break experiments.



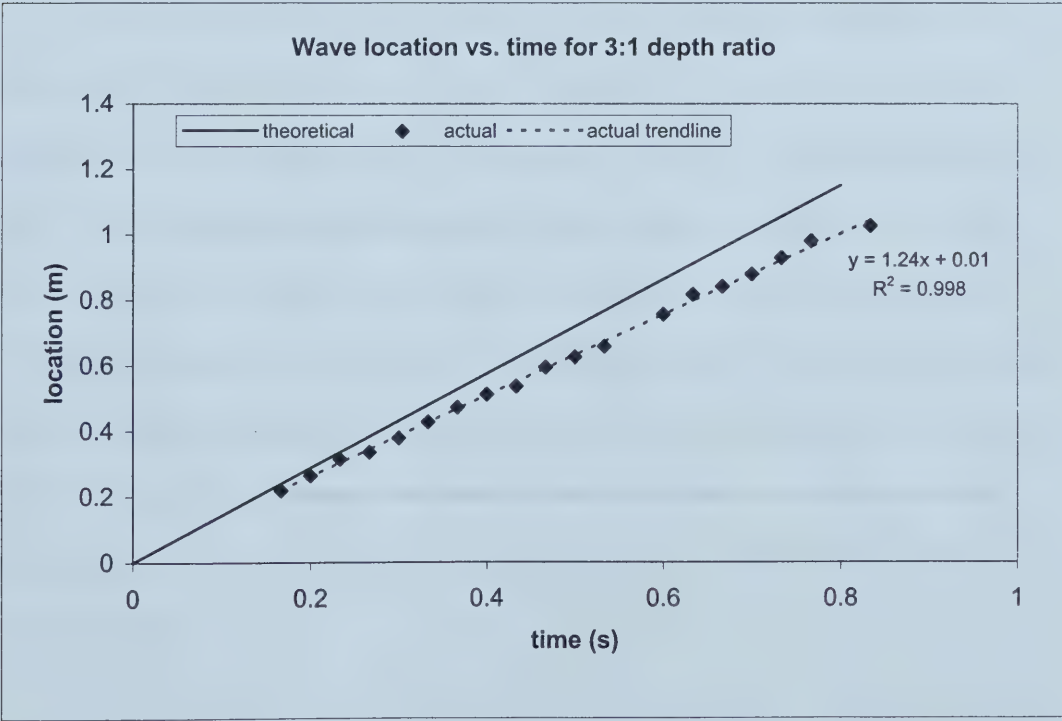
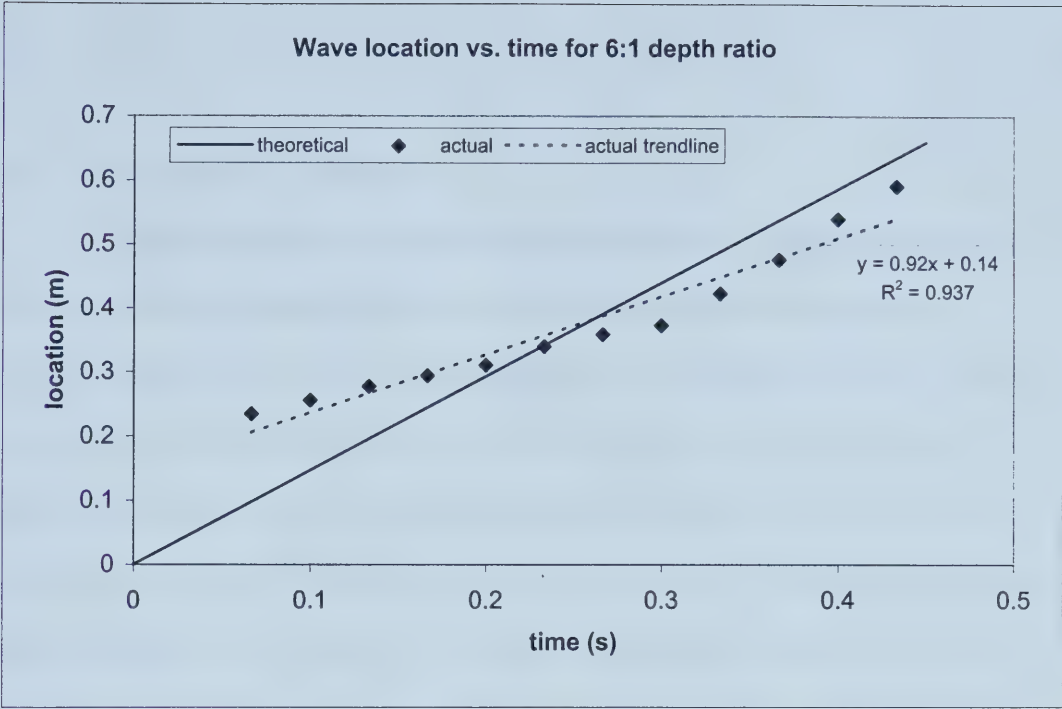


Figure 4.35: Determination of wave velocity for two-dimensional dam break experiments.



## 5.0 CONCLUSIONS AND RECOMMENDATIONS

### 5.1 Summary and Conclusions

The goal of this study was to investigate the feasibility of applying stereoscopy techniques to the measurement of dynamic open channel flows, and to provide recommendations to be considered by researchers who wish to pursue this new approach to unsteady flow measurement. Stereoscopy was investigated as a measurement technique since, due to the rapidly changing water surface shape, traditional flow depth measurement techniques are unsuitable for measuring dynamic flows. Three-dimensional dam break events are the specific type of dynamic flow which were the focus of this research.

Stereoscopy is based on the principle that two photographs of the same scene, taken from two slightly different perspectives (*i.e.*, stereo photographs) can be used to obtain the elevations of objects in the photographs. Three video cameras were mounted above the tank that the experiments were performed in and were used to record the dam break events for a variety of flow conditions. Image pairs from these three cameras comprised the required stereo images. To establish reference points in the stereo images, tracking particles were placed on the water surface and, through stereoscopy, their three-dimensional coordinates were determined. These coordinates were used to obtain a representation of the water surface profile in time and to compute the water surface velocity in time.





### 5.1.1 Discussion of the Stereoscopy Results

Stereoscopy was used to obtain the three-dimensional coordinates of the tracking particles for the duration of each applicable dam break event. For the experiments without tailwater, the spatial (horizontal) coordinates were accurate within 5 mm and the vertical (elevation) coordinates were accurate within 20 mm. For the experiments with tailwater, the spatial coordinates were also accurate to within 5 mm; however, due to particle entrainment, the elevation coordinates of the water surface could not be obtained. These deviations are random errors that were incurred during the experimental and analysis phases. This random error was primarily due to the difficulties encountered in accurately locating the tracking particles in the stereo images (blurring in the images). Particle tilting in zones where the water surface profile was steep exacerbated this error.

The tracking particles appeared as blurred streaks in the stereo images, where the length of the streak was proportional to the distance that the particle traveled during the time period that the camera shutter was open (*i.e.*, 1/60 second). Due to this excessive streaking, it is concluded that the 1/60 second shutter speed is inadequate for highly dynamic events. If the shutter speed were increased, the camera shutter would be open for a shorter time period, and the distance traveled by the particle (particle streaking) would be reduced. However, if this were to be implemented, a considerable increase in light would be required.

The cameras could also be lowered to reduce the blurriness of the tracking particles. This would also facilitate the use of smaller tracking particles, which in turn would reduce the error associated with particle tilting, since the range of depth from one edge of the particle to the other would be greatly reduced. However, this would require



more cameras. Also, it was found that the depth error was at a minimum when the distance between the cameras was maximized (*i.e.*, when the particles were simultaneously viewed by the most upstream and downstream cameras). If the cameras were lowered, this could result in additional errors due to the closer proximity of adjacent cameras.

A noticeable depth error was evident in the interpolated water surface profiles. It is expected that if the depth accuracy were improved, the profiles would be smoother and more representative of the actual wave shape. It is also anticipated that the shape of the interpolated water surface profiles would improve if more tracking particles were used, such that more data points would be available with which to construct the water surface profiles. However one must be careful not to use too many particles; if the water surface is covered too densely, the particles will interact and the velocities obtained will not be accurate. It is important to remember that in experiments with symmetry, such as the dam break example investigated here, the number of resulting data points for defining both the water surface profile and velocities, is effectively double the number of tracking particles.

For both the experiments with and without tailwater, the error in the velocity vector results was found to be 13 percent. If the optimum number of tracking particles were used, more velocity vectors could be computed and the surface velocity over the entire wave surface would be better represented.



### ***5.1.2 Discussion of the Wave Probes Results***

The wave probes were used to measure the flow depth for the downstream dry-bed experiments. Due to considerable probe-flow interaction, the wave probes were not used for the experiments with tailwater. As a result of the large probe diameter, flow interference was significant and the depth results were quite poor (maximum error of 50 mm). Although the depth measurements were quite inaccurate, they were useful for assessing the repeatability and symmetry of the experiments. The experiments were found to be repeatable within 16 mm and symmetrical around the centreline within 7 mm.

It is expected that the wave probe results could be improved by using probes of a smaller diameter. Past researchers obtained accurate results by using wave probes as small as 0.3 mm in diameter (Fraccarollo and Toro, 1995). This small diameter allowed probes to be used downstream of the gate, in areas of supercritical flow, and it was found that the small diameter wires did not significantly impact the flow. If smaller diameter wave probes were used, the results would be considerably more accurate and could be used to verify the depth results obtained from the stereoscopy. However, if the primary desire was to use wave probes to obtain depth measurements over the entire water surface, such that the water surface profile could be accurately represented, the large number of wave probes required would likely make this approach infeasible.

### ***5.1.3 Discussion of the Results from the Experiments with Tailwater***

Due to particle entrainment, stereoscopy was not suitable for the experiments with tailwater; however, the flow characteristics in this case were found to be quite interesting. There was minimal mixing observed between the headwater and the tailwater for the three-dimensional experiments. The tailwater was pushed forward as a smooth wave and



the extremely turbulent reservoir water followed behind. This smooth wave eventually broke, and this breaking was perceived to occur much sooner for the experiments with lower tailwater. To further investigate the flow behaviour, two-dimensional experiments were conducted and it was seen that these interesting flow characteristics were also observed in that case. The two-dimensional experiments were also used to investigate the internal flow dynamics of the dam break wave release.

The leading edge wave velocity for the two- and three-dimensional experiments was computed by tracking the location of the leading edge. For the two-dimensional experiments, the wave velocity was found to be 0.92 m/s for the 6:1 depth ratio and 1.24 m/s for the 3:1 depth ratio. Fair agreement was observed when these velocities were compared to the two-dimensional theoretical wave velocities of 1.47 m/s and 1.44 m/s for the 6:1 and 3:1 depth ratios, respectively. The three-dimensional, experimental wave velocities were found to be 1.98 m/s and 1.64 m/s for the 6:1 and 3:1 depth ratios, respectively. These velocities compared well to the two-dimensional theoretical wave velocities of 1.64 m/s and 1.61 m/s, corresponding to the 6:1 and 3:1 depth ratios, respectively.





## 5.2 Recommendations for Future Investigations

Based on this investigation of the feasibility of applying stereoscopy to the measurement of dynamic open channel flows, the following specific recommendations are offered for future investigations.

- I. The camera shutter speed should be increased to minimize blurring of the tracking particles in the images; this will require a corresponding increase in the ambient light. A variety of shutter speeds should be investigated to achieve a balance in terms of particle clarity and required lighting.
- II. The distance between adjacent cameras should be maximized. Since this requires the cameras to be raised to achieve the same field of view, an optimum balance between camera spacing and camera height must be determined. This could be accomplished either by employing a trial and error approach or by taking the camera parameters into account to theoretically predict the best camera spacing.
- III. To maximize the experimental data, an optimum number of tracking particles should be used to cover the entire water surface. A trial and error method should be applied to determine the maximum number of tracking particles that could be used before particle interaction became an issue. If possible, symmetrical experimental configurations should be used, since this effectively doubles the data obtained.



- IV. The smallest possible tracking particles should be used. This size will be dictated by the camera locations and lens properties. Particle size will have a significant influence on vertical error in experiments with steep water surface profiles.
- V. It would be highly desirable to explore the development of a method to automatically locate the tracking particles in the stereo images.
- VI. A significant improvement in image quality would be realized if high-speed digital cameras were used to record stereo images of the dam break events. The images would be recorded in digital, and therefore would not have to be converted from analog to digital, which would allow the original image quality to be retained. Due to the higher quality images, smaller tracking particles could be used and less particle streaking would occur because of the increased camera recording speed; increased accuracy of the tracking particle coordinates would result. The financial investment required for this type of setup is paramount and would likely be the determining factor for its implementation.
- VII. Once the method of stereoscopy has been researched further, future studies should consider tests on other types of unsteady open channel flow problems (e.g. surge propagation through combining and dividing channel junctions, negative surges, *etc.*).



## REFERENCES

- Alcrudo, F. and Garcia-Navarro, P. (1993). "A High-Resolution Godunov-Type Scheme in Finite Volumes for the 2D Shallow-Water Equations." *International Journal for Numerical Methods in Fluids*, Vol. 16, pp. 489-505.
- Ankamuthu, S., Balachandar, R., and Wood, H. (1999). "Computational Stereoscopy for Three-dimensional Scour Depth Measurement in Channels." *Canadian Journal of Civil Engineering*, Vol. 26, pp. 698-712.
- Bechteler, W., Kulisch, H., and Nujic, M. (1992). "2-D Dam-Break Flooding Waves Comparison between Experimental and Calculated Results." *Third International Conference on Floods and Flood Management*, Florence, Italy, 24-26 November, pp. 247-260.
- Bell, S. W., Elliot, R. C., and Chaudhry, M. H. (1992). "Experimental Results of Two-Dimensional Dam-Break Flows." *Journal of Hydraulic Research*, Vol. 30, No. 2, pp.225-252.
- Bellos, C. V., Soulis, J. V., and Sakkas, J. G. (1991). "Computation of Two-Dimensional Dam-Break-Induced Flows." *Advances in Water Resources*, Vol. 14, No. 1, pp. 31-41.
- Bellos, C. V., Soulis, J. V., and Sakkas, J. G. (1992). "Experimental Investigation of Two-Dimensional Dam-Break Induced Flows." *Journal of Hydraulic Research*, Vol. 30, No. 1, pp. 47-63.
- Chow, V. T. (1959). Open-Channel Hydraulics. McGraw-Hill, USA.
- Davis, R. E., Foote, F. S., Anderson, J. M., and Mikhail, E. M. (1981). Surveying Theory and Practice, 6<sup>th</sup> Edition. McGraw-Hill, USA.



## REFERENCES (continued)

- Fennema, R. J. (1985). "Numerical Solution of Two-Dimensional Transient Free-Surface Flows." Ph. D. Thesis, Washington State University, Pullman.
- Fennema, R. J. and Chaudhry, M. H. (1990). "Explicit Methods for 2-D Transient Free-Surface Flows." *Journal of Hydraulic Engineering*, ASCE, Vol. 116, No. 8, pp. 1013-1034.
- Fraccarollo, L. and Toro, E. F. (1995). "Experimental and Numerical Assessment of the Shallow Water Model for Two-Dimensional Dam-Break Type Problems." *Journal of Hydraulic Research*, Vol. 33, No. 6, pp. 843-864.
- Ghanem, A., Steffler, P., Hicks, F., and Katopodis, C. (1995). "Two Dimensional Finite Element Modeling of Flow in Aquatic Habitats." Water Resources Engineering Report No. 95-S1, Department of Civil Engineering, University of Alberta, Edmonton, Alberta.
- Henderson, F. M. (1966). Open Channel Flow. Macmillian Publishing Co., Inc., New York, NY.
- Jha, A. K., Akiyama, J., and Ura, M. (2000). "Flux Difference Splitting Schemes for 2D Flood Flows." *Journal of Hydraulic Engineering*, ASCE, Vol. 126, No. 1, pp. 33-42.
- Karara, H. M. (1989). Non-Topographic Photogrammetry, 2<sup>nd</sup> Ed. American Society for Photogrammetry and Remote Sensing, Falls Church, Virginia.
- Katopodes, N. and Strelkoff, T. (1978). "Computing Two-Dimensional Dam-Break Flood Waves." *Journal of Hydraulic Engineering*, ASCE, Vol. 104, No. 9, pp. 1269-1288.





## REFERENCES (continued)

Milhail, E. M., Bethel, J. S., and McGlone, J. C. (2001). Introduction to Modern Photogrammetry. John Wiely & Sons, Inc., USA.

Obaidat, M. T., Al-Suleiman, T. I., and Abdul-Jabbar, G. T. (1997). "Quantification of Pavement Rut Depth Using Stereovision Technology." *Journal of Survey Engineering*, ASCE, Vol. 123, No. 2, pp. 55-70.

Obaidat, M. T. and Al-Masaeid, H. R. (1998). "Video System to Monitor Archeological Sites Using Ground-Based Photogrammetry." *Journal of Survey Engineering*, ASCE, Vol. 124, No. 1, pp. 3-25.

Peterson, A. E. and Durdle, N. G. (1999). "Surveying Possibilities with 35mm Cameras." *Annual Conference of the Canadian Society for Civil Engineering*, Vancouver, British Columbia, 29-31 May, pp. 432-440.

Russ, J. C. (1995). The Image Processing Handbook, 2<sup>nd</sup> Ed. CRC Press Inc., Boca Raton, Florida.

Jandel Corporation (1994). *SigmaPlot Version 1.02 Users Manual*.

Soulis, J. V. (1992). "Computation of Two-Dimensional Dam-Break Flood Flows." *International Journal for Numerical Methods in Fluids*, Vol. 14, No. 6, pp. 631-664.

Sturm P. (1998). "Camera Self-Calibration: A Case Against Kruppa's Equations." *IEEE International Conference on Image Processing*, Vol. 2, Chichago, IL, USA, pp. 172-175.



**REFERENCES (continued)**

Wang, J. S., Ni, H. G., and He, Y. S. (2000). "Finite Difference TVD Scheme for Computation of Dam-Break Problems." *Journal of Hydraulic Engineering*, ASCE, Vol. 126, No. 4, pp. 253-562.

Wolf, P. R. (1974). Elements of Photogrammetry. McGraw-Hill, USA.

Wolf, P. R. and Dewitt, B. A. (2000). Elements of Photogrammetry, 3<sup>rd</sup> Ed. McGraw-Hill, USA.



## **APPENDIX A**

**Three-dimensional tracking particle coordinates for experiments performed without tailwater. (See Figure 3.1 for coordinate system.)**



Table A.1: Three-dimensional tracking particle coordinates for Run 10a  
(dimensions in mm).

$t = 0.33 \text{ s}$

particle #	x	y	z
1	354	2019	141
2	387	2021	159

$t = 0.40 \text{ s}$

particle #	x	y	z
1	359	1950	151
2	394	1951	160
3	-347	1996	146
4	389	2047	150

$t = 0.47 \text{ s}$

particle #	x	y	z
1	366	1879	145
2	411	1881	156
3	-349	1923	168
4	400	1984	143
5	-399	2019	134
6	-31	2039	147
7	123	2031	166

$t = 0.53 \text{ s}$

particle #	x	y	z
1	373	1803	151
2	429	1810	147
3	-355	1843	191
4	419	1918	138
5	-415	1950	135
6	-32	1980	147
7	126	1982	138
8	-270	2020	138

$t = 0.60 \text{ s}$

particle #	x	y	z
1	388	1730	145
2	448	1738	149
3	-368	1783	154
4	442	1851	137
5	-433	1887	140
6	-32	1924	143
7	127	1919	148
8	-266	1960	139
9	40	1976	144
10	331	1996	144
11	-374	2021	147
12	-172	2048	140
13	240	2059	142

$t = 0.67 \text{ s}$

particle #	x	y	z
1	402	1662	142
2	470	1674	140
3	-379	1714	161
4	467	1785	139
5	-462	1820	138
6	-31	1857	152
7	124	1854	151
8	-262	1895	155
9	39	1917	147
10	337	1937	140
11	-381	1958	148
12	-166	1997	141
13	233	2004	160
14	42	2033	135





Table A.1 (cont.): Three-dimensional tracking particle coordinates for Run 10a  
(dimensions in mm).

t = 0.73 s

particle #	x	y	z
1	421	1603	121
2	496	1611	119
3	-393	1638	149
4	497	1722	129
5	-489	1755	142
6	-31	1793	158
7	121	1787	157
8	-265	1834	145
9	36	1859	137
10	341	1875	144
11	-392	1895	161
12	-163	1939	151
13	232	1946	155
14	42	1982	130

t = 0.80 s

particle #	x	y	z
1	447	1548	68
2	529	1551	77
3	-407	1566	151
4	525	1662	121
5	-522	1695	123
6	-30	1726	151
7	116	1717	164
8	-266	1767	151
9	37	1794	143
10	350	1810	151
11	-418	1836	137
12	-160	1882	146
13	231	1891	144
14	36	1927	135
15	-199	2000	159

t = 0.87 s

particle #	x	y	z
1	465	1499	55
2	551	1501	64
3	-427	1496	138
4	554	1603	116
5	-556	1637	108
6	-26	1654	160
7	115	1648	145
8	-273	1699	144
9	34	1730	151
10	364	1745	144
11	-440	1772	138
12	-154	1821	151
13	232	1828	142
14	31	1870	140
15	-187	1945	168
16	-51	2060	129
17	44	2026	149

t = 0.93 s

particle #	x	y	z
1	475	1456	50
2	570	1462	50
3	-453	1422	77
4	592	1546	84
5	-579	1577	126
6	-27	1584	145
7	112	1577	146
8	-276	1629	155
9	31	1662	161
10	380	1677	141
11	-464	1707	148
12	-156	1760	150
13	234	1765	141
14	27	1810	144
15	-182	1888	156
16	-45	2011	132
17	40	1976	145



Table A.1 (cont.): Three-dimensional tracking particle coordinates for Run 10a  
(dimensions in mm).

t = 1.00 s

particle #	x	y	z
1	485	1412	57
2	581	1429	51
3	-474	1356	63
4	622	1490	75
5	-623	1523	70
6	-24	1508	92
7	119	1500	83
8	-283	1558	156
9	30	1593	158
10	390	1609	163
11	-494	1643	132
12	-156	1696	158
13	235	1700	151
14	22	1748	159
15	-178	1830	153
16	-40	1959	143
17	36	1926	150

t = 1.07 s

particle #	x	y	z
1	497	1369	48
2	595	1391	56
3	-492	1300	52
4	649	1438	71
5	-651	1472	70
6	-25	1432	95
7	120	1425	81
8	-299	1483	75
9	33	1520	96
10	428	1537	88
11	-520	1581	149
12	-158	1631	149
13	239	1633	141
14	18	1684	161
15	-178	1769	160
16	-37	1904	176
17	34	1870	155
18	-68	2013	126

t = 1.13 s

particle #	x	y	z
1	506	1326	50
2	611	1350	56
3	-502	1245	52
4	674	1384	73
5	-679	1420	71
6	-22	1352	82
7	122	1350	79
8	-311	1411	74
9	35	1445	85
10	451	1468	77
11	-564	1516	77
12	-161	1564	141
13	248	1565	142
14	19	1620	158
15	-183	1707	147
16	-37	1854	138
17	33	1814	152
19	60	2015	146
20	282	2056	150

t = 1.20 s

particle #	x	y	z
1	520	1282	47
2	630	1311	49
3	-522	1197	14
4	702	1336	67
5	-705	1372	64
6	-23	1274	84
7	123	1272	80
8	-322	1333	69
9	38	1370	82
10	470	1400	78
11	-599	1457	62
12	-170	1489	87
13	266	1492	83
14	22	1553	159
15	-183	1643	151
16	-39	1796	159
17	35	1755	167
18	-65	1904	170
19	59	1965	150
20	277	1994	150
21	41	2030	158



Table A.1 (cont.): Three-dimensional tracking particle coordinates for Run 10a  
(dimensions in mm).

t = 1.27 s

particle #	x	y	z
1	531	1236	52
2	648	1270	51
3	-537	1139	5
4	729	1286	62
5	-734	1326	54
6	-24	1195	83
7	127	1192	76
8	-335	1260	66
9	44	1293	86
10	493	1332	70
11	-624	1403	67
12	-179	1418	72
13	277	1420	79
14	27	1480	87
15	-191	1577	157
16	-44	1737	138
17	36	1693	155
18	-65	1853	154
19	60	1914	147
20	283	1930	160
21	43	1988	148

t = 1.33 s

particle #	x	y	z
1	544	1189	55
2	667	1234	50
3	-542	1079	57
4	753	1236	66
5	-759	1286	53
6	-23	1112	83
7	132	1118	86
8	-349	1193	16
9	47	1216	81
10	517	1266	64
11	-652	1349	63
12	-190	1344	81
13	286	1347	75
14	29	1407	85
15	-199	1510	152
16	-45	1676	147
17	40	1632	145
18	-69	1795	160
19	62	1859	151
20	291	1871	141
21	46	1936	145
22	-98	2020	160
23	114	2031	142



Table A.1 (cont.): Three-dimensional tracking particle coordinates for Run 10a  
(dimensions in mm).

$t = 1.40 \text{ s}$

particle #	x	y	z
1	558	1142	53
2	690	1199	39
3	-558	1029	46
4	778	1187	63
5	-786	1249	34
6	-24	1032	76
7	139	1037	83
8	-358	1115	72
9	49	1138	80
10	535	1206	67
11	-680	1300	58
12	-201	1270	74
13	297	1273	80
14	29	1333	81
15	-211	1436	86
16	-48	1612	166
17	40	1565	159
18	-72	1734	159
19	62	1801	157
20	302	1806	147
21	44	1883	148
22	-97	1968	163
23	112	1978	159

$t = 1.47 \text{ s}$

particle #	x	y	z
1	574	1094	51
2	704	1170	43
3	-581	984	-2
4	804	1137	62
5	-798	1227	40
6	-24	950	20
7	153	957	12
8	-371	1043	75
9	53	1061	89
10	556	1149	62
11	-705	1251	57
12	-214	1198	76
13	311	1200	84
14	30	1259	73
15	-225	1363	85
16	-48	1549	166
17	43	1495	89
18	-75	1676	155
19	64	1743	151
20	319	1741	142
21	44	1828	154
22	-98	1918	159
23	115	1926	156
24	-292	2029	151
25	-75	2032	170
26	110	2034	143





Table A.1 (cont.): Three-dimensional tracking particle coordinates for Run 10a  
(dimensions in mm).

t = 1.53 s

particle #	x	y	z
1	587	1045	51
2	724	1137	43
3	-594	937	2
4	827	1091	62
5	-809	1206	39
6	-24	866	11
7	164	876	14
8	-392	973	12
9	60	979	10
10	574	1092	66
11	-728	1206	58
12	-229	1124	76
13	327	1127	83
14	31	1184	76
15	-238	1291	79
16	-51	1480	81
17	46	1426	90
18	-79	1614	167
19	67	1682	154
20	336	1680	146
21	44	1770	154
22	-105	1862	156
23	121	1871	160
24	-295	1969	144
25	-74	1987	151
26	110	1980	152
27	-229	2016	150

t = 1.60 s

particle #	x	y	z
1	609	999	18
2	743	1103	49
3	-609	886	8
4	850	1044	63
5	-829	1187	11
6	-25	783	24
7	170	795	20
8	-407	899	7
9	62	901	17
10	595	1036	64
11	-761	1166	21
12	-240	1047	78
13	343	1053	86
14	32	1106	83
15	-250	1220	78
16	-56	1409	90
17	50	1353	81
18	-83	1549	146
19	71	1618	158
20	360	1615	146
21	49	1709	149
22	-109	1803	162
23	125	1815	145
24	-309	1904	154
25	-76	1941	148
26	114	1927	163
27	-235	1957	152
28	9	2032	159



Table A.1 (cont.): Three-dimensional tracking particle coordinates for Run 10a  
(dimensions in mm).

$t = 1.67 \text{ s}$

particle #	x	y	z
1	625	948	8
2	762	1066	56
3	-629	833	3
4	887	997	27
5	-846	1163	12
6	-27	698	15
7	181	710	10
8	-418	831	17
9	66	819	16
10	628	981	14
11	-786	1124	9
12	-258	971	19
13	372	977	25
14	35	1031	69
15	-269	1149	11
16	-58	1337	79
17	52	1283	86
18	-87	1479	93
19	78	1555	145
20	387	1553	142
21	52	1648	159
22	-117	1745	155
23	134	1753	152
24	-332	1842	137
25	-77	1883	159
26	119	1873	153
27	-241	1897	172
28	9	1987	149
29	-251	2018	136

$t = 1.73 \text{ s}$

particle #	x	y	z
1	639	896	6
2	782	1026	63
3	-645	777	6
4	908	952	23
5	-851	1144	31
6	-26	614	3
7	193	629	17
8	-435	762	10
9	70	738	18
10	645	926	18
11	-791	1077	57
12	-272	893	14
13	392	899	13
14	40	953	13
15	-278	1070	74
16	-61	1266	74
17	55	1207	81
18	-90	1408	88
19	86	1485	94
20	428	1486	84
21	55	1584	158
22	-126	1684	150
23	141	1692	155
24	-354	1777	153
25	-80	1829	142
26	125	1815	144
27	-262	1840	147
28	9	1934	152
29	-258	1954	154
30	-199	1992	174
31	-15	2020	165



Table A.1 (cont.): Three-dimensional tracking particle coordinates for Run 10a  
(dimensions in mm).

t = 1.80 s

particle #	x	y	z
1	654	844	5
2	820	983	24
3	-663	725	17
4	931	906	21
5	-866	1129	21
6	-26	535	17
7	201	549	16
8	-445	701	22
10	672	873	4
11	-814	1032	50
12	-288	813	14
13	415	820	10
14	40	876	14
15	-296	1000	8
16	-65	1193	80
17	60	1132	84
18	-98	1338	83
19	93	1417	80
20	460	1418	83
21	64	1518	93
22	-133	1620	162
23	154	1631	145
24	-382	1716	150
25	-86	1770	164
26	135	1756	138
27	-281	1777	161
28	10	1881	149
29	-272	1896	143
30	-206	1940	146
31	-15	1973	161
32	-340	1989	144
33	-81	2045	142



Table A.2: Three-dimensional tracking particle coordinates for Run 10c  
(dimensions in mm).

t = 0.37 s

particle #	x	y	z
1	-323	2036	130
2	-256	2013	151
3	36	2029	142
4	194	2006	143
5	261	2054	140
6	284	2032	143

t = 0.43 s

particle #	x	y	z
1	-318	1969	145
2	-252	1940	156
3	35	1959	156
4	195	1936	151
5	259	1987	149
6	281	1962	159
7	49	2021	156

t = 0.50 s

particle #	x	y	z
1	-317	1897	153
2	-249	1871	164
3	38	1893	143
4	198	1869	146
5	254	1920	158
6	282	1895	146
7	51	1960	156
8	-286	2015	154
9	-262	1997	139
10	70	2021	139
11	103	2007	144
12	358	2040	147

t = 0.56 s

particle #	x	y	z
1	-320	1827	148
2	-249	1799	160
3	36	1823	146
4	196	1793	165
5	252	1851	153
6	278	1824	164
7	50	1896	151
8	-282	1956	155
9	-258	1936	140
10	69	1965	141
11	103	1947	138
12	363	1982	142
13	110	2020	154





Table A.2 (cont.): Three-dimensional tracking particle coordinates for Run 10c  
(dimensions in mm).

t = 0.63 s

particle #	x	y	z
1	-326	1755	138
2	-250	1724	159
3	35	1749	167
4	195	1721	151
5	248	1777	165
6	282	1753	143
7	50	1828	147
8	-283	1894	141
9	-256	1870	135
10	69	1902	152
11	104	1885	134
12	373	1920	137
13	112	1968	135
14	-244	1993	145

t = 0.70 s

particle #	x	y	z
1	-330	1685	147
2	-250	1651	153
3	34	1678	161
4	193	1647	147
5	250	1704	159
6	282	1679	152
7	47	1761	139
8	-287	1830	137
9	-254	1801	154
10	66	1839	156
11	100	1820	138
12	377	1853	149
13	109	1911	139
14	-241	1937	132
15	91	2030	142
16	214	2018	139

t = 0.77 s

particle #	x	y	z
1	-336	1619	145
2	-251	1578	166
3	35	1605	159
4	190	1571	161
5	252	1630	163
6	286	1601	157
7	45	1690	168
8	-288	1760	151
9	-255	1732	153
10	64	1773	154
11	98	1750	152
12	393	1786	149
13	102	1849	165
14	-239	1876	151
15	86	1977	145
16	208	1959	150
17	-241	2012	142
18	206	2042	146

t = 0.83 s

particle #	x	y	z
1	-348	1554	137
2	-254	1503	155
3	38	1528	87
4	201	1492	84
5	267	1554	90
6	304	1525	87
7	44	1620	151
8	-292	1690	159
9	-255	1659	169
10	63	1706	148
11	93	1682	147
12	415	1718	130
13	99	1786	149
14	-241	1816	141
15	82	1925	142
16	205	1903	138
17	-236	1957	144
18	201	1986	147
19	211	2033	143



Table A.2 (cont.): Three-dimensional tracking particle coordinates for Run 10c  
(dimensions in mm).

$t = 0.90$  s

$t = 0.97$  s

particle #	x	y	z
1	-367	1480	71
2	-266	1417	81
3	39	1450	86
4	201	1409	88
5	276	1477	85
6	313	1448	77
7	49	1543	79
8	-301	1620	149
9	-262	1589	153
10	63	1635	145
11	90	1611	158
12	434	1650	137
13	94	1719	164
14	-242	1749	153
15	74	1866	146
16	205	1845	128
17	-235	1900	139
18	198	1930	151
19	204	1977	146
20	-24	2051	126
21	27	2032	136

particle #	x	y	z
1	-376	1410	73
2	-268	1337	79
3	37	1370	82
4	202	1329	76
5	281	1401	77
6	321	1371	78
7	45	1464	84
8	-312	1551	128
9	-273	1514	77
10	59	1566	166
11	94	1535	78
12	454	1581	138
13	91	1654	146
14	-245	1686	149
15	69	1807	144
16	204	1782	142
17	-238	1838	144
18	198	1872	147
19	201	1921	149
20	-20	2000	136
21	24	1982	147
22	191	2030	142



Table A.2 (cont.): Three-dimensional tracking particle coordinates for Run 10c  
(dimensions in mm).

t = 1.03 s

particle #	x	y	z
1	-388	1339	73
2	-277	1258	71
3	35	1289	73
4	204	1249	76
5	290	1324	74
6	330	1294	69
7	45	1388	83
8	-328	1475	76
9	-281	1438	74
10	62	1492	78
11	91	1459	81
12	489	1513	83
13	89	1586	159
14	-252	1617	153
15	64	1744	151
16	206	1715	143
17	-238	1775	172
18	195	1810	152
19	201	1863	139
20	-17	1951	148
21	22	1932	143
22	185	1976	145
23	-202	2037	138

t = 1.10 s

particle #	x	y	z
1	-401	1272	58
2	-288	1187	3
3	34	1208	78
4	210	1166	74
5	300	1245	67
6	340	1221	67
7	44	1307	80
8	-339	1399	72
9	-288	1360	68
10	61	1415	86
11	91	1382	80
12	515	1448	70
13	95	1513	88
14	-259	1551	146
15	65	1681	146
16	212	1653	148
17	-248	1715	144
18	199	1749	153
19	201	1804	144
20	-16	1902	154
21	20	1878	148
22	184	1921	141



Table A.2 (cont.): Three-dimensional tracking particle coordinates for Run 10c  
(dimensions in mm).

t = 1.17 s

particle #	x	y	z
1	-413	1207	57
2	-288	1105	67
3	34	1126	81
4	214	1089	71
5	306	1171	71
6	349	1152	65
7	44	1225	81
8	-350	1324	72
9	-298	1286	66
10	62	1337	81
11	92	1304	80
12	538	1384	63
13	99	1441	86
14	-265	1482	142
15	67	1616	173
16	213	1584	161
17	-257	1650	140
18	203	1687	149
19	205	1739	138
20	-20	1845	166
21	19	1821	160
22	183	1862	145
23	-188	1923	164
24	-273	2009	143
25	-121	1964	139
26	-102	2043	150

t = 1.23 s

particle #	x	y	z
1	-423	1147	54
2	-296	1034	59
3	33	1042	74
4	224	1015	10
5	315	1098	68
6	359	1085	55
7	44	1144	79
8	-363	1251	69
9	-310	1215	26
10	65	1259	80
11	96	1225	78
12	556	1326	69
13	106	1367	83
14	-282	1402	60
15	80	1545	97
16	232	1513	82
17	-263	1582	132
18	210	1621	154
19	211	1678	148
20	-22	1790	157
21	22	1764	160
22	188	1807	129
23	-193	1868	153
24	-270	1946	137
25	-120	1911	143
26	-99	1995	145
27	14	2026	157





Table A.2 (cont.): Three-dimensional tracking particle coordinates for Run 10c (dimensions in mm).

t = 1.30 s

particle #	x	y	z
1	-436	1088	54
2	-307	966	11
3	36	956	12
4	232	942	9
5	331	1031	14
6	376	1023	17
7	47	1063	89
8	-378	1178	62
9	-316	1134	73
10	70	1180	83
11	101	1145	79
12	582	1268	61
13	110	1294	77
14	-291	1333	71
15	85	1475	86
16	242	1443	79
17	-273	1519	148
18	228	1553	96
19	220	1613	147
20	-22	1732	150
21	24	1705	148
22	189	1742	152
23	-197	1809	145
24	-274	1885	140
25	-122	1856	133
26	-99	1954	56
27	17	1984	147

t = 1.37 s

particle #	x	y	z
1	-447	1029	56
2	-313	896	-2
3	36	871	15
4	234	874	9
5	340	964	5
6	393	957	2
7	55	976	11
8	-392	1106	62
9	-329	1062	65
10	74	1099	74
11	104	1064	75
12	604	1217	50
13	119	1213	75
14	-303	1259	70
15	91	1403	85
16	252	1371	81
17	-292	1444	73
18	243	1485	85
19	240	1545	91
20	-23	1671	154
21	25	1643	152
22	203	1681	148
23	-209	1749	146
24	-287	1825	123
25	-130	1800	140
26	-102	1895	155
27	16	1937	145
28	-45	2016	157



Table A.2 (cont.): Three-dimensional tracking particle coordinates for Run 10c  
(dimensions in mm).

t = 1.43 s

particle #	x	y	z
1	-467	972	2
2	-318	832	7
3	40	788	15
4	239	802	7
5	351	894	-21
6	397	895	13
7	57	891	6
8	-405	1038	65
9	-346	991	6
10	82	1020	14
11	114	986	22
12	619	1175	50
13	125	1139	84
14	-314	1188	80
15	97	1331	81
16	267	1301	79
17	-304	1373	74
18	257	1413	77
19	257	1476	78
20	-20	1609	145
21	25	1579	158
22	215	1618	154
23	-220	1687	141
24	-297	1760	138
25	-136	1739	156
26	-106	1837	152
27	16	1882	156
28	-43	1972	138
29	29	2044	146
30	224	2019	147
31	281	1986	156

t = 1.50 s

particle #	x	y	z
1	-480	917	1
2	-324	766	12
3	39	703	6
4	245	735	13
5	356	828	0
6	413	828	-4
7	60	810	18
8	-425	973	3
9	-357	920	13
10	87	940	19
11	123	901	17
12	639	1128	52
13	132	1060	76
14	-328	1116	73
15	100	1258	84
16	280	1228	74
17	-320	1300	75
18	273	1342	80
19	274	1405	74
20	-22	1543	102
21	30	1510	94
22	240	1553	96
23	-235	1623	154
24	-313	1698	147
25	-143	1679	144
26	-112	1781	144
27	16	1829	154
28	-42	1918	149
29	29	1997	150
30	226	1961	156
31	288	1926	151
32	244	2029	158



Table A.2 (cont.): Three-dimensional tracking particle coordinates for Run 10c  
(dimensions in mm).

t = 1.57 s

particle #	x	y	z
1	-490	860	1
2	-334	700	-1
3	44	619	13
4	251	666	14
5	364	763	4
6	423	767	12
7	63	722	15
8	-436	910	9
9	-369	848	3
10	92	853	-2
11	132	812	4
12	661	1078	52
13	144	982	17
14	-342	1044	73
15	106	1182	76
16	300	1154	75
17	-338	1228	56
18	292	1269	73
19	291	1333	78
20	-23	1476	87
21	33	1440	85
22	260	1486	82
23	-252	1561	154
24	-338	1636	125
25	-151	1617	148
26	-117	1721	167
27	15	1771	154
28	-43	1866	155
29	31	1951	140
30	235	1903	160
31	301	1862	147
32	254	1973	136
33	-78	2043	133

t = 1.63 s

particle #	x	y	z
1	-500	807	10
2	-340	639	7
3	47	533	2
4	260	598	10
5	373	697	3
6	435	714	9
7	69	635	-46
8	-447	847	5
9	-380	786	20
10	99	772	4
11	136	732	6
12	679	1030	64
13	154	900	11
14	-366	973	10
15	112	1108	73
16	317	1080	84
17	-358	1155	79
18	312	1195	77
19	309	1262	74
20	-25	1405	83
21	35	1371	76
22	277	1420	83
23	-272	1498	143
24	-358	1573	147
25	-159	1555	142
26	-124	1659	149
27	16	1712	163
28	-47	1808	153
29	32	1895	158
30	248	1845	151
31	324	1800	140
32	262	1910	147
33	-75	1991	144
34	96	2021	163
35	122	2034	151



Table A.2 (cont.): Three-dimensional tracking particle coordinates for Run 10c  
(dimensions in mm).

t = 1.70 s

particle #	x	y	z
1	-511	757	6
2	-345	576	-12
4	268	531	1
5	376	642	15
6	445	658	14
7	70	559	35
8	-457	788	14
9	-391	716	14
10	103	693	14
11	144	650	10
12	713	981	23
13	160	822	3
14	-384	904	4
15	121	1033	70
16	347	1005	9
17	-381	1084	74
18	331	1124	73
19	329	1190	75
20	-27	1335	81
21	36	1300	83
22	294	1349	75
23	-296	1425	78
24	-399	1505	57
25	-172	1485	76
26	-133	1598	148
27	17	1652	153
28	-49	1753	139
29	34	1842	149
30	267	1784	143
31	349	1739	136
32	277	1852	145
33	-74	1939	147
34	95	1977	144
35	122	1982	161
36	161	2030	157
37	95	2058	157

t = 1.77 s

particle #	x	y	z
1	-521	727	5
2	-353	520	-3
5	384	590	21
6	458	601	7
8	-472	730	6
9	-399	654	15
11	153	570	24
12	737	931	21
13	166	744	23
14	-401	834	8
15	128	956	24
16	366	928	15
17	-409	1012	19
18	350	1053	76
19	349	1118	75
20	-28	1264	74
21	40	1226	74
22	314	1278	74
23	-316	1355	71
24	-422	1440	75
25	-183	1417	80
26	-143	1532	91
27	18	1589	151
28	-51	1691	149
29	36	1784	156
30	283	1723	153
31	379	1675	134
32	292	1787	159
33	-75	1887	151
34	97	1923	163
35	125	1933	150
36	162	1982	145
37	96	2012	153





Table A.2 (cont.): Three-dimensional tracking particle coordinates for Run 10c  
(dimensions in mm).

t = 1.83 s

t = 1.90 s

particle #	x	y	z
1	-526	700	-3
5	397	528	9
6	475	540	1
8	-487	671	-1
9	-410	593	17
10	109	532	9
12	765	881	7
13	172	665	27
14	-422	762	8
15	138	877	14
16	383	852	17
17	-433	939	19
18	379	977	19
19	367	1047	79
20	-31	1192	76
21	41	1154	78
22	334	1208	67
23	-336	1287	77
24	-456	1372	69
25	-195	1346	71
26	-154	1464	83
27	21	1521	93
28	-53	1632	139
29	38	1727	143
30	310	1664	122
31	400	1612	157
32	318	1729	141
33	-79	1830	149
34	99	1869	160
35	130	1879	147
36	164	1926	149
37	98	1962	148
38	31	2013	147
39	31	2012	154

particle #	x	y	z
1	-519	691	45
9	-403	572	120
12	746	859	98
13	165	634	151
14	-412	731	138
15	128	835	149
16	370	812	150
17	-428	896	131
18	370	932	146
19	368	998	147
20	-32	1136	148
21	39	1101	155
22	334	1153	144
23	-340	1231	150
24	-466	1319	140
25	-200	1291	146
26	-159	1403	149
27	19	1460	156
28	-57	1566	152
29	40	1666	145
30	336	1594	123
31	439	1547	131
32	342	1664	139
33	-82	1772	156
34	102	1812	166
35	134	1824	146
36	171	1869	153
37	100	1909	146
38	7	1968	152
39	61	1958	148
40	131	2034	158



Table A.3: Three-dimensional tracking particle coordinates for Run 20d  
(dimensions in mm).

t = 0.37 s

particle #	x	y	z
1	-415	2024	68
2	-268	2040	94
3	-68	2028	81

t = 0.40 s

particle #	x	y	z
1	-422	1969	64
2	-268	1997	83
3	-68	1979	85
4	-344	2015	93
5	-216	2042	124
6	-189	2014	107
7	-101	2036	100
8	11	2049	100

t = 0.43 s

particle #	x	y	z
1	-429	1917	70
2	-260	1946	96
3	-66	1933	76
4	-341	1972	83
5	-214	2003	106
6	-190	1974	89
7	-99	1993	105
8	12	2007	97
9	98	2030	110
10	132	2033	102
11	237	2051	99

t = 0.47 s

particle #	x	y	z
1	-444	1862	70
2	-262	1901	62
3	-67	1880	99
4	-339	1917	88
5	-209	1955	118
6	-186	1923	94
7	-98	1946	103
8	13	1961	94
9	97	1987	115
10	131	1992	101
11	232	2004	113
12	-292	2024	108
13	-276	1982	89
14	-165	2040	121



Table A.3 (cont.): Three-dimensional tracking particle coordinates for Run 20d  
(dimensions in mm).

t = 0.50 s

particle #	x	y	z
1	-460	1812	73
2	-259	1849	77
3	-68	1836	66
4	-346	1869	70
5	-207	1913	93
6	-185	1872	91
7	-98	1895	108
8	10	1913	110
9	96	1946	98
10	128	1943	114
11	227	1958	118
12	-289	1978	96
13	-271	1929	109
14	-162	1998	117
15	-87	2025	105
16	227	2041	121
17	308	2043	115

t = 0.53 s

particle #	x	y	z
1	-487	1758	51
2	-258	1798	69
3	-67	1786	68
4	-351	1814	64
5	-203	1862	91
6	-182	1823	100
7	-97	1847	100
8	11	1867	94
9	93	1898	106
10	126	1900	98
11	228	1912	108
12	-284	1931	110
13	-271	1883	99
14	-157	1955	123
15	-85	1979	117
16	221	1994	134
17	301	1997	128
18	-15	2027	111

t = 0.57 s

particle #	x	y	z
1	-502	1708	56
2	-257	1744	71
3	-66	1733	93
4	-351	1761	79
5	-202	1812	91
6	-181	1775	85
7	-97	1801	101
8	9	1819	102
9	91	1852	97
10	122	1853	105
11	226	1867	85
12	-287	1886	101
13	-271	1836	91
14	-152	1911	106
15	-82	1939	108
16	216	1953	124
17	307	1959	96
18	-15	1993	103

t = 0.60 s

particle #	x	y	z
1	-525	1654	56
2	-260	1691	90
3	-65	1681	89
4	-357	1711	90
5	-199	1761	85
6	-174	1723	95
7	-94	1748	95
8	7	1766	102
9	89	1799	105
10	121	1805	74
11	222	1816	93
12	-292	1839	77
13	-272	1782	100
14	-151	1866	113
15	-79	1891	122
16	216	1912	101
17	308	1910	95
18	-14	1945	108



Table A.3 (cont.): Three-dimensional tracking particle coordinates for Run 20d  
(dimensions in mm).

$t = 0.63 \text{ s}$

particle #	x	y	z
1	-538	1603	70
2	-260	1639	79
3	-61	1625	103
4	-365	1660	72
5	-196	1708	95
6	-173	1670	83
7	-93	1699	91
8	8	1715	90
9	87	1751	95
10	117	1748	99
11	220	1764	95
12	-292	1788	78
13	-273	1729	101
14	-147	1816	105
15	-76	1843	121
16	213	1863	108
17	309	1861	95
18	-13	1906	93
19	-175	2007	129
20	113	2006	144
21	146	2018	123
22	10	2033	120

$t = 0.67 \text{ s}$

particle #	x	y	z
1	-561	1554	64
2	-262	1586	102
3	-60	1574	87
4	-372	1609	73
5	-195	1657	76
6	-171	1615	66
7	-90	1645	110
8	7	1668	87
9	85	1698	96
10	115	1699	104
11	224	1713	83
12	-294	1736	89
13	-278	1678	90
14	-145	1772	107
15	-74	1800	107
16	210	1817	102
17	309	1813	88
18	-15	1859	108
19	-170	1968	119
20	109	1969	136
21	137	1972	144
22	9	1988	141
23	-208	2024	127
24	102	2029	126





Table A.3 (cont.): Three-dimensional tracking particle coordinates for Run 20d  
(dimensions in mm).

$t = 0.70 \text{ s}$

particle #	x	y	z
1	-566	1509	110
2	-269	1533	71
3	-59	1520	72
4	-386	1555	63
5	-194	1605	82
6	-169	1567	81
7	-88	1593	102
8	7	1616	93
9	83	1648	101
10	113	1648	102
11	224	1659	88
12	-296	1684	99
13	-286	1626	81
14	-144	1722	94
15	-71	1752	94
16	211	1770	96
17	318	1766	84
18	-12	1816	93
19	-163	1924	117
20	104	1928	127
21	132	1934	129
22	9	1956	103
23	-200	1983	124
24	96	1990	124

$t = 0.73 \text{ s}$

particle #	x	y	z
1	-585	1460	100
2	-267	1483	123
3	-55	1470	115
4	-392	1501	66
5	-196	1555	82
6	-170	1514	67
7	-87	1542	118
8	8	1565	93
9	86	1596	85
10	112	1597	93
11	234	1606	50
12	-305	1632	82
13	-290	1572	80
14	-143	1671	90
15	-70	1702	105
16	213	1721	84
17	327	1717	64
18	-13	1765	111
19	-159	1881	108
20	96	1886	126
21	127	1892	128
22	6	1912	117
23	-196	1945	108
24	91	1954	123
25	-266	2024	106



Table A.3 (cont.): Three-dimensional tracking particle coordinates for Run 20d  
(dimensions in mm).

$t = 0.77 \text{ s}$

particle #	x	y	z
1	-609	1413	95
2	-281	1427	78
3	-57	1416	113
4	-397	1454	99
5	-197	1501	84
6	-168	1462	86
7	-86	1491	130
8	6	1513	124
9	85	1546	93
10	110	1546	94
11	234	1555	82
12	-312	1578	82
13	-297	1520	82
14	-141	1618	103
15	-68	1651	102
16	212	1669	120
17	334	1668	55
18	-11	1718	107
19	-159	1839	108
20	93	1849	97
21	119	1851	127
22	4	1871	133
23	-195	1903	106
24	87	1914	117
25	-263	1979	103
26	-230	2037	124

$t = 0.80 \text{ s}$

particle #	x	y	z
1	-628	1363	93
2	-281	1378	110
3	-55	1363	114
4	-408	1402	101
5	-197	1451	112
6	-169	1411	98
7	-85	1435	124
8	5	1461	130
9	85	1495	72
10	113	1495	81
11	234	1504	120
12	-321	1529	75
13	-305	1468	84
14	-142	1567	96
15	-66	1602	116
16	223	1618	73
17	340	1611	85
18	-13	1669	119
19	-159	1794	94
20	87	1799	120
21	116	1809	107
22	5	1828	125
23	-196	1858	114
24	83	1873	126
25	-268	1938	78
26	-224	1989	142



Table A.3 (cont.): Three-dimensional tracking particle coordinates for Run 20d  
(dimensions in mm).

$t = 0.83 \text{ s}$

particle #	x	y	z
1	-646	1317	92
2	-288	1326	105
3	-53	1308	124
4	-419	1351	105
5	-199	1398	120
6	-170	1356	86
7	-86	1384	123
8	6	1409	125
9	81	1440	133
10	108	1439	139
11	242	1453	113
12	-328	1472	85
13	-312	1416	74
14	-142	1515	97
15	-66	1548	109
16	227	1565	73
17	350	1562	63
18	-10	1621	101
19	-160	1744	112
20	86	1755	108
21	117	1762	101
22	3	1781	141
23	-201	1812	107
24	82	1827	117
25	-268	1888	100
26	-225	1956	103
27	-245	2025	114

$t = 0.87 \text{ s}$

particle #	x	y	z
1	-669	1268	87
2	-293	1275	100
3	-53	1255	118
4	-432	1300	100
5	-207	1345	103
6	-173	1308	106
7	-87	1332	120
8	6	1353	129
9	83	1386	134
10	109	1387	134
11	246	1399	114
12	-341	1418	68
13	-319	1364	80
14	-141	1463	121
15	-65	1497	133
16	223	1516	119
17	347	1511	114
18	-11	1570	102
19	-163	1696	93
20	86	1708	105
21	116	1713	112
22	4	1738	122
23	-204	1766	109
24	78	1780	126
25	-273	1842	92
26	-224	1909	117
27	-244	1985	104



Table A.3 (cont.): Three-dimensional tracking particle coordinates for Run 20d  
(dimensions in mm).

$t = 0.90 \text{ s}$

particle #	x	y	z
1	-677	1221	106
2	-300	1220	104
3	-52	1197	116
4	-443	1246	112
5	-211	1292	101
6	-175	1255	120
7	-88	1278	119
8	5	1299	130
9	87	1331	125
10	114	1334	122
11	253	1346	108
12	-347	1367	81
13	-330	1310	71
14	-146	1411	128
15	-66	1446	128
16	231	1466	115
17	358	1459	111
18	-9	1519	110
19	-165	1646	106
20	86	1662	94
21	120	1669	95
22	5	1688	125
23	-207	1718	111
24	80	1736	106
25	-280	1795	101
26	-229	1868	101
27	-241	1939	116

$t = 0.93 \text{ s}$

particle #	x	y	z
1	-696	1177	105
2	-304	1166	117
3	-53	1143	120
4	-461	1193	85
5	-213	1242	104
6	-178	1197	137
7	-88	1224	122
8	7	1242	120
9	90	1278	113
10	118	1280	114
11	260	1291	110
12	-353	1320	100
13	-327	1261	117
14	-152	1357	105
15	-69	1387	99
16	237	1411	115
17	371	1409	103
18	-10	1470	128
19	-170	1597	104
20	90	1613	93
21	120	1620	130
22	5	1642	109
23	-213	1674	110
24	82	1688	125
25	-290	1750	90
26	-231	1821	102
27	-245	1896	101





Table A.3 (cont.): Three-dimensional tracking particle coordinates for Run 20d  
(dimensions in mm).

$t = 0.97 \text{ s}$

particle #	x	y	z
1	-722	1134	82
2	-315	1115	103
3	-52	1087	116
4	-472	1146	101
5	-220	1188	107
6	-184	1148	104
7	-91	1168	116
8	7	1188	112
9	97	1223	105
10	122	1225	109
11	265	1239	116
12	-367	1268	90
13	-339	1212	110
14	-159	1306	112
15	-74	1338	120
16	245	1359	111
17	381	1355	99
18	-9	1415	131
19	-180	1549	97
20	94	1561	86
21	127	1567	108
22	6	1592	107
23	-223	1626	100
24	85	1642	101
25	-302	1702	85
26	-241	1776	74
27	-251	1850	100

$t = 1.00 \text{ s}$

particle #	x	y	z
1	-743	1093	82
2	-324	1060	102
3	-54	1029	169
4	-490	1095	94
5	-226	1135	107
6	-186	1095	110
7	-96	1115	114
8	5	1134	117
9	100	1166	111
10	128	1168	108
11	276	1184	110
12	-372	1216	105
13	-348	1158	109
14	-163	1252	115
15	-78	1286	122
16	252	1307	106
17	395	1303	95
18	-9	1362	126
19	-181	1498	132
20	94	1513	137
21	129	1520	129
22	8	1543	123
23	-232	1575	100
24	90	1593	122
25	-314	1653	68
26	-244	1726	107
27	-258	1803	93



Table A.4: Three-dimensional tracking particle coordinates for Run 30b  
(dimensions in mm).

$t = 0.40$  s

particle #	x	y	z
1	266	2065	85

$t = 0.43$  s

particle #	x	y	z
1	258	2008	88
2	49	2022	100

$t = 0.47$  s

particle #	x	y	z
1	256	1954	67
2	48	1968	86
3	16	2023	84
4	-5	2052	100

$t = 0.50$  s

particle #	x	y	z
1	253	1891	57
2	48	1907	74
3	17	1972	71
4	-4	2006	80
5	-235	2011	92
6	50	2034	95
7	174	2033	110
8	242	2033	118

$t = 0.53$  s

particle #	x	y	z
1	246	1825	71
2	44	1852	81
3	16	1912	84
4	-4	1952	76
5	-228	1954	102
6	50	1984	99
7	170	1987	99
8	242	1979	99
9	-123	2027	107

$t = 0.57$  s

particle #	x	y	z
1	244	1764	49
2	43	1792	57
3	15	1846	97
4	-2	1895	82
5	-226	1901	76
6	51	1932	79
7	163	1928	119
8	232	1925	103
9	-116	1978	103
10	-7	2044	115



Table A.4 (cont.): Three-dimensional tracking particle coordinates for Run 30b  
(dimensions in mm).

$t = 0.60$  s

particle #	x	y	z
1	240	1698	67
2	41	1726	105
3	16	1790	96
4	-3	1839	72
5	-223	1841	73
6	47	1873	85
7	160	1876	94
8	229	1868	93
9	-113	1926	91
10	-3	1993	119
11	-305	2041	122
12	-266	2023	106
13	-207	2023	102

$t = 0.63$  s

particle #	x	y	z
1	242	1632	57
2	42	1664	71
3	15	1727	98
4	-3	1775	72
5	-220	1780	73
6	46	1817	68
7	156	1816	84
8	227	1809	68
9	-107	1867	103
10	-2	1944	107
11	-307	1992	92
12	-261	1973	85
13	-196	1967	120
14	-174	2031	127
15	-14	2053	126
16	20	2052	132
17	47	2029	142

$t = 0.67$  s

particle #	x	y	z
1	250	1563	35
2	41	1598	62
3	16	1667	71
4	-3	1713	89
5	-221	1716	58
6	43	1754	84
7	152	1756	77
8	228	1747	54
9	-102	1814	87
10	-2	1887	126
11	-308	1938	72
12	-255	1913	96
13	-190	1914	108
14	-162	1979	137
15	-14	2010	107
16	22	2005	129
17	50	1985	115
18	-270	2057	107
19	-150	2034	135
20	3	2049	133

$t = 0.70$  s

particle #	x	y	z
1	249	1496	78
2	38	1533	63
3	15	1605	79
4	-4	1650	78
5	-223	1649	70
6	42	1693	95
7	152	1690	64
8	227	1680	58
9	-97	1751	95
10	0	1834	111
11	-315	1877	69
12	-260	1857	77
13	-188	1867	67
14	-151	1928	132
15	-10	1957	118
16	23	1955	132
17	48	1934	127
18	-268	2016	71
19	-141	1989	106
20	2	2003	129
21	148	2048	137



Table A.4 (cont.): Three-dimensional tracking particle coordinates for Run 30b  
(dimensions in mm).

$t = 0.73 \text{ s}$

particle #	x	y	z
1	252	1429	83
2	38	1469	101
3	14	1540	94
4	1	1583	77
5	-229	1582	53
6	44	1628	77
7	150	1628	70
8	231	1618	56
9	-93	1691	82
10	1	1778	103
11	-327	1820	45
12	-263	1798	69
13	-185	1805	81
14	-150	1881	84
15	-10	1901	137
16	22	1904	137
17	43	1882	117
18	-263	1959	57
19	-130	1932	125
20	6	1954	118
21	139	2006	136
22	-274	2012	88

$t = 0.77 \text{ s}$

particle #	x	y	z
1	261	1358	71
2	38	1401	99
3	14	1477	111
4	-2	1522	105
5	-236	1514	46
6	44	1563	85
7	151	1560	78
8	236	1552	58
9	-92	1626	79
10	0	1719	112
11	-339	1758	37
12	-271	1737	63
13	-184	1746	105
14	-147	1825	106
15	-11	1853	121
16	20	1851	135
17	43	1831	109
18	-262	1897	77
19	-123	1882	114
20	6	1901	144
21	126	1960	140
22	-271	1957	82
23	-290	2030	110





Table A.4 (cont.): Three-dimensional tracking particle coordinates for Run 30b  
(dimensions in mm).

t = 0.80 s

particle #	x	y	z
1	264	1294	80
2	39	1334	109
3	14	1416	100
4	-3	1458	117
5	-240	1450	81
6	43	1498	124
7	148	1496	112
8	239	1485	84
9	-93	1563	79
10	2	1659	109
11	-353	1693	41
12	-282	1674	58
13	-191	1686	62
14	-145	1766	99
15	-10	1795	135
16	21	1797	127
17	42	1771	132
18	-268	1840	68
19	-120	1829	98
20	3	1846	142
21	123	1910	145
22	-270	1899	87
23	-291	1979	80

t = 0.83 s

particle #	x	y	z
1	279	1223	64
2	40	1266	90
3	15	1345	106
4	-3	1390	108
5	-254	1378	57
6	45	1433	117
7	156	1428	93
8	252	1418	76
9	-91	1500	112
10	3	1597	115
11	-366	1630	46
12	-289	1614	64
13	-196	1625	75
14	-148	1709	77
15	-7	1741	129
16	23	1739	136
17	41	1714	119
18	-273	1777	75
19	-117	1773	98
20	6	1795	135
21	121	1861	129
22	-276	1839	76
23	-290	1922	84
24	-252	2018	80
25	112	1570	78
26	143	1575	71



Table A.4 (cont.): Three-dimensional tracking particle coordinates for Run 30b  
(dimensions in mm).

$t = 0.87$  s

particle #	x	y	z
1	284	1155	61
2	41	1195	89
3	15	1276	108
4	-3	1328	109
5	-262	1314	51
6	46	1364	109
7	164	1362	88
8	259	1354	71
9	-95	1434	105
10	7	1530	63
11	-379	1567	55
12	-302	1549	50
13	-204	1558	51
14	-153	1648	74
15	-7	1684	111
16	22	1683	132
17	42	1656	108
18	-285	1714	77
19	-121	1713	92
20	5	1743	115
21	125	1807	121
22	-287	1777	68
23	-299	1861	74
24	-248	1961	98
25	116	1508	111
26	145	1512	101
27	-269	2023	90
28	-121	2020	161



Table A.5: Three-dimensional tracking particle coordinates for Run 30d  
(dimensions in mm).

$t = 0.43 \text{ s}$

particle #	x	y	z
1	-74	2004	131
2	428	2009	84

$t = 0.47 \text{ s}$

particle #	x	y	z
1	-73	1953	95
2	440	1951	82
3	-207	2002	129

$t = 0.50 \text{ s}$

particle #	x	y	z
1	-72	1891	138
2	461	1892	89
3	-198	1949	148
4	-314	2032	138
5	-181	2013	156

$t = 0.53 \text{ s}$

particle #	x	y	z
1	-70	1836	120
2	488	1837	67
3	-197	1894	150
4	-311	1978	138
5	-176	1964	157
6	-231	2036	163
7	-140	2023	155

$t = 0.57 \text{ s}$

particle #	x	y	z
1	-68	1777	105
2	521	1773	63
3	-193	1833	132
4	-309	1920	140
5	-172	1911	145
6	-222	1993	137
7	-137	1973	149
8	-352	2039	118

$t = 0.60 \text{ s}$

particle #	x	y	z
1	-67	1714	143
2	549	1715	70
3	-192	1771	124
4	-315	1864	123
5	-168	1858	136
6	-214	1937	146
7	-129	1918	152
8	-351	1984	128

$t = 0.63 \text{ s}$

particle #	x	y	z
1	-65	1654	139
2	580	1653	71
3	-191	1709	133
4	-320	1803	114
5	-164	1796	156
6	-208	1881	149
7	-124	1864	157
8	-362	1934	109

$t = 0.67 \text{ s}$

particle #	x	y	z
1	-64	1591	124
2	608	1593	82
3	-191	1644	121
4	-330	1743	100
5	-160	1735	141
6	-202	1823	168
7	-120	1806	183
8	-375	1876	99



Table A.5 (cont.): Three-dimensional tracking particle coordinates for Run 30d  
(dimensions in mm).

$t = 0.70 \text{ s}$

particle #	x	y	z
1	-62	1524	132
2	644	1535	72
3	-192	1580	127
4	-338	1682	110
5	-160	1674	144
6	-205	1767	153
7	-119	1749	169
8	-391	1817	106
9	-233	2007	171

$t = 0.73 \text{ s}$

particle #	x	y	z
1	-63	1463	178
2	654	1484	122
3	-195	1519	158
4	-348	1618	116
5	-162	1610	120
6	-208	1706	133
7	-118	1691	157
8	-411	1762	93
9	-229	1960	152
10	70	1977	205
11	72	2016	200

$t = 0.77 \text{ s}$

particle #	x	y	z
1	-63	1398	172
2	682	1431	119
3	-196	1459	167
4	-363	1555	116
5	-165	1544	119
6	-212	1648	131
7	-115	1631	154
8	-429	1703	96
9	-221	1906	162
10	68	1933	187
11	70	1972	189

$t = 0.80 \text{ s}$

particle #	x	y	z
1	-64	1333	155
2	715	1383	107
3	-204	1395	156
4	-369	1494	143
5	-163	1488	158
6	-217	1582	136
7	-116	1569	132
8	-457	1646	65
9	-227	1850	145
10	62	1882	184
11	63	1928	179





Table A.5 (cont.): Three-dimensional tracking particle coordinates for Run 30d  
(dimensions in mm).

$t = 0.83 \text{ s}$

particle #	x	y	z
1	-68	1268	166
2	743	1336	109
3	-210	1330	152
4	-383	1429	136
5	-172	1421	149
6	-226	1520	122
7	-117	1507	162
8	-476	1585	88
9	-231	1794	144
10	59	1830	198
11	58	1874	191

$t = 0.87 \text{ s}$

particle #	x	y	z
1	-71	1202	164
2	772	1289	104
3	-218	1266	151
4	-403	1365	135
5	-178	1357	167
6	-230	1462	156
7	-122	1444	172
8	-503	1527	77
9	-240	1736	132
10	59	1778	191
11	52	1821	203
12	-249	1980	150
13	133	1977	189

$t = 0.90 \text{ s}$

particle #	x	y	z
1	-77	1133	168
2	801	1241	102
3	-229	1200	150
4	-420	1304	127
5	-185	1295	169
6	-240	1396	161
7	-130	1380	167
8	-513	1472	120
9	-248	1675	148
10	59	1723	192
11	52	1770	182
12	-246	1928	138
13	128	1933	165
14	127	1990	202



## **APPENDIX B**

**Three-dimensional tracking particle coordinates for experiments performed with tailwater.** (See Figure 3.1 for coordinate system.)



Table B.1: Three-dimensional tracking particle coordinates for Run 30-5d  
(dimensions in mm).

t = 0.10 s				t = 0.13 s			
particle #	x	y	z	particle #	x	y	z
1	277	1229	48	1	277	1229	48
2	14	1291	48	2	15	1291	47
3	-106	1378	54	3	-107	1378	54
4	155	1408	48	4	155	1408	48
5	402	1441	58	5	403	1441	58
6	-228	1495	46	6	-227	1497	52
7	-128	1495	46	7	-127	1495	54
8	-106	1544	54	8	-106	1544	54
9	-444	1610	45	9	-443	1610	44
10	160	1620	55	10	163	1617	55
11	187	1673	57	11	188	1672	42
12	238	1735	63	12	238	1735	63
13	220	1783	50	13	220	1783	50
14	-504	1732	41	14	-506	1732	41
15	-255	1799	61	15	-255	1799	61
16	-634	1903	47	16	-632	1902	48
17	-568	1848	47	17	-564	1847	63
18	-119	1923	58	18	-118	1923	59
19	80	1911	68	19	81	1915	52
20	76	1947	58	20	77	1947	59
21	127	1929	55	21	128	1929	54
22	362	1915	58	22	364	1915	57
23	661	1920	61	23	663	1920	60
24	-463	2047	62	24	-467	2047	62
25	13	2045	65	25	13	2041	64
26	72	2018	57	26	73	2015	57
27	312	2074	73	27	313	2066	87
28	343	2078	73	28	343	2069	90
29	542	2042	55	29	542	2042	55
30	607	2107	76	30	607	2107	76



Table B.1 (cont.): Three-dimensional tracking particle coordinates for Run 30-5d  
(dimensions in mm).

t = 0.17 s				t = 0.20 s			
particle #	x	y	z	particle #	x	y	z
1	277	1229	48	1	277	1229	48
2	14	1290	48	2	14	1290	48
3	-108	1379	54	3	-107	1378	47
4	156	1407	49	4	157	1407	41
5	403	1440	59	5	403	1441	58
6	-227	1497	52	6	-226	1495	53
7	-127	1494	47	7	-126	1494	47
8	-106	1544	54	8	-106	1544	54
9	-443	1610	44	9	-443	1610	44
10	163	1617	55	10	163	1617	55
11	190	1672	41	11	188	1669	57
12	238	1735	63	12	237	1735	62
13	220	1783	50	13	222	1783	34
14	-504	1732	41	14	-502	1732	57
15	-254	1799	61	15	-257	1799	45
16	-628	1902	63	16	-634	1906	48
17	-564	1847	63	17	-570	1848	31
18	-118	1923	59	18	-119	1920	58
19	81	1915	52	19	85	1912	52
20	79	1943	59	20	79	1943	59
21	128	1926	53	21	128	1926	53
22	362	1915	58	22	364	1915	57
23	663	1920	60	23	657	1916	76
24	-471	2044	61	24	-484	2037	61
25	12	2030	78	25	15	2013	90
26	75	2008	55	26	75	1994	68
27	315	2060	85	27	315	2048	101
28	342	2058	103	28	346	2052	102
29	543	2042	57	29	538	2039	73
30	607	2107	76	30	607	2107	76





Table B.1 (cont.): Three-dimensional tracking particle coordinates for Run 30-5d  
(dimensions in mm).

$t = 0.23 \text{ s}$

particle #	x	y	z
1	277	1229	48
2	14	1290	48
3	-107	1378	47
4	157	1407	41
5	403	1441	58
6	-226	1495	53
7	-126	1494	47
8	-106	1544	54
9	-443	1610	44
10	163	1617	55
11	188	1669	57
12	237	1735	62
13	222	1783	34
14	-502	1732	57
15	-257	1799	45
16	-629	1902	64
17	-566	1847	63
18	-118	1914	57
19	85	1906	51
20	78	1931	55
21	127	1915	68
22	367	1909	56
23	663	1920	60
24	-491	2037	62
10	17	1995	103
26	77	1972	64
27	315	2034	112
28	348	2040	98
29	546	2045	58
30	614	2113	61

$t = 0.27 \text{ s}$

particle #	x	y	z
1	277	1229	48
2	14	1290	48
3	-107	1378	47
4	157	1407	41
5	403	1441	58
6	-226	1495	53
7	-126	1494	47
8	-106	1544	54
9	-443	1610	44
10	163	1617	55
11	188	1669	57
12	237	1735	62
13	222	1783	34
14	-502	1732	57
15	-257	1799	45
16	-634	1906	48
17	-568	1851	47
18	-117	1891	53
19	85	1890	48
20	80	1911	68
21	131	1896	64
22	374	1896	56
23	663	1920	60
24	-504	2033	62
25	17	1975	114
26	75	1944	91
27	320	2026	95
28	355	2035	63
29	548	2040	74
30	611	2107	76



Table B.1 (cont.): Three-dimensional tracking particle coordinates for Run 30-5d  
(dimensions in mm).

$t = 0.30 \text{ s}$

particle #	x	y	z
1	277	1229	48
2	14	1290	48
3	-107	1378	47
4	157	1407	41
5	403	1441	58
6	-226	1495	53
7	-126	1494	47
8	-106	1544	54
9	-443	1610	44
10	163	1617	55
11	188	1669	57
12	237	1735	62
13	222	1783	34
14	-502	1732	57
15	-258	1795	45
16	-634	1906	48
17	-568	1851	47
18	-121	1867	32
19	85	1870	61
21	132	1868	60
22	383	1870	51
23	663	1920	60
24	-510	2028	79
25	20	1960	111
26	75	1915	101
27	318	2014	94
28	363	2011	40
29	562	2041	61
30	612	2107	77

$t = 0.33 \text{ s}$

particle #	x	y	z
1	277	1229	48
2	14	1290	48
3	-107	1378	47
4	157	1407	41
5	403	1441	58
6	-226	1495	53
7	-126	1494	47
8	-106	1544	54
9	-443	1610	44
10	163	1617	55
11	188	1669	57
12	241	1731	46
13	220	1773	49
14	-507	1732	42
15	-260	1783	43
16	-629	1905	64
17	-569	1847	63
18	-117	1820	59
19	80	1834	87
21	133	1826	70
22	391	1835	63
23	663	1920	60
24	-527	2033	64
25	23	1940	122
26	76	1887	96
27	323	2003	105
29	564	2035	92
30	615	2107	78
31	304	2077	72



Table B.1 (cont.): Three-dimensional tracking particle coordinates for Run 30-5d  
(dimensions in mm).

$t = 0.37 \text{ s}$

particle #	x	y	z
1	277	1229	48
2	14	1290	48
3	-107	1378	47
4	157	1407	41
5	403	1441	58
6	-226	1495	53
7	-126	1494	47
8	-106	1544	54
9	-443	1610	44
10	163	1611	55
11	188	1666	57
12	242	1721	47
13	224	1750	47
14	-506	1729	57
15	-269	1753	24
16	-636	1905	65
17	-577	1844	63
18	-115	1776	36
19	85	1767	62
20	79	1802	82
21	133	1778	64
22	398	1789	77
23	666	1920	60
24	-535	2029	64
25	24	1923	103
26	76	1855	106
27	332	1994	106
29	580	2040	79
30	622	2107	78
31	308	2063	34

$t = 0.40 \text{ s}$

particle #	x	y	z
1	278	1225	48
2	11	1287	42
3	-109	1380	47
4	157	1399	46
5	404	1442	51
6	-226	1497	53
7	-127	1495	54
8	-108	1548	55
9	-443	1608	60
10	165	1609	39
11	190	1662	41
12	245	1708	28
14	-510	1726	58
15	-269	1699	67
16	-639	1900	81
17	-593	1837	64
18	-113	1719	78
19	90	1712	43
20	81	1754	77
21	132	1724	75
22	413	1744	57
23	669	1920	60
24	-545	2029	66
26	73	1823	131
27	339	1981	103
29	596	2041	79
30	633	2114	61
31	311	2022	23
32	-354	2075	-13



Table B.1 (cont.): Three-dimensional tracking particle coordinates for Run 30-5d  
(dimensions in mm).

t = 0.43 s

particle #	x	y	z
1	278	1225	48
2	11	1287	42
3	-109	1380	47
4	157	1399	46
5	404	1442	51
6	-226	1497	53
7	-127	1495	54
8	-108	1548	55
9	-443	1608	60
10	164	1604	55
11	199	1648	27
12	250	1661	10
14	-525	1716	58
15	-274	1646	33
16	-657	1897	83
17	-635	1831	36
18	-113	1664	59
21	136	1672	56
22	427	1696	55
23	673	1915	80
24	-553	2032	67
26	70	1795	127
27	346	1971	85
29	603	2040	81
30	639	2113	65
31	301	1974	35
32	-352	2024	-9
33	-453	2085	-40
34	-323	2064	18
35	444	2102	-45

t = 0.47 s

particle #	x	y	z
1	279	1225	48
2	12	1286	48
3	-110	1379	40
4	157	1398	47
5	408	1444	51
6	-225	1497	60
7	-126	1496	62
8	-108	1545	62
9	-454	1602	28
10	89	1585	39
11	136	1613	54
12	203	1604	41
14	-548	1689	58
16	-675	1896	86
17	-663	1817	36
18	-112	1606	57
21	83	1663	87
22	444	1643	37
23	687	1915	83
24	-559	2035	69
27	359	1961	48
29	609	2044	80
32	-355	1973	-2
33	-473	2036	-91
34	-331	2014	-32
35	445	2043	-38
36	-341	2083	25
37	339	2102	25





Table B.1 (cont.): Three-dimensional tracking particle coordinates for Run 30-5d  
(dimensions in mm).

$t = 0.50 \text{ s}$

particle #	x	y	z
1	280	1225	48
2	11	1286	48
3	-109	1380	47
4	157	1395	54
5	406	1443	59
6	-226	1493	60
7	-128	1493	61
8	-110	1526	74
9	-459	1582	60
10	90	1517	41
11	135	1558	55
14	-575	1653	59
16	-708	1894	72
21	82	1618	85
22	459	1594	39
23	700	1912	99
24	-562	2035	69
27	374	1940	29
29	614	2045	79
35	458	1989	-46
36	-340	2034	-5
37	340	2056	-3

$t = 0.53 \text{ s}$

particle #	x	y	z
1	280	1225	48
2	10	1285	41
3	-109	1380	47
4	157	1394	47
5	406	1443	59
6	-228	1476	79
9	-476	1554	46
10	94	1445	-21
11	139	1496	26
14	-603	1606	43
16	-723	1886	90
21	83	1571	85
22	465	1538	82
23	725	1912	105
24	-570	2040	54
27	390	1917	27
29	616	2048	79
35	491	1928	-51
36	-340	1979	-20
37	338	1999	-13

$t = 0.57 \text{ s}$

particle #	x	y	z
1	280	1225	48
2	11	1285	41
3	-113	1374	47
4	158	1384	60
5	410	1437	59
11	140	1428	16
16	-753	1882	93
21	87	1521	71
22	484	1477	67
23	748	1909	107
24	-570	2045	39
27	404	1880	55
29	617	2051	81
35	501	1878	11
36	-349	1922	-32
37	343	1943	-26

$t = 0.60 \text{ s}$

particle #	x	y	z
1	280	1225	48
2	13	1276	28
3	-108	1351	42
4	161	1372	67
5	415	1428	66
16	-781	1882	81
21	83	1480	120
22	493	1423	53
23	774	1913	111
24	-567	2046	37
27	427	1852	37
29	619	2056	65
35	522	1851	28
36	-362	1869	-41
37	346	1885	1
38	80	2051	50



Table B.2: Three-dimensional tracking particle coordinates for Run 30-10a (dimensions in mm).

t = 0.20 s

particle #	x	y	z
1	-91	1412	98
2	151	1443	100
3	-249	1553	108
4	-167	1521	109
5	-147	1489	103
6	-42	1491	106
7	224	1546	105
8	22	1620	115
9	197	1656	104
10	229	1704	107
11	163	1778	96
12	299	1769	114
13	-696	1876	102
14	-498	1825	102
15	-182	1809	105
16	-264	1955	105
17	173	1919	117
18	392	1912	122
19	75	2058	117

t = 0.23 s

particle #	x	y	z
1	-93	1412	98
2	151	1443	100
3	-249	1553	108
4	-167	1521	109
5	-146	1489	103
6	-41	1491	106
7	224	1546	105
8	22	1620	115
9	196	1653	103
10	229	1704	107
11	164	1778	111
12	301	1769	98
13	-696	1876	102
14	-500	1825	101
15	-182	1809	105
16	-264	1950	121
17	173	1919	117
18	393	1912	123
19	77	2053	132

t = 0.27 s

particle #	x	y	z
1	-93	1412	98
2	151	1443	100
3	-249	1553	108
4	-167	1521	109
5	-146	1489	103
6	-41	1491	106
7	224	1546	105
8	22	1620	115
9	196	1653	103
10	229	1704	107
11	164	1775	111
12	303	1769	99
13	-697	1876	102
14	-500	1825	101
15	-182	1806	120
16	-267	1949	104
17	177	1917	102
18	399	1913	107
19	77	2048	146

t = 0.30 s

particle #	x	y	z
1	-93	1412	98
2	151	1443	100
3	-249	1553	108
4	-167	1521	109
5	-146	1489	103
6	-41	1491	106
7	224	1546	105
8	22	1620	115
9	196	1653	103
10	229	1704	107
11	164	1775	111
12	303	1769	99
13	-697	1876	102
14	-502	1825	102
15	-183	1806	106
16	-267	1935	118
17	175	1906	130
18	402	1907	106
19	77	2045	146



Table B.2 (cont.): Three-dimensional tracking particle coordinates for Run 30-10a (dimensions in mm).

$t = 0.33 \text{ s}$

particle #	x	y	z
1	-92	1411	104
2	152	1442	100
3	-250	1553	108
4	-165	1521	109
5	-146	1489	103
6	-41	1491	106
7	223	1546	104
8	25	1618	100
9	197	1653	103
10	231	1704	107
11	166	1772	110
12	302	1765	115
13	-697	1876	102
14	-503	1825	102
15	-183	1803	105
16	-269	1921	130
17	180	1897	115
18	410	1901	106
19	76	2035	175

$t = 0.37 \text{ s}$

particle #	x	y	z
1	-92	1411	104
2	152	1442	100
3	-250	1553	108
4	-165	1521	109
5	-146	1489	103
6	-41	1491	106
7	223	1546	104
8	25	1618	100
9	199	1653	103
10	229	1701	106
11	168	1769	111
12	306	1762	99
13	-692	1872	117
14	-503	1818	116
15	-184	1793	119
16	-273	1906	127
17	182	1882	111
18	415	1887	122
19	77	2034	159

$t = 0.40 \text{ s}$

particle #	x	y	z
1	-92	1411	104
2	152	1442	100
3	-250	1553	108
4	-165	1521	109
5	-146	1489	103
6	-41	1491	106
7	223	1546	104
8	25	1618	100
9	199	1650	103
10	233	1698	106
11	168	1760	110
12	302	1765	115
13	-694	1872	117
14	-511	1815	101
15	-183	1781	117
16	-271	1884	138
17	184	1863	123
18	421	1871	135
19	77	2026	172

$t = 0.43 \text{ s}$

particle #	x	y	z
1	-93	1410	97
2	151	1442	100
3	-250	1552	93
4	-167	1521	109
5	-149	1489	103
6	-43	1491	106
7	224	1543	105
8	24	1613	115
9	199	1647	103
10	236	1692	108
11	171	1747	108
12	315	1743	98
13	-702	1876	102
14	-517	1805	116
15	-185	1765	115
16	-266	1863	195
17	184	1838	136
18	436	1856	119
19	77	2020	171



Table B.2 (cont.): Three-dimensional tracking particle coordinates for Run 30-10a  
(dimensions in mm).

$t = 0.47 \text{ s}$

particle #	x	y	z
1	-93	1410	97
2	151	1442	100
3	-250	1552	93
4	-167	1521	109
5	-149	1489	103
6	-43	1491	106
7	224	1543	105
8	24	1610	116
9	200	1642	118
10	240	1682	91
11	175	1728	107
12	320	1728	96
13	-702	1872	118
14	-532	1799	100
15	-188	1740	112
16	-281	1847	117
17	185	1813	146
18	450	1838	118
19	75	2014	168

$t = 0.50 \text{ s}$

particle #	x	y	z
1	-93	1410	97
2	151	1442	100
3	-250	1552	93
4	-167	1521	109
5	-149	1489	103
6	-43	1491	106
7	224	1543	105
8	26	1601	115
9	204	1631	102
10	243	1666	91
11	179	1703	105
12	325	1706	111
13	-712	1872	103
14	-548	1783	100
15	-188	1707	139
16	-285	1822	129
17	191	1788	128
18	456	1812	145
19	75	2007	152
20	-460	2083	18
21	-418	2077	-8
22	-371	2064	40
23	-172	2033	120
24	407	2083	78





Table B.2 (cont.): Three-dimensional tracking particle coordinates for Run 30-10a  
(dimensions in mm).

$t = 0.53 \text{ s}$

particle #	x	y	z
1	-93	1408	104
2	152	1438	106
3	-253	1541	108
4	-168	1511	115
5	-150	1483	109
6	-43	1485	105
7	229	1534	106
8	27	1587	100
9	205	1614	118
10	250	1644	90
11	179	1673	118
12	335	1680	95
13	-715	1868	119
14	-561	1764	115
15	-195	1680	108
16	-290	1803	113
17	193	1761	140
18	473	1797	129
19	74	1996	165
23	-195	2045	-25
24	421	2060	58
25	-283	2061	49
26	333	2061	34

$t = 0.57 \text{ s}$

particle #	x	y	z
1	-92	1405	110
2	153	1434	106
3	-255	1531	125
4	-168	1505	121
5	-150	1477	115
6	-44	1479	111
7	233	1522	91
8	29	1565	101
9	212	1587	104
10	252	1611	120
11	185	1637	103
12	344	1648	95
13	-728	1865	120
14	-583	1744	100
15	-196	1646	106
16	-297	1785	124
17	198	1736	123
18	492	1778	115
19	73	1987	162
24	431	2030	67
26	340	2019	24



Table B.2 (cont.): Three-dimensional tracking particle coordinates for Run 30-10a  
(dimensions in mm).

$t = 0.60$  s

particle #	x	y	z
1	-92	1402	110
2	153	1430	106
3	-259	1517	129
4	-169	1493	126
5	-151	1468	114
6	-44	1470	117
7	235	1511	121
8	31	1538	86
9	221	1557	89
10	262	1577	91
11	187	1596	133
12	342	1608	140
13	-735	1861	137
14	-592	1722	130
15	-198	1614	135
16	-301	1769	107
17	198	1711	137
18	495	1760	142
19	75	1985	130
24	443	1996	78
26	340	1971	49

$t = 0.63$  s

particle #	x	y	z
1	-93	1395	110
2	155	1420	118
3	-263	1492	132
4	-173	1472	124
5	-150	1451	119
6	-43	1452	122
7	240	1487	132
8	32	1501	130
9	220	1521	137
10	272	1537	77
11	191	1561	104
12	361	1575	96
13	-749	1857	138
14	-618	1708	100
15	-215	1568	27
16	-311	1747	135
17	204	1683	134
18	510	1745	144
19	73	1974	144
24	463	1977	79
26	347	1938	48



Table B.2 (cont.): Three-dimensional tracking particle coordinates for Run 30-10a  
(dimensions in mm).

$t = 0.67 \text{ s}$

particle #	x	y	z
1	-95	1383	116
2	155	1405	124
4	-179	1445	115
5	-156	1427	110
6	-45	1426	113
7	246	1454	128
8	32	1455	137
9	225	1483	128
10	269	1495	149
11	198	1524	105
12	366	1542	113
13	-771	1858	125
14	-641	1691	86
15	-207	1540	91
16	-320	1732	134
17	211	1657	122
18	529	1732	127
24	488	1955	78
26	360	1914	25

$t = 0.70 \text{ s}$

particle #	x	y	z
1	-95	1360	122
2	165	1380	116
4	-184	1403	118
5	-157	1392	114
6	-44	1388	117
7	256	1412	109
8	35	1404	118
9	234	1438	125
10	277	1456	136
11	198	1489	150
12	372	1513	144
13	-786	1854	127
14	-647	1668	132
15	-205	1508	158
16	-329	1719	134
17	212	1631	134
18	541	1723	143
24	513	1936	78

$t = 0.73 \text{ s}$

particle #	x	y	z
1	-102	1331	108
2	169	1342	116
4	-189	1355	127
5	-162	1341	105
6	-45	1340	113
7	268	1363	121
8	39	1352	120
9	240	1385	135
10	283	1417	145
11	203	1457	139
12	379	1481	147
13	-792	1847	144
14	-662	1657	118
15	-209	1479	146
16	-338	1713	134
17	221	1608	119
18	556	1714	130
24	536	1914	92
26	372	1859	99

$t = 0.77 \text{ s}$

particle #	x	y	z
1	-102	1284	108
2	173	1289	107
4	-195	1304	124
5	-164	1288	117
6	-46	1282	106
7	272	1309	118
8	39	1298	125
9	244	1341	131
10	293	1380	136
11	208	1425	142
12	389	1453	143
13	-819	1850	131
14	-681	1644	119
15	-213	1451	135
16	-350	1709	120
17	227	1584	135
18	569	1707	131
24	558	1894	106



Table B.2 (cont.): Three-dimensional tracking particle coordinates for Run 30-10a  
(dimensions in mm).

$t = 0.80 \text{ s}$

particle #	x	y	z
1	-104	1223	135
2	182	1237	108
4	-202	1255	125
5	-176	1223	150
6	-46	1223	113
7	283	1252	115
8	40	1245	118
9	249	1299	130
10	297	1348	140
11	215	1395	139
12	396	1428	141
13	-828	1850	133
14	-699	1634	121
15	-220	1421	132
17	242	1561	92
18	582	1705	132
24	595	1877	74

$t = 0.83 \text{ s}$

particle #	x	y	z
1	-106	1165	108
2	191	1171	90
4	-206	1203	126
5	-179	1164	112
6	-48	1158	97
7	294	1196	102
8	41	1196	126
9	256	1261	129
10	303	1315	139
11	217	1366	136
12	406	1404	132
13	-839	1856	41
14	-713	1624	123
15	-225	1391	117
17	245	1537	107
18	592	1705	130
24	621	1859	71

$t = 0.87 \text{ s}$

particle #	x	y	z
1	-111	1101	82
2	198	1109	75
4	-212	1153	123
6	-47	1093	89
7	304	1135	92
8	42	1146	116
9	262	1225	131
10	311	1284	138
11	227	1341	122
12	416	1380	138
13	-844	1853	136
14	-734	1616	109
15	-229	1368	122
17	256	1516	130
18	595	1705	130
24	635	1845	105

$t = 0.90 \text{ s}$

particle #	x	y	z
1	-110	1034	77
2	202	1043	69
4	-219	1100	107
6	-52	1027	72
7	311	1074	64
8	44	1097	114
9	269	1191	126
10	320	1259	126
11	230	1315	122
12	425	1359	131
13	-855	1857	122
14	-751	1610	112
15	-237	1341	93
17	266	1493	111
18	603	1711	118
24	675	1837	73

















University of Alberta Library



0 1620 1492 0506

**B45458**